UNIVERSITY OF SOUTHAMPTON

The Design of Adaptive Structures for Wing Morphing

by

Narcis M. Ursache

A thesis submitted in partial fulfillment for the
degree of Doctor of Philosophy

in the
Faculty of Engineering, Science and Mathematics
School of Engineering Sciences

June 2006

UNIVERSITY OF SOUTHAMPTON

ABSTRACT

FACULTY OF ENGINEERING, SCIENCE AND MATHEMATICS
SCHOOL OF ENGINEERING SCIENCES

Doctor of Philosophy

by Narcis M. Ursache

This research is concerned with the design of adaptive structures for achieving global multi-shape morphing aerodynamic configurations, by using slender structures. The proposed methodologies pursue two threads towards global optimisation of morphing structures, by providing means of aerodynamic enhancement, using efficient structural shape optimisation. A heuristic approach is proposed in this work that enables morphing through a range of stable cambered airfoils to achieve aerodynamic properties for different manoeuvres, with the benefit of low powered actuation control. This allows large changes in shape by exploiting a range of incremental non-linear structural solutions while keeping prescribed flow characteristics on an aeroelastically stable airfoil. Such an heuristic argument provides basis for global shape control of three-dimensional wings and is applied to aerodynamic design to provide enhanced roll control. A hierarchical strategy is employed, interleaving parameterisation enhancement followed by structural optimisation into the aerodynamic design process, such that the design paradigm, in conjunction with global approximation techniques, is emphasized by enhanced roll while drag is minimised. This figure of merit is complemented by structural metrics and constraints so as to maintain product integrity.

Contents

Declaration of Authorship **ix**

Nomenclature **x**

Acknowledgements **xii**

1 Introduction **1**
1.1 Morphing - Motivation and Challenges 1
1.1.1 Actuation Mechanisms, Smart Materials 2
1.1.2 Flow Control Devices 4
1.1.3 Wing Morphing Programs 4
1.2 Outline of the Thesis 6

2 Equilibrium Analysis of Slender Structures **8**
2.1 Global Shape Control Strategy 8
2.2 General Introduction to Geometric Non-Linearity 11
2.2.1 Sources of Non-Linearity 11
2.2.2 Levels of Analysis 12
2.3 Background to Non-linear Behaviour of Beam-Columns 14
2.4 General Considerations on Beam-Column Theory 16
2.5 Numerical Algorithms for Non-Linear Problems 19

3 Inverse Design of Structural Enhancements **21**
3.1 Optimisation Approaches 21
3.1.1 Inverse Aerodynamic Shape Design Methodologies 22
3.1.2 Structural Inverse Design 24
3.2 Single Shape Optimisation 25
3.2.1 Parameterisation Techniques 27
3.2.1.1 Discrete Approach (DA) 27
3.2.1.2 Hicks-Henne Bump Functions 30
3.2.1.3 Polynomial Curves 32
3.2.1.4 NURBS 34
3.2.2 Summary and Discussion 35
3.3 Morphing - Multi Shape Optimisation 36
3.3.1 Design Refinement with Pressure Residual Correction 41
3.3.2 Summary and Discussion 44

4 Aerodynamics of Morphing Airfoils **48**

4.1 Stating the CFD Problem . . . 48
4.2 Tuned Aerodynamics using Pressure Residual Correction . . . 52
4.3 Static Aeroelastic Study of Morphing Airfoils . . . 55
4.4 Summary . . . 61

5 Material Fitness **62**
5.1 Overview of Hyperelasticity . . . 62
5.2 Inverse Design of Constitutive Parameters . . . 64
5.3 Concluding Remarks . . . 73

6 Wing Morphing and Roll Control **75**
6.1 Formulation of the problem . . . 75
6.2 Wing analysis . . . 78
6.2.1 Parameterisation strategy . . . 78
6.2.2 Finite Element Formulation . . . 82
6.2.3 CFD Analysis . . . 85
6.3 Kriging and Model Validation . . . 86
6.4 Pareto Framework . . . 99
6.4.1 Roll Enhancement . . . 101
6.5 Concluding Remarks . . . 102

7 Conclusions **110**
7.1 What has been accomplished . . . 110
7.2 Future Research . . . 112

A Conventional Numerical Techniques **114**
A.1 Newton's Method . . . 114
A.2 Arc-Length Method . . . 115

B Aerodynamic Features of NURBS-based Morphing Airfoils **119**
B.1 Global Search . . . 119
B.2 Gradient Search . . . 121
B.3 Aeroelastic Study . . . 123

C Statistical Components **126**
C.1 Linear Least Squares Regression . . . 126
C.2 Weighted Least Squares Regression . . . 127

D Thin shell formulation **129**

E Global Approximation **132**
E.1 Overview of approximation methods . . . 132
E.2 Kriging . . . 134

References **140**

List of Figures

2.1 Structural set up for morphing shape optimisation. 9
2.2 Sensitivity of regular struts to eccentricity of loading (100 beam elements). 10
2.3 Mesh sensitivity of regular struts subject to 0.1% eccentricity of loading. . 10
2.4 Fundamental equilibrium paths. 14

3.1 Preliminary semi-thickness distribution, single-shape morphing beam, DA. 28
3.2 Sensitivity analysis of a 12 section parameterised beam, DA. 28
3.3 Augmented mapping scheme, semi-thickness distribution, single-shape morphing beam, DA. 30
3.4 The deflected states of the optimised single-shape morphing beams, 1% chord, stochastic search with GA and SA, DA. 30
3.5 Semi thickness of the optimised single-shape morphing beams, 1% chord, stochastic search with GA and SA, DA. 31
3.6 Semi thickness distribution of the optimised single-shape morphing beams, Hicks-Henne parameterisation scheme. 32
3.7 Deflected states of the optimised single-shape morphing cambers, Hicks-Henne parameterisation scheme. 33
3.8 Semi thickness distribution of the optimised beam shapes, Polynomial Approach. 34
3.9 Deflected states of the optimised cambers, Polynomial Approach. 34
3.10 Semi thickness distribution of the optimised single-shape morphing beams, NURBS. 35
3.11 Deflected states of the optimised cambers, NURBS. 36
3.12 Deflected beams and targets for initial set up, with no leading edge rotational restraint, cambers 2%, 5%, 10% and 15% chord, global search, DA. 38
3.13 Deflected beams and targets for final set up, with a leading edge linear rotational restraint, cambers 2%, 5%, 10% and 15% chord, global search, DA. 39
3.14 Target and computed airfoils for morphing-optimised beam in a range of deflection states: unstrained, 5%, 10%, global search, DA. 40
3.15 Residuals between optimised and target airfoils for morphing beam in the range of deflection states of 5% and 10%, global search, DA. 41
3.16 Morphing-optimised beam - semi thickness, global search, DA. 41
3.17 Multi-shape morphing airfoils in a range of deflection states: unstrained, 5%, 10%, global search, NURBS. 42
3.18 Residuals between optimised and target airfoils for morphing beam in the range of deflection states of 5% and 10%, global search, NURBS. 43
3.19 Semi thickness of multi-shape morphing beam, global search, NURBS. . . 43

3.20 Refined multi-shape morphing airfoils with pressure residual correction, DA. 44
3.21 Residuals between optimised and target airfoils for morphing beam in the range of deflection states of 5% and 10%, gradient search, DA. 45
3.22 Semi thickness, multi-shape morphing beam, gradient search, DA. 45
3.23 Refined multi-shape morphing airfoils with pressure residual correction, NURBS. 46
3.24 Residuals between optimised and target airfoils for morphing beam in the range of deflection states of 5% and 10%, gradient search, NURBS. 47
3.25 Semi thickness, multi-shape morphing beam, gradient search, NURBS. . . 47

4.1 Typical computational grid for a morphing airfoil. 49
4.2 'M − α' envelope of converged CFD runs on DA parameterised airfoil (global search), where '$\triangleleft$' represents successful runs for the computed airfoil and '$\triangleright$' for the target. 51
4.3 Pressure distributions for morphed and target airfoils (global solution), under mild flow conditions, DA. 52
4.4 Pressure distributions for morphed and target airfoils (global search), under severe flow conditions, DA. 53
4.5 Drag polars for 5% and 10% cambers (global search), DA. 53
4.6 Variation of lift coefficient vs. angle of attack with Mach number, for 5% and 10% cambers (global solution), DA. 54
4.7 Refined pressure distributions for multi-shape morphing airfoils, under mild and severe flows, DA. 55
4.8 Refined drag polars for morphed airfoils, DA. 55
4.9 Variation of lift with incidence for gradient-based optimum solution, 5% and 10% cambers, DA. 56
4.10 Airfoil aeroelastic workflow. 57
4.11 Aeroelastic convergence studies, with relaxation factor $\beta = 0.2,\ , 0.4,\ 0.6,$ DA. 58
4.12 Aeroelastic stability, $\beta = 0.6$, DA. 59
4.13 Aeroelastic pressure distributions, $\beta = 0.6$, DA. 60
4.14 Rigid and aeroelastic airfoils, $\beta = 0.6$, DA. 60

5.1 5% and 10% camber to chord ratio strut deformation with hyperelastic material. 66
5.2 Optimal analytical and experimental airfoils 67
5.3 Residuals between optimised hyperfoam and target airfoils in the range of deflection states of 5% and 10%. 68
5.4 Pressure distributions of 5% and 10% hyperelastic airfoils. 69
5.5 Aerodynamic properties of 5% and 10% hyperelastic airfoils. 69
5.6 Drag polars of 5% and 10% hyperelastic airfoils. 70
5.7 Comparison of pressure distributions of different fitted hyperelastic airfoils for cambers = 10% chord at M = 0.5 and $\alpha = 1$ deg. 71
5.8 Stress contours of hyperlastic airfoil. 72
5.9 Strain contours of hyperlastic airfoil. 73

6.1 Wing planform with typical inboard and outboard patches. The highlighted outboard wing patch is actuated by point forces at the trailing edge of grid sections 'sec 1' and 'sec 3'. Structural related objectives are applied to the sections 'sec' 1, 2 and 3. 76
6.2 Pressure contours of the baseline wing. 79
6.3 Sequential wing workflow (SWF) 80
6.4 Optimisation strategy. 81
6.5 Outboard NURBS parameterisation and a random thickness distribution of the plate during the optimisation process. 82
6.6 Outboard finite element discretisation and the corresponding stress state of the randomly parameterised outboard patch from Figure 6.5. 84
6.7 Shell-to-solid eccentricity coupling. 85
6.8 A common boundary-fitted aerodynamic grid for wings. 86
6.9 Objective f_1 - goodness of fit statistics, full Krig (39 hyper-parameters). . 91
6.10 Objective f_{sec1} - goodness of fit statistics, full Krig (39 hyper-parameters). 92
6.11 Objective f_{sec2} - goodness of fit statistics, full Krig (39 hyper-parameters). 92
6.12 Objective f_{sec3} - goodness of fit statistics, full Krig (39 hyper-parameters). 93
6.13 Constraint g_1 - goodness of fit statistics, full Krig (39 hyper-parameters). 93
6.14 Constraint g_2 - goodness of fit statistics, full Krig (39 hyper-parameters). 94
6.15 Objective f_1 - goodness of fit statistics, reduced Krig (3 hyper-parameters). 96
6.16 Objective f_{sec1} - goodness of fit statistics, reduced Krig (3 hyper-parameters). 96
6.17 Objective f_{sec2} - goodness of fit statistics, reduced Krig (3 hyper-parameters). 97
6.18 Objective f_{sec3} - goodness of fit statistics, reduced Krig (3 hyper-parameters). 97
6.19 Constraint g_1 - goodness of fit statistics, reduced Krig (3 hyper-parameters). 98
6.20 Constraint g_2 - goodness of fit statistics, reduced Krig (3 hyper-parameters). 98
6.21 Full Krig definition, NSGA2 search, Pareto fronts. Filled symbols represent the solvable points from local Pareto front with the true function. Empty symbols are the corresponding points evaluated with the true function. 101
6.22 Reduced Krig definition, NSGA2 search, Pareto fronts. Filled symbols represent the solvable points from local Pareto front with the true function. Empty symbols are the corresponding points evaluated with the true function. 102
6.23 Pressure contours of a design validated point (full Krig), Pareto front $f_1 - f_{sec1}$ 103
6.24 Pressure contours of a design validated point (full Krig), Pareto front $f_1 - f_{sec2}$ 104
6.25 Pressure contours of a design validated point (full Krig), Pareto front $f_1 - f_{sec3}$ 105
6.26 Camber contours for the design validated points (full Krig) from Pareto fronts $f_1 - f_{sec1}$, $f_1 - f_{sec2}$ and $f_1 - f_{sec3}$. 107
6.27 Roll enhancement of a design validated point (full Krig), Pareto front $f_1 - f_{sec1}$ 108
6.28 Roll enhancement of a design validated point (full Krig), Pareto front $f_1 - f_{sec2}$ 108
6.29 Roll enhancement of a design validated point (full Krig), Pareto front $f_1 - f_{sec3}$ 109

A.1 Riks Algorithm. 117

B.1 Envelope of converged CFD runs on NURBS parameterised airfoil (global search), where '$\triangleleft$' represents successful runs for the computed airfoil and '$\triangleright$' for the target. 119
B.2 Pressure distributions for morphed and target airfoils (global search), under mild flow conditions, NURBS. 120
B.3 Pressure distributions for morphed and target airfoils (global search), under severe flow conditions, NURBS. 120
B.4 Drag polars for 5% and 10% cambers (global search), NURBS. 121
B.5 Variation of lift coefficient vs. angle of attack with Mach number, for 5% and 10% cambers (global search), NURBS. 121
B.6 Pressure distributions for morphed and target airfoils under severe flow conditions (gradient search), NURBS. 122
B.7 Variation of lift with incidence across 5% and 10% cambers (gradient search), NURBS. 122
B.8 Drag polar for 10% camber (gradient search), NURBS. 123
B.9 Aeroelastic convergence studies, with relaxation factor $\beta = 0.2,\ 0.3,\ ,0.4,\ 0.6,$ NURBS. 123
B.10 Aeroelastic stability, $\beta = 0.4$, NURBS. 124
B.11 Aeroelastic pressure distributions, $\beta = 0.4$, NURBS. 124
B.12 Rigid and aeroelastic airfoils, $\beta = 0.4$, NURBS. 125

List of Tables

3.1 Summary of single-shape morphing beam optimisation 36

5.1 Parameters for the hyperfoam materials with $N = 2$. 70

6.1 Hyperparameters, full RSM, objectives 1 and 3 94
6.2 Hyperparameters, full RSM, objective 4 and constraints 95
6.3 CLF convergence, full RSM 95
6.4 Hyperparameters, reduced RSM, objectives and constraints 95
6.5 CLF convergence, reduced RSM 99

DECLARATION OF AUTHORSHIP

I, Narcis Marian Ursache, declare that the thesis entitled 'The Design of Adaptive Structures for Wing Morphing' and the work presented in it are my own. I confirm that:

- this work was done wholly or mainly while in candidature for a research degree at this University;
- where any part of this thesis has previously been submitted for a degree or any other qualification at this University or any other institution, this has been clearly stated;
- where I have consulted the published work of others, this is always clearly attributed;
- where I have quoted from the work of others, the source is always given. With the exception of such quotations, this thesis is entirely my own work;
- I have acknowledged all main sources of help;
- where the thesis is based on work done by myself jointly with others, I have made clear exactly what was done by others and what I have contributed myself;
- parts of this work have been published as:

  1. N. M. Ursache, A. J. Keane, and N. W. Bressloff. The Design of Post-Buckled Spinal Structures for Aifoils Camber and Shape Control. *AIAA Journal*, 2006 - provisionally accepted for publication.

  2. N. M. Ursache, A. J. Keane, and N. W. Bressloff. On the Design of Morphing Airfoils using Spinal Structures. *47th AIAA/ASME/ASCE/AHS/ASC Structures, Structural Dynamics, and Materials Conference*, 2006, 1-4 May, Newport, Rhode Island, AIAA 2006-1796.

  3. N. M. Ursache, A. J. Keane, and N. W. Bressloff. The Design of Adaptive Wings using Spinal Structures. *AIAA Journal* (submitted for review).

  4. N. M. Ursache, A. J. Keane, and N. W. Bressloff. The design of post-buckled spinal structures for airfoil shape control using optimization methods. *Proceedings of the 5th ASMO UK/ISSMO Conference on Design Optimisation*, 2004, 12-13 July, Stratford-upon-Avon.

Signed:

Date:

Nomenclature

AAW	Active Aeroelastic Wing
CAD	Computer Aided Design
CFD	Computational Fluid Dynamics
CLF	Concentrated Likelihood Function
CSD	Computational Structural Dynamics
DA	Discrete Approach
DHC	Dynamic Hill Climbing
DoE	Design of Experiments
FEA	Finite Element Analysis
FSI	Fluid-Structure Interation
GA	Genetic Algorithm
HH	Hicks-Henne Bump Functions
IRLS	Iteratively Reweighted Least Squares
MAV	Micro-Air Vehicle
MDO	Multidisciplinary Optimisation
NACA	National Advisory Committee for Aeronautics
NSGA	Non-dominated Sorted Genetic Algorithm
NURBS	Non-Uniform Rational B-Splines
OLS	Ordinary Least Squares
RMSE	Root Mean Square Error
RSM	Response Surface Methodology
SA	Simulated Annealing
SMA	Shape Memory Alloy
SWF	Sequential Work Flow
SWP	Smart Wing Program
UAV	Unmanned Air Vehicles
f	objective function
f_a	aerodynamic loading
f_{sec}	structural related objective function
$\hat{f}$	approximation of objective function
p, θ	Kriging hyperparameters
λ	Kriging regularisation constant

α	angle of attack
β	relaxation factor
E	Young's modulus
M	Mach number
σ	variance of a Gaussian distribution
α_i, β_i	hyperelastic material parameters
μ_0	initial shear modulus
μ_i	shear modulus coefficients
ν_i	Poisson coefficient
$\boldsymbol{\tau}$	Kirchhoff stress
$\boldsymbol{\epsilon}$	strain
g_i	constraint functions
$\mathbf{x}$	vector of design variables
$\mathbf{w}$	optimised displacement field
$\mathbf{w}^t$	target displacement field
n_i	maximum number of increments
n_p	maximum number of structural grid points
a	structural displacement bounds
C_L, C_l	lift coefficient
C_m	pitching moment coefficient
C_D	drag coefficient
C_P	pressure coefficient
C_M	roll moment coefficient
R^2	coefficient of determination
LE_{ij}	component ij of logarithmic strain
Re	Reynolds number
N	order of a hyperelastic material
s_{ij}	component ij of Cauchy stress tensor
sspan	semispan
Y_{CP}	y position of centre of pressure

Acknowledgements

I am deeply indebted to my supervisor, Prof. Andy J. Keane, for providing me his inexhaustible storehouse of knowledge that pervades this thesis. Working and interacting with him fostered my intelectual and scholarly development throughout my time in Computational Engineering and Design Group. His constant search for excellence pursued in guidance and his contribution to this work has been invaluable. I would also like to express my sincere gratitude and appreciation to my co-supervisor, Dr. Neil W. Bressloff for the constant support and advice during the progress of this research.

My gratitude is extended to all the people within the CEDG that have aided and supported my quest for expertise. The attention to details of Dr. András Sóbester imbued in me a great deal appreciation and knowledge on design optimisation and his advice, promptness and corrective nature is very much appreciated. This research could not have been done without the availability of the grid based computing cluster environment, implemented and technically supported by Ivan Voutchkov, Wenbin Song and the GEODISE team, who significantly contributed to the success of the large computations. I acknowledge Gerardo Veredas from Airbus Spain for his invaluable input on API. I would also like to acknowledge Cosmin Papuc from Airbus UK, Andrei Secareanu, Jim Banks, Vijaya Bhaskar and Sachin Sachdeva for the innumerable random discussions, sharing their expertise on everything under the sun.

I gratefully acknowledge Dr. Osvaldo M. Querin and Dr. Guglielmo S. Aglietti for serving on the advisory committee, taking time to review the thesis and providing me their valuable and constructive comments to complete this dissertation.

The financial support is *condicio sine qua non* of research. The present work was supported by a grant from the Faculty of Engineering, Science and Mathematics at the University of Southampton and is deeply acknowledged.

Finally, I dedicate this thesis to my loving and unfailingly supportive family, especially Tudor, whose smile, true love and happiness have given me strength and motivation to complete this marathon.

Chapter 1

Introduction

1.1 Morphing - Motivation and Challenges

The recent advances in new materials and structures have created much interest in bringing to life adaptive structures that can 'morph' through different states and meet specific environment requirements or mimic nature. Much of these technologies and applications allow large changes in shape to maximise performance and efficiency. In particular, this translates into the need for an optimum flight envelope, specific reconfiguration during different mission segments, improved manoeuvrability, increased survivability, optimum weight, etc. Aircraft efficiency also implies manufacturer's and operator's effort, as energy or monetary units (Gilyard et al. (1999)) to achieve a favorable airframe configuration. This requires a design paradigm to control mainly the aerodynamic features during the adaptation to the new environment.

Flow control represents the *sine qua non* of the aerodynamic morphing concept. The study of interaction between fluid dynamics and structures (normally referred to as FSI) has matured in the latter part of the 20th century, to provide means of changing mission environments during flight. Such technologies can be easily claimed by pioneering polymorph planes, e.g., the tilt-rotor V-22 Osprey, swing-wing F-111 Aardvark or F-14 Tomcat. The difficulties of accommodating additional mechanisms for variable geometries and low fuel efficiency make it very difficult to achieve significant advancements in this field.

The availability of new technology and improved analytical tools has, however, opened up many new possibilities for multi-structural systems. Smart aero-structures and compliant control surfaces have consequently become a potential way forward in the development of adaptive wings. Enhancements for wings are being developed to improve their efficiency in off-design regimes. Such implementations are, apart from variable planform, related to effective camber through adaptive structural concepts (also referred to

as flexible, deformable of active structures which allow control of the geometry to adapt to the required flow) or fluidic (mainly used to control the boundary layer such that it is adapted to the geometry).

Modern wing morphing concepts require a structure within the wing that can continuously change the shape of the wing in flight to alter the flow stream and achieve enhanced or changed aerodynamic properties, without the hinge contour discontinuity associated with articulated surfaces. There is a great deal of current interest among aircraft designers in such shape control systems, primarily because engineers seek designs that have low radar or acoustic signatures. An immediate pay-off of such technology is that hingeless control surfaces augment roll performance and reversal speed (Khot et al. (1998), Gern et al. (2002)).

Flapless, variable geometry airfoils are, of course, not a new idea. The original Wright Brothers Flyer used a "wing warping" concept to provide control, following developments with gliders (Anderson (1978)). Ailerons had not been invented at that stage and the Brothers suggested that their approach would provide benefit in flying an aircraft. Their control system worked by pulling on a set of external steel wires which twisted the wing tips relative to the rest of the wing.

1.1.1 Actuation Mechanisms, Smart Materials

Since the 1980's researchers have investigated the use of fully-integrated *smart structures* for performance and shape control to enhance or mimic deformable flight devices. In these cases, the wing becomes adaptive in the sense that it can change its profile spanwise and chordwise to adapt to flow conditions by controlled transitions from one airfoil shape to another, as required for a particular mission. The adaptive strategy resides in geometry parameters that change globally or locally to enhance flight efficiency. Global changes are desirable in the literature by means of mechanical actuation approaches or compliant devices. On a local scale, deformable surfaces can be enhanced or replaced by micro-surface effectors (e.g., piezoelectric actuators or shape material alloys) or fluidic devices (e.g., synthetic jet actuators that adapt the boundary layer to the geometry). Such approaches offer further potential for controlling the baseline aerodynamic characteristics of the airfoil.

For global shape morphing, a number of complex schemes of internal actuators have been proposed in the literature to augment the morphing concept. For instance, Austin et al. (1994) proposed a model with active ribs by means of translational actuators to reduce shock induced drag in cruise flight conditions. At an early stage of a such an approach, flow control can be yet achieved by means of wing thickness change, based on optimised lightweight and reliable actuation schemes. Extensive research into the physics of FSI of the baseline morphing structure has been proposed by Gern et al. (2002). Their complex

actuation scheme, used to deform a plate-like lambda wing, generates equivalent torsions seeded at span-wise rib stations, thus making manoeuvre control of the aircraft possible.

For local shape changes, smart materials using piezoelectric actuators or shape memory alloys (SMA) are mentioned in the literature. For instance, an experimental model has been proposed by Seifert et al. (1998). The airfoil was seeded with piezoelectric actuators chord wise and upstream of the separation point, to interact with the boundary layer. Such an approach led to enhanced aerodynamic properties in terms of improved lift coefficient and lift-drag ratio. Similarly, Munday and Jacob (2001) and Pinkerton and Moses (1997) used an internally mounted piezoceramic Thunder actuator (i.e., Lead Zirconate Titanate) to change the effective camber of the airfoil via a flexible skin, and thus, control on the boundary layer separation is possible. The smart material deflection is *a priori* driven by a voltage, and leads to augmented upper surface curvature, with the benefit of enhanced lift and drag, but with an overall negative impact on aerodynamics at low Reynolds numbers. Placed span wise, such actuators would provide an immediate roll control, if deflected sequentially.

Chaundhry and Rogers (1991) investigated the use of external shape memory alloy (SMA) actuators for shape control of beams. The structural deformation is *a priori* determined by discrete span wise locations of the actuators. The deformation gradient of the beam can be augmented if imperfections or eccentricities are considered, to trigger post-critical regime, enhancing the authority of the actuator. Such behavior would not readily be exhibited by bonded smart materials, however, as the strain actuation is rather transversal. The study also shows that SMAs have a large stroke for modest bandwidth, which is in contrast to piezoelectric actuator systems which feature small strain at high frequency bandwidth, outlined by a similar example with a moon shape-like actuator by Lalande et al. (1995). Such limitations are also emphasised in a comprehensive review of structures and materials by Frecker (2003). Perhaps an optimised structure might encapsulate both definitions of smart materials, to enhance its properties. The performance of many mechanical structures, such as antenna reflectors and adaptive wings is related to local shape control. Various adaptive shape systems applied in conditions of high-precision operation and finite deformation have been investigated Balas (1985), and Yoon et al. (2000) using piezoelectric actuators.

The use of smart structures such as compliant mechanisms to achieve local shape control has also been suggested by Saggere and Kota (1999). Such mechanisms rely on flexible structures that can deform the attached surface under an input actuation. The performance of the actuation is strictly related to the output to the environment and usually involves truss/beam structures that need to be optimised to keep the aerodynamic surface smooth. This synthesis method proved to be viable for practical applications, but still required design experience or intuition. A more generalised scheme of two-dimensional compliant mechanism systems with multiple output points, has been been approached in Lu and Kota (2003) for the topology and dimensions of the structure.

Such problems are often tackled by inverse design of a morphing boundary, where a metric with respect to a target boundary is achieved.

1.1.2 Flow Control Devices

The morphing concept applies not only to structural deformations, but also to local flow control, by means of passive, active or reactive techniques that mimic effective camber and optimise aerodynamic forces. The passive methods are the simplest and seek to shed the laminar flow by inducing a favorable pressure gradient. Vortex generators (which re-energise the boundary layer and prevent flow separation), porous surfaces (Rasheed (2001)) or stall strips (which disturb the boundary layer and so preserve maximum lift capability, but deteriorate handling qualities) are just a few techniques that fall into this category. Active control devices reshape the boundary layer through an open or closed loop control methodology. These methods have come a long way since 1950-1960's, when experiments on cross-flow instabilities on swept wings had been performed using suction(Carmichael and Pfenninger (1957) and Carmichael et al. (1957)). Subsequent experiments had been performed on the F-111 and F-14 and also the F-16XL for laminar flow control by NASA (Norris (1994)) and the tail fin of an A320 (Collier (1993)). Similarly, blowing, synthetic jet actuators, and solid surface relative motion have all been tried. Reactive control is characterised by a closed loop control technique in order to delay separation and imply more complicated structural schemes and in-depth knowledge of instability waves under controlled acoustic or vibrating environments.

By and large, passive devices are built from miniature surface-mounted obstructions to control turbulence and onset or spread of boundary layer separation, whereas active controllers tend to rely on tubes and pumps within the enclosure of the wing, leading to significant weight increase, but with the pay-off on improvement of flight characteristics. For instance, Crowther (2005) made use of jet vortex generators to control relaxation of high lift devices, by recovering the effective camber. Similarly, the effectiveness of such virtual reshapes is studied by Gilarranz et al. (2005a,b) at high angles of attach with variable exit slot geometry, for full-scale flow control applications, whereas Chatlynne et al. (2001) and Chen and Beeler (2002) studied the same profiles under low incidences, with diminished virtual shape control if the jet is under the separated flow.

1.1.3 Wing Morphing Programs

Given such a strong theoretical background, US government sponsored research programs have developed applications to investigate their feasibility in practice. The Defense Advanced Research Projetcs Agency (DARPA)/NASA/Air Force Research Laboratory (AFRL) project, led by a Northrop Grumman Corporation (NGC) team, was built on the Smart Wing Program (SWP). Its purpose was to explore the benefits of

smart materials and structures in aircraft structures. In the first phase, the program developed adaptive wing structures based on mechanical actuation and SMAs to provide optimal aerodynamic shapes, with performance gains on pitching moment and roll moment (Sanders et al. (2003), Scherer et al. (1997), Kudva (1999), Martin et al. (1999)). In another programme, rigid link mechanisms were used for the Mission Adaptive Wing, which was developed on a F-111 test bed (Bjarke (1990)), where automated electrical systems (i.e., smoothing camber devices) replaced high-lift and lateral control to improve stability (Gilyard (1997); Gilyard et al. (1999)). This ended in 2001, when the program culminated with the demonstrations of hingeless control surfaces augmenting aileron effectiveness and lift by 17% (Scherer et al. (1999), Kudva (2004)).

In the Active Aeroelastic Wing (AAW) programme, another AFRL/NASA effort, the impact of aerodynamic forces on morphing surfaces was studied to enhance manoeuvrability of high-performance aircraft. The goal was a test bed of a full-size F/A-18, with active controls and optimised structural aeroelastic performance (Voracek et al. (2003); Diebler and Cumming (2005)). Significant roll control was gained by differential actuation of inboard and outboard leading edge flaps, while reducing the wing weight by up to 17 percent.

One of today's most ambitious programs, funded by DARPA, the Morphing Aircraft Structures programme (MAS) develops multidisciplinary technologies integrated into the aircraft structure and aerodynamics. These studies are enhanced by previously investigated approaches to provide systems robustness, aerodynamic performance during complex military missions and the ability to morph without reconfiguration. Some interesting designs have been proposed by the main contractors of the program, i.e., NextGen and Lockheed (Love et al. (2004)). University research level works are also present in the literature: Neal et al. (2004) proposed a fully scalable morphed aircraft by means of variable wing twist, camber, sweep and span; Cadogan et al. (2004) eliminated mechanical actuation, by using inflatable wings on UAVs, and enhanced roll control is achieved by means of piezoelectric actuators in lieu of the conventional hinge line.

Unmanned Air Vehicles (UAVs) have been a significant subject of interest over recent decades. Historically, UAVs were designed to maximise endurance and range during flight, but lately the role of aerodynamics on the UAVs has been emphasised, enhancing the manoeuvrability in complex multi-role missions. The problems raised imply an inherent trade-off between endurance-range and manoeuvrability within the same design. This difficulty is investigated in Gano et al. (2003) on a buckle-wing UAV, by splitting the initial one-shape wing configuration into two parts linked during morphing, with the benefit of augmented coupled performance.

The morphing concept has also been successfully applied to Micro Air Vehicles (MAV) (i.e., a small-sized class within the general class of UAVs). The benefits of low mass, simplicity of design concept and low maintenance provide significant benefit for both

military and civilian aviation. Lind et al. (2004) and Abdulrahim et al. (2005) proposed several uncoupled active control laws for morphing of a MAV (i.e., twisted, curled and gull wings) with high agility manoeuvring, but the results are somewhat limited due to the aerodynamics and the lack of pressure sensors on the MAV.

1.2 Outline of the Thesis

Having briefly set out the background to existing morphing technology, this thesis considers a novel approach for achieving global multi-shape morphing aerodynamic configurations by using slender buckled structures. This work pursues two threads towards global optimisation, by providing means of aerodynamic enhancement during morphing using efficient structural shape optimisation.

When controlling the shape of a wing, internal structures must be used. The displacement field that results from the actuation function determines a structural-related metric that is intrinsically linked to the overall aerodynamic performance of the system. Here, such a metric is *a priori* derived by the structural configuration and the longitudinal loading function through an outer cladding that forms the aerodynamic shape. Given the space and weight restrictions that apply inside aircraft wings, design requirements lead to the need for simple yet powerful ways of controlling the airfoil external shape. Therefore, it is desirable to address some of the key problems identified in existing research in this field, i.e., the complexity of the internal actuator schemes currently needed (Kudva et al. (1995)), the difficulties associated with scaling them to relatively large, heavily loaded airfoils and excessive power consumption (Stanewski (2001)).

Non-linear post-critical structural deformation theory provides the analytical background for the global shape control law proposed in this thesis. Described in Chapter 2, the non-linear considerations of slender structures are highlighted in broad terms for easy access to the underlying theory.

To enhance the performance of the spinal structures, a two-pronged optimisation process is performed. Chapter 3 provides the background to a number of parameterisation schemes analysed in conjunction with the metrics chosen. The first metric is emphasised by a global structural optimisation following a single-shape morphing control law, whereas the secondary metric is related to enhanced structural features of the spinal structures, by means of multi-shape morphing control law.

Subsequently, Chapter 4 has a similar flavor, but from an aerodynamic perspective. The aircraft structures are modeled for different flight conditions, and the aerodynamic features of the optimum structural configuration are derived. Since a global structural search would not guarantee a minima in the landscape of the aerodynamic function, a secondary local search is necessary to augment the aerodynamic properties. These are

presented along with a static aeroelastic study of the multi-shape morphing optimum airfoil.

Here, the optimised airfoils have been constructed from the beginning using an implicit definition of four-digit NACA thickness distribution, but the mean camber line is controlled by a deforming structure, since it is given by the spinal system. This approach assumes a non-responsive aerodynamic cladding during deformation of the multi-shape morphing airfoils. A means to improve upon the established implicit correlation between the spinal structure and the aerodynamic surface is investigated in Chapter 5. This study adds a practical touch to the present global shape control law, by means of a material fitness (the cladding), i.e., an inverse design of the constitutive parameters of a hyperelastic material. This chapter also provides a background on material studies for the subsequent optimisation studies.

Moving on to the three-dimensional case of the scheme investigated in this thesis, Chapter 6 deals with global approximation of wings that provide good aerodynamic properties and roll control. The global shape control approach is based on slender plates. Such analyses usually rely on sequences of parameterisation, structural analysis and aerodynamic assessment, and the large computational costs involved lead to the use of response surface models in lieu of direct searches. The goal of this approach allows enhanced wings that rely only on low power actuation systems (McGowan et al. (2002)).

Chapter 7 concludes with a summary of the steps achieved during this work, and emphasises the topics that need to be further investigated using the current approaches for global shape control.

Chapter 2

Equilibrium Analysis of Slender Structures

This chapter provides a summary of the theoretical background for slender structures. To provide perspective for the use of spinal structures, the nonlinear control-state responses are discussed. Strategies for the numerical solutions of nonlinear equations are emphasised to provide an insight into appropriate structural engineering analysis.

2.1 Global Shape Control Strategy

Wing morphing technology involves changing control surface shapes during flight to provide varying aerodynamic properties (i.e., for changes in mission or maneuver). The means of airfoil reshaping presented in the literature mainly focus on targeted local changes using a flexible outer skin (see for instance the studies by Saggere and Kota (1999) and Natarajan et al. (2004)). A flexible outer skin is also adopted here, but in contrast to much of the work reported in the literature, the entire airfoil shape is altered. This global reshaping is achieved by distorting a slender internal spinal structure which is attached to a hyperelastic outer cladding that forms the aerodynamic surface of the morphed airfoil. Since each manoeuvre during flight may require a different camber configuration, the system proposed here morphs through a significant camber range using an incremental loading scheme. This allows a series of target aerodynamic shapes to be realised (in this study a set of NACA-four digit airfoils).

The spinal structure considered here is a simply supported Euler strut subject to an eccentric load, as depicted in Figure 2.1 (n.b., the eccentricity is exaggerated in the figure to highlight the asymmetrical nature of the loading). The unloaded strut is connected to a flexible outer cladding of airfoil shape via a foam core (here a base-line un-cambered NACA-four digit thickness definition is chosen for its analytical simplicity).

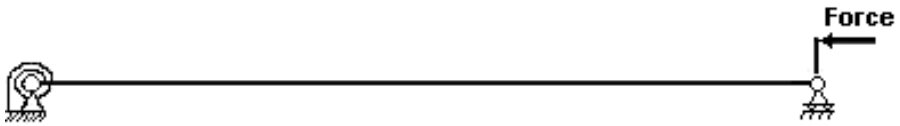

FIGURE 2.1: Structural set up for morphing shape optimisation.

This provides a datum symmetrical shape, with the camber line identical to the neutral fiber of the spinal structure. To change this shape the strut is loaded and allowed to buckle so that the camber line of the airfoil is then curved, taking the foam core and entire outer skin with it. Obviously, if the strut were uniform this would lead to a half sine wave spinal shape (given by the first structural eigenmode) whose amplitude is intrinsically controlled by the end point load - such a curve is not very helpful as a camber line although, given the airfoil shaped foam core proposed, a range of airfoil shapes with varying cambers is nonetheless generated. If, however, a strut with varying structural properties is used (for example varying lateral stiffness, material, etc.) the strut ceases to take up such a simple deflected shape when loaded. By suitable choice of material properties, shapes that resemble camber profiles can then be derived. This naturally leads to an inverse structural design problem that can be solved to achieve NACA-like (or any other) camber shapes and thus a range of suitably cambered airfoils. Since for airfoil definitions like the NACA series, the overall aerodynamic shape is separable between thickness distribution and camber line, this means that the morphing process can be made to sweep through an entire NACA series provided the spinal structure deflects through the required series of camber shapes. Moreover this series of shapes is generated using a single actuator - control simplicity being achieved by structural sophistication. It is noted in passing that this basic idea could also be applied to control of twist or dihedral by using appropriately placed struts.

As well as overall shape control, the adoption of a buckled spinal structure allows for changes in shape with modest force levels. Figure 2.2 shows the impact of end forces for struts with varying degrees of eccentricity in their end loading (n.b. here, a 1000 mm strut is discretised into 100 linear elements with width=8 mm and height=4 mm, assuming its operational elastic range with Young's modulus E=209 GPa and Poisson coefficient $\nu = 0.3$. The choice of this mesh density comes after a mesh sensitivity analysis showed in Figure 2.3, with no significant solution improvement for meshes consisting more than 100 elements. Consequently, throughout this work, the struts under investigation consist 100 elements mesh density). It is clear that if the end loads are varied at levels close to the critical Euler buckling load then large changes in deflections can be achieved with modest changes in end force level. Therefore, in the work presented here the structural systems proposed are operated with forces close to their critical loads.

Since the aim during operation is to move the spinal structure smoothly between a series

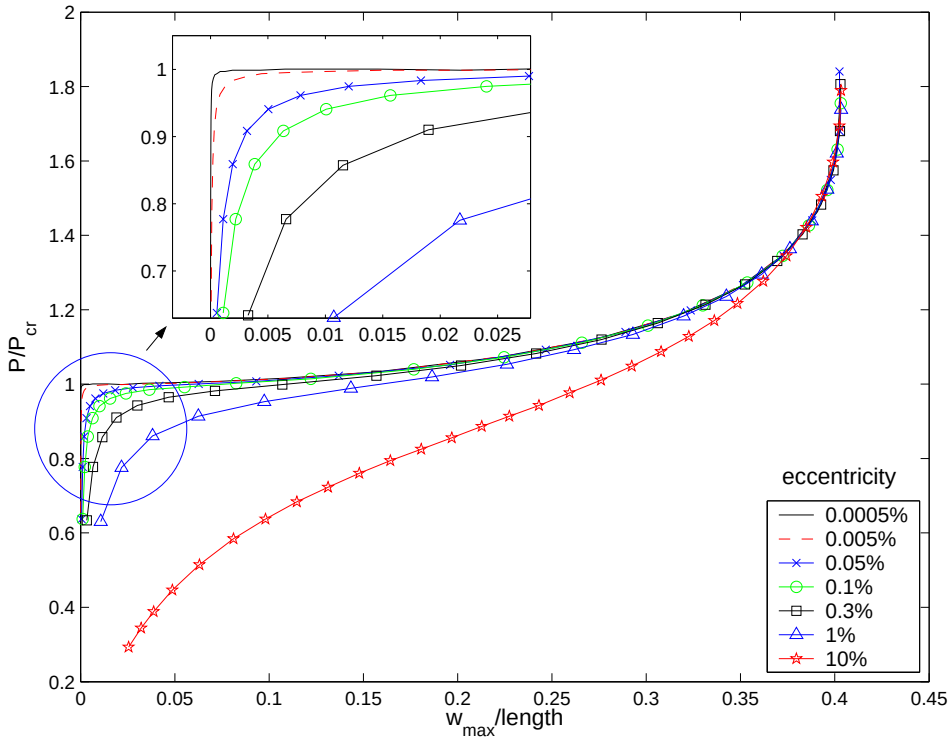

FIGURE 2.2: Sensitivity of regular struts to eccentricity of loading (100 beam elements).

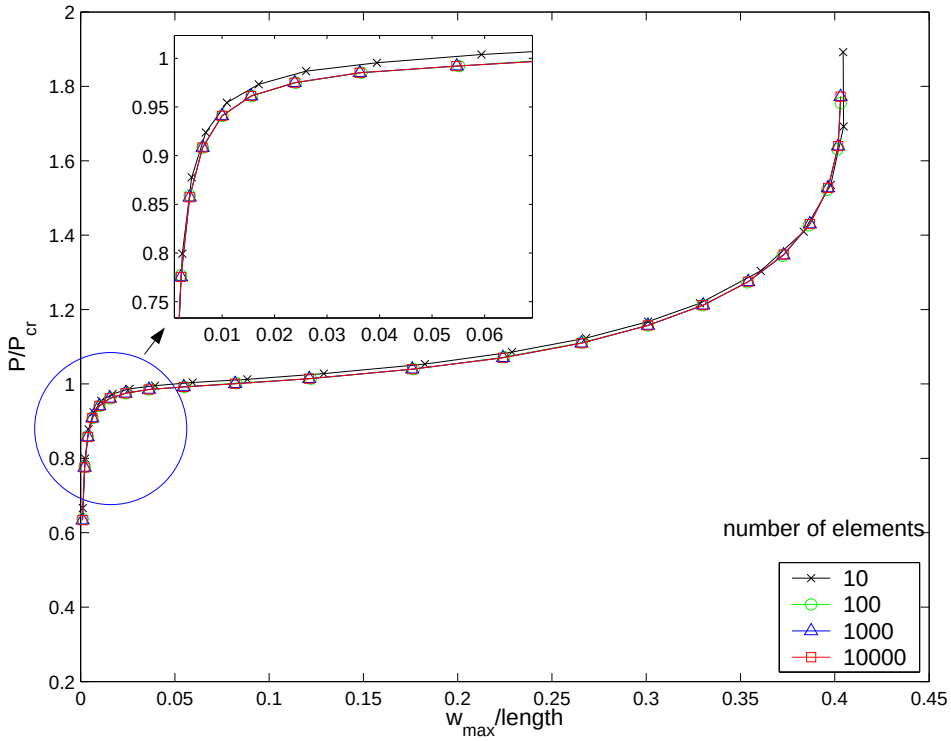

FIGURE 2.3: Mesh sensitivity of regular struts subject to 0.1% eccentricity of loading.

of pre-defined camber line shapes it is necessary to find structures that deform through such shapes during their post-buckling behavior - this is, of course, more difficult than finding a strut that produces a single desired camber line at one fixed load value. To solve this problem a non-linear finite element analysis is performed using an incremental loading scheme (Wempner (1971), Riks (1972), Crisfield (1997)), with a static equilibrium being obtained after each load increment. This allows the full range of shapes possible for any particular material layout to be assessed. Then, during design, optimisers are used to try and match these shapes to a series of NACA camber lines by adjusting the properties of the strut. Inevitably such matches cannot be perfect throughout the range of loading but surprisingly good agreement can be achieved so that the resulting sequences of wing morphs are remarkable close to the desired airfoil shapes. The quality of these shape sequences are assessed in later chapters using full potential Computational Fluid Dynamics (CFD) simulations and compared to those of the target airfoils. Even when there are slight differences between the shapes considered, the differences in the resulting pressure distributions are modest. To minimise such differences, a second optimisation process can be entered which seeks to further refine the structural design by assessing a metric related to the achieved pressure distributions of the deformed airfoils (i.e., least squares formulation), requiring linked CFD and structural analyses.

It should be noted that, throughout the structural optimisation sections, it is assumed that the applied foam core on to the spinal structure exhibits a minimal volumetric response. This assumption is made because of the prohibitive computational cost of a full coupled analysis. Consequently, the airfoils constructed during optimisation are *ab initio* based on the analytical definition of the four-digit NACA thickness distribution. Means to improve upon established implicit correlation between the deflected spinal structure and the theoretical airfoil surface are examined in Chapter 5.

2.2 General Introduction to Geometric Non-Linearity

An insight into the non-linear response of structures is necessary to capture large scale deflection behavior via analytical mathematical algorithms or computational methods.

2.2.1 Sources of Non-Linearity

If there is a linear relationship between the applied loading function and the response of a structural system, then a linear analysis suffices. In such cases the response of the structure needs to be calculated only once, and then solutions may be superimposed to determine the complete response of the system. This principle of solution assumes that the same boundary conditions are used for all the solutions. If the stiffness matrix

depends on the displacement, the flexibility can no longer be obtained by a linear analysis. In this case each solution must be defined and solved as a separate case and the structural behavior is referred to as nonlinear.

There are four sources of nonlinearity in structural mechanics simulations:

- material nonlinearity - occurs at finite strains when the material yields and the response of the structure becomes nonlinear. As material behaviour is dependent on the current deformation state, variables such as temperature, pre-stress, electromagnetic fields, etc., may interact. The mathematical source of such behaviour is defined by the general stress-strain relation $\boldsymbol{\sigma} = \mathbf{E}(\boldsymbol{\epsilon})\boldsymbol{\epsilon}$.

  Material nonlinearity also refers to time-independent behavior such as plasticity, time-dependent behavior such as creep, viscoelastic/viscoplastic behavior with simultaneous creep and plasticity.

- displacement boundary nonlinearity, when the boundary conditions change during the analysis (e.g., contact problems), and the state variables are mapped at boundaries under affine transformations (i.e., rotation, translation, stretching).

- force boundary nonlinearity is related to non-conservative analysis enviroments, such as aerodynamics, hydrodynamics (e.g., gust, wave loads). The loading function is dependent on the displacement field. In such cases, surface tractions are of interest.

- geometric nonlinearity occurs whenever the magnitude of the displacements affects the response of the structure. The kinematic constitutive equations encapsulate second-order effects due to large deflections or rotations, initial stresses, load stiffening or initial imperfections in geometry.

2.2.2 Levels of Analysis

Most engineering applications are based on structures that exhibit linearity in kinematics. Exceptions are slender structures that can no longer be described under the linearity assumptions (i.e., the superposition principle and perfect elasticity under any load function). These are crude assumptions which are physically un-realistic and often contradictory. In reality almost all structures exhibit nonlinear response prior to reaching their ultimate limit, usually characterised by moderately large displacements and small strains.

In computational mechanics, one of the major objectives is to improve predictions for quantities such as critical loads and equilibrium paths. This is not always an easy task for the designer seeking to build a reliable model. Uncertainty regarding actual behaviour depends on the analytical and computational tools that can, in some form, address issues

related to boundary conditions, material behaviour, etc. Despite its obvious limitations, linear theory can still provide a good approach in the vicinity of the reference state (i.e., the linear side of the fundamental path provides uniqueness) but its usefulness diminishes in problems with multiple branch equilibrium paths. The need to perform nonlinear analyses also originates problems with time effects (e.g., crack growth, material properties), push-over, crash analyses, etc.

Varying the boundary conditions and the type of the loading function, one can get different equilibrium responses, as follows:

- A *First-order analysis* in elasticity is *linear* and neglects the higher order terms in the strain-displacement relations. Responses to different load functions can be achieved by the principle of superposition.

- A *Second-order elastic analysis* is strongly influenced by the nonlinear terms in the kinematics equation and captures significant components of the applied forces out of the initial directions of action (i.e., follower forces), caused by the geometric changes in the structure. This approach can predict the existence of the bifurcation points in the equilibrium path of the structure. Yet, this is not enough to yield the subsequent equilibrium path after the branch. The higher nonlinear terms in strain-displacement relations are required to establish the connection between the axial and transverse displacement.

  The stability response can be defined locally or globally as a matter of nonlinearity magnitude on structure. Commonly, these are referred to as the $P-\Delta$ or $P-\delta$ effects. $P-\Delta$ that is a global effect and refers to a combined axial load and lateral deflection, which may lead to an overall structural instability, but has no ability to reflect material nonlinearity, while the $P-\delta$ refer to the local collapse or individual member buckling, taking into account the transverse deflection span wise of slender members;

  In Figure 2.4, the second-order equilibrium path shows some possible modes for equilibrium:

  (a) branching or bifurcation. At such points more than one response path is possible and the structure dynamically takes off, following the lower-energy path;

  (b) nonlinearity is gradually increased up to the elastic limit, i.e., a point which reflects the system's capacity in carrying additional load. Numerically, this is a singularity for global stiffness, which can become negative (i.e., an unstable region under a further loading). A decomposition of the stiffness can be followed to detect the limit. The diagram shows a further instability (i.e., the response branch between two limit points) which is referred to as *snap-through*. The change of the sign of the second derivative of the equilibrium curve defines the two turning points, which help to build the snap-through response, when the structure takes off

dynamically (e.g., shallow arches). To a larger scale, the control-state response may also exhibit an exaggerated form of snap-through, viz. *snap-back*, with a physically realisable behavior between two turning points. Such response is exhibited mainly by thin shell structures and trussed domes;

(c) a hardening effect shown here after increasing the nonlinearity from the onset load.

- A *First-order inelastic analysis* occurs gradually when plastic hinges are used. It reflects the equilibrium in the undeformed state. The plastic limit load is asymptotically reached when destabilising deformations are insignificant and the behavior can be approximated to an elastic-plastic one.
- A *Second-order inelastic analysis* takes into account the deterministic factors (i.e., material, geometry) in calculating the inelastic stability limit.

It is noticeable that engineering structures exhibit small strain and pre and postbuckling response under large displacements analysis even when the stability limit is reached.

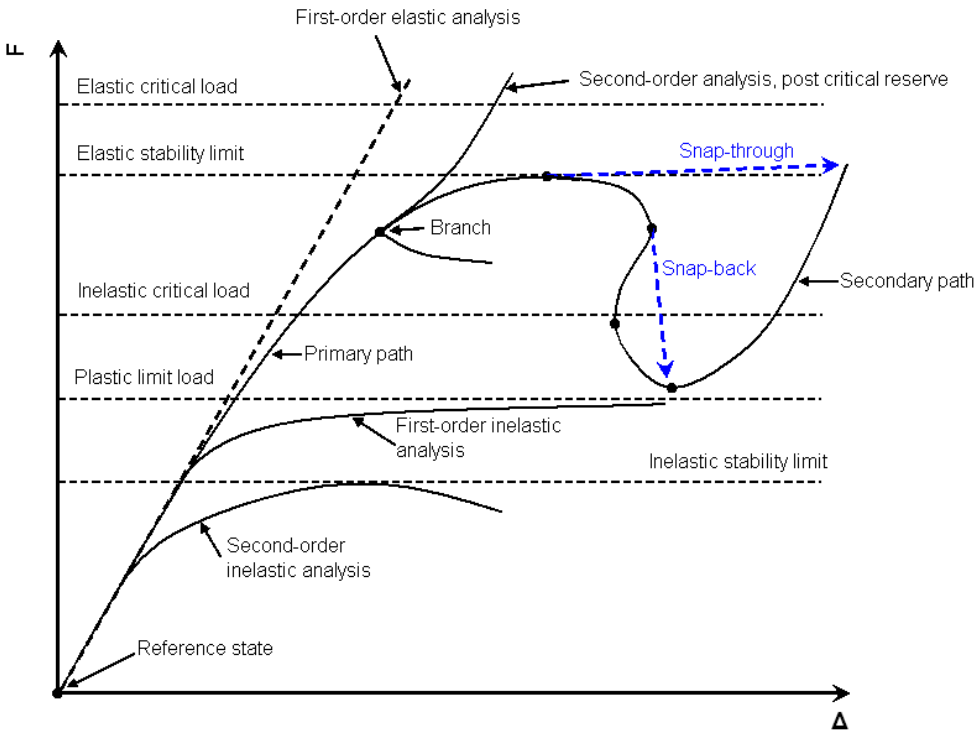

FIGURE 2.4: Fundamental equilibrium paths.

2.3 Background to Non-linear Behaviour of Beam-Columns

The mechanics of common structures (e.g., column-beams) under nonlinear theory has been of a significant interest in finding their strength limits under complex loading. The

work of Timoshenko and Gere (1961) became an important starting point for many researchers reporting in the literature, investigating the fundamental and secondary equilibrium path in analyses of complex restrained structural models, including initial imperfections and various loading functions. Similar approaches on approximation of post-critical regimes are also investigated by Torkamani et al. (1997) by numerical algorithms, while Bolotin (1964) made use of the Galerkin variational technique, whereas Budiansky et al. (1948) and Rivello (1969) used the Rayleigh-Ritz variational approach on similar restrained slender structures.

Much of the work in the literature overcomes limitations of critical regime studies by various algorithms proposed on the basis that the structure under investigation has an initially assumed analytical definition of the displacement field. For instance, Pardo and Ochoa (1999) described a prismatic beam-column with an initial camber, partially restrained against axial deformation, under any transverse loads, deriving pre- and post-buckling behaviour. Their algorithm involved nondimensional shooting parameters with respect to the trigonometric camber terms and geometry-related dimensions (e.g., varying cross-sections and end restraints). The post-critical behaviour along with inherent instabilities such as snap-back and snap-through (outlined by axial stiffness reduction) is derived in a closed form that, qualitatively and quantitatively, is strictly related to the accuracy required (i.e., terms in Taylor expansion) derived from the normalised lateral deflections.

As an alternative to the classical solutions of elastica approach (Timoshenko and Gere (1961), i.e., nonlinear behavior of free-buit-in slender beam-column, Wang (1997) investigates a two point boundary value problem, i.e., hinged-built-in beam-column. The numerical algorithm proposed captured asymptotic post-critical behavior, with emphasis on non-uniqueness of the solution (i.e., non-monotonic $P - \delta$ curve). Vaz and Silva (2003) extended this case of the elastica, where the generic term two-boundary problem resides on a monotonically augmented stiffness of a rotational restraint up to built-in end properties. The approach pointed out the dependence of control-state behavior upon the augmented stiffness, and clearly the post-critical pattern is a function of the restrained state variables. These studies are generalised by Ochoa (2004) where semirigid restraints are considered on both ends of an elastica, but the complexity of boundary conditions determines the use of numerical algorithms for elliptical integrals to capture accurately the equilibrium path under follower forces and imperfections.

Interest in structures with elastic restraints has been strong since the early 1950's. As a comprehensive application to aerospace structures, Budiansky et al. (1948) performed a study on a large and yet simple scheme of boundary conditions (e.g., deflection and rotation constraints) on slender structures, using closed forms of stability criteria. The work emphasises the independence of additional rotational stiffnesses on infinite-span structures, as the deflection state tends to zero.

In a similar work, Stein (1959) studied the behaviour of slender structures and changes in buckle patterns where complex schemes of boundary conditions exhibit nonlinear behavior. An energy-based algorithm was applied to simulate the characteristics of discontinuous slender structures (e.g., stringers, panel assemblies). The model was considered as a symmetric assembly of columns with rotational springs at each end. Such discontinuous structures, locally restrained, exhibit a dependence between the change of buckle pattern and the type of loading, although the change in equilibrium path is independent of the magnitude of loading. Such conclusions have a significant applicability when considering step-wise varying cross-sections of slender structures or span-wise additional point stiffnesses, where the primary fundamental equilibrium path is dictated by localised analyses.

To improve upon structural response under certain load conditions, practical structures can present locally augmented properties, such as stiffness, ply orientation, etc. Buckling loads in non-uniform beams subjected to axial load and different boundary conditions have been of significant interest for engineering applications (Timoshenko and Gere (1961), Karman (1940)), where simple models were analysed to achieve closed-form solutions. A general method for analysing a multi-step non-uniform beam with different elastic restraints has been approached by Li (2003). A closed form of the governing equations of the multi-restraint bar with stiffness augmented locally, under compression loads is derived using Bessel functions. When resting on a foundation of Winkler type (i.e., elastic supports), this choice lessens the computational cost of a buckling analysis using a recurrence algorithm. Such algorithms provide a good starting point for post-critical problems, where the complexity of boundary conditions based on by localised augmented stiffnesses would not be an easy task, although most real-life structures have operational ranges in the linear elastic range.

2.4 General Considerations on Beam-Column Theory

A structure with length greater than any other dimension, e.g., width, thickness, can be regarded as a beam. This context rely on the assumption that the problem can be reduced to one dimensional which defines an axis, such that any distance between axis and any point on the surface of the continuum in the vicinity of the axis is small compared to the length. Beam theory is based on the assumption that the deformations can be determined entirely from state variables that are functions of position along the structure's length.

A simple approach to beam theory, first suggested in 1705 by Bernoulli and systematically developed by Navier in 1826, is based on the following fundamental assumptions: the plane cross-sections initially normal to the beam's axis remain plane, normal to the beam axis and undistorted. The transverse normal stresses are negligible although

they are recovered from the equilibrium and only longitudinal stress becomes important Timoshenko and Gere (1961). For Euler beam theory to produce realistic results, the cross-section dimension should be less than 1/10 of the structure's typical axial dimension, which can be: distance between supports, distance between gross changes in cross section, wavelength of the highest vibration mode of interest. For slender beams, the theory of bending represents a very good approximation to the exact solution according to three-dimensional elasticity (Bažant and Cedolin (1991)). This beam is also known in the literature as a C^1 beam due to continuity being assured along the longitudinal axis.

An alternative to the Euler theory is the Timoshenko beam approach. Here, the classical beam theory is corrected with first-order shear deformation. It is assumed that cross sections remain plane and rotate about the same neutral axis as the Euler-Bernoulli model but deviated from the normal to the deformed longitudinal axis due to transverse shear, assumed to be constant over the cross-section. This beam is also known as a C^0 since transverse displacement and rotation preserve only positional connectivity.

The model considered here works under the Euler-Bernoulli beam theory and is constructed making the following assumptions:

- It is made of an isotropic homogeneous linear-elastic material with a modulus of elasticity E and large displacements and large rotations of the neutral axis occur only in the elastic regime of the material;
- It is subject to small strains with the assumption that cross-sections of the beam-column always remain plane and normal to the longitudinal axis during the deformation;
- Deformations only occur in the plane of buckling, under the assumption that the direction with the minimum I of the cross-section will be the critical one for the direction of buckling;
- Shear and torsional effects are not significant.

Perfect columns, like perfect mechanisms, are a theoretical ideal. In practice, the response of many structures depends strongly on the imperfections in the baseline geometry of the model[1]. A reliable prediction of control-state response in terms of critical loads, depends mainly on the availability of information (i.e., typically statistical in nature) about geometric irregularities in structures and also depends on the accuracy and type of approximation method used.

[1]Sensitivity studies have come a long way since 1945, when Warner Koiter revealed in his PhD thesis at Delft University of Technology the disastrous effect of initial geometric imperfections on the load-carrying capacity of structures.

For structures that undergo large displacements, when a geometrically nonlinear analysis is appropriate, the existence of imperfections in the form of offset load or manufacture geometric irregularities must be accounted for. The load-carrying capacity of such structures is significantly affected by the presence of imperfections. Such sensitivity trends of a regular strut are depicted in Figure 2.2. Throughout this work, the imperfection is due to an offset load that modifies the potential load-carrying capability of perfect beam-columns (Fichter and Pinson (1989)).

By and large, the sensitivity analysis of structures can be broken into several segments, as shown in Figure 2.4 that can outline the type of analysis approached. To emphasise the second-order effects on a slender beam during stable post-critical response, canonical examples of an imperfect regular strut with varying offset loads have been analysed. The sensitivity trends from Figure 2.2 show a smooth equilibrium path up the vicinity of the critical load, as the beam is loaded from its unstrained state. The response of the structure grows rapidly and continuously until the critical load is reached and the transition into the post-critical state (i.e., post-buckling) is smooth (n.b. stable post-critical paths are highly dependent on the structural properties of the set up, as mentioned in previous sections). The incremental stiffness of the system tends to a singular state as the axial force approaches the critical Euler load, accelerated by the second-order effects in the kinematics definition, including the initial irregularities. Such trends are intrinsically linked to the magnitude of the imperfections (Bažant and Cedolin (1991)). If the eccentricity is large, bending deformations are more rapidly augmented than buckling ones and the bifurcation point becomes regular. If the eccentricity is smaller, the implicit correlation $P - \Delta$ becomes asymptotic in the vicinity of critical load and small force gradients lead to large changes in the displacement field. In this particular case, the structure presents not only a post-critical load-carrying reserve trend, but also has an impact on pre-buckling behavior, by small displacement gradients, which makes the analysis more accurate than via linearised pre-buckling.

Analytically, in linear analysis, the deflection of a perfect beam is indeterminate at a critical axial load, because of the nature of the differential equations which governs the deflections:

$$EI\frac{d^4w}{dx^4} + P\frac{d^2w}{dx^2} = 0, \tag{2.1}$$

where w is the transverse deflection of the beam-column, E is the Young modulus, I is section inertia and P is the compressive load. Beyond this load, if the exact expression for curvature is used, there will be no indefiniteness in the value of the deflection. The shape of the elastic curve, when found from the exact differential equation, is called the *elastica* (Timoshenko and Gere (1961); Bažant and Cedolin (1991)). The small displacement hypothesis, usually accepted for stress analysis of the structures is, of course, not suitable in such circumstances.

The elementary theory neglects second order effects (i.e., square of the first derivative in the curvature formula) and provides no correction for the modifying of the moment arm as the loaded end of the beam deflects. The general equations governing the large-deflection bending of elastic beams can be stated as:

$$-\frac{d}{dx}\left\{EA\left[\frac{du}{dx}+\frac{1}{2}\left(\frac{dw}{dx}\right)^2\right]\right\}-q=0, \tag{2.2}$$

$$\frac{d^2}{dx^2}\left(EI\frac{d^2w}{dx^2}\right)-\frac{d}{dx}\left\{EA\frac{dw}{dx}\left[\frac{du}{dx}+\frac{1}{2}\left(\frac{dw}{dx}\right)^2\right]\right\}-f=0, \tag{2.3}$$

in which: u is the longitudinal displacement, w is the transverse deflection, E is the Young's modulus of elasticity, A is the cross-sectional area, q is the axial load, f is the lateral distributed loading.

This set of non-linear equations reverts to equation 2.1 if the slope $\frac{dw}{dx} \approx 0$ and then the terms $\frac{du}{dx} \approx 0$ and $\frac{dw}{dx}^2 \approx 0$.

Such complex differential equations have received a great deal of attention in the last four decades. Analytical methods with the form of elliptical integrals have offered a potential way forward to solve complex boundary conditions and yet simple structures. Complicated shapes and topologies can only be analysed using numerical methods.

2.5 Numerical Algorithms for Non-Linear Problems

The mechanical behaviour of materials and structures can be mathematically described by a set of (differential) equations and large deformations and/or complex material behaviour may cause these equations to be nonlinear. Due to the complex continuum mechanics definition, domain discretisation is often a crucial aspect when accuracy is required in numerical solutions. Methods for solving this class of problems have been developed over the past 40 years and present a history of strategies that comes along with the development of analytical and numerical tools. Initial techniques were based on purely incremental methods. These 'predictor-only' techniques lack corrective algorithms and become inaccurate (i.e., large drift errors) due to repeated linearisation of highly non-linear problems (Oden (1967)). These issues led to the various forms of residual-based approaches, where incremental solutions are iteratively augmented based on tangent stiffness and out-of-balance forces (i.e., residuals). The traditional approaches are based on Newton-type methods used in the additional corrective stage (Stricklin et al. (1971), Haisler et al. (1977). The literature on this type of numerical algorithms used in collapse problems, readily identified with the development of the finite element methods, emerged its publications in the early seventies, e.g., Brogan and Almroth (1971).

However, since these algorithms were designed to explore the post-critical regime, capturing and traversing critical points was still an issue. Consequently, further development of numerical schemes on tracing equilibrium paths associated with instabilities, led to the development of 'load/displacement control' (Bergan et al. (1978), Powell and Simons (1981)) and more powerful in passing limit points 'arc-length' control (Wempner (1971), Riks (1979)). Various forms of implementations of such algorithms have been described, see for example Crisfield and Shi (1991), Carrera (1994) and Eriksson et al. (1999). For instance, this last author reported a general numerical approach in capturing the core of fold lines, i.e., critical state, in the context of a quasi-static conservative loading. In a parametric hyperspace of arc-length variables, the stiffness matrix is computed from the non-linear eigenvalue problem and the non-linear algorithm employed dictates the efficiency in capturing pre- and post-asymptotic equilibrium paths.

In the present study, two conventional numerical solution techniques are employed (i.e., Newton's method and Riks-Wempner arc-length method, described in Appendix A) in order to emphasise the characteristics of the post-critical regime that the proposed slender structure undergoes.

Chapter 3

Inverse Design of Structural Enhancements

This chapter briefly describes background research on inverse design methodologies in the literature of both aerodynamic and structural fields. It then tackles two threads in global optimisation of the slender structures considered here, by means of improved aerodynamic properties of single and multi-shape morphing airfoils, where an aerodynamically-related structural target is met. Such enhancements are strongly linked to the parameterisation schemes employed.

3.1 Optimisation Approaches

Optimisation tools provide a means to achieve better devices during a shape design process, ideally with as little expert knowledge as possible, involving strategies such as *direct analysis* or an *inverse approach*. In the first case, one studies the effects of parameter variations via an objective function which is formulated with respect to some performance metric (e.g., low drag). Typically, the parameterisation of the design space comes in the form of geometric and material quantities (e.g.., elasticity, mass, length, etc). Constraints can be structural in nature (e.g., mechanical stability, manufacturing requirements such as thickness or camber of airfoils) or aerodynamically related (e.g., desired lift coefficient, etc.). This method is easy to implement due to its simplicity, but often requires a significant number of iterations (i.e., monolithic or uncoupled analyses) with no guarantee that the optimised shapes achieve desired performance levels. The *inverse approach* works towards a given shape by attempting to push some derived characteristic towards a desired configuration. The derived characteristic is usually specified as a field variable (e.g., static pressure or freestream flow) that is *a priori* known to yield desirable performance. Inverse methods are useful when designing systems with specific characteristics, as undesirable physical effects such as shocks, or flaws in shapes

can be explicitly avoided. The main difficulty lies in choosing the target performance of the parameterised model.

3.1.1 Inverse Aerodynamic Shape Design Methodologies

The earliest approaches to aerodynamic shape design appear to be by inverse methods. This class offers a myriad of analytical and numerical techniques that can structurally and aerodynamically improve the flow performance associated with boundary surfaces. Such methods control physical quantities related to a target performance, i.e., a flow field, associated with a boundary geometry. The inverse methodologies provide potential means of achieving prescribed flow fields, where loss mechanisms can be avoided, but come with inherent difficulties associated with specifying a comprehensive target field. This drawback is often augmented by geometrical considerations, that can translate into non-physical boundaries (usually associated with constrained problems). Therefore, the feasibility of the solution may lead to a further reconsideration of the problem, increasing its time-cost properties. There are a number of methods in the literature that try to mitigate these drawbacks, or require as little designer's expertise as possible, and are briefly presented in the following.

The idea of attaining a specified and desirable pressure distribution has come a long way since the mid 1940's, when work was based on *conformal mapping*. The basic idea is that an airfoil is generated from a circle through a mapping function. Lighthill (1945a,b) applied conformal mapping in the case of two-dimensional incompressible flow to the design of cascade blades. A constraint was applied to ensure the profile/cascade is closed and a closed form solution is readily derived, as the solution ϕ is known for incompressible inviscid flow over a circle, therefore the analytical mapping is easily derived through the general relation of the speed over the profile

$$q = \frac{\phi}{h} = q_{target}. \tag{3.1}$$

where ϕ is the velocity potential for flow past a circle and h is the modulus of the conformal mapping function between the closed profile and the circle. A two-dimensional compressible potential flow was modeled using this approach (McFadden (1979)) with a remapping function and extended to transonic regime, with artificial viscosity to mitigate the occurence of shock waves.

An inverse method for two and three dimensional potential flows with prescribed velocities along the boundary surface was developed by Stanitz (1953, 1980). The governing equations of flow permitted a system of independent variables (i.e., the coordinates) related to streamlines to be formulated. This method considered a pair of stream functions η(x, y, z), ψ(x, y, z) and the second independent coordinate was the the velocity

vector potential $\phi(x, y, z)$, implicitly satisfying mass conservation. For different choices of natural coordinate (i.e., the potential), further research (see Finnigan (1983), Keller (1998), Keller (1999)) was somewhat limited to axially symmetric flows. This drawback is overcome by the *streamfunction-as-a-coordinate* method, where the axial coordinate x is used as an independent variable and the only remaining variables are $y(x, \eta, \psi)$ and $z(x, \eta, \psi)$ (Giles and Drela (1987); An and Barron (2005)).

On a different basis, the *surface approach* is an alternative method suggested in the literature for inverse design (Campbell (1992)) . In this method the difference between the target and actual pressures is translated into surface changes in subsonic and supersonic flow. It has been successfully applied for 2D flows and Navier-Stokes equations, but it meets difficulties for 3D flows, where the surface curvature and slopes are calculated plane by plane. The grid points of the surface are iteratively loaded with ΔC_p (i.e., the difference between the actual and target distributions) until some form of convergence is met (i.e., a stable surface). The surface is governed by a second order partial differential equation, whose coefficients β_i are user specified entities, chosen based on the designer's experience or flow parameters (Dulikravich and Dennis (2000)):

$$\beta_0 n + \beta_1 \partial_x n + \beta_2 \partial_y n + \beta_3 \partial_{xx} n + \beta_4 \partial_{yy} n = \Delta C_p, \tag{3.2}$$

where n=n(x,y) denotes a local normal surface displacement. Such approaches, based on residual correction, are also presented in the literature in monolithic schemes, where the shapes of boundaries are updated iteratively, and the governing flow parameters are solved under as artificial time parameter scheme (Varona (1999)). This last approach usually requires many iterations, is computationally complex and there are issues with the compatibility of target pressure distribution. An alternative to this limitation is provided by Campbell (1998), using a weighted averaged of geometries, based on principal design requirements and desired gradients.

The formulation of inverse design problems also considers the constraints in *boundary value* problems. The inverse methodology can either be applied to the solid boundary where the pressure fields coincide and requires non-zero boundary velocity, so that the flow distorsion is possible (Leonard (1990)), or keeps the boundaries fixed and updates in geometry are linked to the computed residuals (Demeulenaere (1997)). The last author outlines that mechanical constraints are readily achieved only if a limited area of pressure surface is prescribed, and an additional degree of freedom is introduced to control the target flow angle.

Boundary problems can also be posed with respect to geometry updates, to enhance the feasibility of the solutions (Volpe and Melnik (1986) first addressed the issue of ill-posed inverse transonic design, by using constraints). If the flow field has a non-zero velocity on the boundary (i.e., Dirichlet boundary), the updates are determined by a

transpiration model, based on mass flux conservation between the old geometry and the current one (transonic wing conditions are studied by Henne (1981), Demeulenaere (1997)). A streamline model, based on flow tangency $\mathbf{u} \cdot \mathbf{n} = 0$, in the inviscid case ($\mathbf{u}$ is the tangential velocity described by target velocity and $\mathbf{n}$ is the surface normal and unknown in the problem), is studied by Meauze (1982), Dang et al. (2000).

An alternative for the design of transonic airfoils is offered by the *hodograph* method. Although it can guarantee the design of shock-free airfoils in transonic flows (Garabedian and Korn (1971), the hodograph transformation (i.e., spatial variables are functions of velocity components) lacks control over flow characteristics and geometry and also engineering applicability, as it cannot be applied to three-dimensional cases (Bauer et al. (1972)).

3.1.2 Structural Inverse Design

Rapid increases in the availability of high-performance analysis tools have enabled integration of finite element theories with numerical optimisation of complicated structures. Such capabilities augment the use of structural optimisation as a design tool for product development. In application-oriented problems, mechanical principles are used to determine specific product configurations that lead to a target structural response. Such an approach is referred to as *inverse design*. A typical goal in inverse structural design is achieving meaningful shapes that conform to specified boundary conditions and fulfill functions such as structural integrity with acceptable performance (e.g., acceptable nominal stress). In broad terms, the structural optimisation components can be distinguished as size, shape and topology, as functions of parameterisation and freedom of boundary change.

A large number of papers dealing with optimal structural design problems via inverse strategies can be found in the literature. These are broadly classified as functions of analysis models (e.g., linear, nonlinear, time-transient), domain design (i.e., discretisation, material properties) and optimisation techniques (e.g., nonlinear programming algorithms, metaheuristic methods, etc.). Combining implicit nonlinear functionals with boundary conditions and displacement and stress constraints, an immense body of work on the stability of structures has been developed since the early 1970s, as noted in a survey by Haftka and Prasad (1981). Optimisation techniques have become a more effective option to enhance product development, and methods like sequential programming and optimality criteria are now applied (Rozvany (1989), Vanderplaats (1984), Kirsch (1993), Zhou et al. (1995)).

Typical goals in structural optimisation are related to the performance of the product under a specific design criteria. Depending on the parameterisation of the design domain and the target performance, for instance, shape and size related problems are now

studied as well as the classical goal of stiffness maximisation (minimisation of total energy) (Calahan and Weeks (1992), Bochenek (1995)). This has led to multi-disciplinary applications, e.g., crashworthiness (Redhe and Nilsson (2002)), fluid structure interactions (Lund et al. (2003)), microelectromechanical systems (MEMS) (Ye et al. (1998)), acoustics (Dong et al. (2004)), compliant mechanisms (Xu and Anamthasuresh (2003)), vibrations (Olhoff et al. (1995)), etc.

Where considering topology optimisation, the parameterisation of the fixed domain may be split into subclasses, viz. discrete and continuum. Whereas the discrete formulation might lead to a crude optimum design, depending on the initial layout (Rozvany et al. (1995)), the continuous topology optimisation techniques gained a mainstream popularity among researchers, but they come with associated inherent difficulties in parameterisation of the fixed domain (Rossen and Grosse (1992), Eschenhauer et al. (1994)).

3.2 Single Shape Optimisation

As already noted, this chapter pursues two threads towards global optimisation, by providing aerodynamic enhancements, which are directly linked to the structural shapes achieved. The primary goal is the novel control of the aerodynamic NACA-based parameterised shapes, driven mainly by a stochastic parent-based search (i.e., Genetic Algorithm, Holland (1992)), Simulated Annealing (Metropolis et al. (1953)), followed by a gradient-based search on the structural problems (i.e., Dynamic Hill Climbing, Yuret and de la Maza (1993)).

Initially, single-shape morphing structural optimisation is used before considering multi-shape morphing enhancements. These are based on heuristic evaluations, and consequently, would employ only searches with stochastic engines (i.e., GA and SA taken from the Options design exploration toolkit[1]). Stochastic methods have the advantage of not requiring gradient information and this is important when large variations in geometry are being considered during the initial calculations of the optimisation process. They are, however, not at their best when converging to final designs, when gradient-based schemes are to be preferred (Keane and Nair (2005)).

During the first stage of design (i.e., 1% four-digit NACA camber with maximum deflection at 25% of chord), the geometrically non-linear behavior of the structure is optimised with respect to its deformed shape, allowing for instabilities in the non-linear response, such as snap-through or snap-back, which can arise from widely varying flexural stiffness and rotational restraints. These instabilities are checked against the load proportionality factor which can exhibit one or more limits and/or turning points before achieving the

[1] see http://www.soton.ac.uk/∼ajk/options/welcome.html

final cambers of interest. This process requires some care when setting up but can be directly handled using commercial FEA codes (here Abaqus®). The global load control algorithm used to solve the non-linear problem posed breaks the simulation into a number of increments, for each of which a stable equilibrium is achieved by minimisation of the residual force. This allows the optimisation problem to be stated in terms of the deflected shapes of the strut and the functional to be minimised is defined by the L_2-norm of the difference between the deflected shape $\mathbf{w}(\mathbf{x})$ and the target $\mathbf{w}(\mathbf{x})^t$, which is the based on four-digit NACA camber definition, chosen here for its simplistic analytical representation (see Abbott and Doenhoff (1959)). The NACA airfoils combine a thickness envelope y_t with a mean camber line y_c, and are defined at upper and lower surfaces by grid points coordinates in the Cartesian plane (x_u, y_u) and (x_l, y_l), respectively, as follows:

$$\begin{aligned} x_u &= x - y_t(x) \cdot \sin(\theta) \quad y_u = y_c + y_t(x) \cdot \cos(\theta), \\ x_l &= x + y_t(x) \cdot \sin(\theta) \quad y_l = y_c - y_t(x) \cdot \cos(\theta), \end{aligned} \tag{3.3}$$

where $\theta = \tan^{-1}\left(\dfrac{dy_c}{dx}\right)$ is the camber line slope, and the thickness distribution and the camber line are given by:

$$y_c = \begin{cases} f_m \left(1/(x_m)^2\right) \left(2x_m x/c - (x/c)^2\right), & 0 \le x/c \le x_m, \\ f_m \left(1/(1-x_m)^2\right) \left(1 - 2x_m + 2x_m x/c - (x/c)^2\right), & x_m < x/c \le 1, \end{cases} \tag{3.4}$$

$$y_t = 5t \left(0.2969\sqrt{x} - 0.1260x - 0.3516x^2 + 0.2843x^3 - 0.1015x^4\right), \tag{3.5}$$

where x_m is the position of maximum camber in tenths of the chord c, f_m is the maximum camber in hundredths of chord and t is the maximum thickness in percent chord.

Having set out the definition of the target shapes as a function of the maximum camber f_m, based on a single increment shape control (see section 2.1), the single-shape morphing optimisation problem can be stated as follows:

$$\begin{aligned} &\text{Minimise } f(\mathbf{x}) = \|\mathbf{w}^t - \mathbf{w}\|, \\ &\text{Subject to } g_i(\mathbf{x}) = \max\big|_j \, w_{ij} - a \le 0, \\ &\qquad \mathbf{x} \in \mathbf{X}, \; \forall \, j \in \{1, \ldots, n_p\}, \; \forall \, i \in \{1, \ldots, n_i\}, \end{aligned} \tag{3.6}$$

where $\mathbf{X} = \{\mathbf{x} \in \mathbb{R}^n \mid x_k^{min} \le x_k \le x_k^{max}, \; k = 1, \ldots, n_v\}$ with x_k^{min} and x_k^{max} bounds on the n_v structural variables set by the user (i.e., x_k^{min}=0.2 mm and x_k^{max}=20 mm for structural related variables, $x_k^{min}\big|_{Force}$=-1 N, $x_k^{max}\big|_{Force}$=200 N); w_{ij} are the grid point deflections of the strut at load increment i and structural location j. The constraint g_i considered at each load increment is checked against the failure criteria (i.e., snap-back

and snap-through), by imposing the bound $a \approx 1\%$ chord of the displacement field. The target shapes $\mathbf{w}^t$ are given by the equations 3.4, where $f_m = \max\big|_j w_{ij} \approx 1\%$ chord and $x_m = 25\%$ chord.

In order to optimise the design of the spinal structure, some form of parameterisation scheme is needed to link the optimiser to the structural properties, since tackled size and shape features become crucial when used in conjunction with an optimiser. Consequently, shape parameterisation schemes are discussed in the following sections.

3.2.1 Parameterisation Techniques

A high-fidelity optimisation for feasible and enhanced structures requires a shape parameterisation concept. The aim of most parameterisations is to use mathematical methods to describe curves which can be flexible enough to represent a wide range of shapes, which can be easily controlled, increasing the number of potential solutions. Robust parameterisation techniques have been available in the literature since the late 1970's, as comprehensively described in a survey by Samareh (2001), along with their shortcomings. The challenge of choosing the parameterisation scheme that best describes the shape of the boundary still remains, since there are always problem-specific heuristics that can alter to a large extent the complexity of the problem. The choice of parameterised design space dictates how the shape of the boundary changes and are usually locally or globally targeted.

3.2.1.1 Discrete Approach (DA)

First a Discrete Approach is adopted, using a subset of the finite element grid point coordinates in the structural model to define the regions for the application of design variables. To allow for a wide range of possible shapes, the cross-sectional areas of twelve sections of the spinal beam are varied by parameterising the thickness distribution along its length (as depicted in Figure 3.3 and note that the width of the spine is held fixed at 8 mm). The resulting design is used to achieve aerodynamic-related shapes, e.g., a four-digit NACA camber definition. An equidistant finite element discretisation scheme is chosen here in such a manner as to provide equidistant mapping of the parameterised design space. This mapping provides a means for controlled displacement field of the spinal structure, which becomes more significant in the vicinity of the maximum camber of the target shape.

Some preliminary results obtained during global optimisation show the variation of parameterised space with structured configuration, as depicted in Figure 3.1 (due to the symmetry, only the upper half of the parameterised spinal structure is shown).

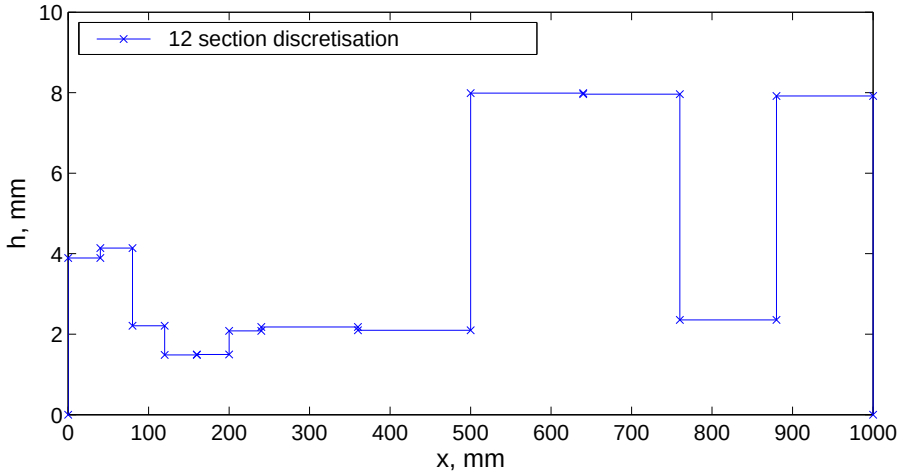

FIGURE 3.1: Preliminary semi-thickness distribution, single-shape morphing beam, DA.

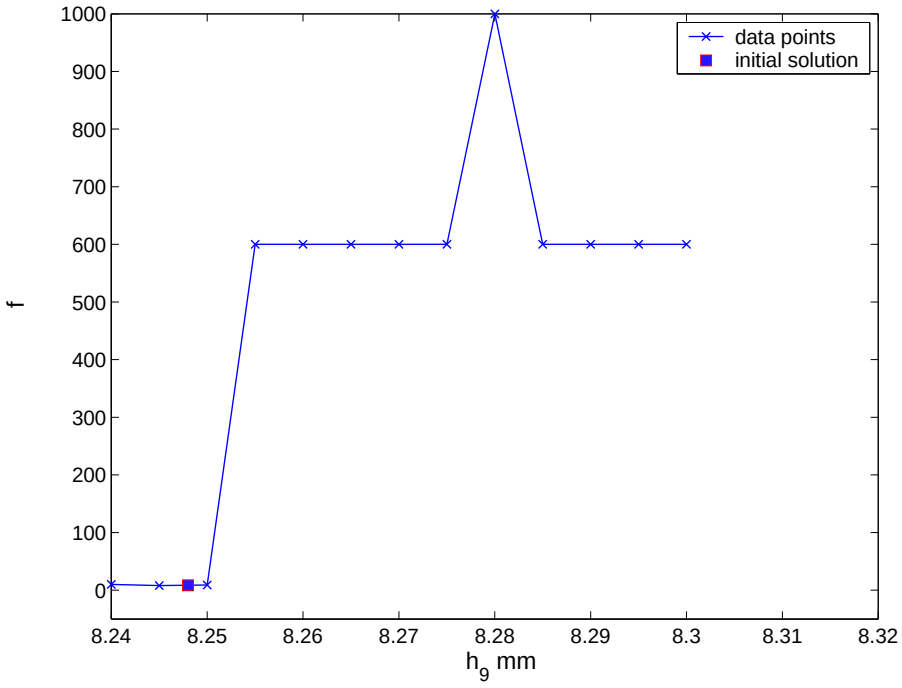

FIGURE 3.2: Sensitivity analysis of a 12 section parameterised beam, DA.

During this initial study, very abrupt transitions between sections were produced that may clearly alter the displacement field required. Therefore, a sensitivity analysis was performed, using Dynamic Hill Climbing. This study outlines the feasibility of the mapping and also the bounds of the parameterised design space. The analysis can be carried out based on the optimal set of design variables and may be used to infer changes in the solution as a result of some parameter variations or constraints, without re-optimising the entire system, Braun et al. (1993). The results (objective function) can be plotted systematically (see Figure 3.2) by varying the parameters through user

selected ranges of values, while other variables are held constant, in order to study the impact on the cost function. The sensitivity analysis is performed here on the 9^{th} design parameter, since it governs the continuum deflection state of the problem and can alter the convergence trend of the functional (see Figure 3.2). Setting the bounds of the local changes of the parameter under investigation, the system not only shows no improvement over the cost function, but exhibits a behavior akin to shear locking (n.b., first-order elements are prone to shear locking for thin elements) and significantly alter the solution vector. Numerical instabilities may also be encountered in systems where:

- adjacent elements have widely varying stiffness and there is a source of insufficient information in the original stiffness coefficients (e.g., a stiff region supported by a much more flexible region);
- large rigid body rotations occur in the system without any significant strain;
- global stiffness becomes singular at a limit point, therefore the transition to post limit is stopped and the Newton-Raphson nonlinear solver under-performs, indicating a diminishing of the accuracy of the solution in the vicinity of a critical point.

To overcome such numerical instabilities for this model, a Kirchhoff constraint enforces well-posed numerical solution to anticipate the approximate field. This translates into a choice of C^1 displacement type finite elements, i.e., Euler-Bernoulli formulation. Such instabilities are also mitigated by augmented eccentricity from 0.1% to 0.3% of chord, without altering the scope of global shape control proposed in this thesis. These instabilites can also originate in the numerical procedure employed, i.e., Newton-Raphson, with slow rate convergence in the vicinity of critical points. It is noted that difficulties in detecting and traversing critical points have been a challenge for post-buckling and post-collapse analyses since early 1970's and have led to the development of the arc-length control and alternating load-displacement control methods for handling cases where the response is unstable during part of its loading history (further details can be found in section 2.5).

A second mapping scheme is proposed in Figure 3.3, and the parameterised design space is augmented with two more variables, to yield a more gradual section transformation in regions of high curvature. After 60 generations of the GA, each of 50 members, and alternatively, 300 iterations of SA, Figure 3.4 shows the best designs in terms of deflected shapes. These deflections are governed by the optimised shapes shown in Figure 3.5. The optimised design achieved with the GA presents reduced variations in stiffness of adjacent elements. Consequently, the metric employed here to numerically analyse the fitness of the deflected states, viz. root mean square error (RMSE), in comparison with the target, shows better agreement than with SA (see table 3.1). Note however that

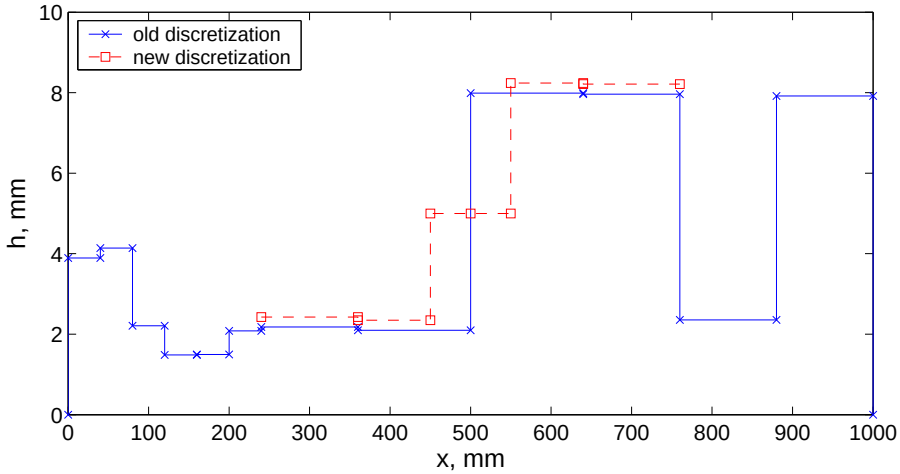

FIGURE 3.3: Augmented mapping scheme, semi-thickness distribution, single-shape morphing beam, DA.

both the resulting structural geometries lack smoothness and runs the risk of limiting the manufacturability, as pointed out by Braibant and Fleury (1984).

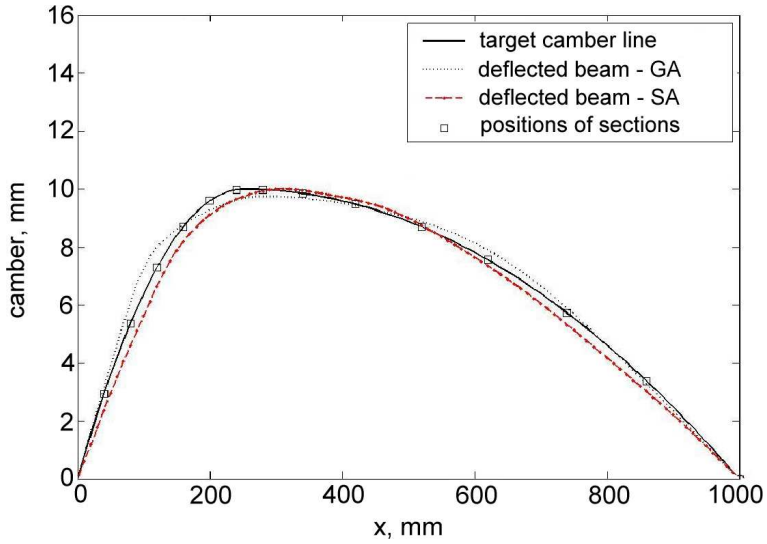

FIGURE 3.4: The deflected states of the optimised single-shape morphing beams, 1% chord, stochastic search with GA and SA, DA.

3.2.1.2 Hicks-Henne Bump Functions

Alternative parameterisation techniques have also been investigated here, initially, by means of Hicks-Henne curves (HH), which provide a compact formulation in airfoil section parameterisation (Henne (1978)). Such curves are smooth and can be compactly described by three variables per bump. Their main feature is their ability to represent

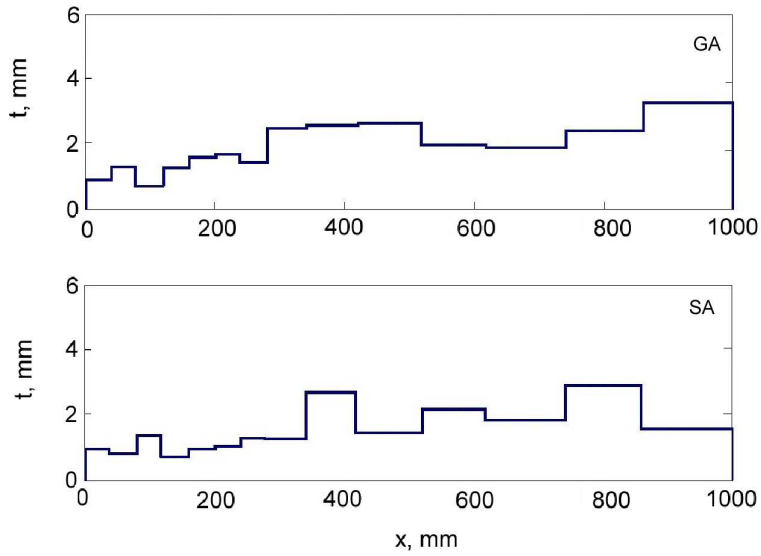

FIGURE 3.5: Semi thickness of the optimised single-shape morphing beams, 1% chord, stochastic search with GA and SA, DA.

global shape control but they can also be used for local shape control on pre-existing curves, since they can control the shape gradients on either side.

A typical Hicks-Henne bump can be defined as:

$$h(x) = A\left[sin\left(\pi x^{-\frac{\ln 2}{\ln x_p}}\right)\right]^t, \quad x \in [0,1], \tag{3.7}$$

where A is the height of the bump , x_p is the location of the peak of the bump and t is a parameter that controls the width of the bump.

To provide a full control of the shape parameterisation of the spine structure, a piecewise HH bump functions is used:

$$y(x) = L(x) + h_1(x) + h_2(x), \tag{3.8}$$

where $L(x) = a \cdot x + b$ is a linear function that adds flexibility in sided shape gradients on the baseline bump curves.

The optimum solutions achieved using both stochastic engines with this parameterisation scheme on a 100 elements discretisation of the beam are shown in Figure 3.6 for the semi-thickness parameterised shapes[2] and Figure 3.7 for the deflected state of the spinal structures. These were achieved after 50 generations of GA and 3000 SA iterations.

[2]The constitutive geometric parameters of the 100 elements mesh density for the analytical parameterisation schemes including NURBS are still generated in a discrete fashion, but provides smoothness.

The thickness distribution of the beams control the displacement field after actuation and the their fitness agreement with the target camber line can be numerically analysed from Table 3.1. Graphically, for the GA-based solution, augmented stiffness towards the trailing edge controls the displacement gradient somewhat better than SA, but the fitness is worse in the vicinity of the maximum camber where the deflection state is somewhat symmetrical. Clearly, SA with augmented stiffness mid chord got stuck in finding the optimum due to slow and pre-mature convergence on long ridges, although overall shows a better fitness than the GA design.

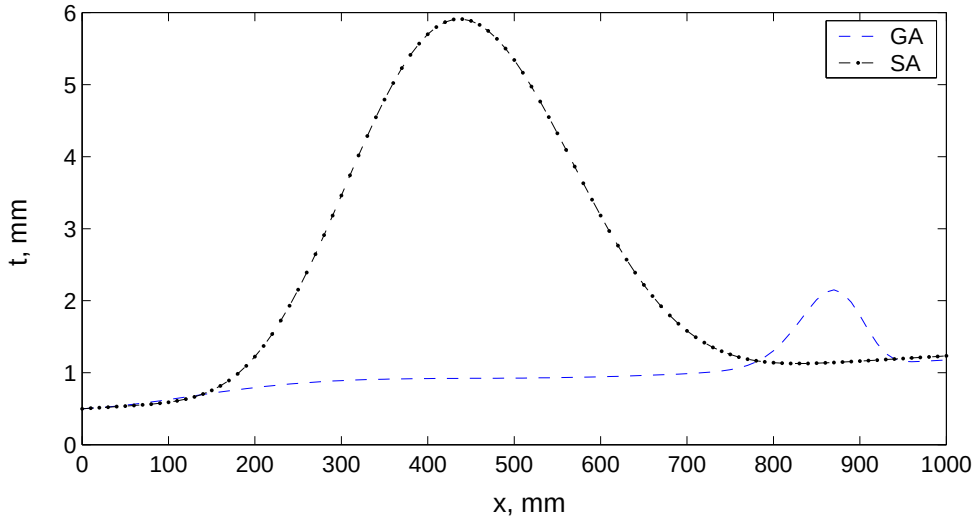

FIGURE 3.6: Semi thickness distribution of the optimised single-shape morphing beams, Hicks-Henne parameterisation scheme.

3.2.1.3 Polynomial Curves

The Spline approach (piecewise polynomials) also offers means of smooth shape parameterisation. The main advantage of such curves is that they can represent any form of curve, but high order polynomials may be required to accurately represent the boundaries; manipulation is not robust and may present discontinuities at join points. The main drawbacks are that the coefficients do not posses a straightforward relationship with engineering purposes (they are geometrically meaningless), being difficult to understand and, also, that the error is rounded-off if coefficients are alternating signs for high order polynomials.

The standard form of a polynomial with monomial basis u^i can be represented as:

$$\bar{R}(u) = \sum_{i=0}^{n-1} \bar{c}_i u^i, \tag{3.9}$$

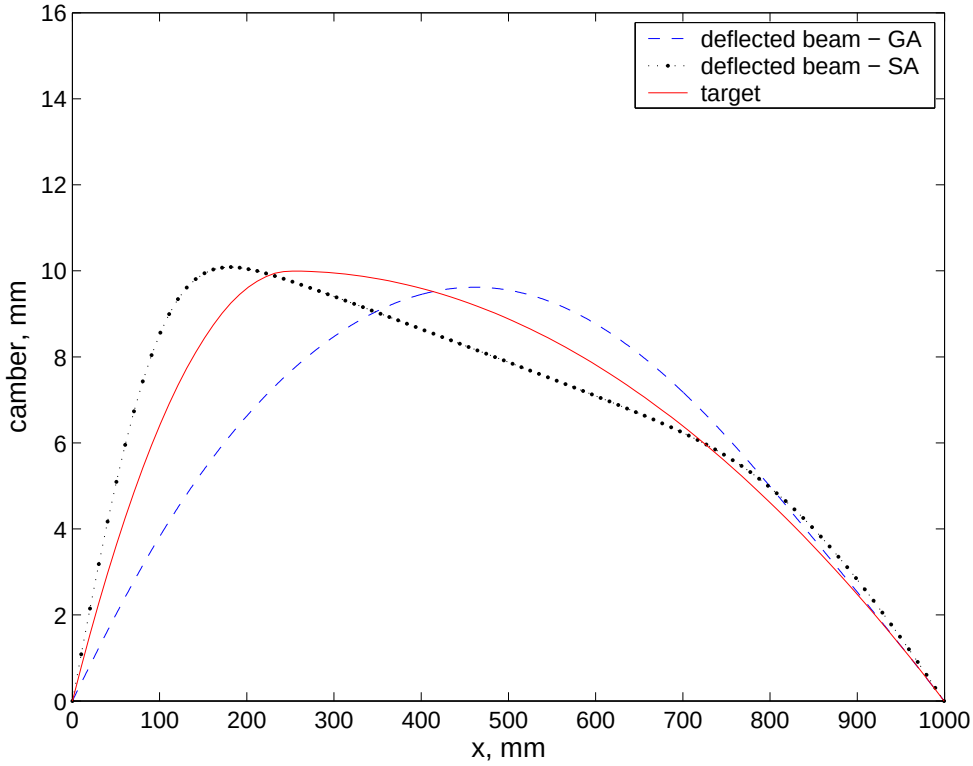

FIGURE 3.7: Deflected states of the optimised single-shape morphing cambers, Hicks-Henne parameterisation scheme.

where n is the number of design variables, u is the parameter coordinate along the curve and c_i are the unkown coefficients in the parametric space.

Here a piecewise parametric quartic polynomial is employed to augment the flexibility of the parametric space, and is defined as:

$$y(x) = L(x) + R_1(x(u)) + R_2(x(u)), \tag{3.10}$$

where $L(x)$ is a linear function and $R_{1,2}$ are mapping blending functions from parametric space to the Cartesian coordinate system (x, y) (Farin (1992)).

The resulting optimised structures, after 50 generations of GA and 300 SA iterations, are shown in Figure 3.8 and the deflected states towards a 1% NACA camber are shown in Figure 3.9. The shapes of the two beams are somewhat similar, with increased stiffness towards the trailing edge that can control the deformation gradient.

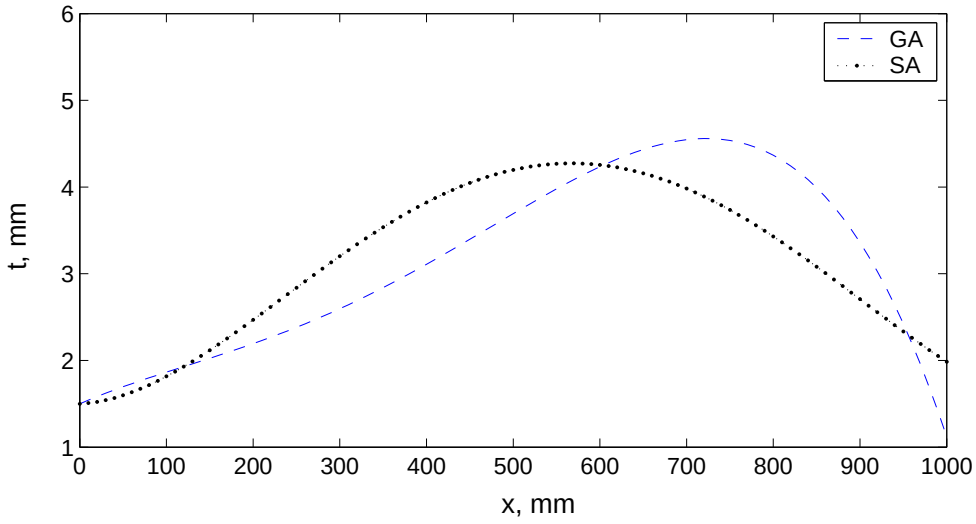

FIGURE 3.8: Semi thickness distribution of the optimised beam shapes, Polynomial Approach.

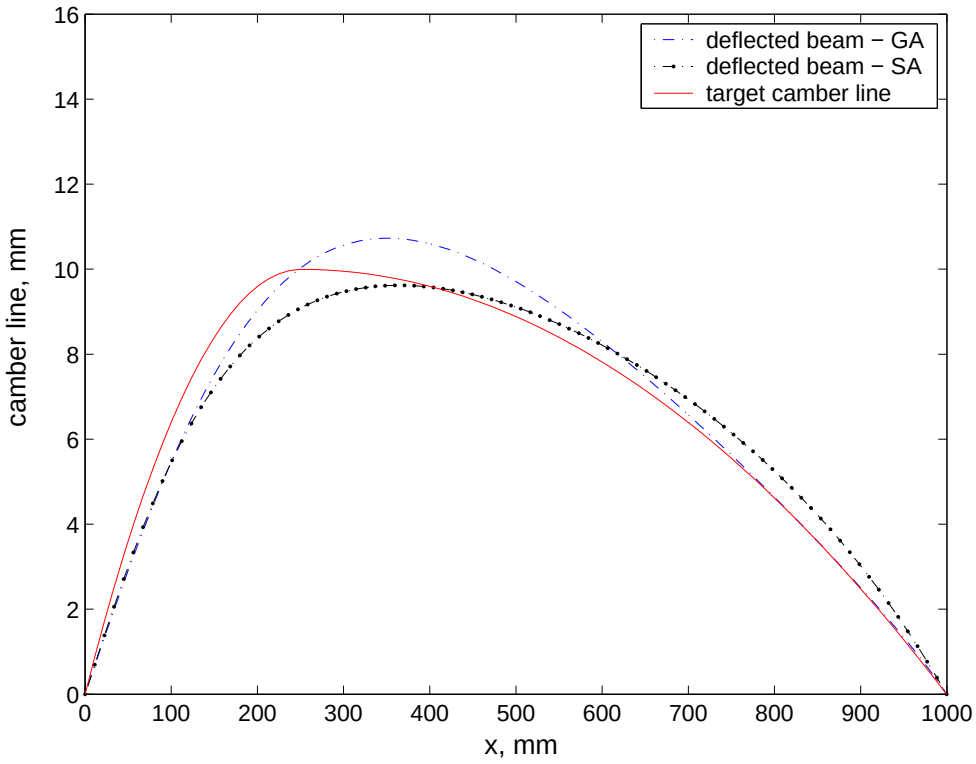

FIGURE 3.9: Deflected states of the optimised cambers, Polynomial Approach.

3.2.1.4 NURBS

CAD systems are now a reliable and accepted engine for MDO processes. Using such tools, complex curved geometry designs based on basis functions can be modeled using the control parameters of NURBS (non-uniform rational B-spline) curves as design

variables (see, for instance, Schram and Pilkey (1995)). This provides great flexibility over the process at a relatively low cost, and also, derived as rational of the polynomial class, NURBS permit much better control over the derivatives of curves. This translates into the ability to satisfactorily modify organic shapes with minimum control variables, while pertaining smooth surfaces and high control over the tessellation of the model.

Here, control of the beam is achieved by manipulating an interpolating NURBS-based parameterised curve using Catia® V5 and then mapping this geometry to the structural-fitted grid in the FEA analysis as a thickness distribution. This involves moving six evenly spaced points in the Cartesian plane (x, y) (see the textbook by Farin (1992) for more detailed discussion on the algorithms behind CAD packages). The optimised shapes produced are very similar to the DA-based designs (see Figures 3.4 and 3.11), but have reduced variations in consecutive flexural stiffness and are smooth. The similarity in shapes from Figures 3.5 and 3.10 produced by these very different parameterisations suggests that the structural solution to the camber matching is not highly modal and that either form presents a good basis from which to make further heuristic evaluations. This is perhaps to be expected since the first buckled mode of a strut is always a well defined shape, i.e., the problem is well posed structurally, even if occasionally tedious to solve.

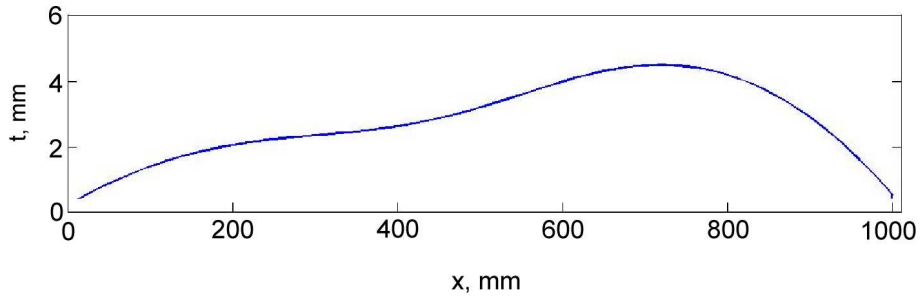

FIGURE 3.10: Semi thickness distribution of the optimised single-shape morphing beams, NURBS.

3.2.2 Summary and Discussion

This section was concerned with the design of single-shape morphing structures that deform to a given camber shape (i.e., camber of 1% chord), by employing a number of parameterisation schemes, viz., Discrete, Hicks-Henne, Polynomial and NURBS. The structural optimisation here was meant to be background information for use when considering multi-shape morphing airfoils. In terms of fitness, the Discrete approach and NURBS under GA provide the most accurate control of deflected shape (see table 3.1), with high similarities in the parameterised shapes. These results are also augmented by the convergence rates of the two stochastic searches. It has been found that SA converged slowly, a common problem that plagues stochastic methods in global optimisation. As a

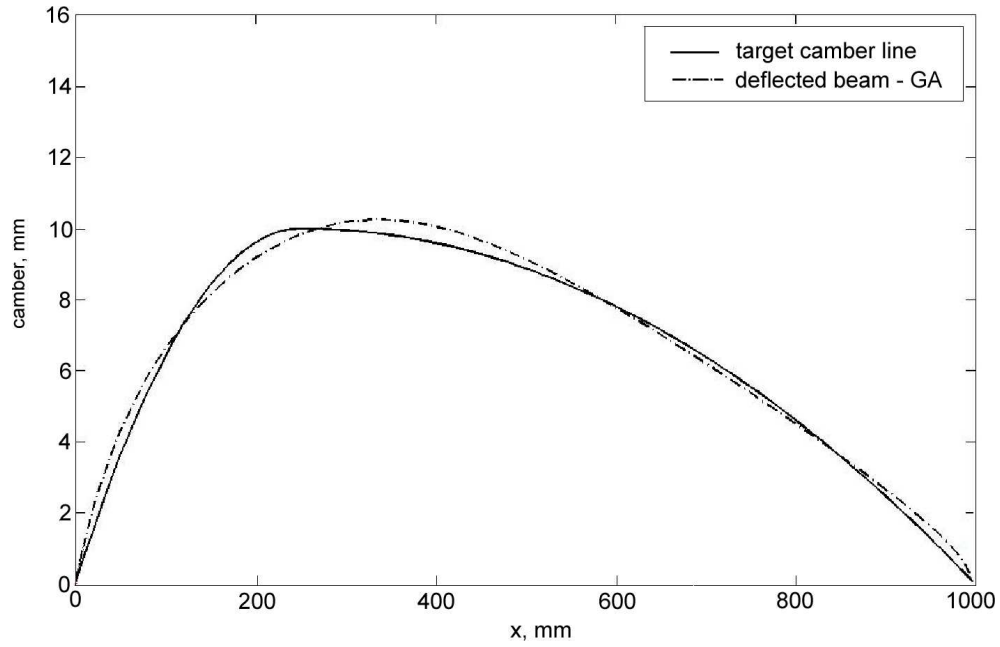

FIGURE 3.11: Deflected states of the optimised cambers, NURBS.

result of this study, further searches to provide morphing enhancements are tackled by using discrete and NURBS schemes, under GA search.

TABLE 3.1: Summary of single-shape morphing beam optimisation

Parameterisation	RMSE	
	GA	SA
Discrete	0.267	0.307
Hicks-Henne	1.06	0.86
Polynomial	0.59	0.61
NURBS	0.3	0.9

3.3 Morphing - Multi Shape Optimisation

Here, the global shape control is achieved by distorting a slender structure which is attached to a hyperelastic outer cladding that forms the aerodynamic surface of the morphed airfoil. Since each manoeuvre during flight may require a different camber configuration, the system proposed here morphs through a significant camber range using an incremental loading scheme. This allows a series of target aerodynamic shapes to be realised. As a reminder, in this study the structural systems are all operated with forces close to the critical load of the strut. This allows global shape control with implicit small loading gradients in controlling large displacement approximations. Since the aim during operation is to move the spinal structure smoothly between a series of

predefined camber line shapes, each equilibrium state can be posed as single-shape. This allows the optimisation problem to be stated in terms of deflected shapes of the strut for each stable load increment as:

$$\text{Minimise } f(\mathbf{x}) = \frac{1}{n_i}\sum_{i=1}^{n_i} \parallel \mathbf{w}(\mathbf{x})^t - \mathbf{w}(\mathbf{x}) \parallel^i, \tag{3.11}$$

$$\begin{aligned} \text{Subject to } {}^1g_i(\mathbf{x}) &= \max\big|_j w_{ij} - a_2 \leq 0, \\ {}^2g_i(\mathbf{x}) &= a_1 - \max\big|_j w_{ij} \leq 0, \\ \mathbf{x} &\in \mathbf{X},\ \forall\, j \in \{1,\ldots,n_p\},\ \forall\, i \in \{1,\ldots,n_i\}, \end{aligned}$$

where $\mathbf{X} = \{\mathbf{x} \in \mathbb{R}^n \mid x_k^{min} \leq x_k \leq x_k^{max},\ k = 1,\ldots,n_v\}$ with x_k^{min} and x_k^{max} bounds on the n_v structural variables set by the user (i.e., the same range as for single-shape morphing airfoils); w_{ij} are the deflections at load increment i and structural location j, and $a \in \{a_1, a_2\} = \{5\%, 15\%\}$ chord define the lower and upper displacement constraints at each load increment, for each airfoil defined at n_p structural grid points. Note that $\mathbf{w}(\mathbf{x})^t$ are chosen from the target camber lines by selecting cambers that have closest overall maximum deflections to those arising at any specific load increment i and satisfy the inequality constraint:

$$\max\big|_j w_{ij} \approx 5\% \leq f_m\big|_i \leq \max\big|_j w_{ij} \approx 15\%, \tag{3.12}$$

so that the target shapes during morphing are fully defined using the equations 3.4, with $x_m = 30\%$ chord. This further speeds up the design process since it is then no longer necessary to know the specific control force needed to achieve a given shape.

Following the searches from the previous section, the DA and NURBS parameterisation schemes are employed during a global search with GA. The structural optimisation procedure is conducted iteratively to the optimum camber configuration, and the designs are presented after 100 generations of the GA. The current analysis goes through a wide range of stable solutions, emphasising the post-critical reserve of the structural set up. Instabilities may occur during the optimisation, since large loading gradients are tackled to encapsulate the structural response. Therefore, post-critical response checking for such instabilities is included as a penalty function by applying feasibility bounds for the displacement field (i.e., $a_1 = 2\%$ and $a_2 = 15\%$ of the initial beam length). Since morphing methodology is tackled in this thesis, the resulting designs are used to achieve aerodynamic shapes by applying a fixed NACA-based 12% thickness distribution to yield the morphed shape (n.b. means to improve upon the correlation between the analytical aerodynamic shapes and the aerodynamic cladding are provided in Chapter 5).

In the initial stage of the global search, where the spinal structure is free of any trailing edge rotational restraint, the fitness of the deflected beam state is diminished as the

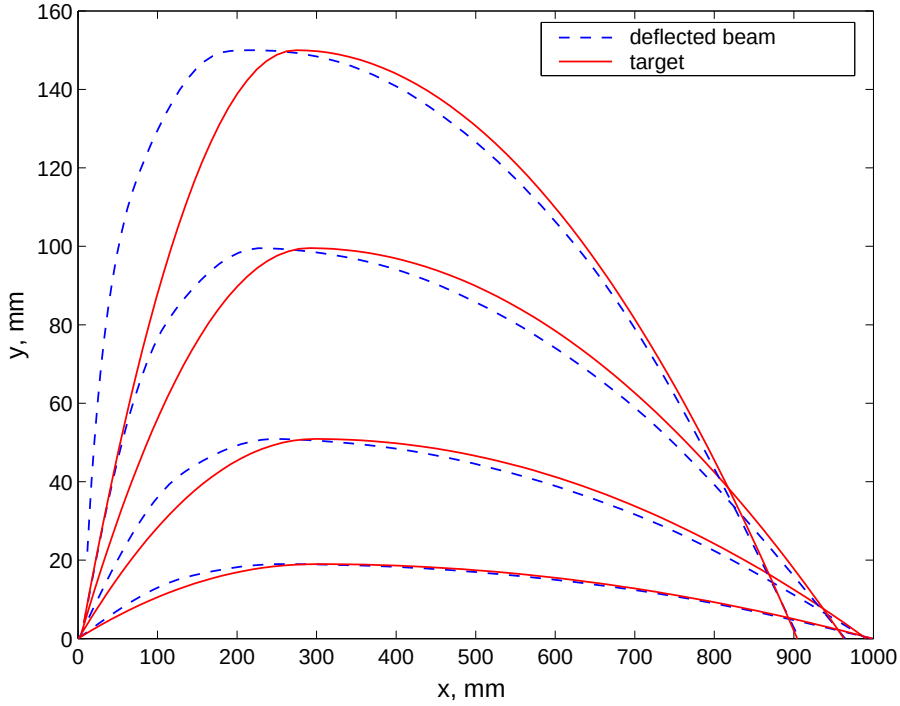

FIGURE 3.12: Deflected beams and targets for initial set up, with no leading edge rotational restraint, cambers 2%, 5%, 10% and 15% chord, global search, DA.

camber becomes larger, as shown in Figure 3.12. This typical behaviour is strictly related to the augmented displacement field towards the leading edge, even if there is a good agreement with the associated target camber in the vicinity of the sliding restraint. Such designs are free to rotate at the leading edge and cannot capture the rotational gradient of its counterpart. Clearly, the airfoils constructed around the underlying set up will be severely distorted by this lack of fitness. However, this drawback can be alleviated by an additional rotational restraint at the hinge point, so as to provide control over the rotational gradient of the deflected strut (see Figure 3.13). Arguably, the kinematics of the strut can be fully controlled by a nonlinear spring, by imposing a set of field variables for each stable solution, but the problem will be more difficult to search. However, a linear restraint appears to satisfactorily control designs by up to 10% deflection, and the upper range of larger cambered shapes are also enforced somewhat by the CFD tool limitations.

Typical deflected shapes resulting from the global DA scheme, spanning a wide range of cambers, i.e., up to 10% chord are depicted in Figures 3.14 and 3.16 and the equivalent designs achieved with NURBS are shown in Figures 3.17 and 3.19.

These figures show typical deflection fields of the optimised multi-shape morphing airfoils, from an unstrained state up to the maximum feasible camber considered here. Both parameterised airfoils show a similar lack of fitness with respect to the associated targets, that is augmented towards the leading edge where the rotational gradient has to

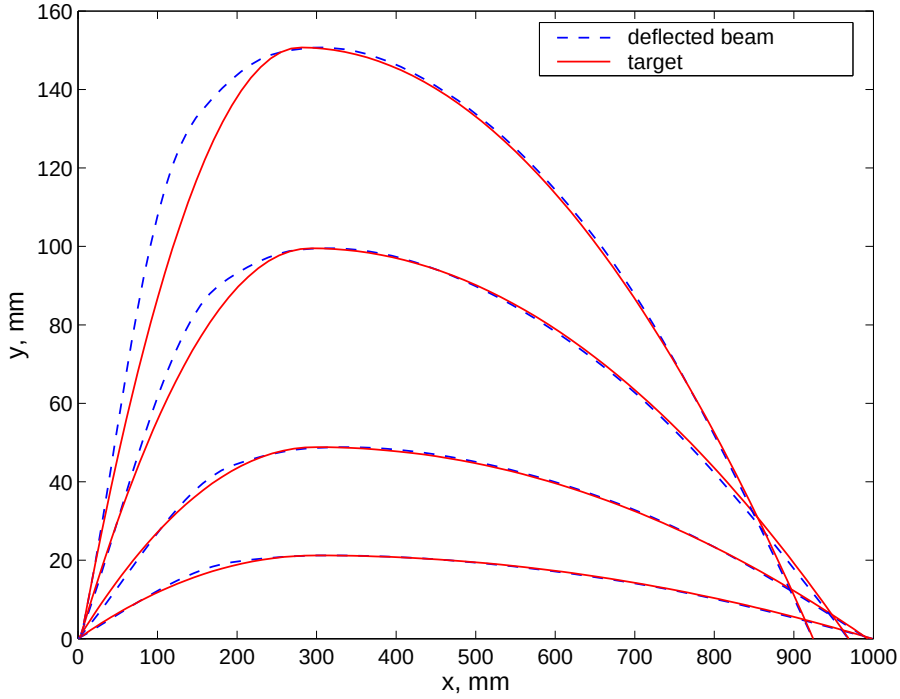

FIGURE 3.13: Deflected beams and targets for final set up, with a leading edge linear rotational restraint, cambers 2%, 5%, 10% and 15% chord, global search, DA.

be controlled and increases with the camber. This geometric deviation from the corresponding target airfoils is also presented in terms residuals (i.e., the difference between the optimised and target deflected states) in Figures 3.15 for DA and 3.18 for NURBS, and augments the lack of fitness chordwise (n.b. the accuracy of the residuals is diminished towards the leading edge due to the fitting procedure of the target airfoil, as only positive defined airfoils can be used with the CFD tool).

As a reminder, all stable increments between imposed deflection bounds are considered in the optimisation. The optimised shapes produced in both approaches are very similar, but reduced variations in consecutive flexural stiffness in the NURBS approach allow for slightly smoother aerodynamic designs. Note, however, that even a stepwise irregular beam deflects into a shape with at least curvature continuity - this is a key feature of using the structural system in this way. The boundary similarity between Figures 3.16 and 3.19 suggests that the structural solution is not highly multi-modal and a further geometry tuning may be required towards a global solution.

For the structures considered here, which are of 1 m length, 8 mm width and E=209 GPa, typical end forces are in the range of 40-90 N, with variations of less than 2 N being needed to deflect the camber from 5% to 10%, typically around 2% changes in end force. Of course, for any practical design account would need to be taken of any structural deflections that might be caused by aerodynamic forces. Such a study, in a decoupled manner, is tackled in section 4.3. Note also, that although this study is

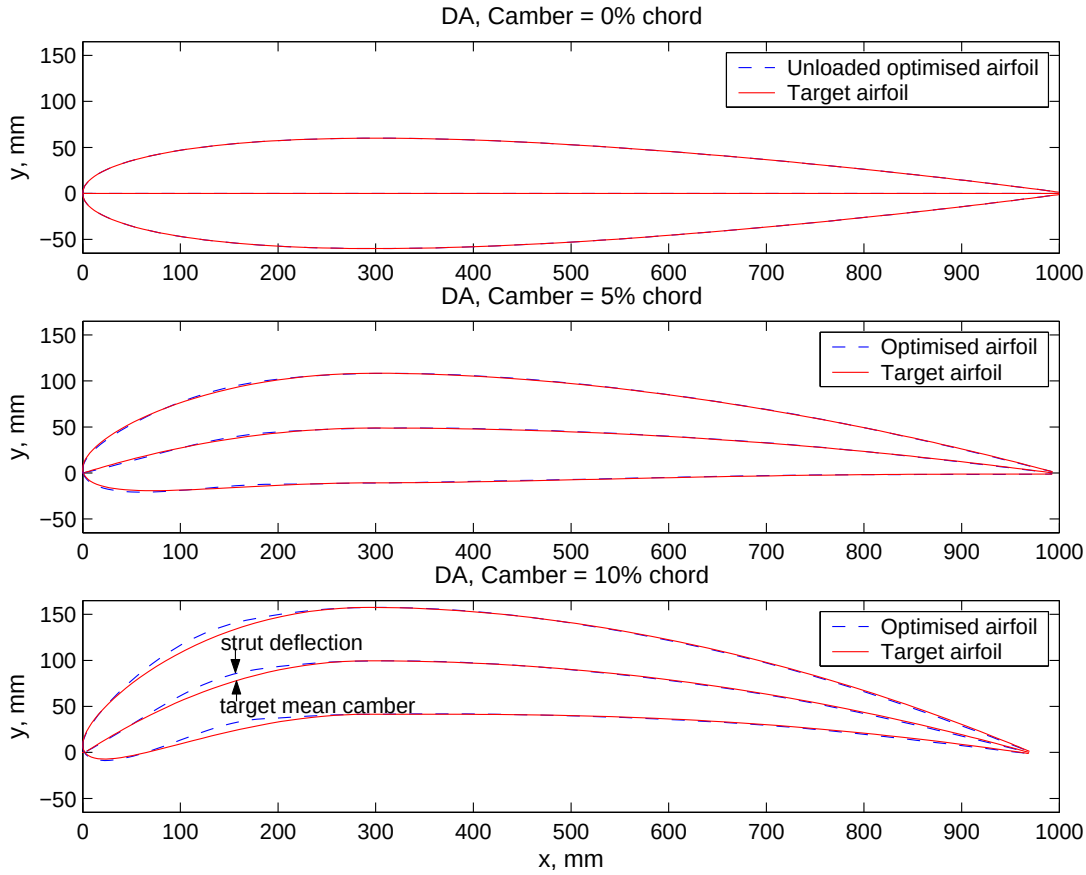

FIGURE 3.14: Target and computed airfoils for morphing-optimised beam in a range of deflection states: unstrained, 5%, 10%, global search, DA.

restricted to rather moderate changes in camber, the concept can be shown to work for cambers of up to 25% if means to control rotational gradient towards the leading edge are provided, which being applied to the whole wing surface would provide all the control authority needed for dramatic manoeuvres. Designing for such large camber changes does, however, lead to the need for high-fidelity CFD tools.

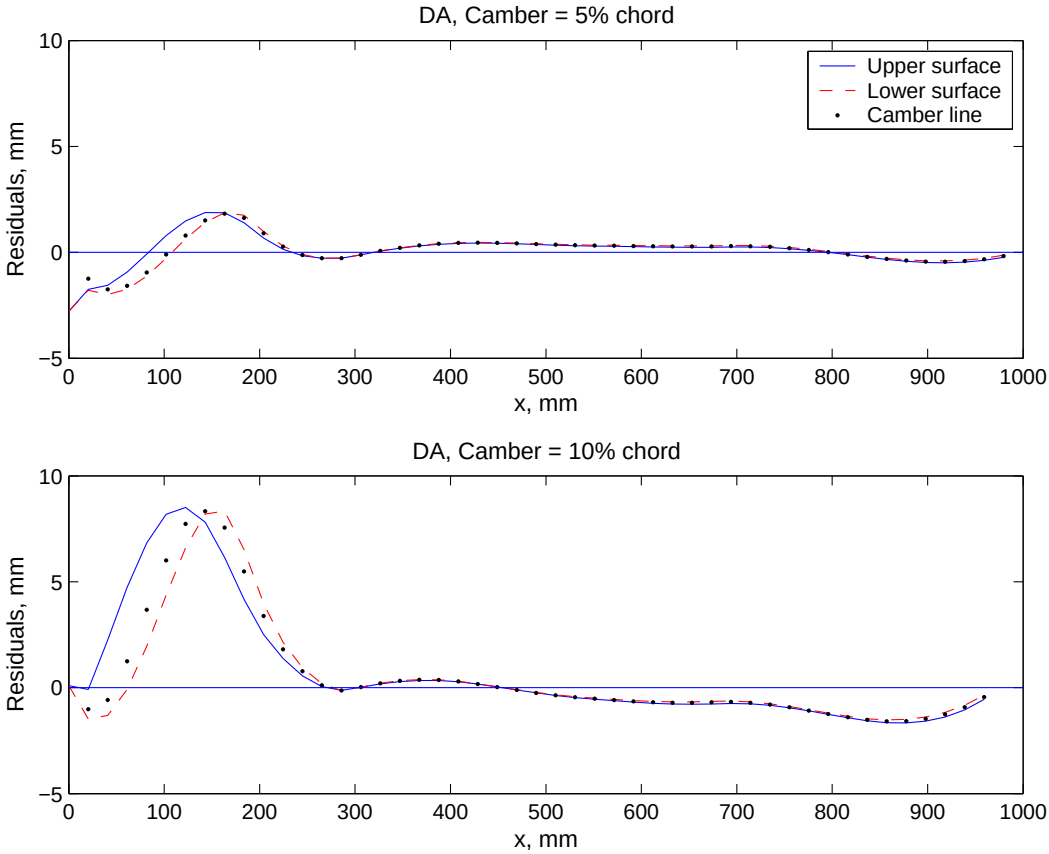

FIGURE 3.15: Residuals between optimised and target airfoils for morphing beam in the range of deflection states of 5% and 10%, global search, DA.

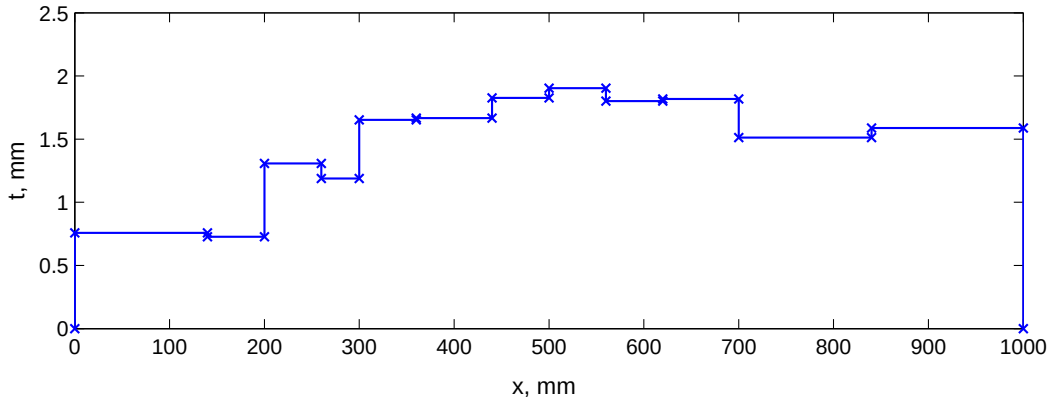

FIGURE 3.16: Morphing-optimised beam - semi thickness, global search, DA.

3.3.1 Design Refinement with Pressure Residual Correction

The metric for the morphing structural enhancements is related to the aerodynamic features provided by using a target structural shape. Of course, similar paradigms are available in the literature, where the target is aerodynamic in nature, e.g., drag polars or pressure distributions. Clearly, the flow characteristics are sensitive to the geometry

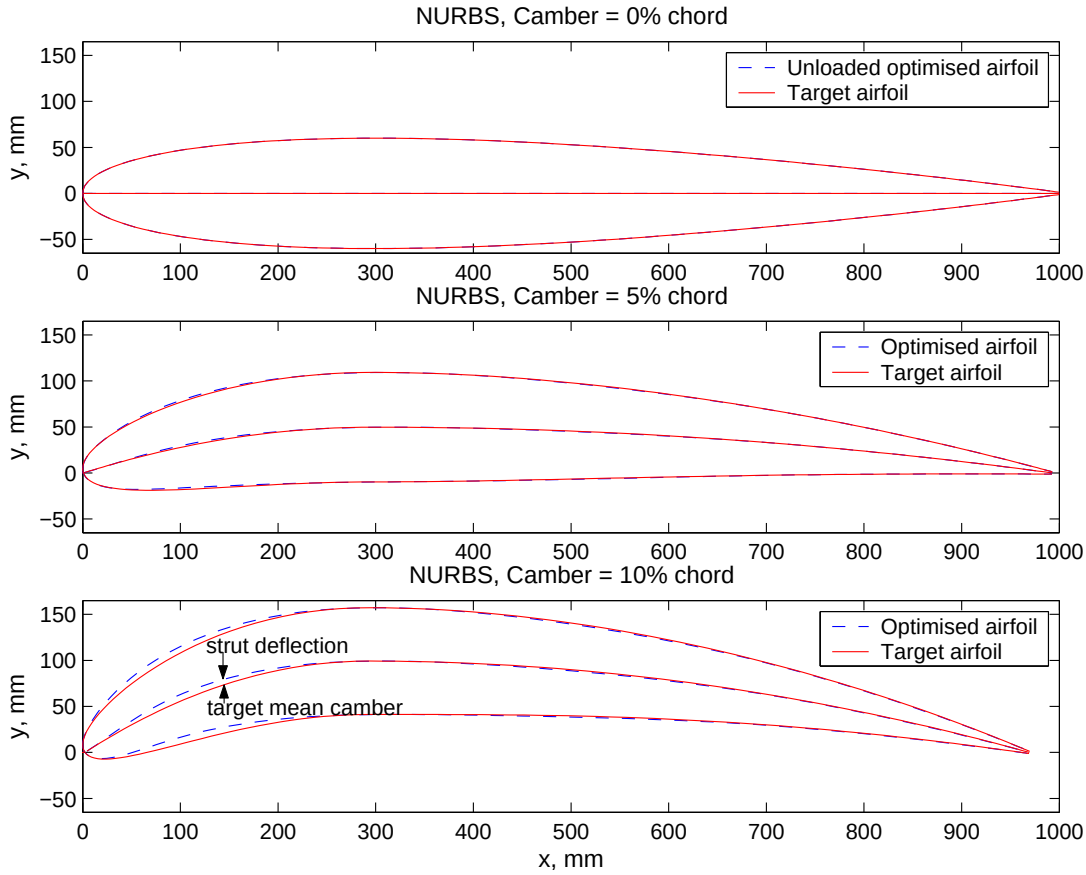

FIGURE 3.17: Multi-shape morphing airfoils in a range of deflection states: unstrained, 5%, 10%, global search, NURBS.

perturbations, and to improve upon the structural solution achieved with the global search, a design refinement in terms of aerodynamic properties is performed, using a CFD-based inverse optimisation (i.e., residual correction method), with a gradient-based engine. The optimisation problem requires minimising the functional:

$$\text{Minimise } f(\mathbf{x}) = \|\mathbf{C_p}(\mathbf{x})^t - \mathbf{C_p}(\mathbf{x})\|^i, \tag{3.13}$$

$$\text{Subject to } {}^1g_i(\mathbf{x}) = \max\big|_j w_{ij} - a_2 \leq 0,$$

$${}^2g_i(\mathbf{x}) = a_1 - \max\big|_j w_{ij} \leq 0,$$

$$\mathbf{x} \in \mathbf{X},\ \forall j \in \{1, \ldots, n_p\},$$

where $\mathbf{X} = \{\mathbf{x} \in \mathbb{R}^n \mid x_k^{min} \leq x_k \leq x_k^{max},\ k = 1, \ldots, n_v\}$ with x_k^{min} and x_k^{max} bounds on the n_v structural variables set by the user; w_{ij} are the deflections at load increment i and structural location j, and $a \in \{a_1, a_2\}$ define the lower and upper displacement constraints at each load increment, with a maximum number of increments n_{inc}, for each airfoil defined at n_p structural grid points. The load increment, i, represents the

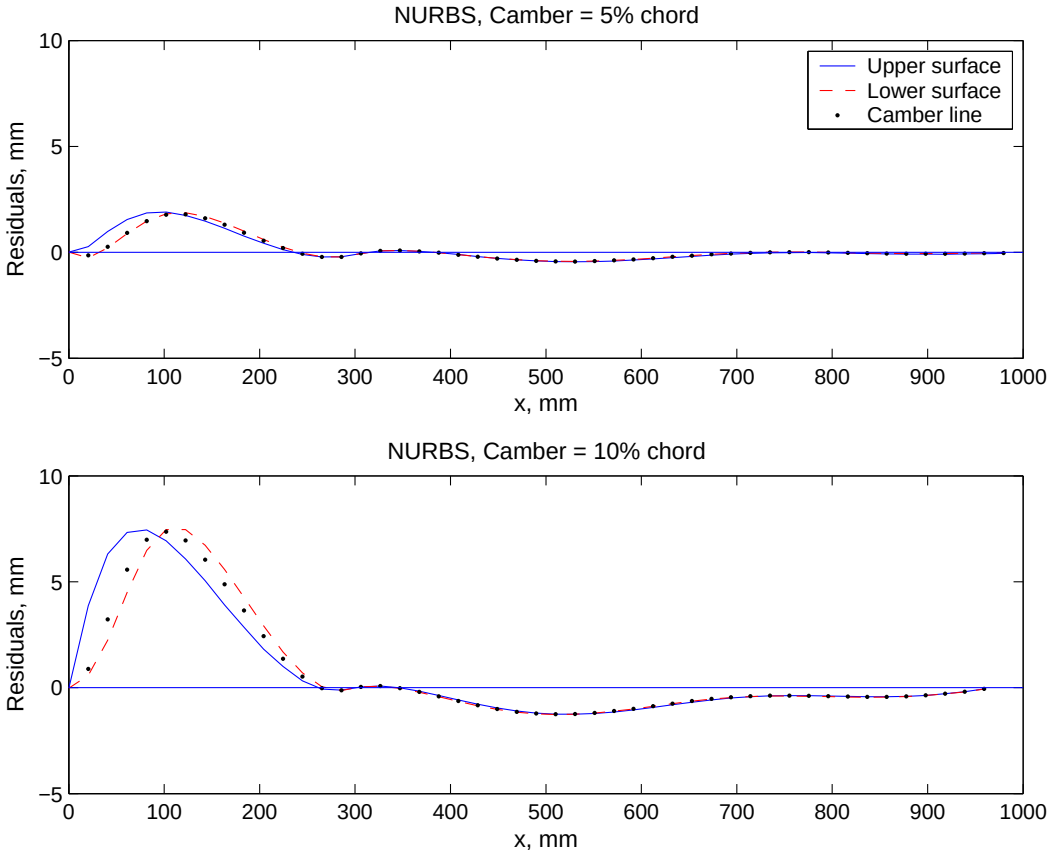

FIGURE 3.18: Residuals between optimised and target airfoils for morphing beam in the range of deflection states of 5% and 10%, global search, NURBS.

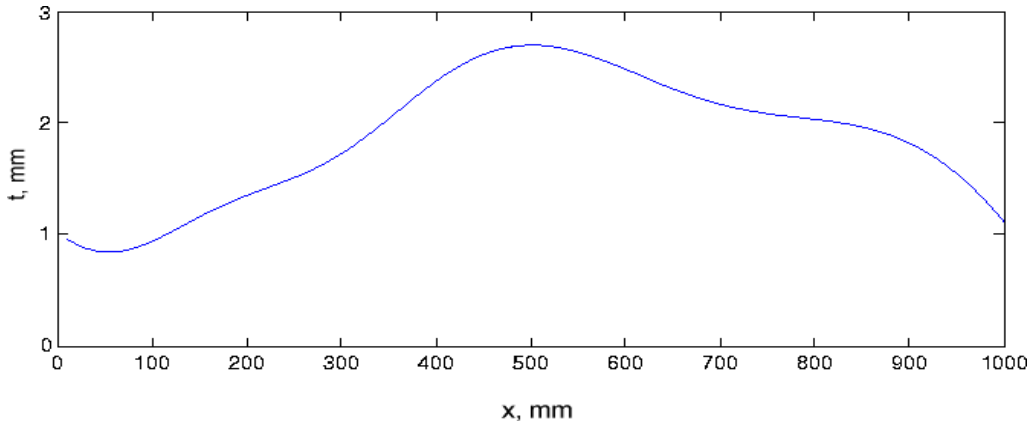

FIGURE 3.19: Semi thickness of multi-shape morphing beam, global search, NURBS.

structural solution corresponding to an airfoil with maximum camber of 10% chord, therefore, the flow parameters are kept fixed (i.e., M=0.5 and α=2 degrees) over a single cambered airfoil.

As already noted, this refining optimisation process is driven by a dynamic hill-climbing, a gradient-based method to carry out a local search, using as a starting point the solution

of the best design from the global search. Here 1600 design evaluations are used and this further significantly improves the geometric matching (see Figures 3.20 and 3.14 with DA scheme and 3.23 and 3.17 with NURBS parameterisation), and has hardly noticeable impact on the overall aerodynamics (the metric of tuning the pressure distribution is analysed in Chapter 4). The dramatic geometric improvement is also outlined by the residual plots in Figures 3.21 for DA and 3.24 for NURBS, which are diminished and smoother chordwide when compared to the residuals from global search, showed in Figures 3.15 and 3.18. With both parameterisation schemes, the thickness of the beam is slightly augmented chordwise and keeps the same shape of the boundaries, leading to the a global solution, thus, the underlying approach is well posed and is parameterisation independent.

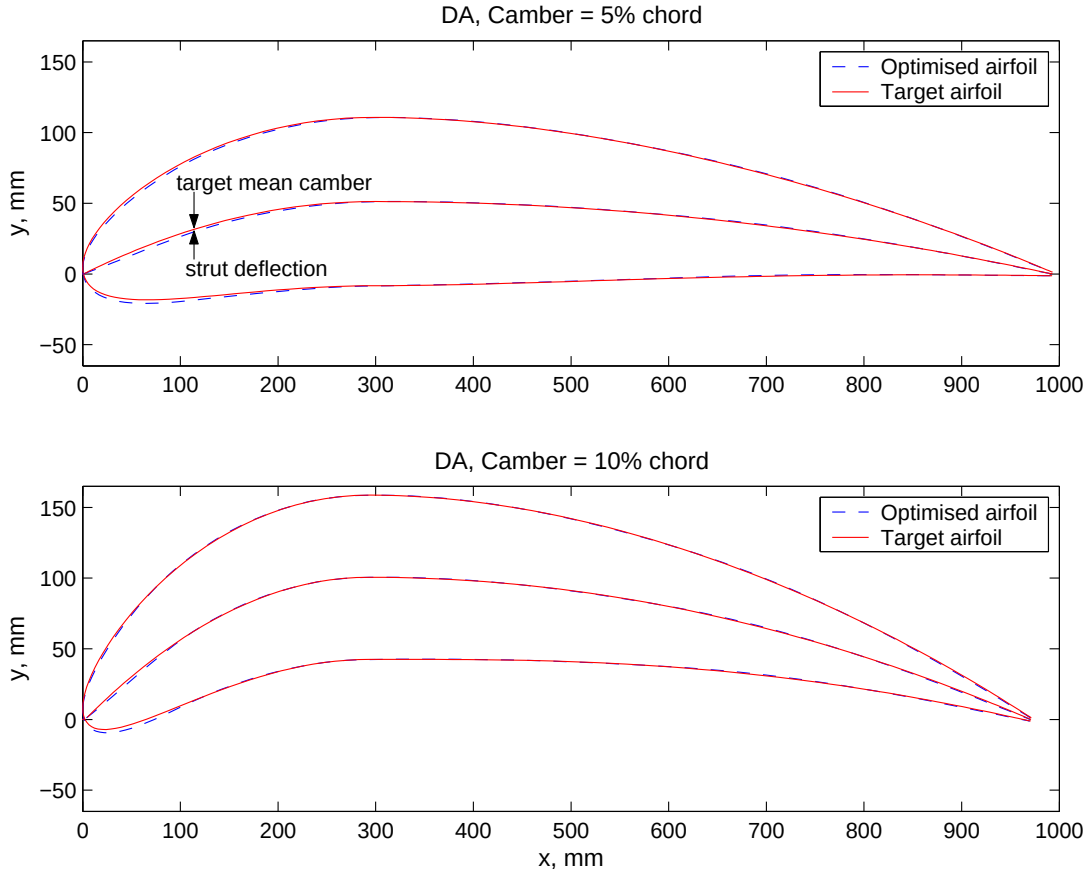

FIGURE 3.20: Refined multi-shape morphing airfoils with pressure residual correction, DA.

3.3.2 Summary and Discussion

Morphing through different cambered airfoils to achieve aerodynamic properties for different maneuvers is possible by exploiting a range of incremental non-linear structural solutions. Further, by using structures that are acting in the post-buckling regime, it

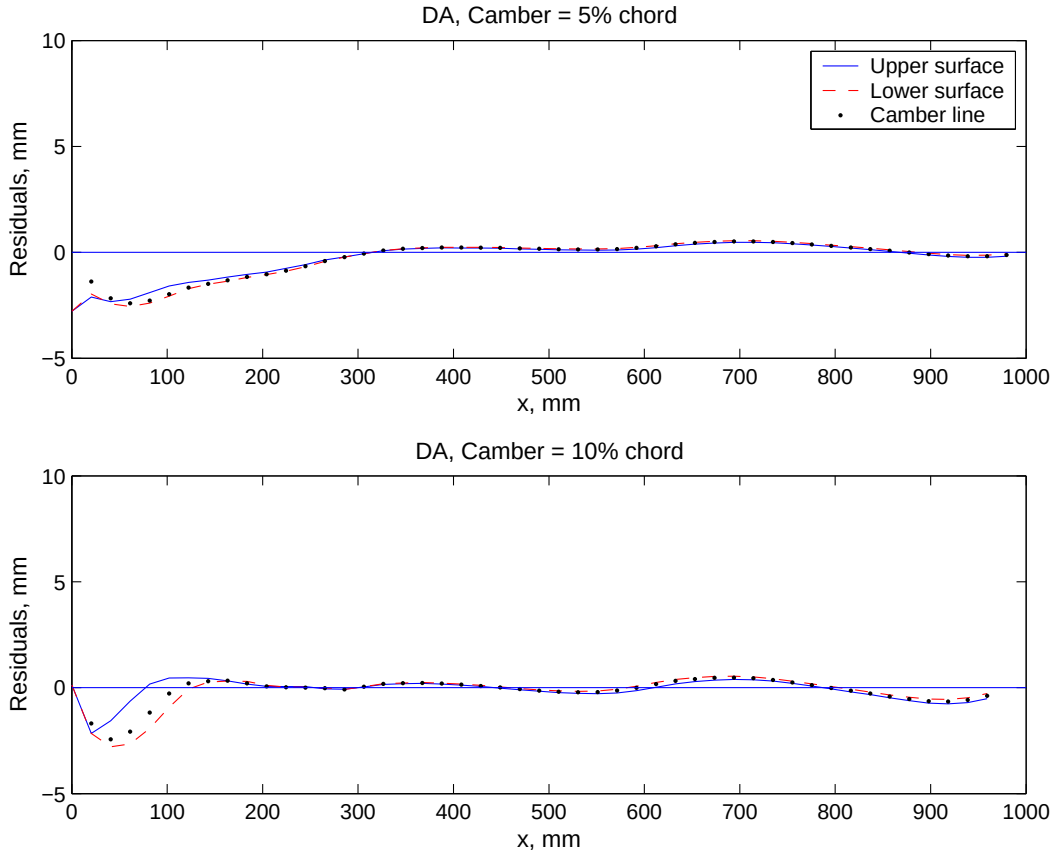

FIGURE 3.21: Residuals between optimised and target airfoils for morphing beam in the range of deflection states of 5% and 10%, gradient search, DA.

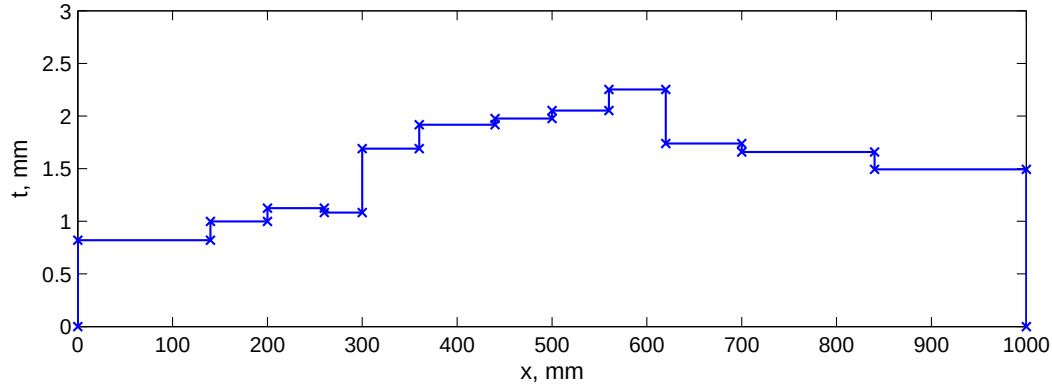

FIGURE 3.22: Semi thickness, multi-shape morphing beam, gradient search, DA.

is possible to obtain significant changes in shape with only modest changes in applied load. The study described in this chapter employed DA and NURBS parameterisation schemes, to seek a potential feasible fast paradigm for finding global structural solutions. Such heuristics are constructed on a metric related to target cambered airfoil achieved for each structural solution, leading to a compact strut definition that can span a wide range of aerodynamics related shapes, with very good agreement between morphing

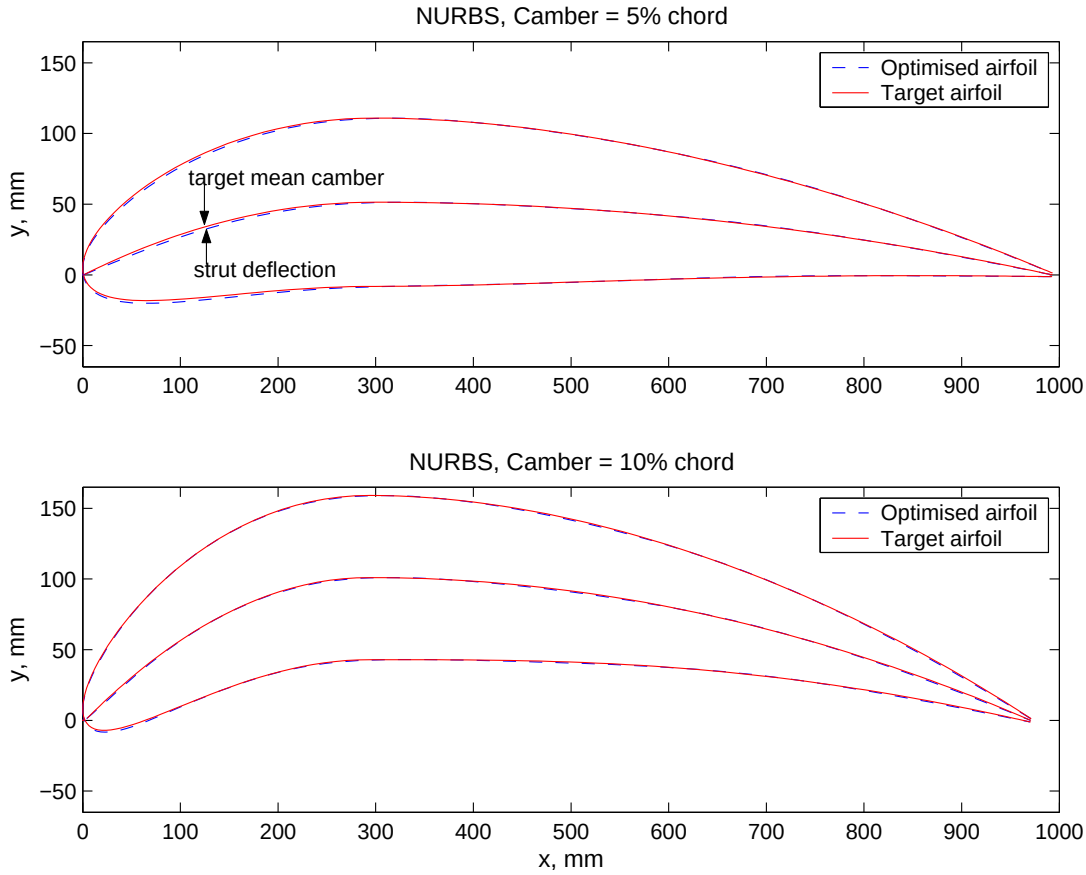

FIGURE 3.23: Refined multi-shape morphing airfoils with pressure residual correction, NURBS.

airfoils and their target.

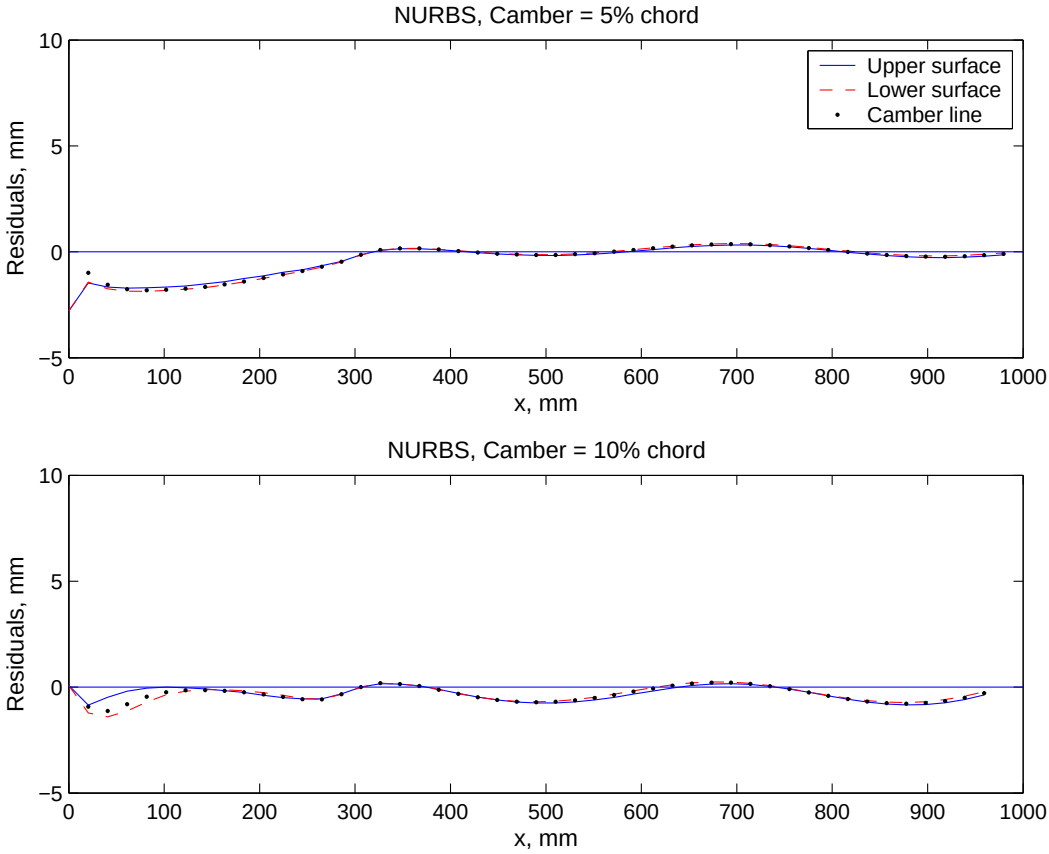

FIGURE 3.24: Residuals between optimised and target airfoils for morphing beam in the range of deflection states of 5% and 10%, gradient search, NURBS.

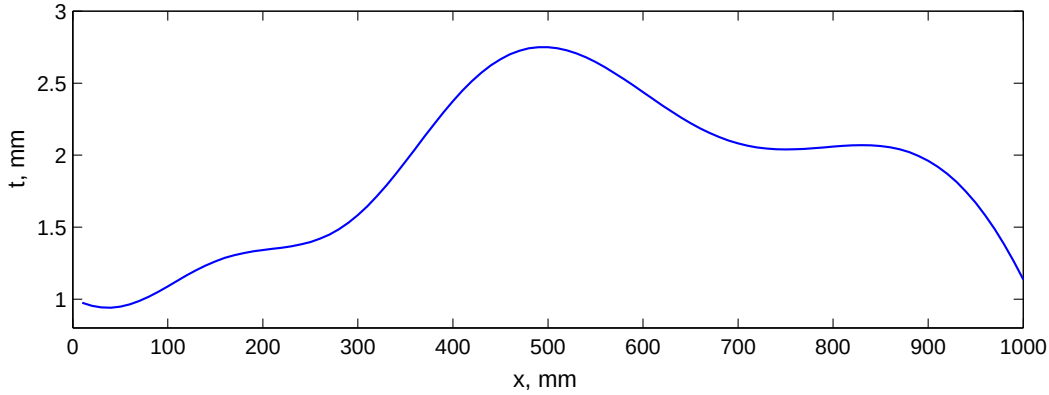

FIGURE 3.25: Semi thickness, multi-shape morphing beam, gradient search, NURBS.

Chapter 4

Aerodynamics of Morphing Airfoils

Having set out the methodology to provide global shape control of morphing airfoils that span a wide range of cambers required for different manoeuvres during flight, this chapter extends the features of the proposed model with a study on the aerodynamics of such airfoils. This study also outlines that it is possible to achieve large structural changes and keep prescribed flow characteristics on an aeroelastically stable airfoil.

4.1 Stating the CFD Problem

Computational Fluid Dynamics (CFD) is a tool that can predict physical fluid flow phenomena for a variety of situations and can model flows where experimental data is hard to measure. CFD can carry out two and three-dimensional solutions for complex applications (e.g., a complete airplane configuration), by providing means to calculate the detailed flow field around the model.

As the shape of an airfoil changes, the flow field around the airfoil also changes. This leads to an altered state of pressure distribution, which, in turn, modifies the aerodynamic properties and actively adapts the aircraft towards a new maneuver. In the given system, CFD solutions are used to predict the aerodynamic properties of the morphing airfoils as they change through the incremental range of cambers so that an estimate of lift, drag would be possible. Of course, this method can be parameterised and automated for optimisation purposes, driving an inverse optimisation methodology to update the boundaries under certain constraints, where an aerodynamically-related cost functional is minimised, following one of the techniques presented in section 3.1.1.

The CFD package used here to tackle the aerodynamic features of the morphing airfoils is VGK (1997), a full potential code developed by DERA Farnborough and distributed by

ESDU as part of the Transonic Aerodynamics pack. VGK is a two-dimensional viscous coupled finite difference code that solves the full potential equations, with Rankine-Hugoniot conditions to initialise shocks (AGARD-AR-211 (1985)). VGK finds the solution iteratively for flows with attached boundary layer, and couples inviscid flow solutions with solutions for the displacement and momentum thickness distributions of boundary layer and wake. The computational grid is based on detailed geometry representation and is constructed radially and circumferentially around the surface (see Figure 4.1 for a typical grid). The grid-sequencing convergence of the aerodynamic iterative solution depends upon the flow characteristics, i.e., Mach number, freestream incidence, Reynolds number, transition location, but also on the airfoil grid coordinates (surface definition points have to be closely pitched near leading and trailing edge to yield smooth first and second boundary derivatives). VGK provides good accuracy for flows with weak shocks and attached boundary layers and fair predictions of local and overall parameters when the upstream Mach number just before weak shocks does not exceed 1.3 with separation of the boundary layer. If these flows are violated, it will lead to slow convergence or failure of the simulation.

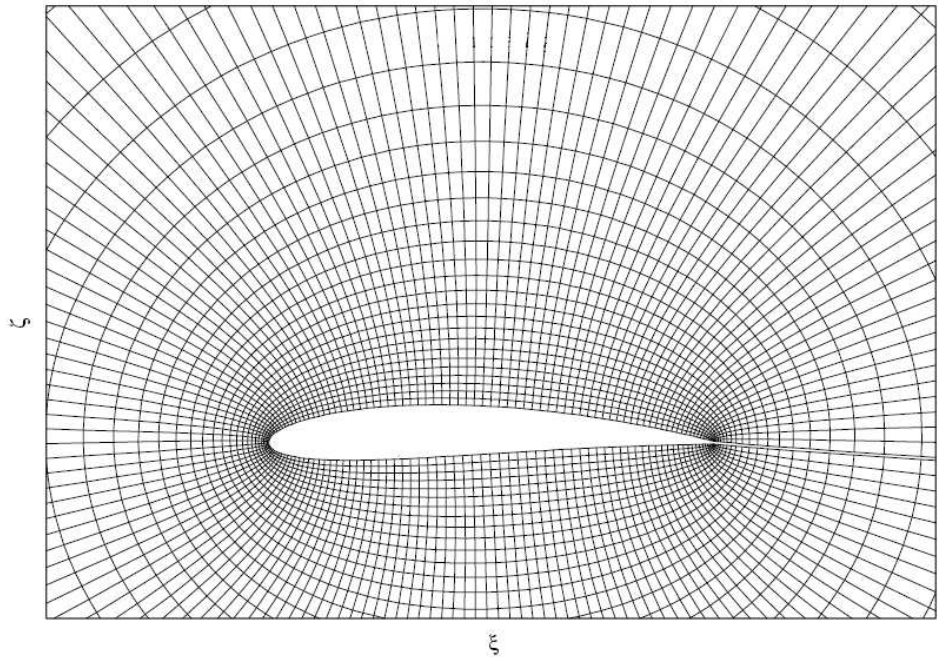

FIGURE 4.1: Typical computational grid for a morphing airfoil.

Morphing concepts are based on active changes of the flow field around the aircraft to adapt it to new flight conditions. This process usually implies a change in speed, altitude and attitude, intrinsically linked to incidence, drag and thrust, which inherently describe the flight envelope. However, for simplicity, in this work, considering a constant Reynolds number $\mathrm{Re} = 5{\cdot}10^6$, a standard setup in terms of Mach number and freestream incidence has been built for the parameterised airfoils and the associated targets. This

covers Mach numbers between 0.4 and 0.8, freestream incidence between -5 and +10 degrees, and ranges incremental shapes between 2% and 15% camber to chord ratio.

The structural solutions of the parameterised airfoils (viz. discrete and NURBS), resulting after the global search, are depicted in Figures 3.14 and 3.17 respectively. These designs present similar aerodynamic surfaces for low cambers, but the augmented rotational gradient of the spinal structure deforms somewhat the airfoil from its target (as previously mentioned, this drawback can be alleviated to some extent by a leading edge nonlinear rotational restraint for cambers larger than 12%). Such large structural changes alter the resulting aerodynamic boundaries due to chordwise variations of the flexural stiffness (see Figure 3.16), more significantly in the case of the discrete approach. Such perturbations in the surface, even though small, have a dramatic impact on the overall aerodynamic features of the morphing airfoil. Although both paremeterisation schemes have been employed here to emphasise the underlying approach, with overall similar performance results, only the discrete-based results are presented here as the geometry is easier to define and the structural and aerodynamic analyses are performed faster (n.b., further results on NURBS-based airfoils are presented in Appendix B). This choice outlines here the design paradigm and the features of the morphing concept and is also reasoned by the dramatic improvement of the geometry and pressure distributions from an initial geometry prone to surface irregularities (see section 3.3).

Figure 4.2 shows a typical 'M$-\alpha$' envelope over a range of cambered airfoils and outlines the limits for which VGK can converge, represented by closed symbols. These capabilities are strongly related to a number of issues: the critical flow velocity that occurs at high angles of attack and high cambers, where strong shocks or boundary layer separation occur; the computed flow is associated to unrealistically high lift coefficients; large local gradients of velocity can also cause unsuccessful runs in CFD and an iterative strategy with a change in relaxation factor would alleviate this issue; the geometry accuracy has a large impact on local surface Mach numbers close to unit and the pressure coefficient is very sensitive to minor surface irregularities, that can also be dictated by the boundary layer growth. The landscape of such unsuccessful runs can also be depicted in Keane and Nair (2005), page 442.

Here, for instance, Figure 4.3 shows converged CFD runs over 5% and 10% cambered airfoils, for mild flow conditions, i.e., M = 0.4. Here a slightly lower pressure on the upper surface of the optimised airfoil is achieved for higher incidence, which leads to augmented pressure gradients, thus enhanced lift, and very good agreement in terms of pressure distribution is achieved aft shocks. Clearly, as the camber and angle of attack increase, the tendency to upper surface boundary layer separation becomes more significant. Note also the slight lack of smoothness in the target pressures for $\alpha = 6$ degrees is damped out by the inverse process of the geometry definition being used (i.e., smooth representation of the structural grid of the airfoil under DA scheme that would be alleviated under NURBS, see Figure B.2 for a closer agreement).

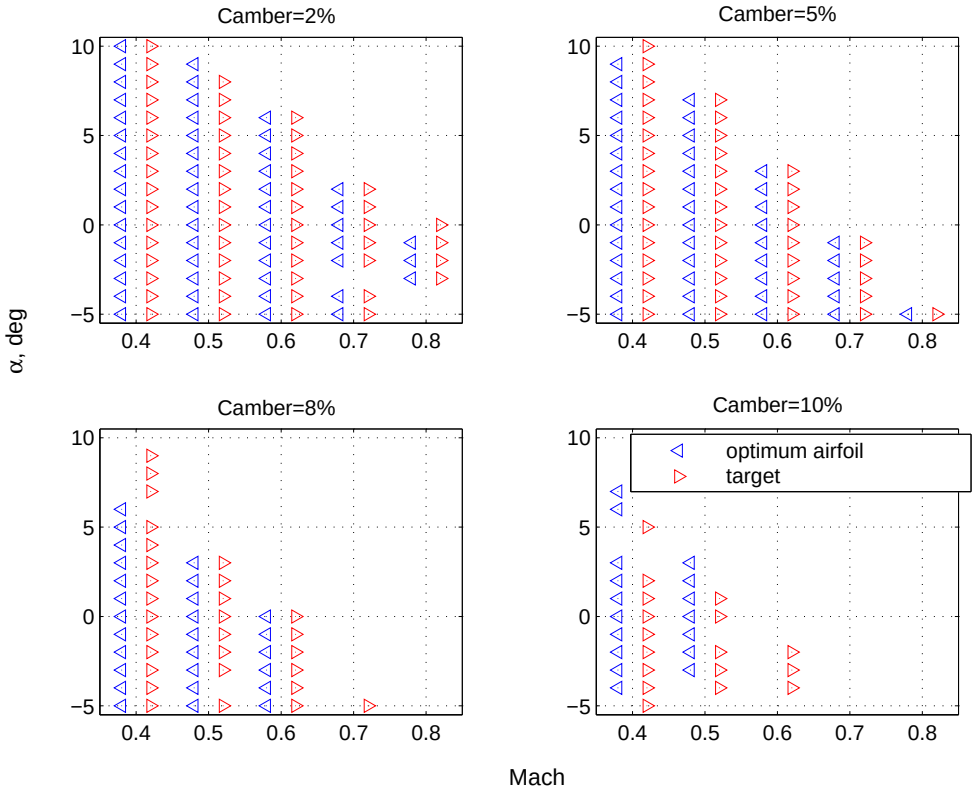

FIGURE 4.2: 'M – α' envelope of converged CFD runs on DA parameterised airfoil (global search), where '$\triangleleft$' represents successful runs for the computed airfoil and '$\triangleright$' for the target.

Figure 4.4 shows similar results for slightly more extreme operating conditions in the envelope, including one at M = 0.8, and also a very good agreement even aft of the upper surface shock position (the equivalent NURBS-based airfoils show, at this stage, smoother pressure distributions and better agreement to the target, see Figure B.3). Clearly, the pressure distributions are sensitive to changes in geometry, flow parameters and boundary layer growth and the flow can readily degenerate into a weak shock for transonic conditions with higher cambers, contributing wave drag. This behaviour is seen in the drag polars of Figure 4.5 for the two cambered airfoils. The drag trends are similar across a wide range of incidences, with particularly good agreement for the low camber point. When morphing between the two cambered shapes analysed in these plots, good aerodynamic performance is obtained throughout. Moreover, the differences in drag polars seen at 10% camber, can be considerably reduced by a further stage of design optimisation which is considered in the next section (the drag polars metric can also be used in an inverse design, rather than pressure residuals). A typical variation of C_L with freestream incidence across a Mach number range depicted in Figure 4.6 outlines the linear case before the stall occurs, with locally lower lift for the optimised structures at high flow velocities due to adverse pressure gradients developed.

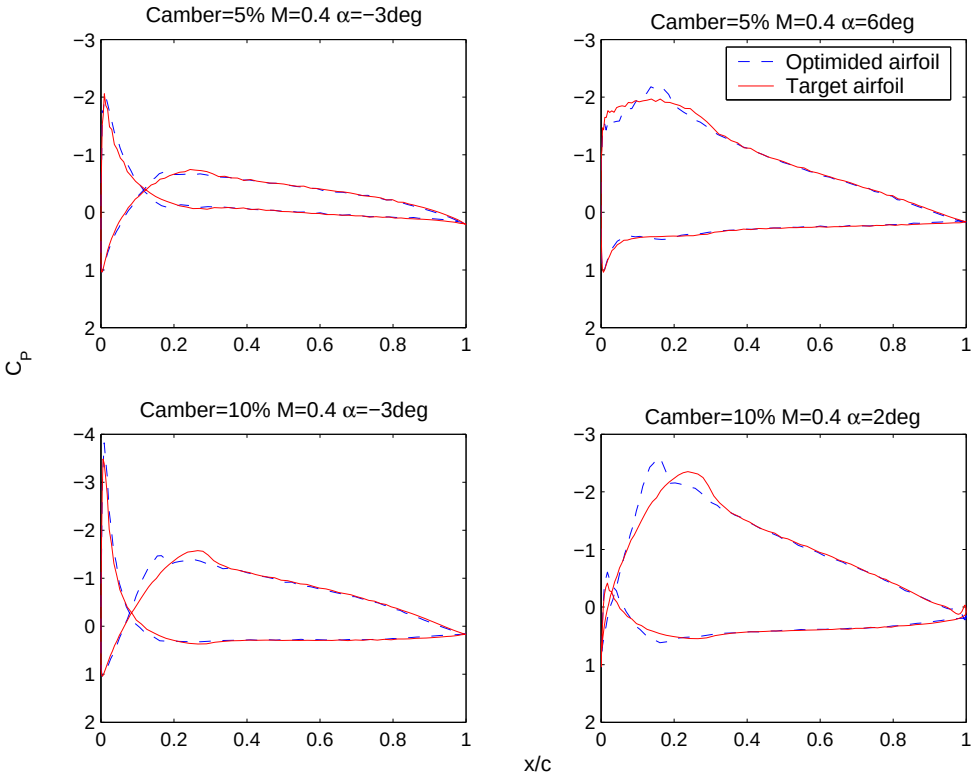

FIGURE 4.3: Pressure distributions for morphed and target airfoils (global solution), under mild flow conditions, DA.

4.2 Tuned Aerodynamics using Pressure Residual Correction

As a reminder from section 3.3.1, to achieve a better aerodynamic agreement in terms of pressure distributions and drag polars than those shown in Figures 4.3, 4.4 and 4.5, produced by multi-shape morphing airfoils under DA scheme from Figure 3.14 (n.b. similar results for NURBS-based airfoils are presented in Appendix B), an inverse CFD-based design optimisation is followed. For this, a residual correction scheme can be stated as:

$$\text{Minimise } f(\mathbf{x}) = \|\mathbf{C_p}(\mathbf{x})^t - \mathbf{C_p}(\mathbf{x})\|^i, \tag{4.1}$$

$$\text{Subject to } {}^1g_i(\mathbf{x}) = \max\big|_j w_{ij} - a_2 \leq 0,$$

$${}^2g_i(\mathbf{x}) = a_1 - \max\big|_j w_{ij} \leq 0,$$

$$\mathbf{x} \in \mathbf{X},\ \forall j \in \{1, \ldots, n_p\},$$

where $\mathbf{X} = \{\mathbf{x} \in \mathbb{R}^n \mid x_k^{min} \leq x_k \leq x_k^{max},\ k = 1, \ldots, n_v\}$ with x_k^{min} and x_k^{max} bounds on the n_v structural variables set by the user; w_{ij} are the deflections at load increment

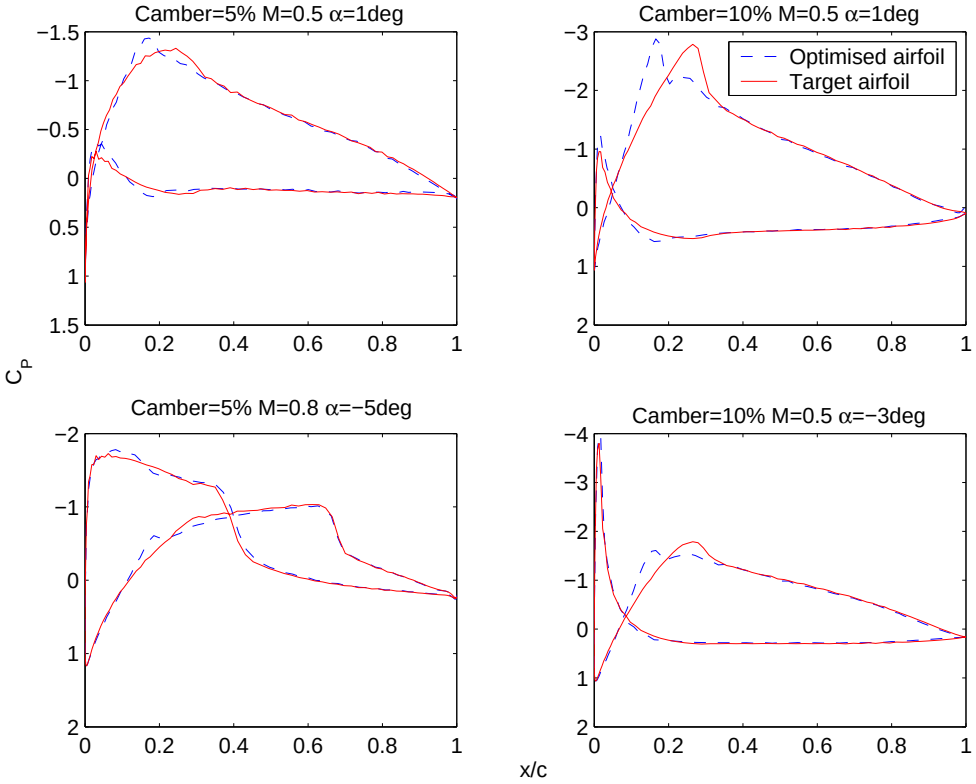

FIGURE 4.4: Pressure distributions for morphed and target airfoils (global search), under severe flow conditions, DA.

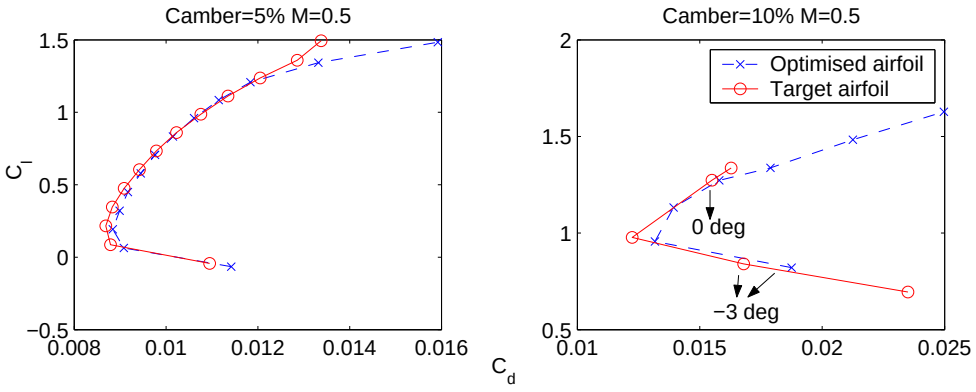

FIGURE 4.5: Drag polars for 5% and 10% cambers (global search), DA.

i and structural location j, and $a \in \{a_1, a_2\}$ define the lower and upper displacement constraints at each load increment, with a maximum number of increments n_{inc}, for each airfoil defined at n_p structural grid points. Here, the load increment i represents the structural solution corresponding to an airfoil with maximum camber of 10% chord, therefore, the flow parameters are kept fixed (i.e., M = 0.5 and α=2 degrees) over a single cambered airfoil.

As already noted, this refining optimisation process was driven by DHC for local search,

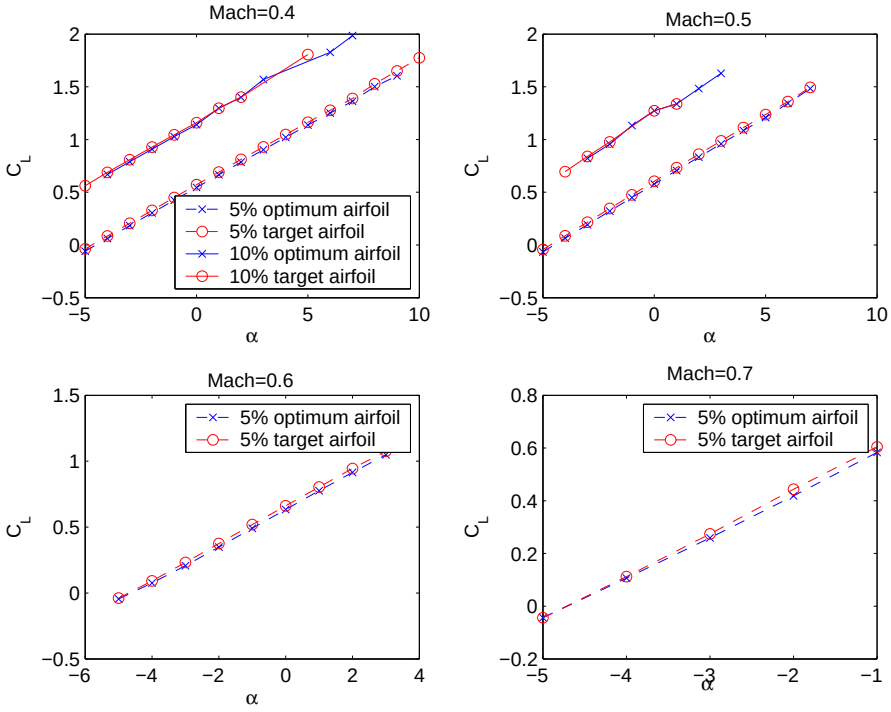

FIGURE 4.6: Variation of lift coefficient vs. angle of attack with Mach number, for 5% and 10% cambers (global solution), DA.

starting with the best design from the previous optimisation. Here 1600 DHC iterations were needed to improve the structural response of the set up (see again Figure 3.20). Clearly, this leads to a very good agreement in terms of pressure distribution, including shock positions for the higher camber results (see Figure 4.7). This also yields more closely engineering drag performance shown in Figure 4.8. Quantitatively, the performance in the matching of drag polars is 10 drag counts for 5% camber airfoil at -5 degrees incidence and 9 drag counts for 10% camber at 1 degree incidence (n.b. similar performance is achieved with the NURBS-based airfoils, i.e., 8 drag counts at 1 degree incidence for 10% camber, as depicted in Figure B.8). These results, augmented also by the improvement over the $C_L - \alpha$ variation depicted in Figure 4.9, justifies the significant extra effort required for the CFD-based optimisation, and serves to ensure that good drag performance is maintained while still allowing significant camber control. This is a particularly important feature of the design process, since any gains achieved from flapless control in terms of stealth or reduced noise must not be achieved at the expense of deteriorating aerodynamic behavior. Of course, it would be possible to carry out the entire optimisation process using the fully coupled structural and CFD analysis throughout, but this would be considerably more costly than the two-stage process used here.

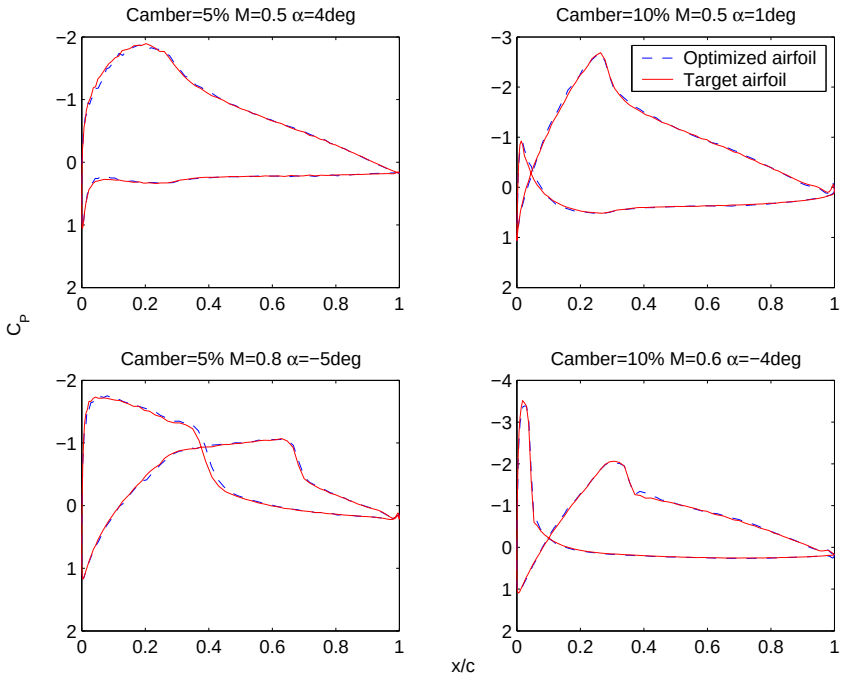

FIGURE 4.7: Refined pressure distributions for multi-shape morphing airfoils, under mild and severe flows, DA.

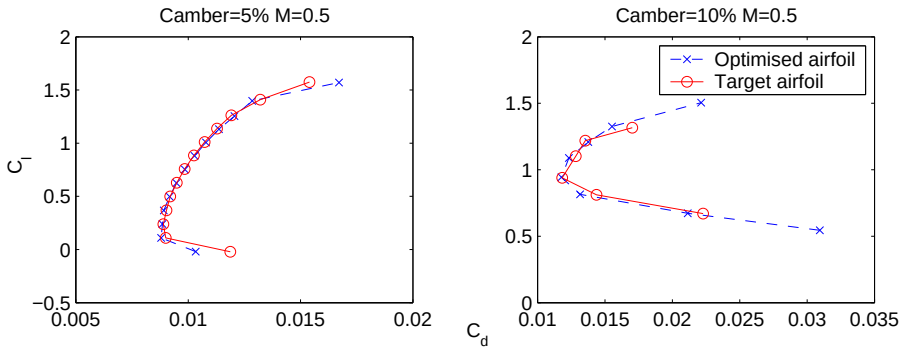

FIGURE 4.8: Refined drag polars for morphed airfoils, DA.

4.3 Static Aeroelastic Study of Morphing Airfoils

Aeroelasticity plays a significant role in describing the stability, rigidity and control of lifting bodies. The performance and behaviour of a lifting body is dictated overall by competing disciplines, viz, structures and flow dynamics, that need to be coupled in some form to provide aeroelastic solutions. In the literature there are usually two approaches for coupling: *single domain* or *fully coupled*, where the solutions are results of a monolithic system of equations that represent both disciplines, with a trade-off on numerical implementation (see for instance Guruswamy (1992) in the early stages of developing such schemes) and *loosely coupled*, where an explicit interfacing boundary

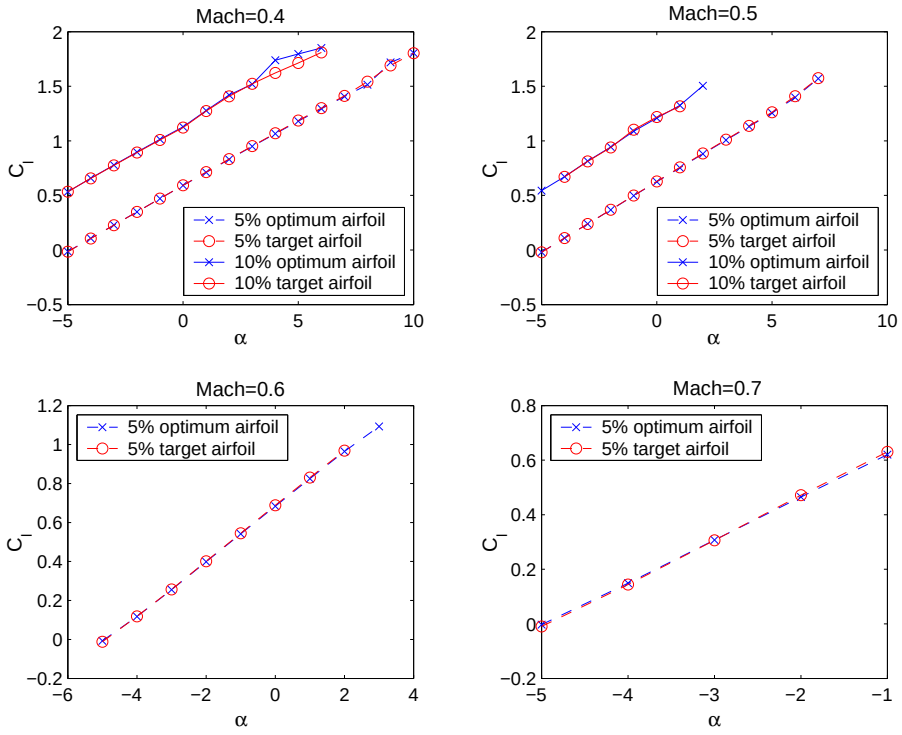

FIGURE 4.9: Variation of lift with incidence for gradient-based optimum solution, 5% and 10% cambers, DA.

information between disciplines is provided (i.e., *integrated* within the source codes by Love et al. (2000) or *modular* external mapping schemes between tools, see Cai and Liu (2001) and Alonso et al. (2004)).

The primary focus of this section is a static aeroelastic study under a loosely coupled and modular method, since time-accurate solutions are not considered. The interaction between fluid and structures can be achieved through a wide variety of mapping algorithms (a comprehensive review of such interpolating schemes can be found in Smith et al. (1995)). In the loosely coupled approach, the boundary interface between the two disciplines has a dual character, providing means of mapping the pressure field onto the structural grid, and also interpolating the displacement field into the CFD grid. To obtain an aeroelastic solution, these two mappings are repeated and updated in an iterative manner until a convergence criterion is satisfied. In VGK (1997) the infinite region outside the airfoil is mapped conformally onto the inside of a circle and the computational grid utilised by the finite-difference method is built upon radial lines and concentric circles. A fine CFD grid is utilised initially in order to maintain the accuracy of the solution for any small geometry changes. Therefore, the aeroelastic solution is based upon the boundary interface corresponding to a fixed CFD grid and an iteratively updated displacement field (i.e., a pressure field is obtained from a rigid steady state CFD solution and is mapped onto the boundary-fitted structural grid with impact on

structural response computed by FEM solver) as depicted in the workflow from Figure 4.10.

Static aeroelasticity requires geometry conservation through the mapping of the conservative aerodynamic loads f_a, which becomes intrinsic when, under a relaxation procedure, the pressure field is updated with the current and the previous states (see, for instance, Cai and Liu (2001) or Alonso et al. (2004)). The updating process is controlled by a relaxation factor, β, that determines the magnitude of the pressure perturbation (i.e., oscillatory), such that

$$f_a^n = f_a^{n-1} + \beta(f_a^n - f_a^{n-1}), \tag{4.2}$$

$$0 < \beta < 1.$$

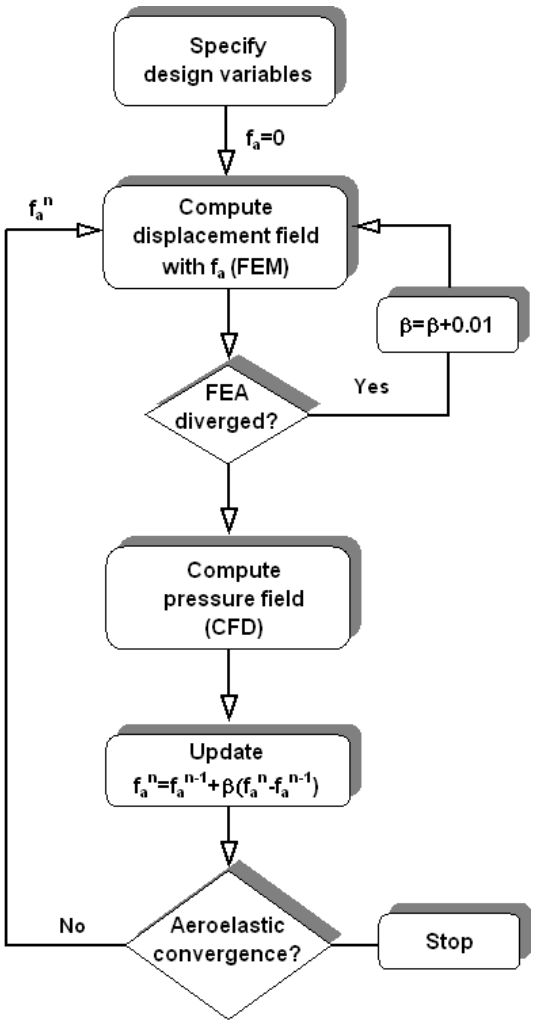

FIGURE 4.10: Airfoil aeroelastic workflow.

A canonical example consisting a 5% cambered airfoil under moderate flow conditions with M = 0.5 and $\alpha = 2$ degrees is studied. The airfoil under investigation is considered to be fixed between the boundary conditions, as the wing shape control paradigm can be

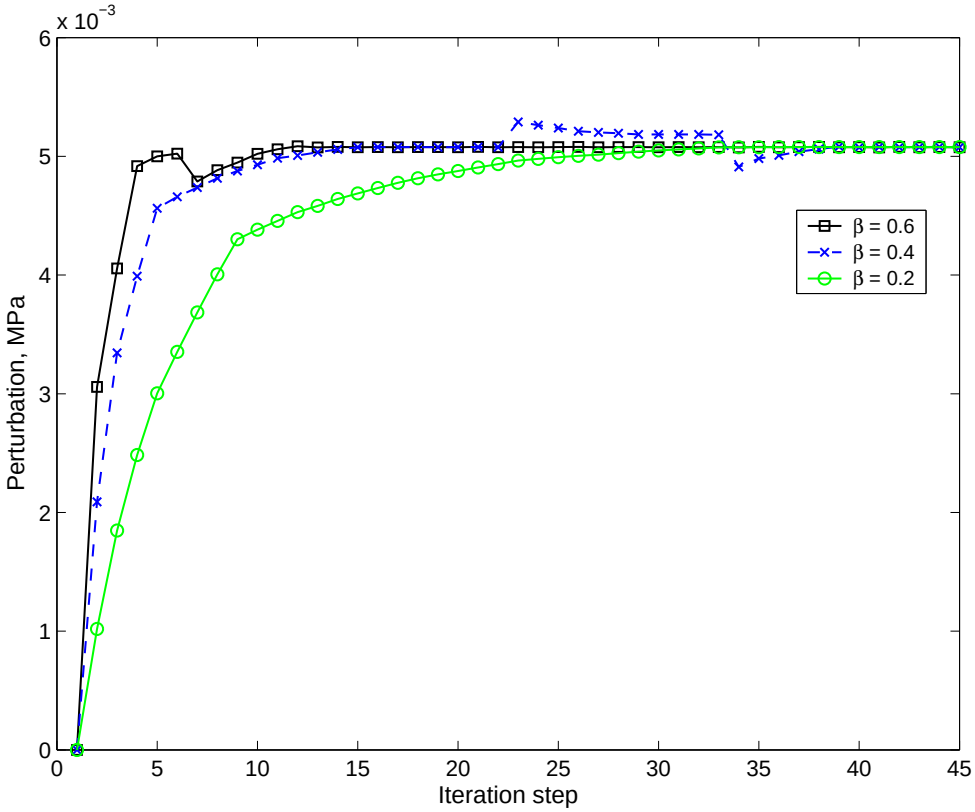

FIGURE 4.11: Aeroelastic convergence studies, with relaxation factor β = 0.2, ,0.4, 0.6, DA.

thought as a two-spar structure anchored within the enclosure of the outboard or fuselage and can simulate the boundary conditions, i.e., the pinned leading edge and sliding trailing edge, so that the global shape control of the wing is possible. The structural set up consist the best solution from gradient search including boundary conditions and the pressure distribution is mapped onto the structural grid so that lift and drag are accounted for (n.b., on a unit width beam, the pressure is discretised into equivalent concentrated forces orthogonal to the aerodynamic surface and applied on the structural boundary-fitted grid). The conversion factor that tunes the pressure distribution also takes into account the width of the beam (i.e., 8 mm) so that the aeroelastic updates are based on full structural strength of the beam (n.b. the NURBS-based aeroelastic results presented in Appendix B.3 are computed for a unit width airfoil to emphasise the aeroelastic feature of the proposed model).

In the aeroelastic cycle, the convergence of the solution is accelerated when large relaxation factors are used. Such trends can be seen in Figure 4.11 for the DA-based airfoils (n.b. similar results for the airfoils under NURBS scheme are presented in Appendix B.3), where a relaxation sensitivity study shows the convergence of the solution in the aeroelastic cycle in terms of perturbation f_a (i.e., the non-regular C_P distribution mapped onto the structural-fitted grid and integrated over the width of the beam). For a relaxation factor $\beta = 0.6$ the aeroelastic solution converges after 15 iterations, whereas

for $\beta = 0.2$, 35 iterations are needed (similar trends are obtained for NURBS-based airfoils in Appendix B.3).

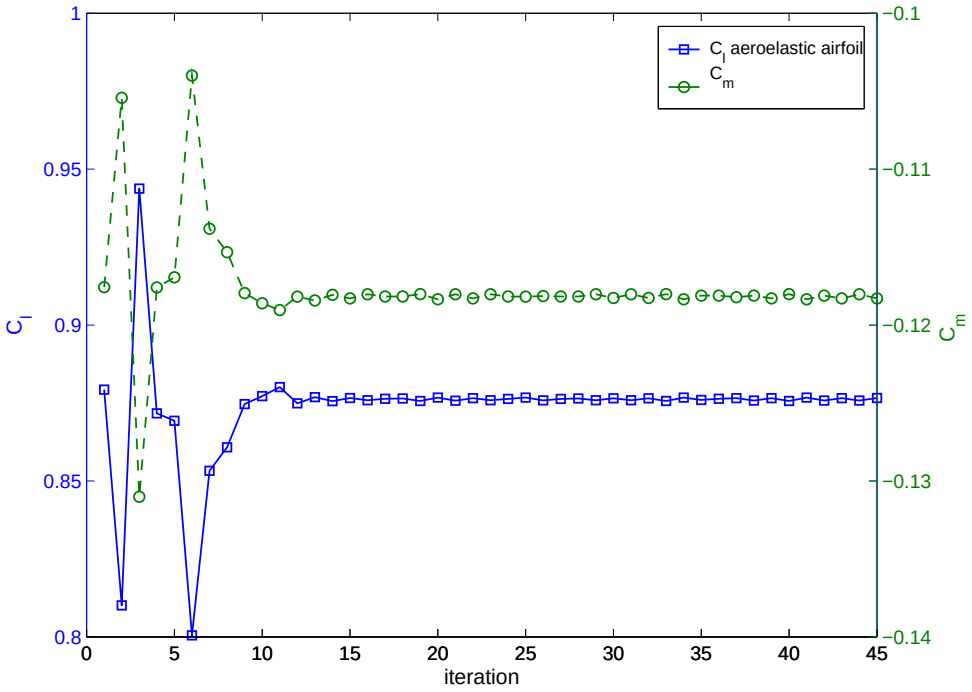

FIGURE 4.12: Aeroelastic stability, $\beta = 0.6$, DA.

The convergence history in terms of perturbation in Figure 4.11 and also in terms of lift and pitching moment coefficients in Figure 4.12, shows large oscillations due to the incremental-iterative FEM procedure. The difference between two consecutive incremental solutions can be large and then the minimum norm of the desired camber and the surrounding solutions is chosen, which may lead to large oscillations in aerodynamic properties due to somewhat smaller camber variations. This variation is intrinsically dictated by the non-linear solution and has a magnitude of an increment. Structural instabilities may also occur, in which case the relaxation factor is augmented by one percent so that the perturbation to the system is augmented, thus obtaining a stable solution. The convergence history also shows that the aeroelastic solution is only slightly changed from the rigid steady state one, with a maximum of one percent, which proves the airfoil is stiff enough to preserve its optimised rigid state properties (see Figure 4.13 for the aeroelastic pressure distribution and the resultant airfoils in Figure 4.14, under a relaxation factor $\beta = 0.6$). The nature of the aeroelastic study of the DA-based airfoils is also emphasised by the wavy pressure distribution, inherently determined by the irregular stiffness variation chordwise under the non-uniform pressure field onto the boundary-fitted grid of the airfoil.

In such analyses, although there is a high interdependence between conflicting FEM and CFD systems, here the pressure transfer from the CFD algorithm onto the FEM grid has essentially negligible impact on overall aerodynamic performance of the airfoils.

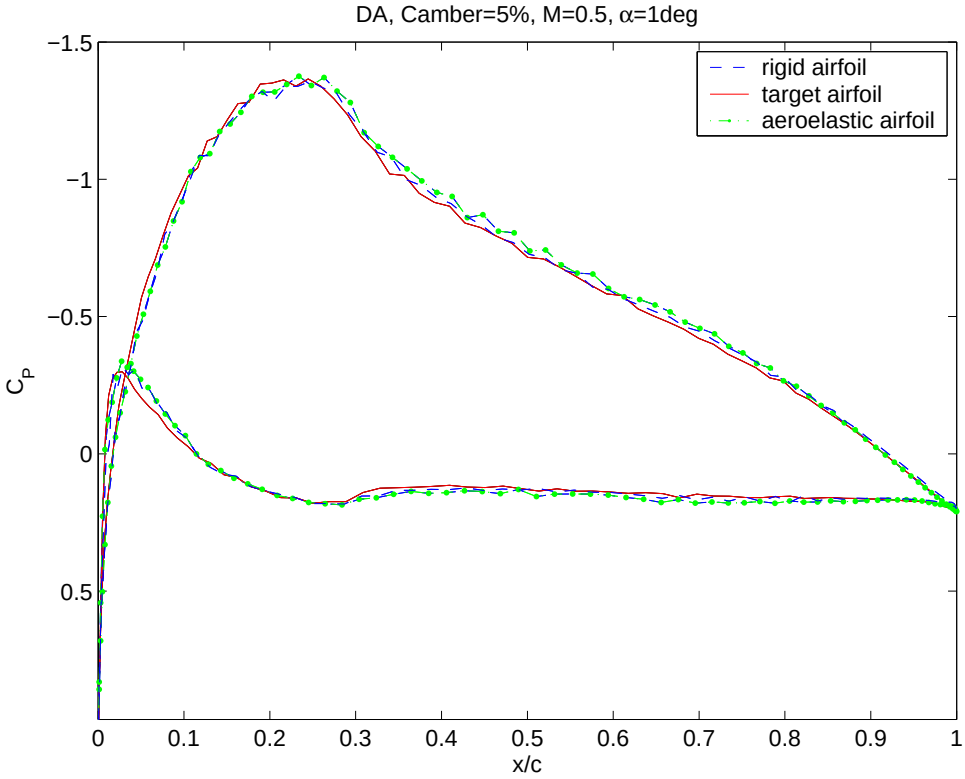

FIGURE 4.13: Aeroelastic pressure distributions, $\beta = 0.6$, DA.

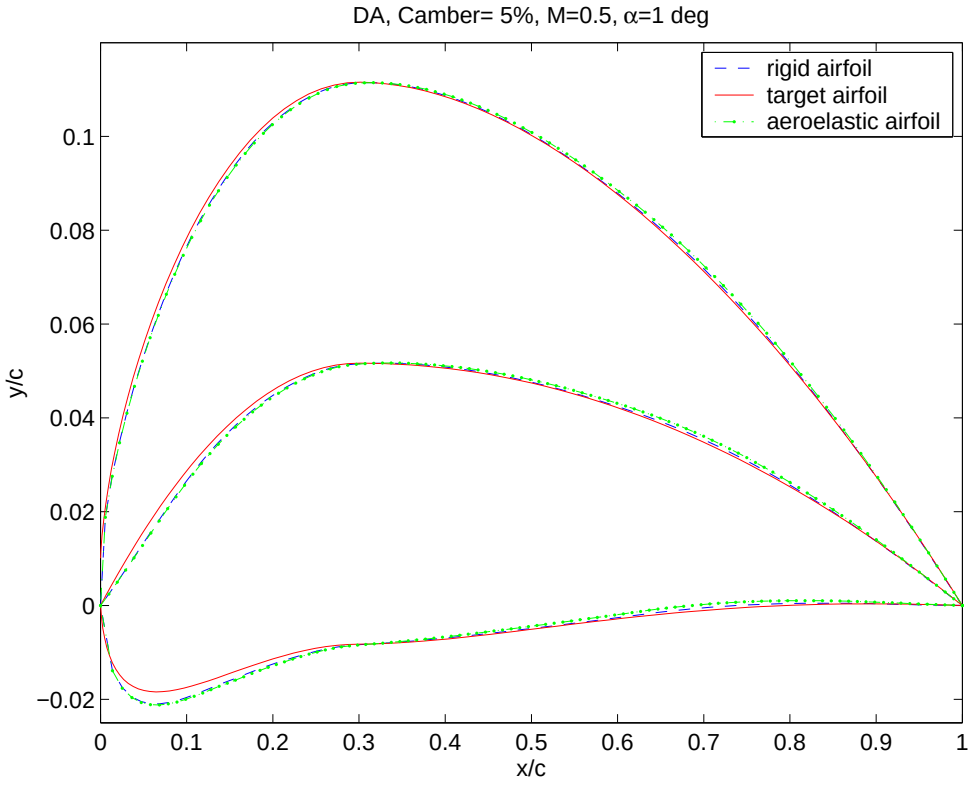

FIGURE 4.14: Rigid and aeroelastic airfoils, $\beta = 0.6$, DA.

4.4 Summary

Linked to the previous chapter, where a two-pronged optimisation was performed by means of structural enhancements, this chapter augments the features of the multi-shape morphing airfoils. The main focus was a study on the aerodynamic gradients when large structural changes occur during morphing. The DA boundary-fitted grid is emphasised here due to its lack of smoothness that can produce large disturbances in the flow, across a wide range of cambers, although similar results for the NURBS based airfoils are presented in Appendix B. Using a full potential solver and a two-stage aerodynamic analysis (i.e., a GA-based structural solution is followed by a DHC-based local search with the residual correction method), very good agreement between optimised airfoils and their associated targets has been obtained in terms of aerodynamic performance and boundary geometries. Such airfoils deliver aerodynamic characteristics that match a set of pre-specified target shapes, under aeroelastically stable conditions, and the similarity between the results of the two parameterisation schemes employed concludes that the approach is well posed and it parameterisation independent.

Chapter 5

Material Fitness

The global optimisation of morphing structures has so far been built on the assumption that the airfoils are constructed from predefined thickness (i.e., the analytical NACA definition). In this chapter, the fitness of the cladding material is considered in order to validate the assumption on unchanging thickness distribution on the morphing airfoils. An inverse optimisation of the constitutive parameters of a hyperlastic material is provided such that the aerodynamic performance of morphing airfoils is maintained while structural setup is fixed and based on gradient-search solution.

5.1 Overview of Hyperelasticity

Hyperelastic materials and especially elastomeric foams have a wide range of applicability in industry, ranging from biomedical engineering (e.g., arterial stents, artifical heart valves) to sport engineering and also the vehicle industry (e.g., suspension), mainly because of their excellent energy absorption and moulding capabilities. The constitutive law admits a continuous potential function that can control the stress-strain responses through the 'performance' parameters. The hyperfoams are cellular materials that can deform elastically up to 90% in compression, and also allow for large volumetric deformation (i.e., the effective Poisson ratio is less that 0.45-5) due to their porosity.

The linear elastic constitutive laws can only be used for linearised strain-stress relationships, under the assumption of small deformations. However, there are complex models where small strains (e.g., soils) and also finite strains (e.g., polymers) can be analysed on a elastic foundation, but exhibit non-linear stress-strain behavior. The emergence of non-linear constitutive laws begun nearly 60 years ago when exact non-linear solutions to incompressible isotropic material problems (i.e., hyperelasticity) were found due to Rivlin's discovery (Rivlin (1948)). Hyperelasticity comprises both non-linear material response and non-linear kinematics, with applications in both incompressible (i.e., rubberlike material) and highly compressible (i.e., elastomeric foam) responses.

The main features of the mechanical behavior on hyperelastic materials are that (1) the material behavior is elastic (i.e., there is no history dependence of stress, in addition to the reversibility assumption); (2) the material is temperature dependent in shear (i.e., that heat causes stiffening);(3) the shear modulus is very small compared to that of metals; (4) an isotropy assumption (i.e., the molecular chain, although randomly distributed in the mass of the material, exhibits deformation in the direction of straining).

Hyperelastic materials are described in terms of a strain energy density function (i.e., strain energy in the material per unit of reference volume), whose derivative with respect to a strain component ϵ_{ij}, determines the corresponding stress component σ_{ij}, as follows:

$$s_{ij} = \frac{\partial U}{\partial \epsilon_{ij}}. \tag{5.1}$$

A number of forms of the potential are available in the literature, such as Mooney-Rivlin, Neo-Hookean, and Ogden forms (Freakley and Payne (1978)), providing means to achieve accurate responses in different deformation modes (e.g., axial tension-compression, shear, volumetric changes), and using different formulations for the temperature-dependent material parameters to fit a particular material. These forms also offer the flexibility of deriving stress measures by defining the energy functional in terms of strain invariants and elastic deformation which are inextricably linked to kinematic quantities, such as principal stretches (Ogden (1984)) or the deformation matrix.

Since hyperelastic materials exhibit large deformations over a wide range of compressibility, a suitable form of the strain-energy functional has been proposed by Ogden (1972) for low-density foams, derived from slightly compressible rubber definitions, including terms of the strain invariants and principal stretches. The elastic behaviour of the foam is based on a modified Hill strain energy function:

$$U = \sum_{i=1}^{N} \frac{2\mu_i}{\alpha_i^2} \left[\hat{\lambda_1}^{\alpha_i} + \hat{\lambda_2}^{\alpha_i} + \hat{\lambda_3}^{\alpha_i} - 3 + \frac{1}{\beta_i}(J_{el}^{-\alpha_i \beta_i} - 1) \right], \tag{5.2}$$

defined by $\hat{\lambda_i} = J_{th}^{-\frac{1}{3}} \lambda_i$, where λ_i are the principal deviatoric stretches that give a measure of relative elastic volume $J_{el} = \hat{\lambda_1}\hat{\lambda_2}\hat{\lambda_3}$ ($J_{el} = 1$ for incompressibility) and also the total volume ratio J (i.e., current volume divided by original volume) is defined as temperature variant through the thermal strain ϵ_{th}:

$$J_{el} = \frac{J}{J_{th}} = \frac{1}{J_{th}} \frac{\delta V}{\delta V_0}, \tag{5.3}$$

$$J_{th} = (1 + \epsilon_{th})^3, \tag{5.4}$$

Here, μ_i, α_i and β_i are the material parameters to fit experimental data and define the initial shear modulus μ_0 by shear modulus coefficients μ_i,

$$\mu_0 = \sum_{i=1}^{N} \mu_i. \tag{5.5}$$

β_i specifies the shape of the volumetric response, being related to the effective Poisson ratio ν_i defining the initial bulk modulus K_0

$$K_0 = \sum_{i=1}^{N} 2\mu_i \left(\frac{1}{3} + \beta_i \right), \tag{5.6}$$

$$\beta_i = \frac{\nu_i}{1 - 2\nu_i}. \tag{5.7}$$

and α_i represents the shape of the stress-strain curve, i.e., a low α increases the curvature of the response and produces a rapid initial compression and stiffening.

In the current study large deformations of the strut occur (i.e., up to 10%-15% chord in the post critical regime) and it was assumed that the thickness distribution of the deflected airfoil using the spinal structure, kept its analytical definition throughout the deformation. In reality, the constitutive hyperelastic models are phenomenological and may affect the structural strength of the set up. Therefore, a low density elastomeric foam is studied here to simulate a true mechanical response, to bring closure to the initial assumption on deformation simplicity of the fixed thickness distribution. A comprehensive overview on the potential materials along with the test beds can be found in Kikuta (2003).

A direct search of parameters on structural behaviour of hyperelastic models is also present in the literature, for instance, Twizell and Odgen (1983) and Ogden et al. (2004), derive a benchmark of non-linear least squares fit (i.e., optimisation) on experimental data, outlining the non-singular optimal solutions to such problems.

5.2 Inverse Design of Constitutive Parameters

The elastic properties of elastomeric foams are highly dependent upon the stiffness of the cellular chain and its structural density (Gibson and Ashby (1977)). Since the experimental test data for the material in terms of stress-nominal strain pairs in combinations of uni-equiaxial, planar, simple shear and volumetric expansion are not provided, the hyperfoam material properties can be tackled using direct input of coefficients into the potential function, to predefine the mechanical response of the model. Both hyperelastic

and elastomeric foams have their constitutive laws implemented in several industry commercial non-linear FEM codes, such as Abaqus®/Standard (Version 6.5). That enables the user to choose the functional parameters and the order N, so that a mechanical response of the material is achieved. Here an inverse design method is approached as discussed in previous chapters, whilst a functional defined in terms of aerodynamic properties of the deformed set up is assessed using VGK.

The current section improves upon the equivalent implicit correlation between the deflected strut and the theoretical airfoil surface, providing a more practical approach of the setup, i.e., a hyperelastic material intrinsically linked to the camber-like strut. Since *a priori* knowledge of the proposed material is not provided, an optimisation of the material parameters is carried out via an inverse procedure, using a parent-based search engine (i.e., a GA).

As a starting point, the set up comprises the optimum strut design from the previous gradient-based optimisation that featured good aerodynamic properties in terms of the increment-based morphing airfoil and the thickness distribution is represented now by an elastomeric foam constitutive law. A four-digit NACA definition is used to represent the aerodynamic shape of the airfoil in its undeformed state. During the deformation, volumetric changes along with compression-tension states are allowed to occur (keeping in mind that the effect of undesirable ripples and bulges is to be minimised as secondary effect during optimisation) so that good aerodynamic features can be achieved (i.e, when compared to the properties derived from its equivalent target airfoil, under the same flow conditions as in the gradient-based search). Therefore, a functional related to the aerodynamics of the set up is to be minimised and can be stated as follows:

$$\begin{aligned} \text{Minimise } f(\mathbf{x}) &= \|\mathbf{C_p}(\mathbf{x})^t - \mathbf{C_p}(\mathbf{x})\ \|, \\ \text{Subject to } g_i(\mathbf{x}) &= d\boldsymbol{\tau} : d\boldsymbol{\epsilon} > 0, \\ \mathbf{x} &\in \mathbf{X},\ \forall\ i \in \{1, \ldots, n_{inc}\}, \end{aligned} \tag{5.8}$$

where $\mathbf{X} = \{\mathbf{x} \in \mathbb{R}^n \mid x \equiv \{\mu_k, \alpha_k, \beta_k\},\ k = 1, \ldots, N\}$ with N the order of the material. The implicit constraint g_i is defined by the Drucker stability check (i.e., intrinsic to the FEM solver) and is evaluated at each load increment i until the maximum number of increments n_{inc} is reached, to reduce the computational burden of the optimisation. The constraint can be expressed with respect to increments of the principal Kirchhoff stress $d\boldsymbol{\tau}$ following a non-specified principal logarithmic strain $d\boldsymbol{\epsilon} = d(ln\boldsymbol{\lambda})$:

$$d\boldsymbol{\tau} : d\boldsymbol{\epsilon} > 0. \tag{5.9}$$

or as positiveness of the tangential stiffness matrix $\boldsymbol{D}$ in Krichhoff-Cauchy stress relationship $d\boldsymbol{\tau} = Jd\boldsymbol{s}$:

$$d\boldsymbol{\epsilon} : \boldsymbol{D} : d\boldsymbol{\epsilon} > 0. \tag{5.10}$$

A number of papers in the literature deal with the estimation of the constitutive parameters of elastomeric foams, searching for rather discrete values that can fit different experimental data. Such research emphasises that a higher order N of the model coupled with a inconsistent choice of the parameters may lead to high sensitivity, instabilities or a poor fit to the experimental data. Mills and Gilchrist (2000) established consistent agreement to the stress-strain response curve of a second order low density polymer using pairs (α_i, μ_i) of discrete values to quantify tensile (e.g., $\alpha_2 = 20$) and compressive (e.g., $\alpha_2 = -2$) hardening coefficients at high strains while intermediate values increase the strain rate in uniaxial compressive response, commenting that first order model lead to a poor fit of the material.

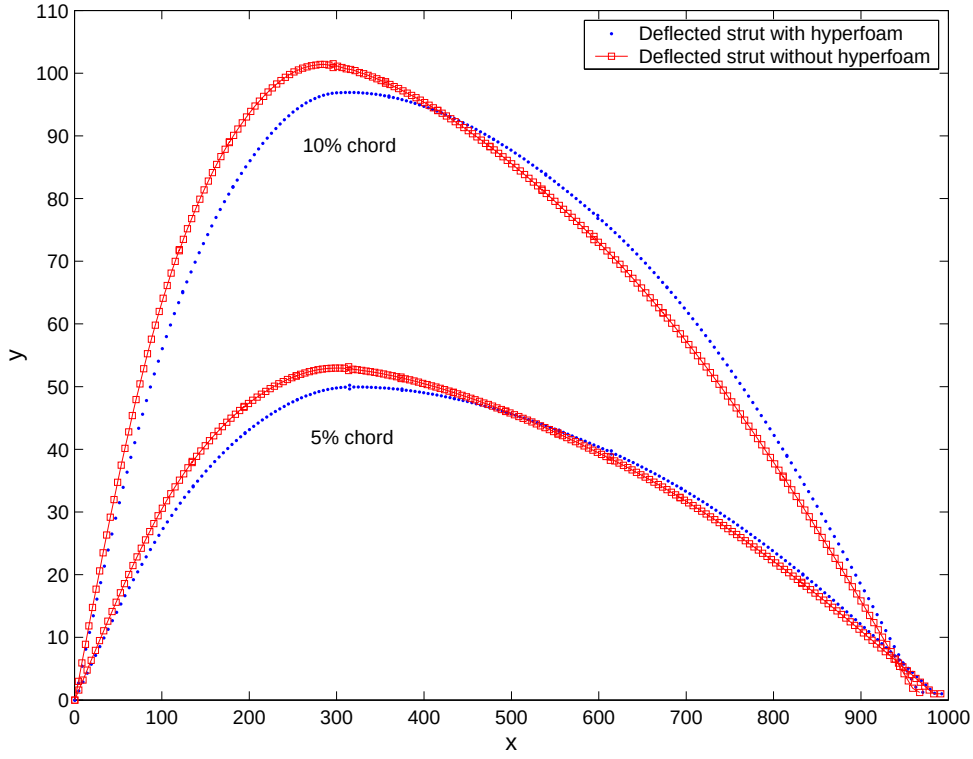

FIGURE 5.1: 5% and 10% camber to chord ratio strut deformation with hyperelastic material.

Therefore, for the current model an elastomeric foam material with the order of the series expansion N=2 is chosen, to ensure sufficient flexibility and stability of the constitutive law in modeling the structural behaviour of the foam. The elastomeric allows for high compressibility (i.e., flexibility), enabling small reactions of the foam on the camber-like spinal structure in an optimum configuration (see Figure 5.1). The lateral deflection of

the beam for larger cambers is controllable, since the hardening behavior is driven by physical arguments in the outlined functional. The optimisation here accounts for large strains and rotations, since the structural solution is found employing an iterative based non-linear procedure. Although in the previous optimisation of the beam the structural constraint was expressed in terms of bounds for maximum deflection achievable, only the solution (i.e., load-displacement discrete values) represented by a minimum norm to the bound is chosen. The norm can range up to a maximum increment size, which often varies between 0.001% and 0.1% of the final solution achieved.[1] Such a norm can also be expressed as change in the displacement field when using a set up comprising of the beam and the elastomeric foam, as shown in Figure 5.1 for 5% and 10% camber to chord ratio. As expected, the gradient deformation is larger at the position of the maximum camber due to the augmented stiffness of the set up in the presence of the foam.

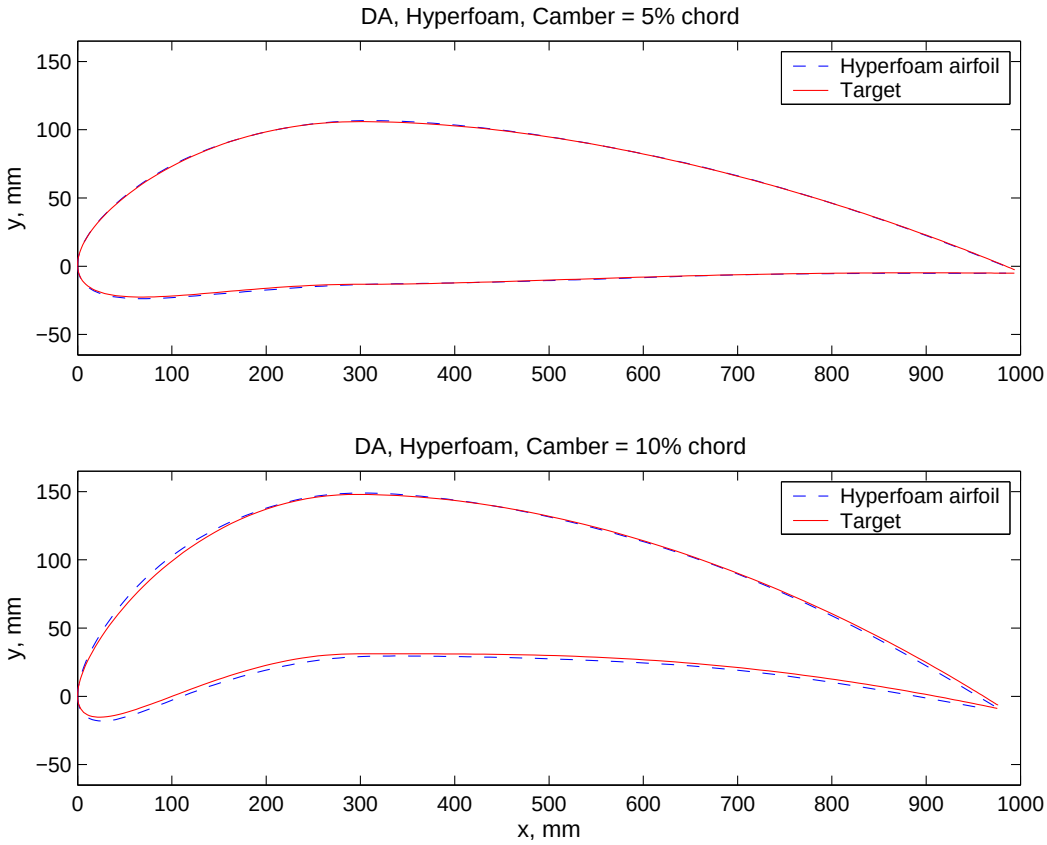

FIGURE 5.2: Optimal analytical and experimental airfoils

The global optimisation in this section is based on the same features (i.e., structural set up and flow conditions) as the previous gradient-based search. The optimal aerodynamic shapes of the computed airfoils are plotted against the target ones for both 5% and 10% cambers in Figure 5.2 showing a very good agreement.[2] The aerodynamic properties of

[1]The increment size varies during the deformation and is highly dependent on the non-linearity degree of the model, since an incremental-iterative procedure is employed to minimise the residuals

[2]The figures may lack of accuracy of plotting due to fitting procedures for larger deformations, as only positive defined airfoils can be used in VGK

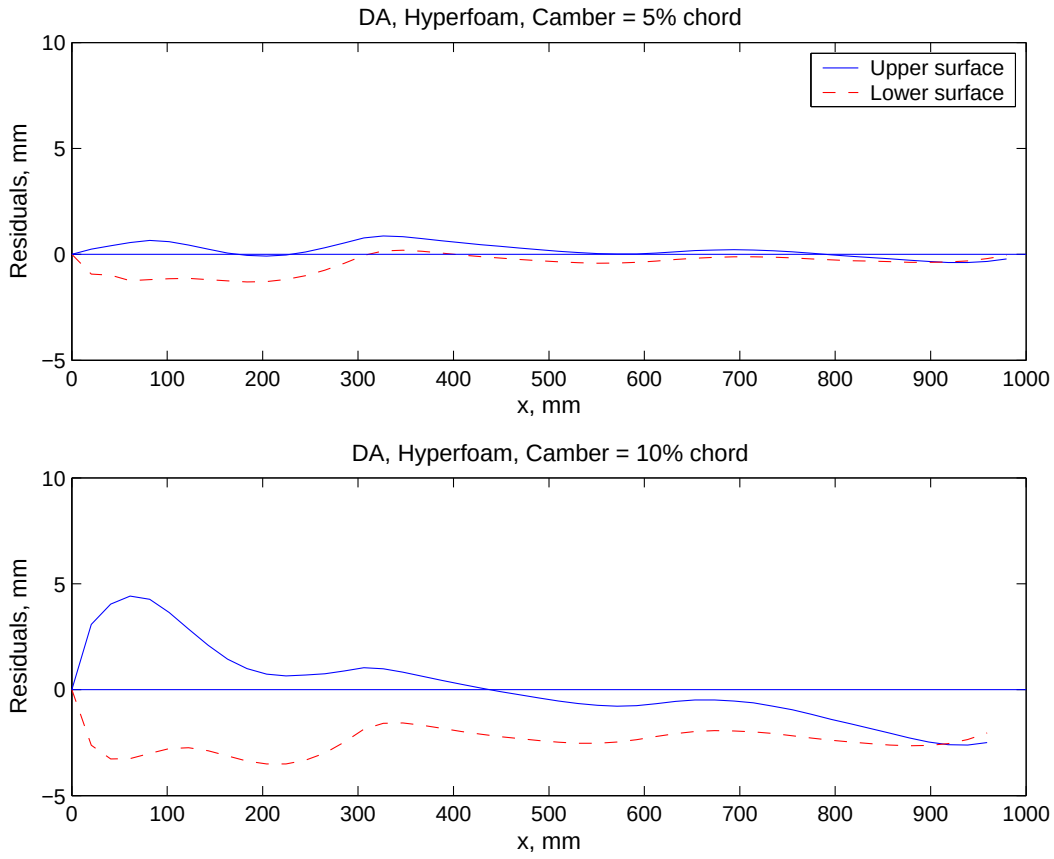

FIGURE 5.3: Residuals between optimised hyperfoam and target airfoils in the range of deflection states of 5% and 10%.

the airfoils are sensitive to the perturbations in the aerodynamic shape, but the proposed model, studied over a wide range of flows, indicates a very good agreement in terms of pressure distribution, including mild shock position (see Figure 5.4 for 5% and 10% cambered airfoils). This agreement is complemented by a linear $C_L - \alpha$ variation over the range of computed incidences, with higher variations of drag towards the end of the Mach-incidence envelope (Figure 5.5), where shocks are likely to occur. The drag polars also outline the true aerodynamic feature of the model, yielding a very similar drag performance to the target shape (Figure 5.6).

The optimised set of the hyperfoam potential parameters for the underlying model is compared with a number of valid models from the literature, to check its validity within a wide design space encapsulated by experimental data. Here, the validity basis is set by the studies of fitting constitutive parameters to experimental data provided by Mills and Lyn (2001), Schrodt et al. (2005) and HKS Abaqus® manual for hyperfoams of order $N = 2$. The resulting materials based on the fitted experimental data from Table 5.1 are analysed in Figure 5.7 for camber of 10% chord at Mach 0.5 and incidence -1 degree. Clearly, the pressure distributions of the hyperfoam airfoils are intrinsically linked to the structural response of the foam-core, *a priori* determined by the potential definition in uni-bi-axial compression and tension and shear so that to fit a target. The numerical

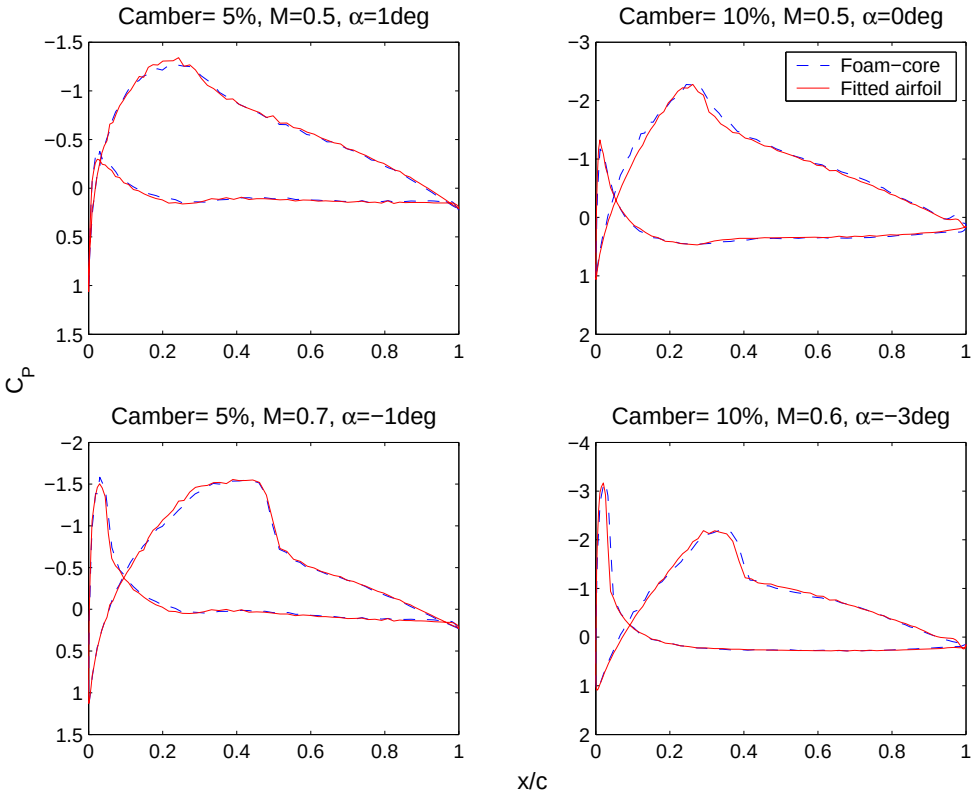

FIGURE 5.4: Pressure distributions of 5% and 10% hyperelastic airfoils.

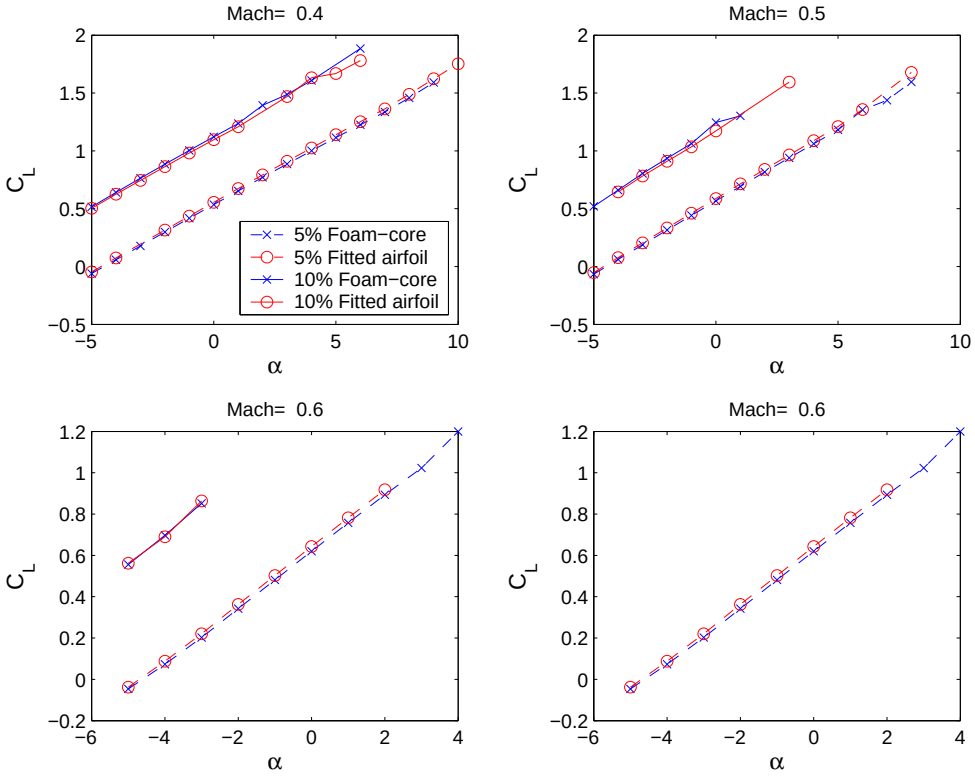

FIGURE 5.5: Aerodynamic properties of 5% and 10% hyperelastic airfoils.

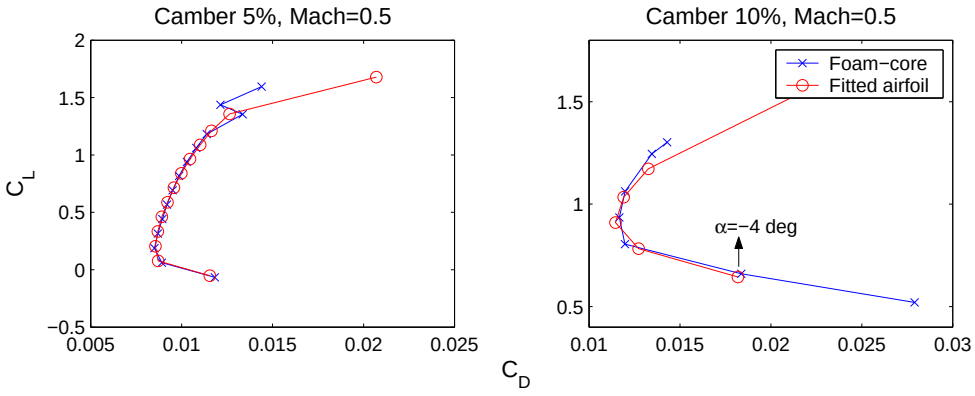

FIGURE 5.6: Drag polars of 5% and 10% hyperelastic airfoils.

fitness of the studied hyperfoams is presented here as a root mean square error (see table 5.1). The optimised hyperfoam presents a good trade-off between the experimental configurations and exhibits a better fitness with the constitutive parameters close to experimental ones, by controlling the potential definition, thus the stress-strain curve through the μ_i, α_i and ν_i parameters.

TABLE 5.1: Parameters for the hyperfoam materials with $N = 2$.

	Optimised set	Mills and Lyn (2001)	HKS Abaqus®	Schrodt et al. (2005)
μ_1	0.041280	0.018	0.16709	0.00481
α_1	16.021013	8	9.00665	19.8
μ_2	0.246407	0.012	2.153721E-5	0.00360
α_2	7.457265	-2	-4.86940	19.8
ν_1	0.340440	0	0	0.014091
ν_2	0.273473	0.45	0	0.006416
RMSE	0.0772824	0.123	0.09487	0.158537

Qualitatively, the performance of the elastomeric foam can also be emphasised using stability conditions within the constitutive law.[3] The physical arguments of the potential from which stress states are derived have a large impact on the local structural behavior of the foam. The optimal solution here presents an inhomogeneous stress field (Figure 5.8 and the contours are rather bunched in the radial direction. Concentration factors outlined by large consecutive variation of stiffness (i.e., the discrete thickness distribution scheme used to represent the strut) constitute the origin for small stress concentrations, that 'weed out' with large deflections and also change with the bending curvature of the strut. The inhomogeneous stress field also captures the vertical component of the Cauchy stress tensor s_{33} towards the leading edge, where the stiffness of the foam decreases.

[3]Here the design space is large and for constitutive constants highly negative leading to nominal strain range of $-0.9 \leq \epsilon_1 \leq 9$ (the material is prone to instabilities), Abaqus performs data checks for nine forms of loading: uni-biaxial, shear, planar and volumetric tension and compression and issues warnings for minimum strain for which the instability is observed

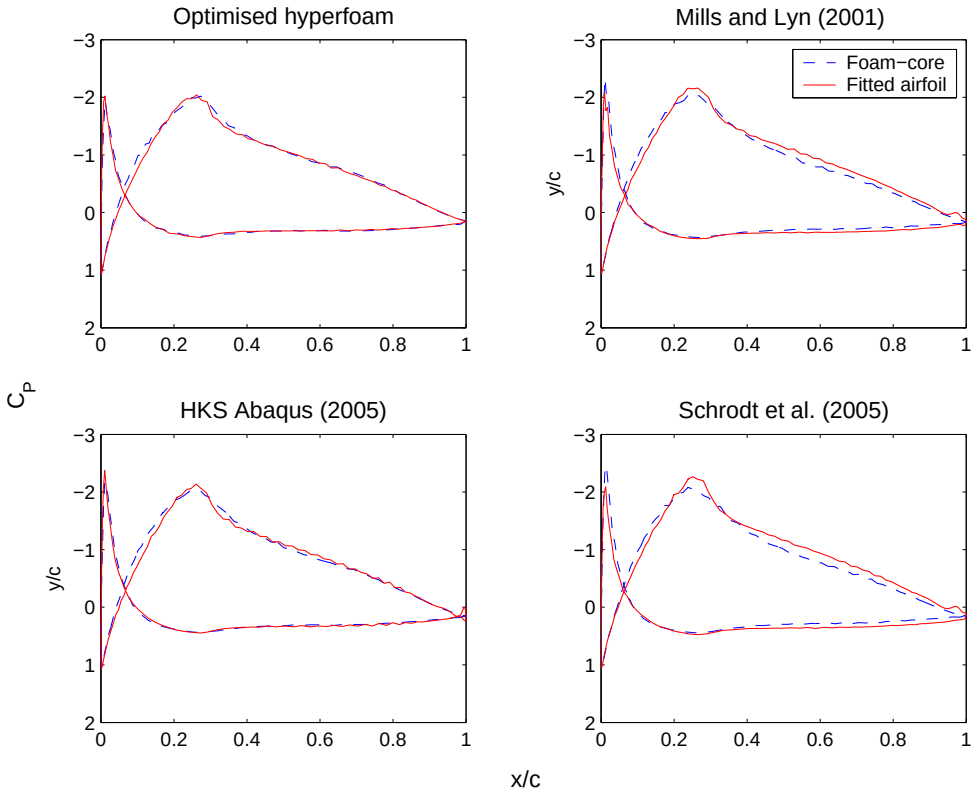

FIGURE 5.7: Comparison of pressure distributions of different fitted hyperelastic airfoils for cambers = 10% chord at M = 0.5 and $\alpha = 1$ deg.

The maximum vertical stress for 10% camber $s_{33} = 34$ KPa, i.e., very low compared to stresses in a shoe cushioning system ($N = 1$) of 80kPa in Thomson et al. (1999) or 70kPa in an impact of a headform on crash mats ($N = 2$) in Lyn and Mills (2001). The main feature of elastomeric foams concerns the compressibility and this is depicted in Figure 5.9. The maximum logarithmic compression strain for the 10% cambered airfoil LE_{22} is on the order of -0.0239, which is equivalent to a stretch of $\lambda = e^{-0.0239}$ or a nominal compressive strain of 2%. Similarly, $LE_{11} = -0.09323$, which leads to a nominal strain of 9%, indicating a mild axial compression of the foam. These invariants predicts the behaviour of the foam with respect to the stress-strain equilibrium path, as for strains smaller than 5%, linear elastic deformations occur due to bending of the cells, followed by a plateau at almost constant stress due to elastic buckling of cell walls.

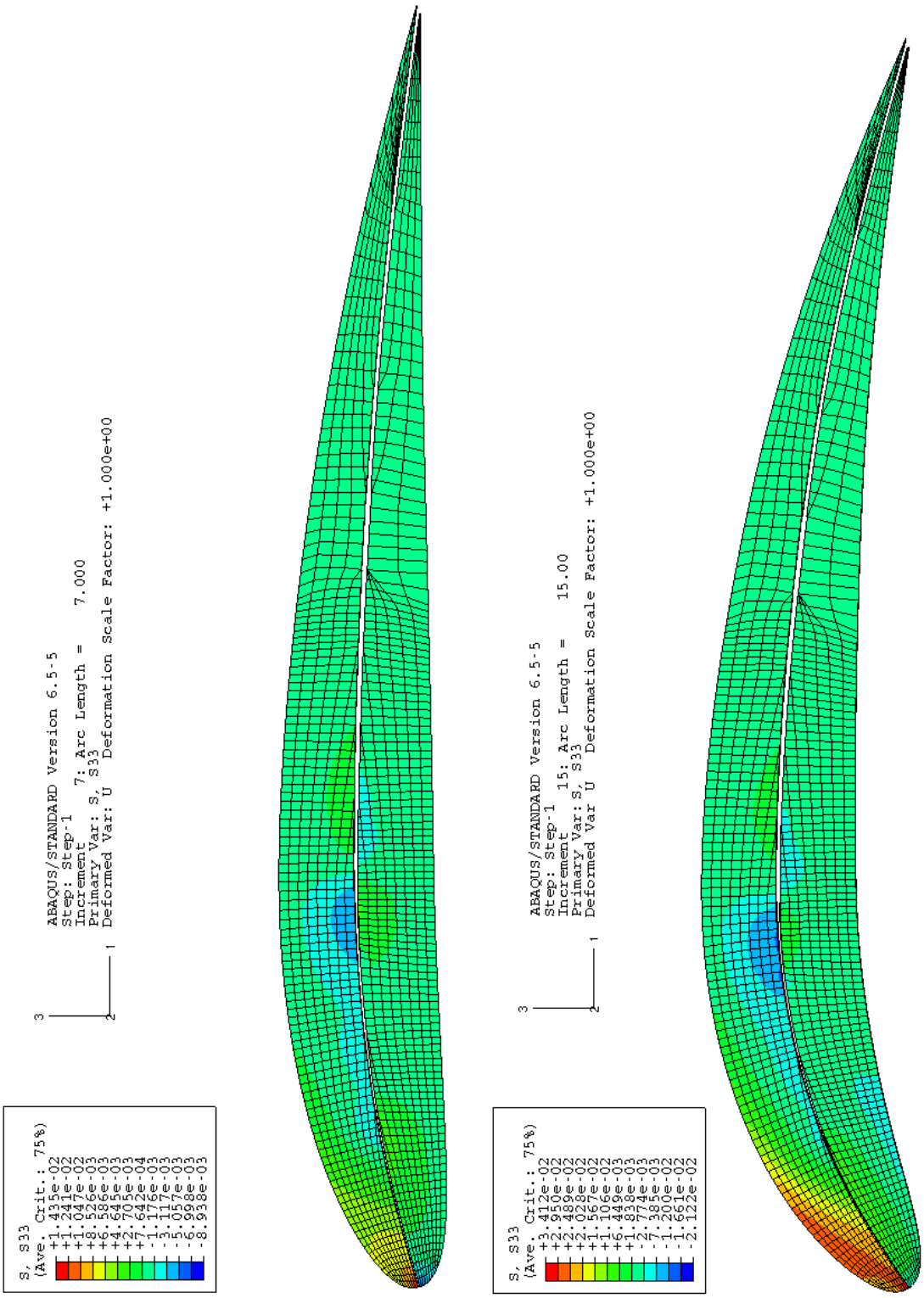

FIGURE 5.8: Stress contours of hyperlastic airfoil.

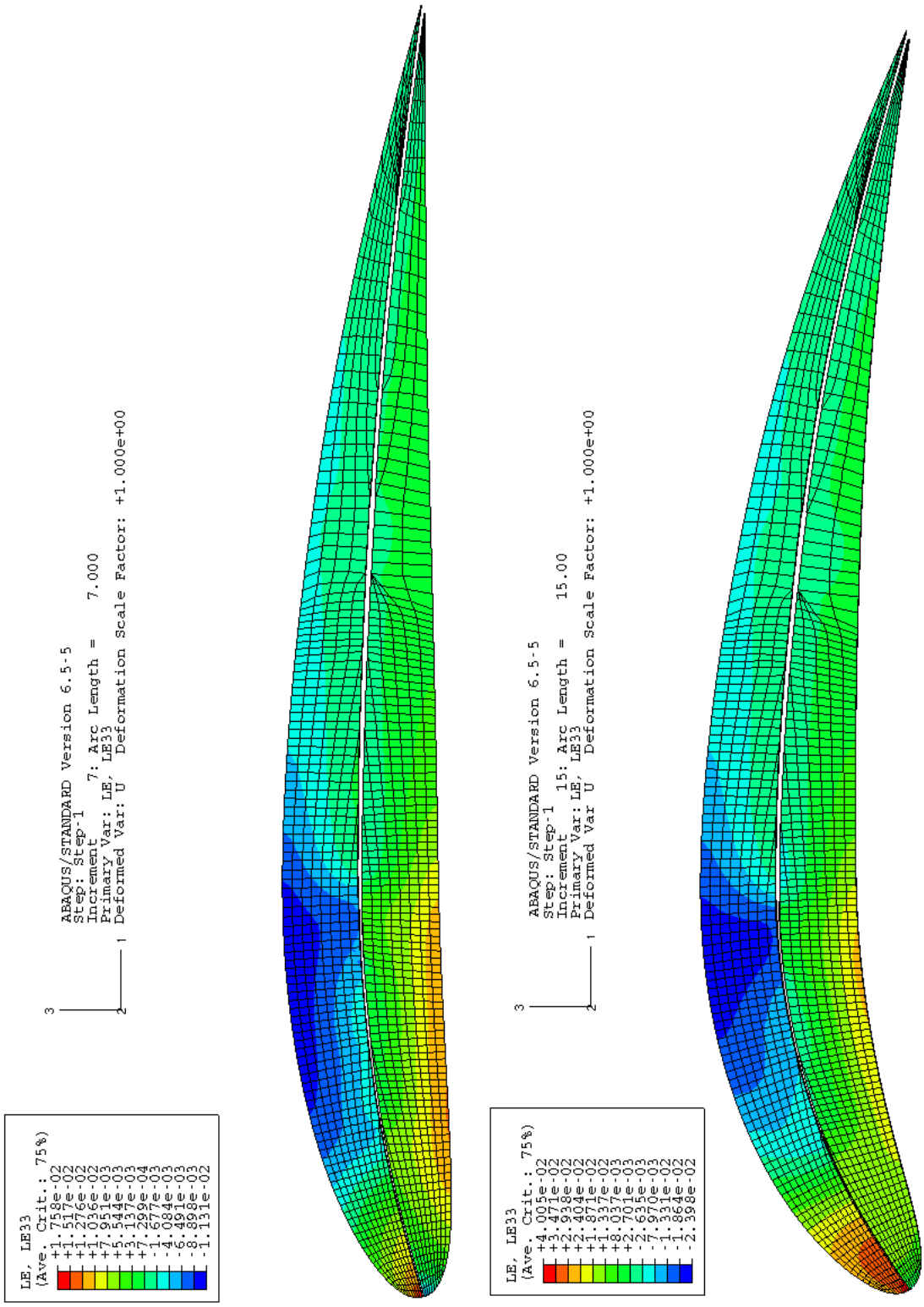

FIGURE 5.9: Strain contours of hyperlastic airfoil.

5.3 Concluding Remarks

Finite element analysis of the elastomeric foam requires a very fine mesh to capture small perturbations in the aerodynamic surface, and a significant computational burden

is associated with it. This chapter described a methodology to perform a best fit material, by setting up the optimisation problem for the aerodynamic performance required. Although a solution of the optimal constitutive parameters has been found using a global GA search with only 60 generations and a population size of 50, the optimisation is still computationally expensive. This was alleviated in earlier chapters under the assumption that the distribution of the foam-core throughout the deformation is represented by the theoretical four-digit NACA definition. The current optimisation has been performed to validate this assumption, demonstrating that the simplifying assumption can be justified.

Chapter 6

Wing Morphing and Roll Control

The heuristic methodology of global shape control, applied initially to achieve multi-shape morphing airfoils, is extended in this chapter to the three-dimensional case. The concept is applied to aerodynamic wing design to enhance roll control and combines the FEM and CFD analyses of parametric CAD models, wrapped in a multi-objective optimisation. The development of effective designs is a complex and computationally expensive task, and is tackled by means of surrogate modeling.

6.1 Formulation of the problem

In real life aircraft applications, wing morphing concepts rely on actively and continuously changing the shape of the wing to adapt it to new flight conditions, without the hinge contours discontinuity associated with conventional control/high lift devices. Aerodynamic wing design is a complex task, multi-disciplinary in nature, which often requires *a priori* knowledge about likely performance based on semi-empirical methods or previous experimental data to enhance the design solutions. This often translates into the use of multi-objective optimisation to capture the performance metrics of interest, but can limit the improvement of the design and runs the risk of limiting the feasible design space.

An application of the proposed methodology to transonic wing design for a general civil transport aircraft is considered (see Figure 6.1). The wing morphing methodology proposed here extends the two-dimensional concept of morphing airfoils by means of plates. Perhaps the simplest way to envisage this is to consider a two-dimensional spinal structure, extruded into an orthogonal direction to obtain a flat plate model. By means of a simplistic control law, akin to the actuation scheme employed in the previous methodology, global shape control of the new spinal structure is possible, through offset point loads at the extreme sections of the controllable outboard wing patch.

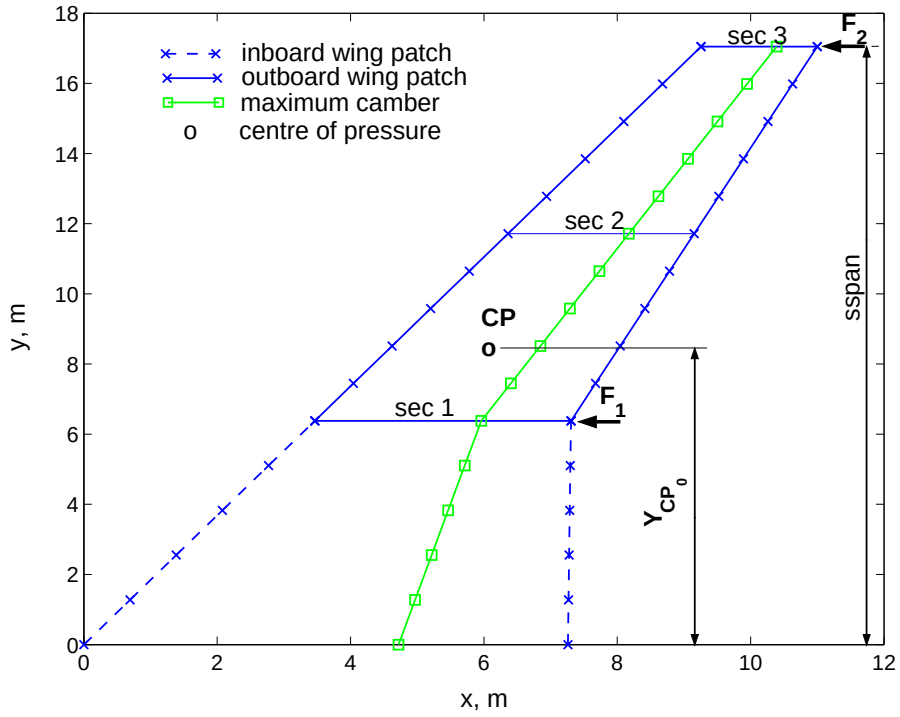

FIGURE 6.1: Wing planform with typical inboard and outboard patches. The highlighted outboard wing patch is actuated by point forces at the trailing edge of grid sections 'sec 1' and 'sec 3'. Structural related objectives are applied to the sections 'sec' 1, 2 and 3.

The overall aerodynamic shape of the wing is intrinsically linked to the structural setup and large changes in the shape of the spinal structure can have a dramatic effect on the aerodynamic performance of the wing. Here, these issues are tackled by means of constrained multi-objective optimisation, with both aerodynamic and structural related cost functions and constraints. The geometry of the underlying spinal structure is characterised by a fixed planform and uses two patches, viz. inboard and outboard. Since the current methodology makes use of a simplistic actuation law and a global shape control of the wing is needed to provide enhanced roll, the outboard wing patch is chosen to be the active element during morphing.

The selection of the objectives in multi-disciplinary analysis has a strong impact on the success of the optimisation process. These are often imposed by the aircraft manufacturer, such as lift, drag, weight, etc., that have a strong influence on the costs and performance of the product. Here, the main objective used defines the roll performance of the wing, while minimising drag. The flow performance is highly sensitive to the smoothness of the aerodynamic shape of the wing, controlling somewhat the pressure distributions (Scherer et al. (1997)), and thus, the overall aerodynamic performance of the wing. This leads to additional aerodynamic and structural objectives and constraints, so as to aerodynamically maintain product integrity, by enabling the morphed outboard surface to smoothly blend the controlled prescribed sections (n.b. the grid sections on which the structural related objectives are studied here are the crank, tip

and mid outboard path positions, i.e., sec 1, sec 2 and sec 3, respectively). This translates into the use of a target wing shape, *a priori* generated by four-digit NACA airfoils with significant aft camber (i.e., 65% chord), so as to alleviate the inherent transonic flow issues over the wing and also, to avoid spurious designs (to keep to the spirit of the two-dimensional approach)[1].

As already mentioned, the underlying model is designed to enhance roll control over the wing and also to maintain the aerodynamic integrity. These two issues are tackled in a single heuristic objective, f_1, by minimising the gradient of drag with respect to the position of centre of pressure, so that the feasible design solutions encounter low drag for a large change of centre of pressure towards the tip. Here, the smoothness of the design is imposed by the objectives f_{sec} on the grid sections highlighted in Figure 6.1 (i.e., sec 1, 2 and 3, corresponding to the crank, tip and section mid outboard patch), using metrics that define the fitness of the morphed airfoils to equivalent NACA airfoils. The aerodynamic constraints g_1 and g_2 are expressed with respect to the baseline wing geometry (i.e., 2% camber spanwise, as depicted in Figure 6.2), and structural constraints g_3 and g_4 control the upper and lower bounds of the displacement field of the crank and tip grid sections. Therefore, the multi-objective optimisation problem can be stated as follows:

$$\text{Minimise } f_1(\mathbf{x}) = \frac{d\bar{C}_D}{dY_{cp}}, \tag{6.1}$$

$$f_{sec}(\mathbf{x}) = \parallel \mathbf{w}^t - \mathbf{w} \parallel^{sec}, \tag{6.2}$$

$$\text{Subject to } g_1(\mathbf{x}) = C_{L_0} - C_L < 0, \tag{6.3}$$

$$g_2(\mathbf{x}) = Y_{cp_0} - Y_{cp} < 0, \tag{6.4}$$

$$g_3(\mathbf{x}) = \max\big|_j \, w_j - a_2 \leq 0, \text{ at sec 1}, \tag{6.5}$$

$$g_4(\mathbf{x}) = a_1 - \max\big|_j \, w_j \leq 0, \text{ at sec 3}, \tag{6.6}$$

$$\mathbf{x} \in \mathbf{X}, \; \forall \; j \in \{1, \ldots, n_p\}, \; \forall \, \text{sec} \in \{1, 2, 3\},$$

with $\bar{C_D} = C_D \cdot sspan$, $\mathbf{X} = \{\mathbf{x} \in \mathbb{R}^n \mid x_k^{min} \leq x_k \leq x_k^{max}, \; k = 1, \ldots, n_v\}$ with x_k^{min} and x_k^{max} bounds on the n_v structural variables set by the user (x_k^{min}=0.2 mm and x_k^{max}=8 mm for control points, $x_k^{min}\big|_{F_1}$=-5 kN, $x_k^{min}\big|_{F_2}$=-100 kN, $x_k^{max}\big|_{F_1}$=3 kN and $x_k^{max}\big|_{F_2}$=-3 kN); w_j are the deflections at the structural position j at final load increment[2] for each of the three sections s considered defined by n_p structural grid points, and $a \in \{a_1, a_2\}$ with $a_1 = g_3(\mathbf{x})$ define the lower and upper displacement bounds for crank sections (sec 1) and tip (sec 3). The increments $d\bar{C}_D = \bar{C_D} - \bar{C_{D_0}}$ and $dY_{cp} = Y_{cp} - Y_{cp_0}$ are computed

[1] In the emergence of transonic research, a young aerodynamicist at NACA, Roger Whitcomb, suggested that the upper surface shocks at critical speeds can be alleviated by the right curvature, and his design strategy led later to the development of transonic airfoils.

[2] Due to high computational expense, only the final increment from the non-linear solver is analysed and is set by a stopping criterion, i.e., $a_1 = \max\big|_j w_j$ at section sec 1.

with respect to baseline geometry characteristics (i.e. $\bar{C_D} = 0.015402$, $Y_{cp_0} = 7.5$ m and $C_{L_0} = 0.51$), which consist 2% cambered grid sections spanwise (see Figure 6.2).

6.2 Wing analysis

For the wing analysis, a hierarchical strategy is employed, interleaving parameterisation enhancement by means of a CAD tool, followed by structural optimisation into an aerodynamic design process, in order to study the performance of the underlying model, as shown in Figure 6.3). Due to the complexity of the problem, this MDO paradigm is used in conjunction with a response surface approximation, such that design optimisation is achieved, as depicted in Figure 6.4. The programming challenges are augmented with the automated strategy of the MDO, since different 'black-boxes' are interdependent and provide means to study the aerodynamic and structural enhancement of such models.

The aerodynamic shape design is, of course, intrinsically linked to the deformable shape of the spinal plate that satisfies the imposed design goals and constraints. The design process encapsulates the features of the underlying model by interacting both structural and aerodynamic goals, as defined in equations 6.1-6.6. The main goal of the underlying MDO process is to achieve enhanced roll of the wing while minimising the drag, designed here by minimisation of the gradient of the drag with respect to the position of the centre of pressure. In the literature, a great deal of research on the optimisation of aerodynamic features of wings is undertaken. The metrics used are offered mainly with respect to drag in cruise. Such criteria do not suffice for a true aerodynamic goal, so that other metrics in terms of objectives and constraints need to be involved so that enhanced properties of the optimum aircraft design are captured, e.g., buffet at high lift, pitch constraint near stall, $C_{l_{max}}$ for clean wing, etc. (see, for instance, Lynch (1982), Jameson and Vassberg (2001)), along with structural constraints. Intuitively, the complexity of such optimisation problems is mitigated by choosing a limited number of goals and design variables and fidelity required to assess them, but runs the risk of limiting the study on the features of the aircraft.

6.2.1 Parameterisation strategy

As already noted, a myriad of feasible strategies with respect to geometry parameterisation have been available in the literature since the late 1970s, see for example the survey provided by Samareh (2001). If combined with an optimiser, the choice of such methods becomes central to meeting the required flexibility in geometry representation through an appropriate set of design variables.

The shape parameterisation technique employed in this chapter is based on NURBS surfaces definitions (Piegl and Tiller (1997)). It has been tailored to enhance the flexibility

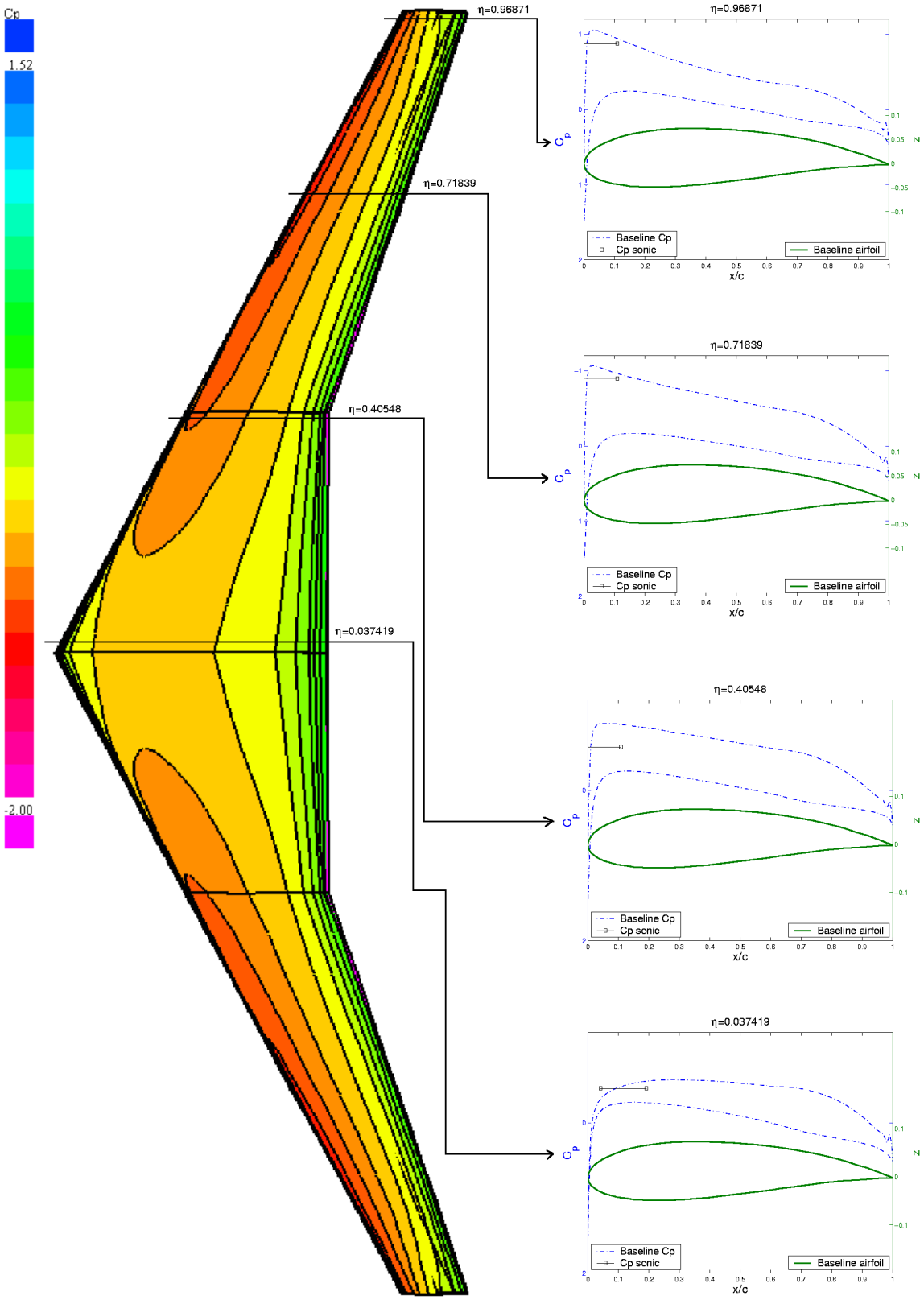

FIGURE 6.2: Pressure contours of the baseline wing.

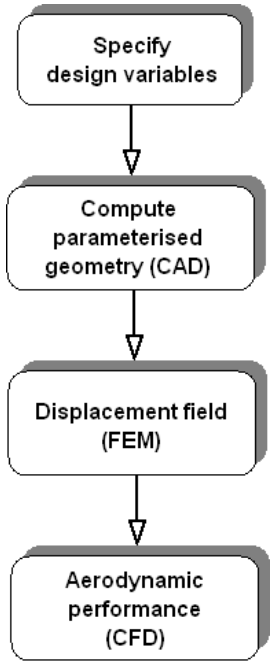

FIGURE 6.3: Sequential wing workflow (SWF)

of such surfaces and to provide a reasonable hyperspace for the design variables. Since the planform of the wing is *a priori* known, only the boundary shape of the outboard section is tackled, such that a full control of the displacement field is achieved during actuation. The choice of the design variables directly dictates the dependence of the kinematics of the model on the geometric NURBS patches that control the shape of the boundary, and thus, the thickness of the plate. The design space is represented by sets of interpolating points active in the NURBS-based parameterised curves that define the bounds of the NURBS surface. Each NURBS curve is chosen to be planar, so that the defining points have two degrees of freedom only. Intuitively, a fully parameterised curve would allow the parametric space to be controlled by all degrees of freedom of defining points, but the problem would be more difficult to search within the augmented design space. In the current work, only vertical displacements of the points are taken into account, reducing the size of the parametric space. Here, the design space comprises mainly the interpolating points that define the bounding NURBS curves, i.e., six points for each parameterised section (i.e., crank and tip) and five points in the orthogonal direction. This scheme of points is chosen to keep to the spirit of the two-dimensional approach and also to allow a large variation of the curvature of the surface, that intrinsically dictates the thickness distribution of the plate-like outboard wing. A random set of variables during the optimisation process leads to the variation of the surface based on interpolating points of the NURBS in crank, leading edge and tip positions is shown in Figure 6.5.

The NURBS surface is constructed based on quadrilateral patches such that the geometry of the outboard wing is fully captured, as shown in Figure 6.5. The structure of the

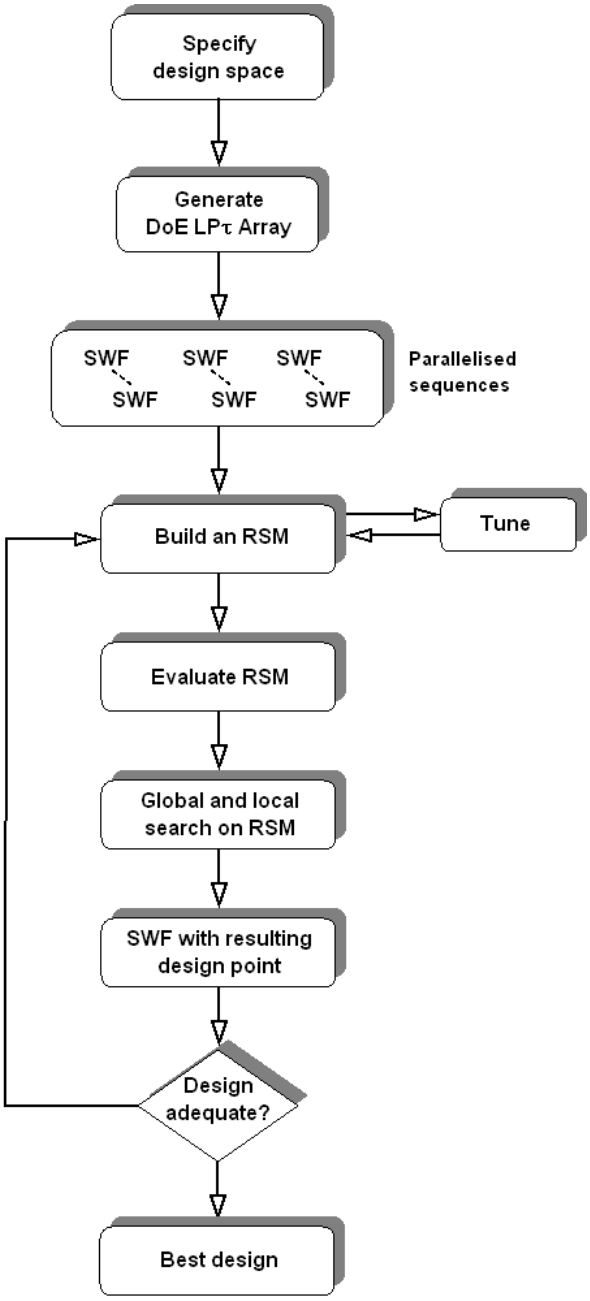

FIGURE 6.4: Optimisation strategy.

patches (i.e., the control net) is fully defined by control and/or interpolating points of the bounding NURBS. This allows the surface to be discretised evenly in the geometric space, by creating a set of internal nodes, such that an iso-parametric mapping of the discretised surface onto the finite element space is possible. This equidistant mapping in the parametric design space augments the finite element discretisation properties, by exporting the internal node set and also the nodal thickness to create a shell structure, using a standard format, viz. IGES (Initial Graphics Exchange Specification)(Smith et al. (1988)).

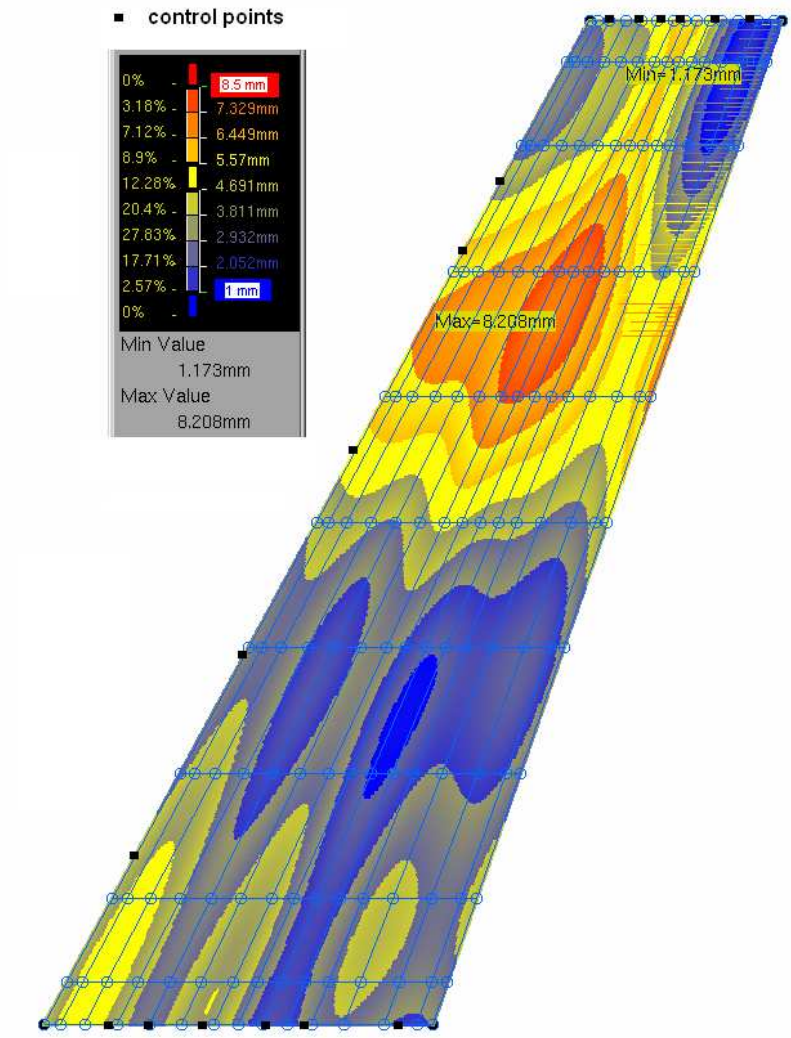

FIGURE 6.5: Outboard NURBS parameterisation and a random thickness distribution of the plate during the optimisation process.

6.2.2 Finite Element Formulation

As mentioned in section 2.5, tracing smooth equilibrium paths of a loaded structure that encounters critical points becomes impossible for classic load or displacement control techniques (Crisfield (1997)), as the perturbation parameter should follow the non-linear path in a constant gradual manner. The solution becomes in this case non-unique in the hyperspace with snap-through or snap-back behaviour. To capture the instabilities, such methods can be enhanced by the *arc length* method, initially introduced by Riks (1979), in conjunction with an incremental numerical Newton-Raphson algorithm. A multi-dimensional control parameter technique, within the field of perturbation theory, is approached by Steen (1998), with the benefit of reducing the dimensionality of the problem to a single parameter approach. First and second path derivatives, based on a Taylor expansion consistent to Koiter's theory (Koiter (1976)) are used to set the subsequent equilibrium path, which is in contrast to classic methodology.

A considerable amount of work has been done in the field of structural optimisation of frames and plate structures. Primarily, these are designed with respect to state variables to enhance buckling resistance (Spillers and Levy (1990), Levy and Ganz (1991), Pandey and Sherbourne (1992), Manickarajah et al. (1998), etc). As an alternative to numerical approaches to solve complex structures, closed-form solutions of plates under different schemes of discretisation are also offered in the literature, with the aim of achieving global closed-form solution of the continuum model. The analysis context of such models is to capture static or dynamic behaviour, in a combination of wide analytical element definitions (specifically for thin or thick plate assumptions) (see the comprehensive review of Lovejoy and Kapania (1994)).

Within plate theory, one can classify the existing methods according to the deformation assumptions used, namely: classical plate theory (CPT), first-order shear deformation theory (FSDT), or high-order shear deformation theory (HSDT). For the purpose of buckling calculation, CPT is valid for thin shells and, based on Von-Karman (1970) equations (for moderate rotations), based on Love-Kirchhoff (LK) hypothesis, that is, a normal to the plane middle surface remains normal and straight after deformation. This hypothesis is weakened by high transverse shear strain, therefore the baseline model is prone to transverse failure (Dawe (1985)). This drawback is overcome with FSDT, that uses the Reissner-Mindlin (RM) hypothesis, where the normal is allowed to rotate relative to the reference surface (Reissner (1945), Mindlin (1951)). A general approach to thick and anisotropic plates, but more computationally expensive, is HSDT, as this requires computation of high order strains.

These theories are readily accounted for within Abaqus®, the commercial finite element tool used in this work by means of a wide library of elements consisting general purpose, thin and thick shell elements. Here, the parameterised outboard wing spans 10m and has a maximum thickness of 15 mm, so it would be considered to be a 'thin' shell, under the LK hypothesis (the thickness-to-span ratio is less than 1/15). Abaqus imposes such hypotheses numerically on the shell definition, where the transverse shear stiffness K_γ is treated as a penalty (Hughes et al. (1977)):

$$K_\gamma = \frac{G_\gamma t \Delta\mathcal{A}}{1 + \frac{q\Delta\mathcal{A}}{t^2}}, \tag{6.7}$$

where G_γ is the elastic moduli, t thickness of shell, q a relaxation factor and $\Delta\mathcal{A}$ is the area of reference surface (see more details in Appendix D).

The element type chosen for this type of analysis is a quadrilateral small-strain thin shell element S4R5 (i.e., four nodes, reduced integration with five degrees of freedom per node), suitable to capture non-linearities where the surface and the displacement field are assumed to be smooth, but with a trade-off in accuracy (Wong and Pellegrino (2002)). These shear flexible small strain shell elements are computationally more relaxed, since

they account for five degrees of freedom per node, as the normal to the surface (the metric from which most variables are derived) is defined by only two independent variables (i.e., two arbitrary initial orthogonal directions)(see Appendix D for more details). Further, the points on the surface and the component vectors of the normal to the surface are interpolated separately.

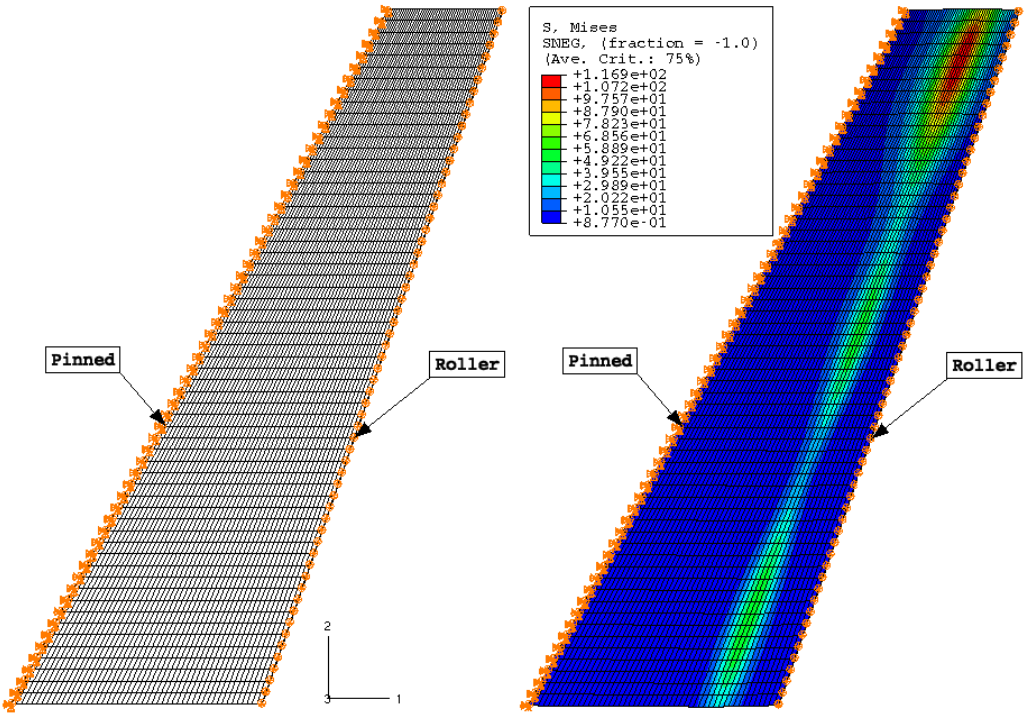

FIGURE 6.6: Outboard finite element discretisation and the corresponding stress state of the randomly parameterised outboard patch from Figure 6.5.

Mapping equally spaced points from the CAD tool onto the finite element boundaries, a detailed FEA structural discretisation and the corresponding stress state of the randomly parameterised outboard patch from Figure 6.5 are shown in Figure 6.6 (clearly, larger displacements can occur in the area of interest, i.e., the tip of the wing, if the stiffness is diminished, as depicted in Figure 6.5). This consists 3000 shell elements and 121 solid elements used to model the eccentricity, as shown in Figure 6.7 (n.b., the eccentricity is modeled with solid elements to accurately transmit the load and resulting torque spanwinse to the shell). A shell-to-solid coupling is used here to provide continuity to the stress state and displacement field. The model consists 19,642 degrees of freedom, which needs a significant amount of CPU time and computational capacity, making the cost of the analysis quite high. The run time is also augmented by the high degree of non-linearity encountered by the model (this is mainly dictated by the constitutive kinematics definition). Such issues, for this particular analysis, make Abaqus a limiting factor in the performance of the MDO, even if the process is parallelised. Therefore a careful manipulation of input/output data is needed to avoid bottlenecks on disk and memory issues.

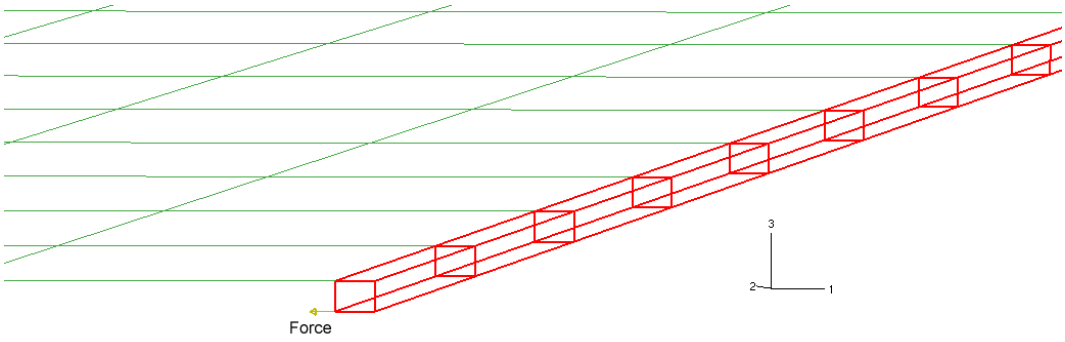

FIGURE 6.7: Shell-to-solid eccentricity coupling.

6.2.3 CFD Analysis

The aerodynamic characteristics of the morphing wing are provided here by VSAERO, a panel or boundary element method which solves the linearised potential equations for inviscid, irrotational incompressible flow, with additional compressibility correction (i.e., Prandtl-Glauert and Karman-Tsien rules). The method is enhanced for boundary layer calculations, provided by a viscous-potential flow coupling. The advantage of using VSAERO is that only a surface discretisation is necessary, since it based on a classical panel method, and does not require a grid in the flow field. The method is limited to certain flows which include relatively high Reynolds numbers and small angles of attack, applied to slim bodies with closed surfaces, up to low transonic speeds.

A typical VSAERO model of the wing surface and wake panels is shown in Figure 6.8. The generating airfoils are based on cosine spaced grid coordinates, to provide closely spaced panels at the leading and trailing edge of the wing. The streamwise wake panels are chosen to provide a fine mesh downstream of the wing tip, after which their density decreases following a cosine rule.

The choice of the design variables in an optimisation problem becomes particularly important using aerodynamic elements related to the performance of the aircraft. These elements are inherently linked to drag, which, here, becomes the direct measure of aerodynamic performance. Several methodologies proposed in the field of concept design deal with optimisations based on performance assumptions, including sections, planform, etc., and is usually associated with a large design space and low fidelity analyses. The detail design, consisting of smaller design space but high fidelity analyses, limits the improvement over the design during optimisation, but may converge more quickly to a feasible solution. Therefore, the selection of airfoils with *a priori* known performance is crucial. Since the present approach is studied in transonic conditions, and is based on similar methodology described in previous chapters, an extreme aft camber NACA airfoil is chosen to define the wing spanwise.

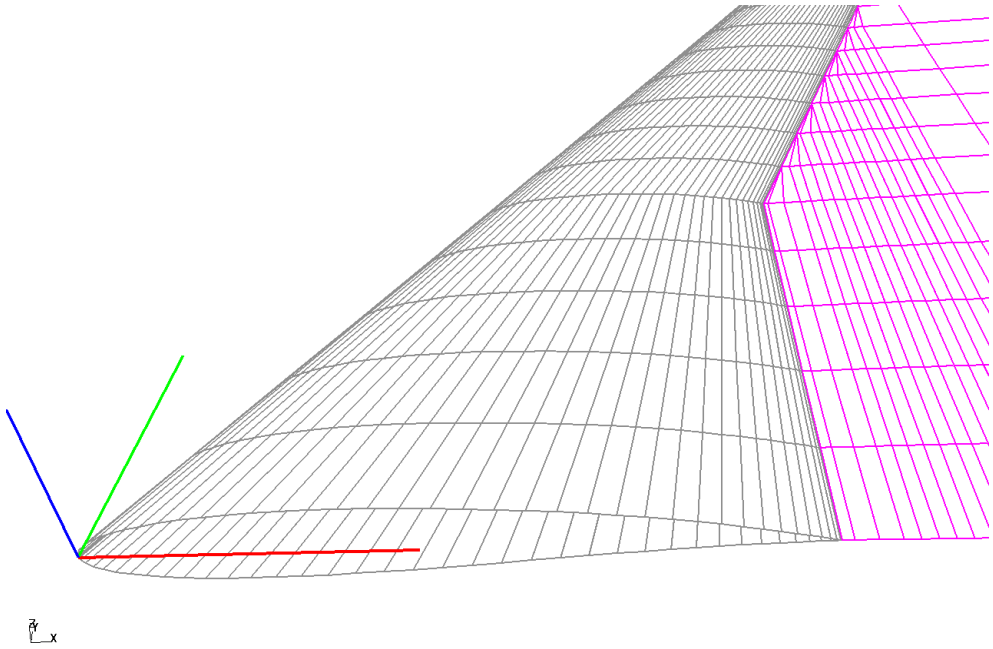

FIGURE 6.8: A common boundary-fitted aerodynamic grid for wings.

6.3 Kriging and Model Validation

As already mentioned, the MDO paradigm is based on response surface approximation, following the strategy in Figure 6.4. The quality of the response surface depends upon the values of the true function evaluated at sample points within the domain, often defined as *hypercube*, generated by Design of Experiments algorithms (Mead (1998)). The design optimisation process is carried out on the surface approximation so as to meet the cost functional required. The strategy also involves an update process, where feasible solutions found on the fitted RSM to the initial data, may be fed back to the training pool for further updates and surface refinement. This process is repeated until some form of convergence is met. There are a number of techniques of DoE available in the literature, that seek to sample the entire design space to capture most of the landscape of the function (see Keane and Nair (2005)). Here an $LP\tau$ DoE array (Sobol (1979)) is used for its space filling characteristics and capability of updating the training pool without the repositioning the already evaluated design arrays and running the risk of clustering the data sets.

Based on an $LP\tau$ array, here the Krig definition is employed (see Appendix E.2 for a detailed definition) due to its ability to capture complex functions and provide error estimates, to provide means of global approximation of the underlying model (n.b. the Krig methodology is applied for each of the objectives and also for aerodynamics related constraints). Two forms of Krig are employed in this study, to provide a parallel on cost effective approaches, and are referred to as full Krig (i.e., the hyperparameters θ and p are assigned to each variable):

$$\mathbf{R}(\mathbf{x}_i, \mathbf{x}_j) = \exp\left[-\sum_{j=1}^{k} 10^{\theta_j} \left(\| \mathbf{x}_{n+1,j} - \mathbf{x}_{i,j} \|^{p_j}\right)\right] + 10^{\lambda}\delta_{ij}. \tag{6.8}$$

and a reduced form of Krig (i.e., the hyperparameters are assigned to groups of variables):

$$\mathbf{R}(\mathbf{x}_i, \mathbf{x}_j) = \exp\left[-10^{\theta} \sum_{j=1}^{k} \left(\| \mathbf{x}_{n+1,j} - \mathbf{x}_{i,j} \|^{p}\right)\right] + 10^{\lambda}\delta_{ij}. \tag{6.9}$$

where the hyperparameter p_j can be thought of as determining the smoothness of the approximation function, θ_j can be though as of determining the impact on the approximation function with changes of $\mathbf{x}_{n+1,j}$ with respect to $\mathbf{x}_{i,j}$.

The initial stage of the workflow from Figure 6.4 is based on computing an initial set of experiments, after which an approximation surface is fitted to the data. This Krig is then tuned with respect to the hyperparameters so as to maximise the likelihood function in a two-stage search, i.e., GA for 3000 steps with a population of 100 and then a further 2000 steps in a DHC search to locate maxima in an invariably highly multi-modal problem. Here, the initial LPτ array comprises 200 design points directly evaluated within the sequential workflow (SWF) presented in Figure 6.3 and is augmented by another 155 design points used for prediction that provide a means to assess the quality of the response surface. This work flow is computed for each of the objectives (i.e., aerodynamics related f_1 and structural related f_{sec} from equations 6.1 and 6.2, respectively), and aerodynamics related constraints (i.e., g_1 and g_2 from equations 6.3 and 6.4, respectively). The design space comprises 17 parameterisation points, in addition to two point forces, which translates into an approximation parametric space with 39 hyper-parameters for the full Krig definition and only 3 hype-parameters for the reduced Krig definition.

Based on the approximation surfaces built for each objective and the aerodynamics related constraints, a quality check of the RSMs is possible. This procedure is enhanced when using a set of prediction points already evaluated within the SWF, which are then compared with the predicted values by the RSMs at the specified locations of the prediction points. Consequently, the quality of the RSMs is based on the linear regression between the current data (i.e., prediction points) and the predicted values by the RSMs, as depicted in Figures 6.9 - 6.14 for the full Krig and 6.15 - 6.20 for the reduced Krig.

Here both numerical and graphical measures of the fitness of the entire data set are employed. When using numerical methods, a measure of the goodness of fit statistics may mislead the true features of such large metamodels, by compressing some aspects of the data into a single predictor, such as the factor of determination R^2 or standard error

RMSE (Simpson et al. (2001) and Martin and Simpson (2005)). Graphical methods have the advantage over numerical ones by encapsulating more features of the candidate model, e.g., change in spread of the residuals, leading to various assumptions on standard deviation and also methods to validate the fitness.

Graphical methods are employed here by means of residuals plots, initially based on the assumption of constant standard deviation across the data. The method employed for such assumption is an *ordinary least squares* regression (OLS) to determine the parameter estimates (see Appendix C for more details). A potential pitfall of using OLS is that the variation trend exhibited by the residuals might not model the deterministic part of the data accurately, leading to a changing variance across the model. In such cases, the residuals won't follow an evenly spread trend, but will emphasise the presence of the *outliers*, that can bias the prediction and alter the parameter estimates. Therefore, a weighted procedure is also employed by means of *iteratively reweighted least squares* (IRLS) (Rousseuw and Leroy (1987)) on the assumption of non-constant standard deviation. The outliers reside in inconsistencies with the bulk data and can dominate the regression, but, although if dropped can increase the correlation between the independent and dependent variables, the outliers may also contain engineering interpretation about the data under investigation and, therefore, ideally should not be removed. The source of the outliers might be partly converged solutions (i.e., structural or aerodynamic in nature) and can be repaired by making use of high-fidelity analysis tools (see Kim (2001)). The negative impact of the outliers on the regression plane can be alleviated by using the IRLS method, as it assigns different levels of quality to data through quantitative means of *weights* to control the contribution of each observation to the parameter estimates. The advantage of using IRLS over a number of hybrids of OLS (e.g., IRLS with Huber weighting technique, univariate outlier and multivariate outlier removal) is also emphasised by Wager et al. (2005) in a neuro-imaging study on hemodynamic shapes, achieving robust parameter estimates with artificial influential outliers, iteratively down-weighted onthe principles of DuMouchel and O'Brien (1989) (i.e., the residuals are standardised with respect to the median absolute deviation, technique that is also used in the current work, see Appendix C for the numerical approach).

By means of numerical measures, the figures of merit are represented here by R^2 and RMSE. The coefficient of determination R^2 measures the variability of the prediction with the independent variable and is a non-dimensional figure with higher values, usually, leading to a better correlation of the responses. Often, however, larger correlations also occur due to data dependency, leading to residual auto-correlation and does not guarantee that the model fits the data as expected (see Myers and Montgomery (1995), pp. 30-31), and further, cannot explain the the underlying model. The correlation factor is defined as:

$$\mathrm{R}^2 = \frac{S_{f\hat{f}}}{S_f S_{\hat{f}}} = \\ = \left(\frac{n\sum f_i \hat{f}_i - \sum f_i \sum \hat{f}_i}{\sqrt{n\sum {f_i}^2 - (\sum f_i)^2}\sqrt{n\sum {\hat{f}_i}^2 - \left(\sum \hat{f}_i\right)^2}} \right)^2 \tag{6.10}$$

where S_f is the covariance between independent variable f and the approximate function $\hat{f}$ and n is the number of data points for regression.

To mitigate any false fitness, an additional statistical component is used here, namely RMSE, which is the root mean squared error exhibited by the underlying model and values closer to zero indicate a better fit:

$$\mathrm{RMSE} = \sqrt{\frac{\sum w_i (f_i - \hat{f}_i)}{n-2}} \tag{6.11}$$

where w_i are the weights associated to the residuals.

The scatter in the residuals shown in Figures 6.13 to 6.20 adequately describes the systematic variation in the data, with a nearly even spread trend, apart from the regions where outliers occur. The scatter also outlines the validity of the initial error assumption of constant variance across the data in most of the cases, which would allow the OLS to perform well. But this would not suffice in drawing a silver-bullet conclusion on the fitness of the model, and the IRLS technique is also performed in conjunction with the outliers present in the data. The IRLS is used to alleviate the false significance of some parameter estimates under influential outliers. Clearly the IRLS is more flexible in accommodating levels of quality to the responses on the assumption of non-constant variance (see Appendix C) and is also resistant to the influence of the outliers[3], so that better correlations and standard errors are achieved. Optimising the weight vector to find the parameter estimates allows IRLS some improvement on the quality of the model, more noticeable in cases with multiple outliers that can heavily alter the regression plane computed with OLS (see Figures 6.12, 6.18, and 6.20). RMSE also augments the improvement and goodness of fitness, encountering diminished values.

Statistically, the improvement of the fitness has similar degrees in both Kriging approaches. This comes in addition to similar trends of the cross-validated residuals, exhibiting large variations around the same predictor sets (depending upon the predictor's quality in the feasible design space, OLS and IRLS often cannot return the same

[3]Herein, the outliers have been computed using both OLS and IRLS techniques on the standardised cross-validated residuals and have been highlighted those with absolute value larger than three.

outliers, since the regression plane is computed differently and also levels of quality of the responses varies across the data when IRLS is performed). This behaviour is set *a priori* by the regularisation factor λ, encountered on a higher degree in the latter Kriging form. Clearly, the quality of the surface is also controlled by the weighting factor θ and smoothness exponent p across the data, which exhibit small variation of the same vector to the counterpart (see tables 6.1, 6.2 and 6.4), augmenting the similarity of the qualities of the two surrogates.

Overall, both Krigs exhibit a high degree of accuracy (i.e., correlation). This comes in conjunction with the design space exploration[4] under a two-stage hybrid search of the hyperparameters (i.e., 30 GA generations with a population size of 100 members used to locate maxima, followed by 2000 DHC evaluations). The performance of the underlying models is also augmented by the convergence rates of the concentrated likelihood function. The results from tables 6.3 and 6.5 indicate that the problem posed is highly modal or presents long ridges, i.e., within the same bounds of the parameters, the sequential rates of the convergence of the CLF functional for full Krig spans a wider range than for the reduced Krig. Nevertheless, the rate of sequential convergence of full Krig computation is approximately two times that of the reduced Krig definition. Although the exploration of the design space is performed on a larger scale in the first case, a similar performance is achieved by the latter Krig. These issues (i.e., multi modality and long ridges) are also augmented by the optimisation results for the 2^{nd} constraint from table 6.5: the local optimum found with DHC corresponds to the global solution found by the GA after a few iterations, indicating that the optimiser has become stuck in a peak, caused by long ridges and may cause a 'pre-mature' convergence.

A set of guidelines on scales of magnitudes of the correlations is suggested by Cohen (1992). He suggested that correlation of 0.5 is 'large', 0.3 is 'medium' and 0.1 is 'small' effect. Cohen subjectively set some conventions of the medium effect, that should have a day to day natural consequence and be visible to people, whereas the small effect is 'noticeably smaller' but not trivial and the large effect should be the same distance above the medium effect as small was below it. Under these conventions, the correlations for all the objectives and constraints in both RSMs approaches can be regarded as large, considering the noise produced by the MDO process for such a large metamodel (the transonic flow conditions have a large impact on the data, as the shocks are very difficult to capture in the trend of the true function). The correlations are also dependent upon the Krig regularisation coefficient λ which indicates very small regression needed for the 3^{rd} objective with full RSM (see table 6.1) and for the objectives 2, 3 and 4 in case of the reduced Krig (see table 6.4). Intuitively, all these issues conclude that the latter form of

[4]As a reminder, the full formulation of Krig comprises three hyperparameters, 19 parameters in the deterministic space, therefore there are 39 surrogate variables, whereas, in the reduced form of Krig, there are three hyparameters, but the smoothness factor p and weight θ have a global definition, therefore 3 variables, including regression factor λ.

Krig is more robust and efficient in terms of model fit and computational expense[5] and certainly good enough to predict with.

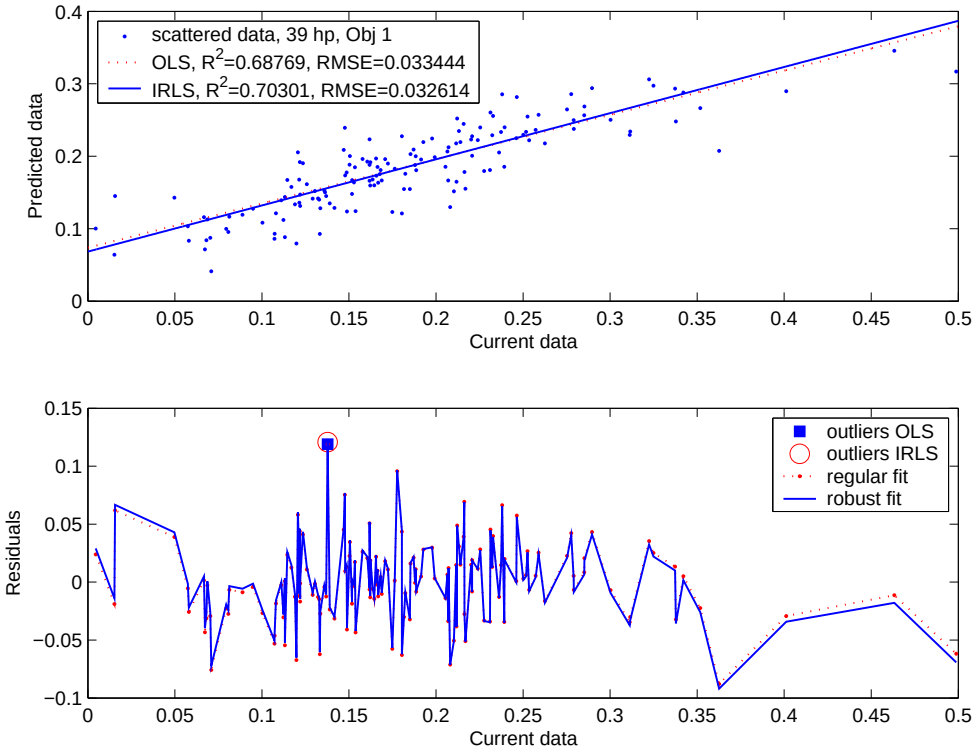

FIGURE 6.9: Objective f_1 - goodness of fit statistics, full Krig (39 hyper-parameters).

[5]Each full Krig computation with a training pool of 200 DoE LPτ points took around 75 CPU minutes, whereas each reduced definition around 45 CPU minutes, on a dual-Xeon 2800+ 2MB machine.

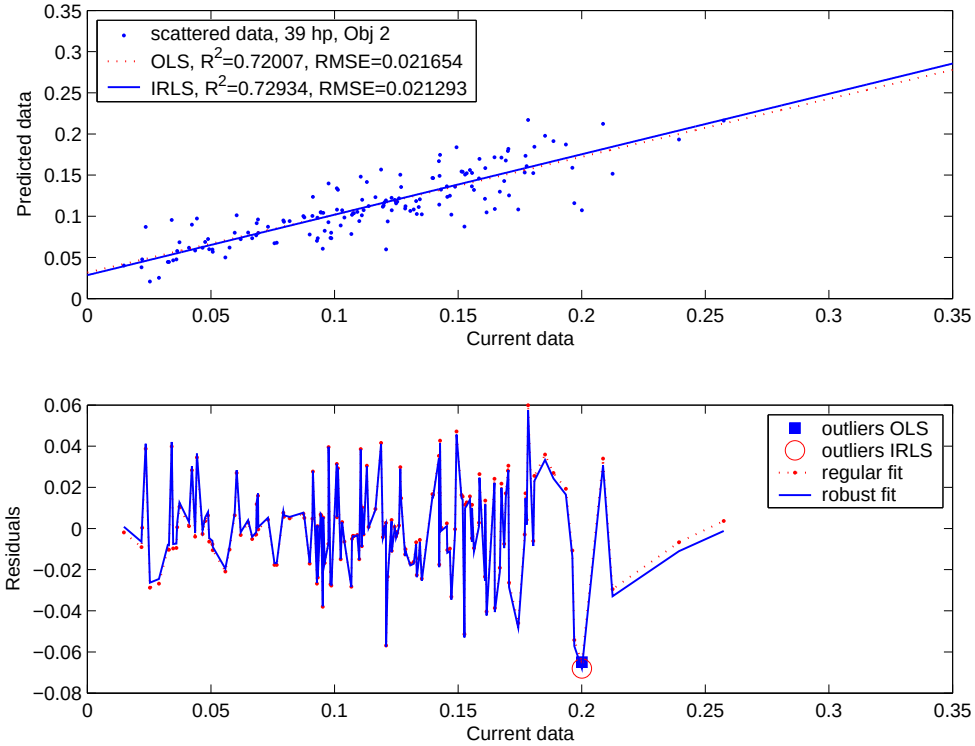

FIGURE 6.10: Objective f_{sec1} - goodness of fit statistics, full Krig (39 hyper-parameters).

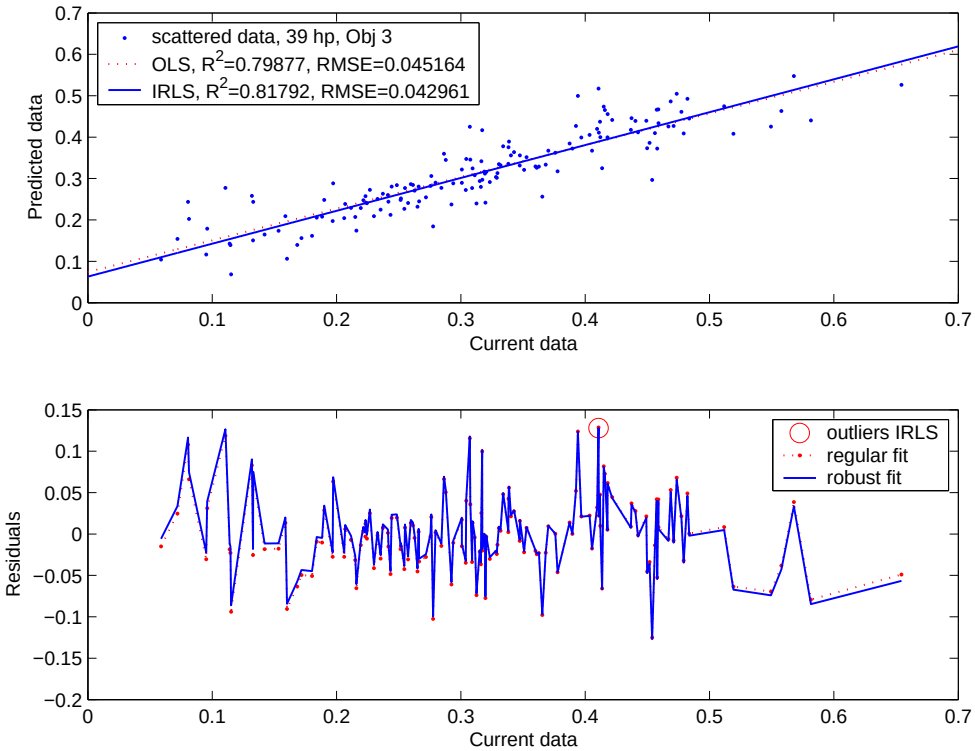

FIGURE 6.11: Objective f_{sec2} - goodness of fit statistics, full Krig (39 hyper-parameters).

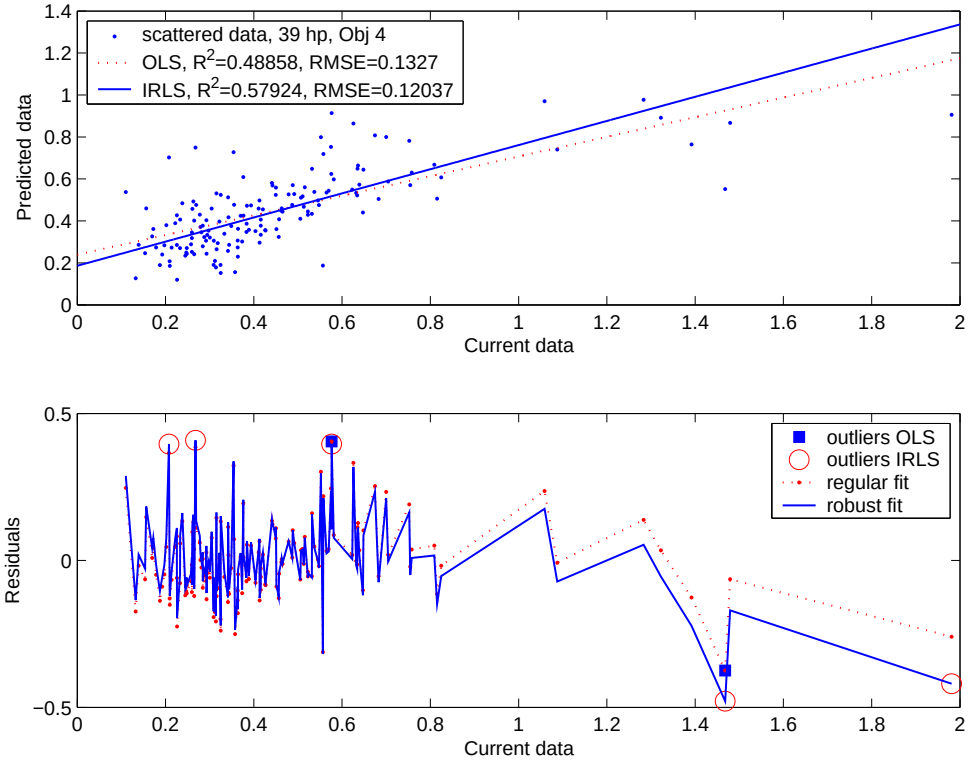

FIGURE 6.12: Objective f_{sec3} - goodness of fit statistics, full Krig (39 hyper-parameters).

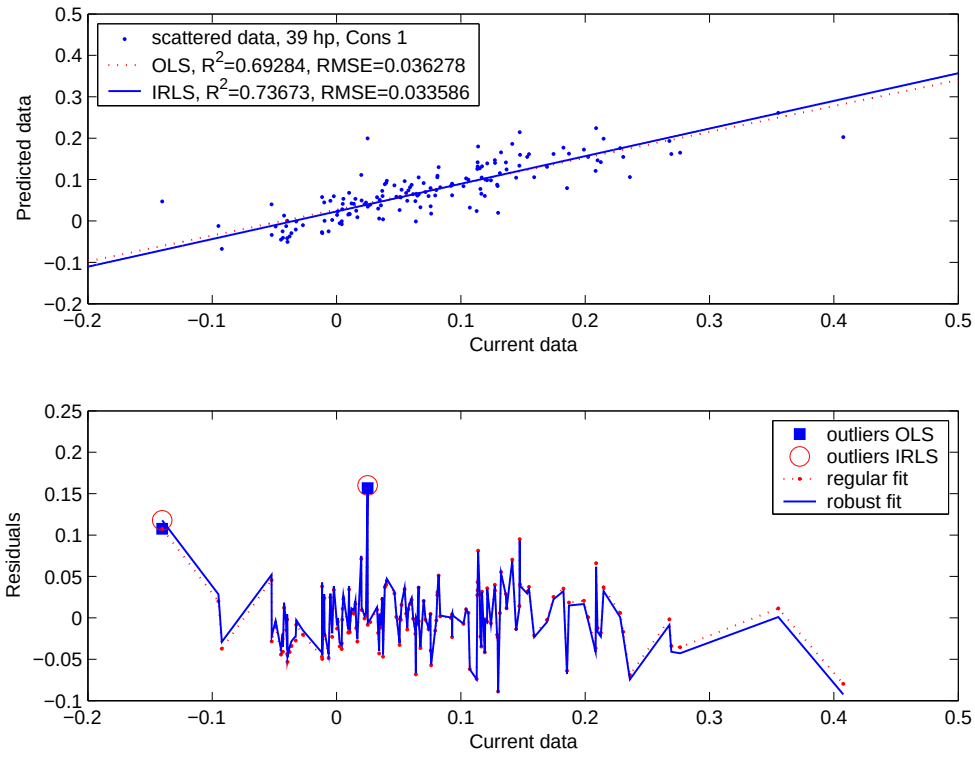

FIGURE 6.13: Constraint g_1 - goodness of fit statistics, full Krig (39 hyper-parameters).

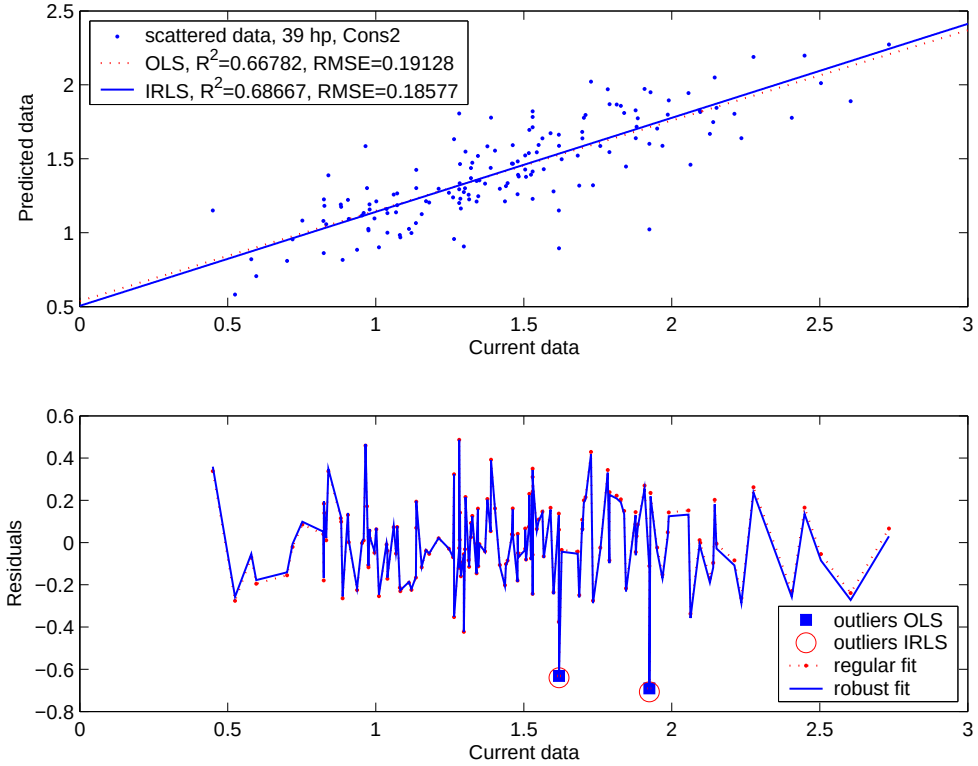

FIGURE 6.14: Constraint g_2 - goodness of fit statistics, full Krig (39 hyper-parameters).

TABLE 6.1: Hyperparameters, full RSM, objectives 1 and 3

Obj 1		Obj 2		Obj 3	
θ	p_h	θ	p_h	θ	p_h
-1.126055	1.999293	-1.985911	1.999225	-0.799206	1.299058
-1.020545	1.550626	-0.396032	1.894310	-0.999206	1.774789
-1.077970	1.971379	-1.178287	1.058657	-7.500793	2.000000
-1.026861	1.995078	-1.005556	1.991835	-1.107911	1.553443
-1.895638	1.997737	-0.688095	1.996956	-0.796081	1.882988
-1.586786	1.999763	-0.992857	1.258804	-1.315118	1.995489
-1.828593	1.002424	-1.141795	1.999817	-1.050000	1.976291
-1.106125	1.962259	-8.521377	1.999328	-0.999206	1.005263
-1.658463	1.995322	-0.694444	1.006119	-7.475396	1.876740
-8.431727	1.046339	-1.949714	1.999309	-0.999206	2.000000
-2.073760	1.998424	-7.680737	1.357814	-2.415980	1.999084
-1.410175	1.771182	-0.799206	1.417534	-1.002381	1.723454
-1.271454	1.000794	-7.069047	1.091392	-0.999206	1.039807
-1.685227	1.952683	-0.850000	1.712079	-0.999206	1.892458
-1.335191	1.996612	-0.856349	1.482083	-0.999206	1.166722
-1.065604	1.996013	-0.802381	1.952058	-0.986508	1.764776
-1.350893	1.667178	-1.008730	1.992392	-0.697693	2.000000
-8.320337	1.064916	-2.052327	1.999260	-0.973809	1.995473
-5.363691	1.927934	-8.302181	1.140232	-0.589354	1.952131
$\lambda = -0.609419$		$\lambda = -13.752930$		$\lambda = -19.695300$	

TABLE 6.2: Hyperparameters, full RSM, objective 4 and constraints

Obj 4		Cons 1		Cons 2	
θ	p_h	θ	p_h	θ	p_h
-1.005556	1.996154	-0.999206	1.999817	-1.343729	1.997719
-1.037302	1.997941	-1.002381	1.414301	-7.775972	1.075082
-0.923016	1.793559	-0.999206	1.657922	-1.766107	1.996169
-7.910218	1.325092	-0.999206	1.999328	-1.404127	1.240534
-1.814881	1.996516	-0.973809	1.683150	-1.398350	1.997964
-7.500793	1.523382	-0.999206	1.471735	-1.552872	1.712149
-0.999206	1.004055	-1.715446	1.098821	-1.800244	1.205359
-0.961111	1.057858	-0.986508	1.841796	-1.605524	1.949767
-8.518303	1.968071	-1.549286	1.991824	-1.783214	1.998397
-0.999206	1.740156	-0.999206	1.171978	-9.705460	1.012842
-0.935739	1.740110	-1.242024	1.437618	-1.005943	1.994818
-0.973785	1.997682	-0.999206	1.574973	-2.172607	1.997168
-7.361111	1.303602	-1.811905	1.999461	-7.542588	1.078316
-1.008730	1.995872	-0.999206	1.649594	-1.723414	1.722117
-0.453175	1.562576	-0.999206	2.000000	-0.918349	1.999356
-0.275421	1.872344	-0.999206	2.000000	-0.968278	1.994823
-0.646875	1.800200	-0.853175	1.334147	-1.285785	1.659906
-7.284921	1.057937	-0.973809	1.979283	-1.431930	1.995032
-7.907142	1.031807	-0.897619	1.126801	-0.403634	1.998032
$\lambda = -11.270390$		$\lambda = -18.493350$		$\lambda = -0.448961$	

TABLE 6.3: CLF convergence, full RSM

CLF			
	Start	GA	DHC
Obj 1	800.942452	816.222644	834.997591
Obj 2	1006.911077	1029.803165	1049.705452
Obj 3	684.699715	707.608782	731.491381
Obj 4	208.567649	252.455852	268.567448
Cons 1	778.307891	793.609029	802.677094
Cons 2	111.787838	126.929068	137.855793

TABLE 6.4: Hyperparameters, reduced RSM, objectives and constraints

	Obj 1	Obj 2	Obj 3	Obj 4	Cons 1	Cons 2
θ	-1.369714	-1.236933	-1.261030	-1.060956	-1.285720	-1.056349
p_h	1.996265	1.993637	1.994086	1.658170	1.995587	1.875031
λ	-0.580227	-0.770161	-0.726345	-7.048201	-0.661743	-15.701890

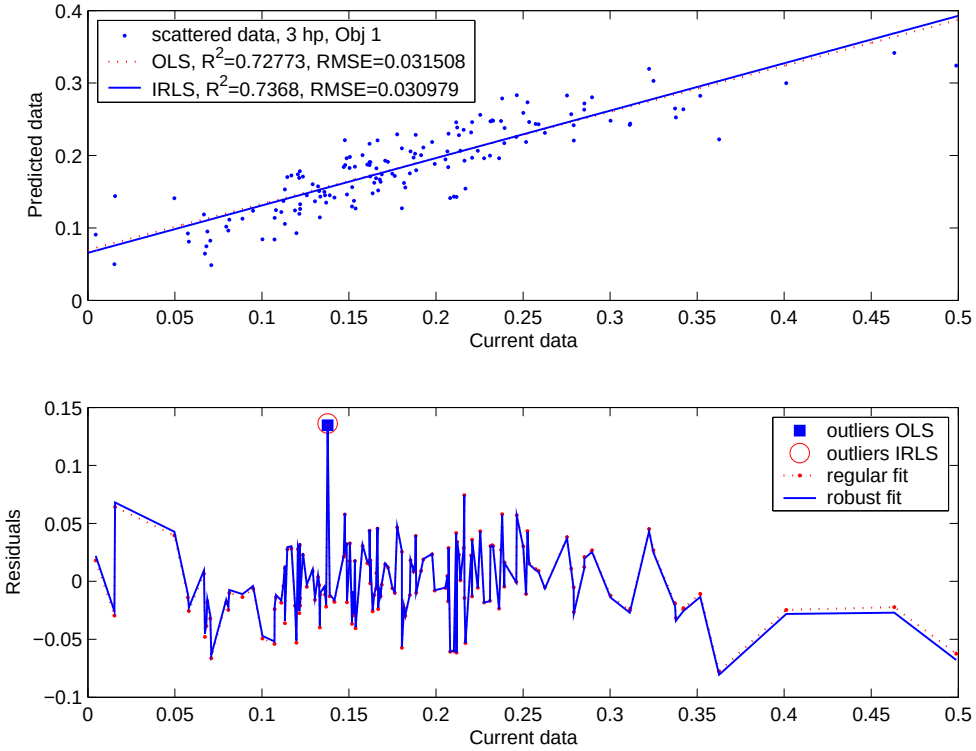

FIGURE 6.15: Objective f_1 - goodness of fit statistics, reduced Krig (3 hyper-parameters).

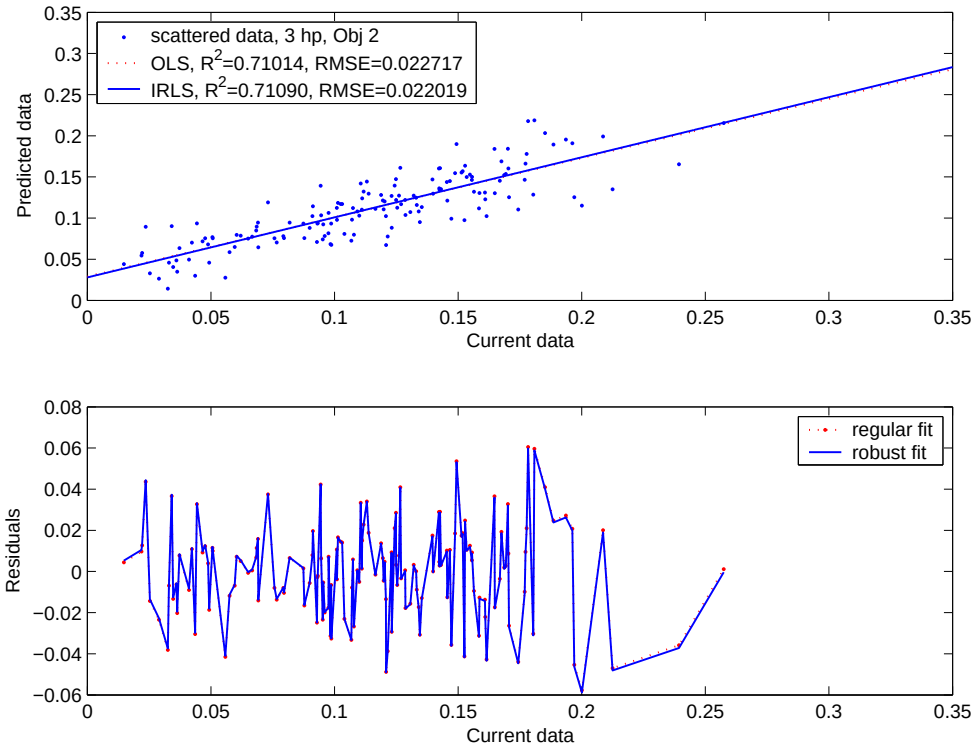

FIGURE 6.16: Objective f_{sec1} - goodness of fit statistics, reduced Krig (3 hyper-parameters).

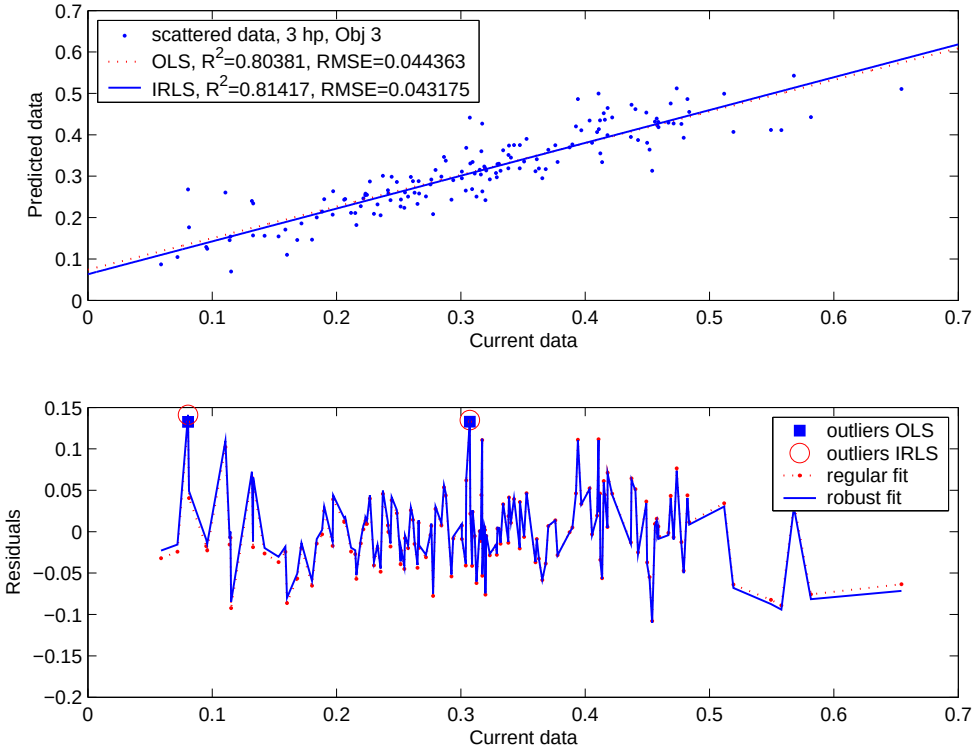

FIGURE 6.17: Objective f_{sec2} - goodness of fit statistics, reduced Krig (3 hyper-parameters).

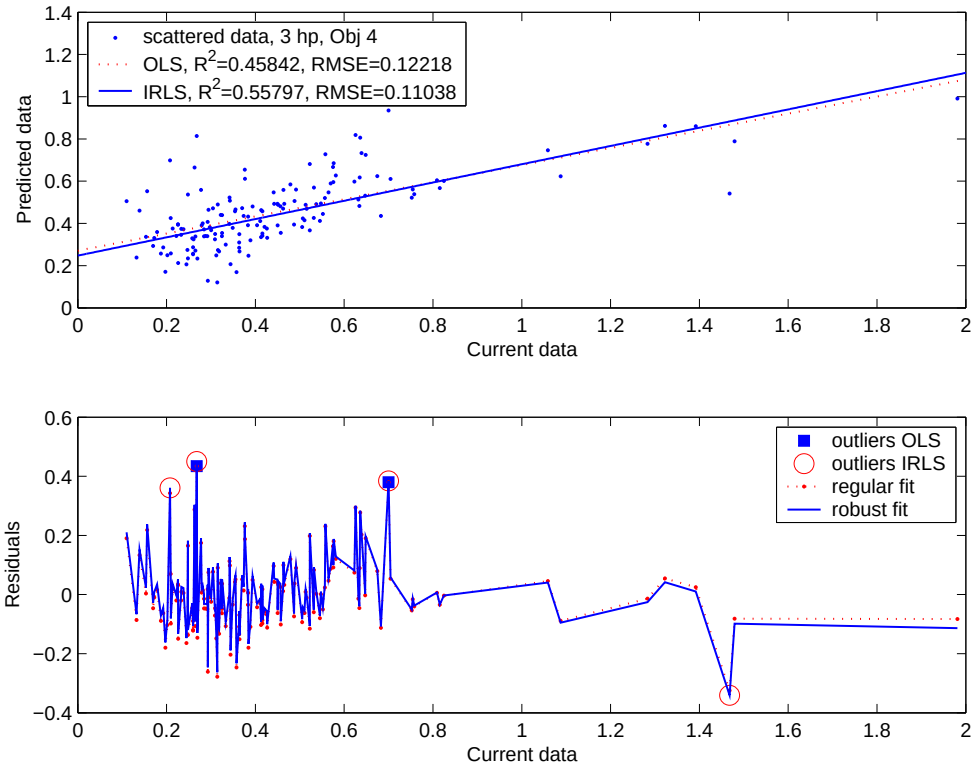

FIGURE 6.18: Objective f_{sec3} - goodness of fit statistics, reduced Krig (3 hyper-parameters).

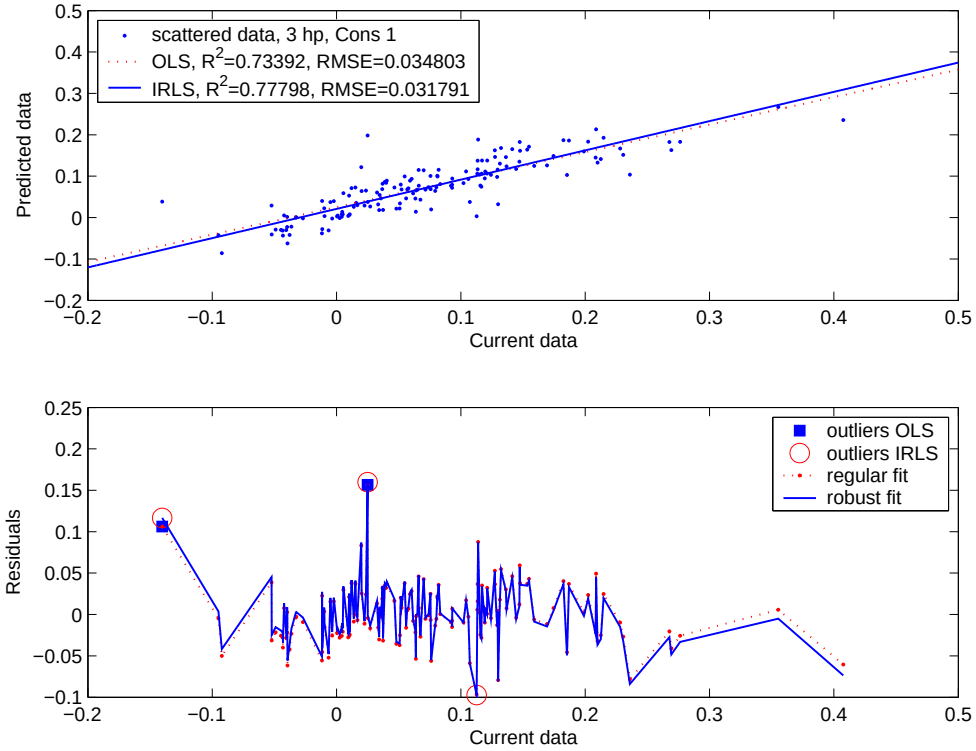

FIGURE 6.19: Constraint g_1 - goodness of fit statistics, reduced Krig (3 hyper-parameters).

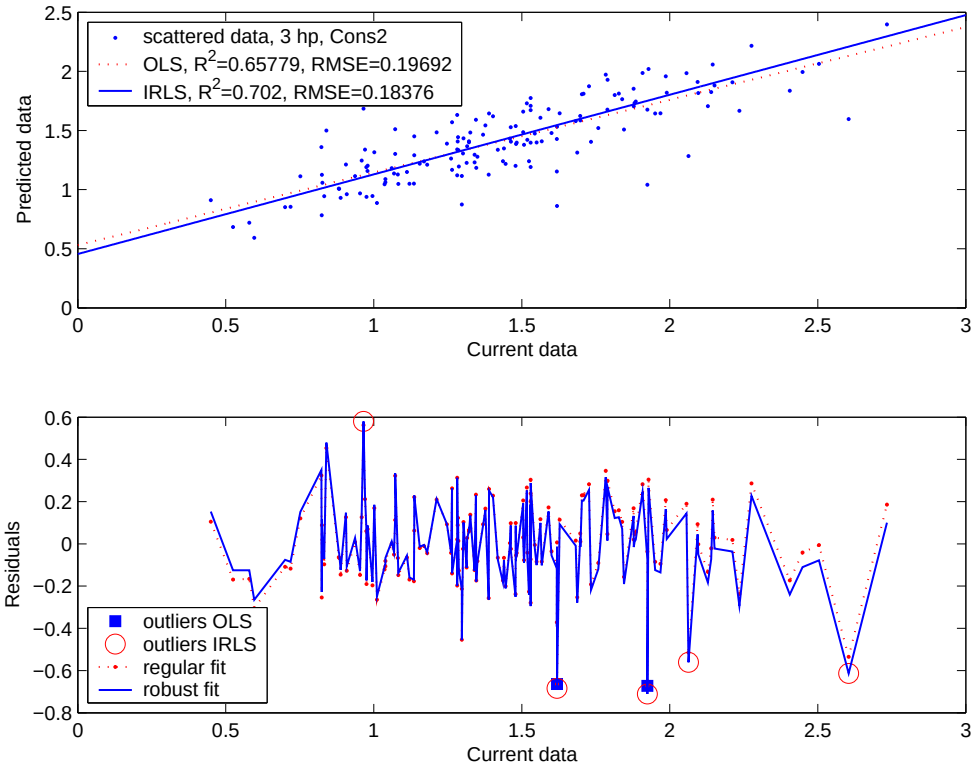

FIGURE 6.20: Constraint g_2 - goodness of fit statistics, reduced Krig (3 hyper-parameters).

TABLE 6.5: CLF convergence, reduced RSM

CLF			
	Start	GA	DHC
Obj 1	800.942452	811.709476	816.852984
Obj 2	1006.911077	1016.636324	1023.859018
Obj 3	684.699715	699.455100	708.469826
Obj 4	208.567649	214.996547	215.042716
Cons 1	778.307891	792.140937	798.252709
Cons 2	111.787838	123.222285	123.222285

6.4 Pareto Framework

Practical engineering problems often have multiple and conflicting design objectives that are accompanied by a large number of design variables. Such problems usually present multiple optimum solutions which may be encapsulated by Pareto optimality criteria (Miettinen (1999)). Each Pareto solution contains a set of data that are optimum in the sense that any improvement towards one objective would worsen another. This interaction between conflicting goals is based on the 'non-dominance' concept with respect to the performance criteria. Traditionally, such problems are tackled in a weighted fashion, where multiple objectives are combined into a single goal. Such an approach runs the risk of limiting the conflicting feature of the design sets, and therefore is limited in searching for global optimum. This drawback is overcome by another class of algorithms, based on globally non-dominated design sets, that comprise the frontier of best trade-off between competing designs. These problems are well tackled by population-based algorithms, e.g., genetic algorithms, that offer diversity in manipulating solutions. A number of approaches in the literature are related to the measure of non-dominance, e.g., Fonseca and Fleming (1993) in their Multi-Objective GA (MOGA) rank each individual according to the number of dominated solutions (rank one are the individuals on the Pareto front); Zitzler and Thiele (1998) developed the strengthened Pareto evolutionary algorithm (SPEA), relating the fitness of the best individuals as a function of the dominance in two correlated populations and used a clustering concept to reduce the non-dominated crowded solutions; NSGA-II proposed by Deb et al. (2000), is based on a crowding comparison operator as part of the elitism scheme that attempts to produce an uniformly distributed Pareto front.

As well as encountering multiple conflicting objectives, engineering problems are also often expensive to search. Depending on the design space and the accuracy required, these problems can be tackled using hybrid formulations of non-dominated solutions by means of approximation models combined with genetic operators (Voutchkov and Keane (2006)). In this study, the NSGA-II approach is used to search the parametric space built on pre-existing Krigs to find the best combinations of the design variables that can

minimise the approximated functionals proposed in equations 6.1 - 6.6. The approximation surfaces are based on sampled points from the true function. This constrained search (n.b. a Fiacco-McCormick penalty function was used[6]) is based on a population size of 50 for 50 generations and leads to Pareto sets of approximated designs, for both Krig definitions, as shown in Figures 6.21 and 6.22, accompanied by the rank one DoE LPτ design points from both training and predictions data sets. The approximated solutions from the Pareto fronts are then evaluated on the true function by calling the expensive analysis codes, so as to check quantitatively and qualitatively the surface-based solutions. Since all the Pareto fronts are weak in the constitutive approximated objective space, all the points are checked with the validation scheme (i.e., SWF). This process is limited somewhat due to solver failures (i.e., structural divergence or computational issues) in the design process. The placing of the validated points (taking as a valid basis the Pareto front definition) is inconclusive at this stage with regard to the prediction quality of the metamodels, although, locally, the currently known Pareto front is close to the approximated one, on which the validation was performed. It should be noted that the Pareto front from the reduced definition under-performs within the same training pool of data sets and prediction, taking as a valid basis for comparison the non-dominated solutions from DoE (see Figure 6.22). Although an exhaustive search on the hyperparameters indicated that the reduced form is robust with good validation metrics, the quality of the surface may suffer in approximating a multi-modal function (n.b., the constitutive hyperparameters clearly affect the shape of the surface through p and θ, thus the quality). These issues lead to the need for an update strategy to be involved, as shown in Figure 6.4, until some form of convergence is met (e.g., minimising the residuals between the approximated and the true function Pareto fronts).

Returning to the initial scope of this section, namely to analyse the roll enhancement of the underlying model, the best validated points from the Pareto fronts from full Krig, involving the first objective are analysed. The choice of the first objective is strongly emphasised by its definition and scope, that is to provide a direct metric of the aerodynamic properties of the morphed wing. The resulting designs in terms of pressure contours are presented in Figures 6.23, 6.24 and 6.25 and the equivalent camber contours for these design points are shown in Figure 6.26. All the designs show pressure distributions somewhat similar to flapped airfoils, due to the curvature changes in the spinal structure. Larger cambers at sections towards the tip of the wing tend to shift the suction peaks towards mid chord, and lead to larger residuals with respect to the structural and aerodynamic shapes. The morphed airfoils tend to have a 'two-part' form of pressure distribution over the rear, i.e, a low severity adverse pressure gradient as the trailing edge is approached, followed at $\xi \simeq 0.99$ by a small suction peaks that indicates a sudden boundary layer separation.

[6]see http://www.soton.ac.uk/~ajk/options/welcome.html

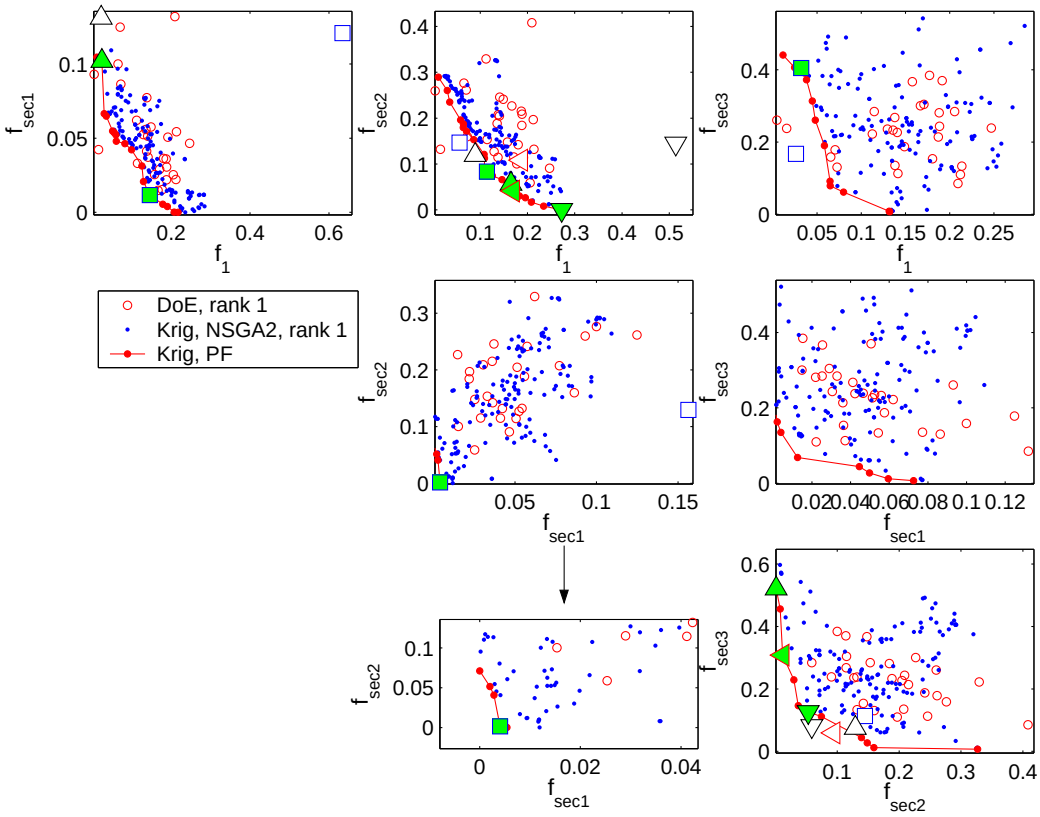

FIGURE 6.21: Full Krig definition, NSGA2 search, Pareto fronts. Filled symbols represent the solvable points from local Pareto front with the true function. Empty symbols are the corresponding points evaluated with the true function.

6.4.1 Roll Enhancement

These designs may offer a valid basis for comparison with a wing with conventional control surfaces (25% flap-to-wing-chord ratio), under similar planform parameters in order to provide a roll performance metric as a measure of the morphing wing effectiveness (n.b., the roll here is provided by a wing when the tip is deflected in the positive direction only and the roll for the whole aircraft can be obtained by a differential positive deflection of the tips of the wings). A standard set up comprising aileron deflection, Mach number and angle of attack has been built for the conventional and morphing wings. This covers aileron deployment δ in the range of 0-20 degrees, Mach numbers between 0.4 and 0.8 and angle of attack between 0 and 10 degrees. The points under investigation represent the best achieved validated solutions in terms of objective f_1 from the Pareto fronts $f_1 - f_{sec1}$, $f_1 - f_{sec2}$ and $f_1 - f_{sec3}$. The results in terms of roll moment coefficient and dynamic pressure are depicted in Figures 6.27, 6.28 and 6.29. For aileron deployment up to 5 degrees, the morphing wing is able to produce more roll than its counterpart. Further increasing the deployment, the differences gradually diminish. An immediate benefit of the morphing wing is the continuous control surface that alleviates the wash-out effect, encountered by the classical wing hinge line discontinuities. For larger aileron deflections, the slight under-performance of the morphing wing at these

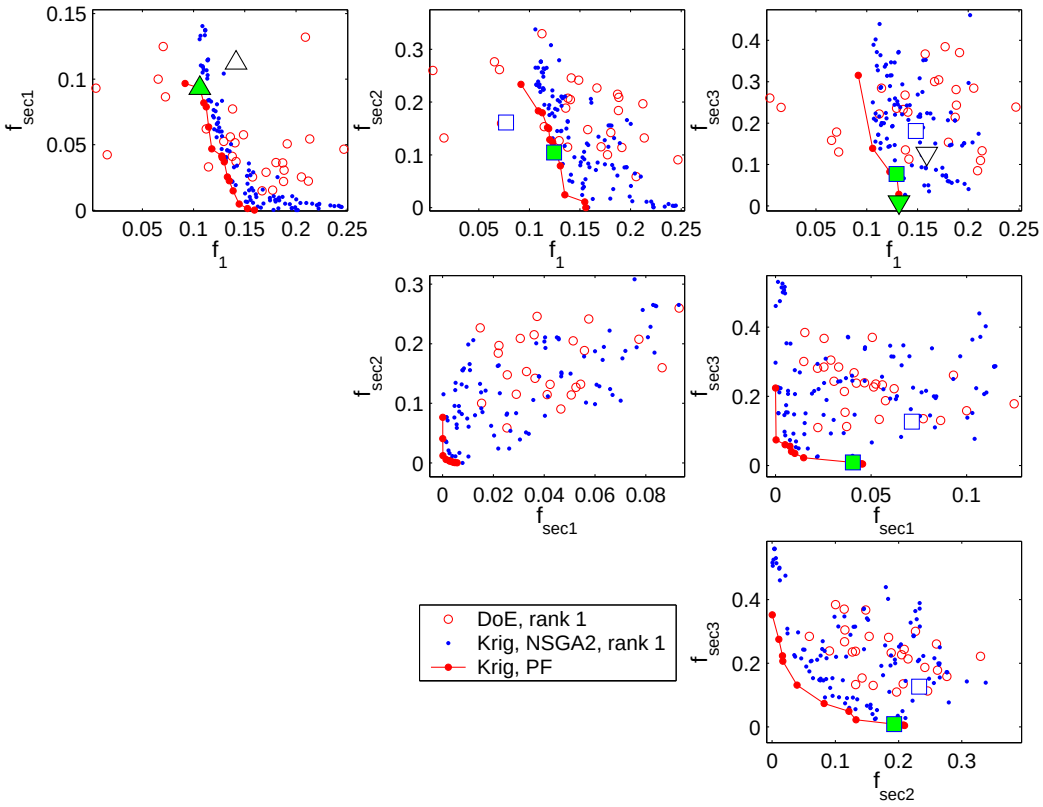

FIGURE 6.22: Reduced Krig definition, NSGA2 search, Pareto fronts. Filled symbols represent the solvable points from local Pareto front with the true function. Empty symbols are the corresponding points evaluated with the true function.

design points is somewhat expected and is significantly influenced by several factors. For instance, the small tip deflection (i.e., the largest tip camber deflection is 4%, exhibited by the design point from the Pareto front $f_1 - f_{sec3}$); a zero dihedral angle, twist and constant thickness distribution spanwise. Since the structural deflection is linked to the loading function, the stopping criterion runs the risk of limiting the search on the point forces that produce the controlled bounds of the displacement field and thus, the loading solution becomes non-unique. The performance is also determined by the accuracy of the metamodels built in the initial design stage, where the correlation factor for the objectives vary between 0.51 and 0.81 (see Figures 6.9 - 6.12). Clearly, these results give confidence that further updates and refinement of the approximation surfaces will conform the performance improvement.

6.5 Concluding Remarks

This chapter described a heuristic methodology for designing wings with global shape control. Extending the approach for multi-shape morphing airfoils into the spanwise direction, and based on a simple loading scheme, the wing morphing concept is applied to provide roll control. The aerodynamic wing design is tackled in a hierarchical

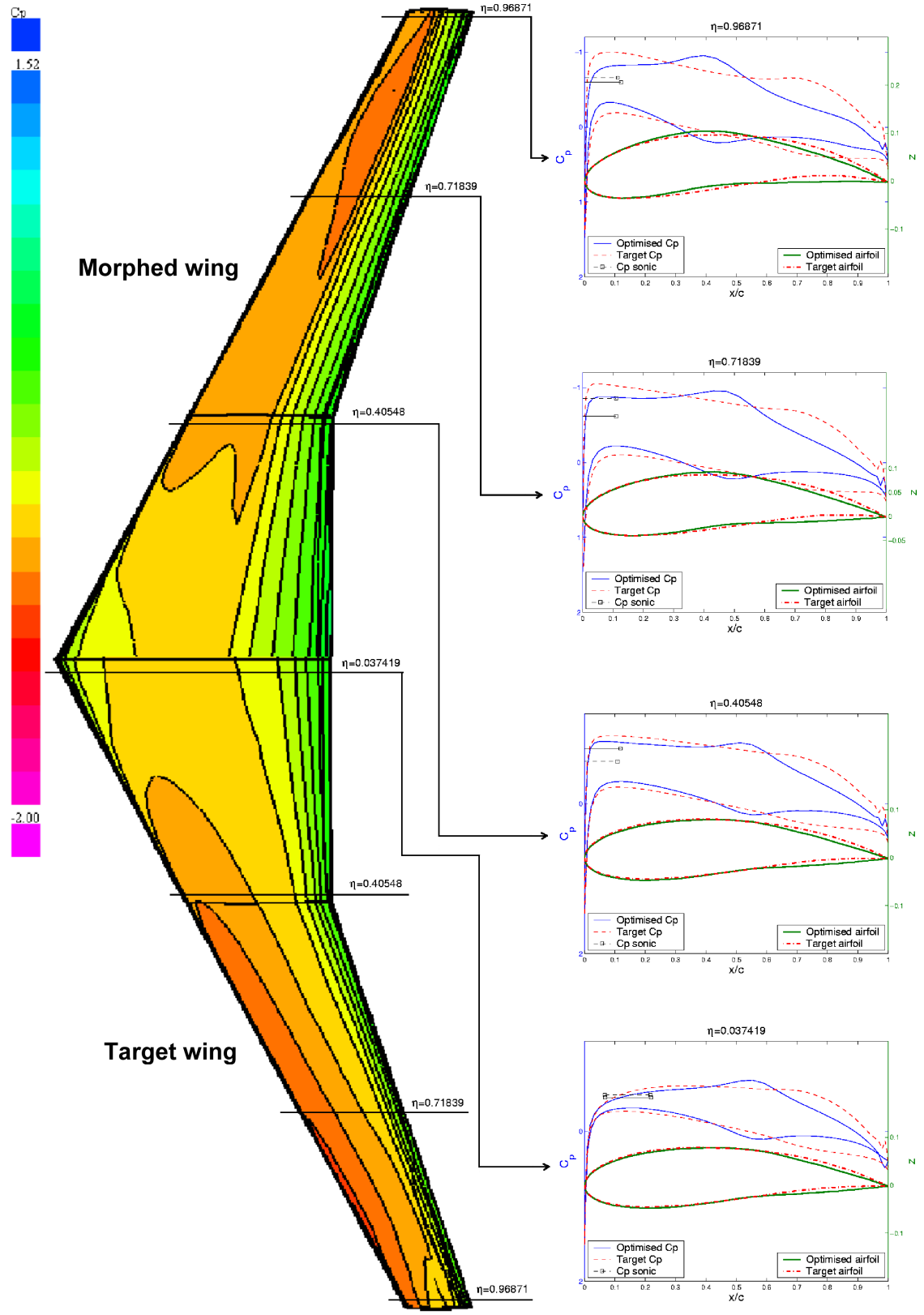

FIGURE 6.23: Pressure contours of a design validated point (full Krig), Pareto front $f_1 - f_{sec1}$

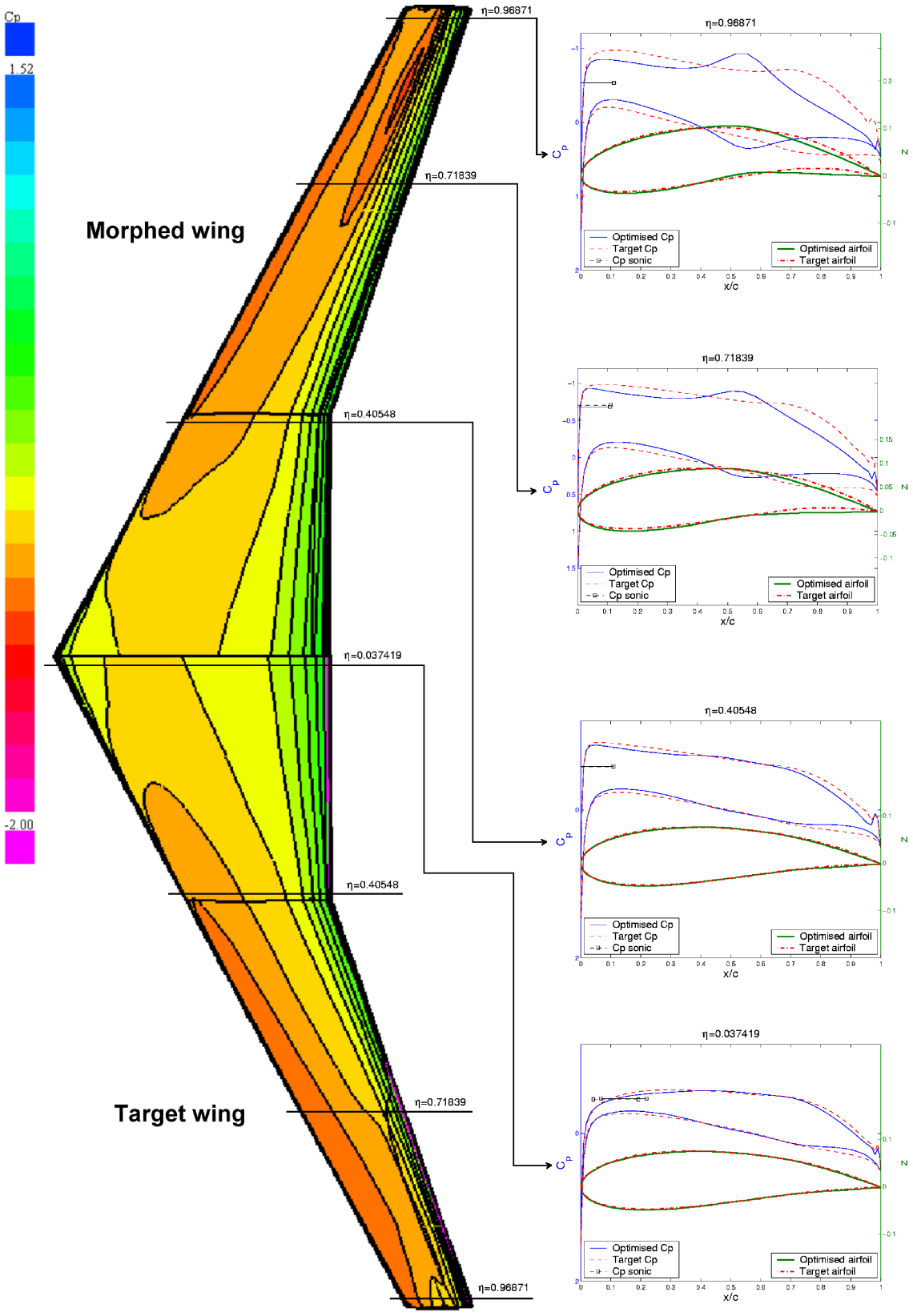

FIGURE 6.24: Pressure contours of a design validated point (full Krig), Pareto front $f_1 - f_{sec2}$

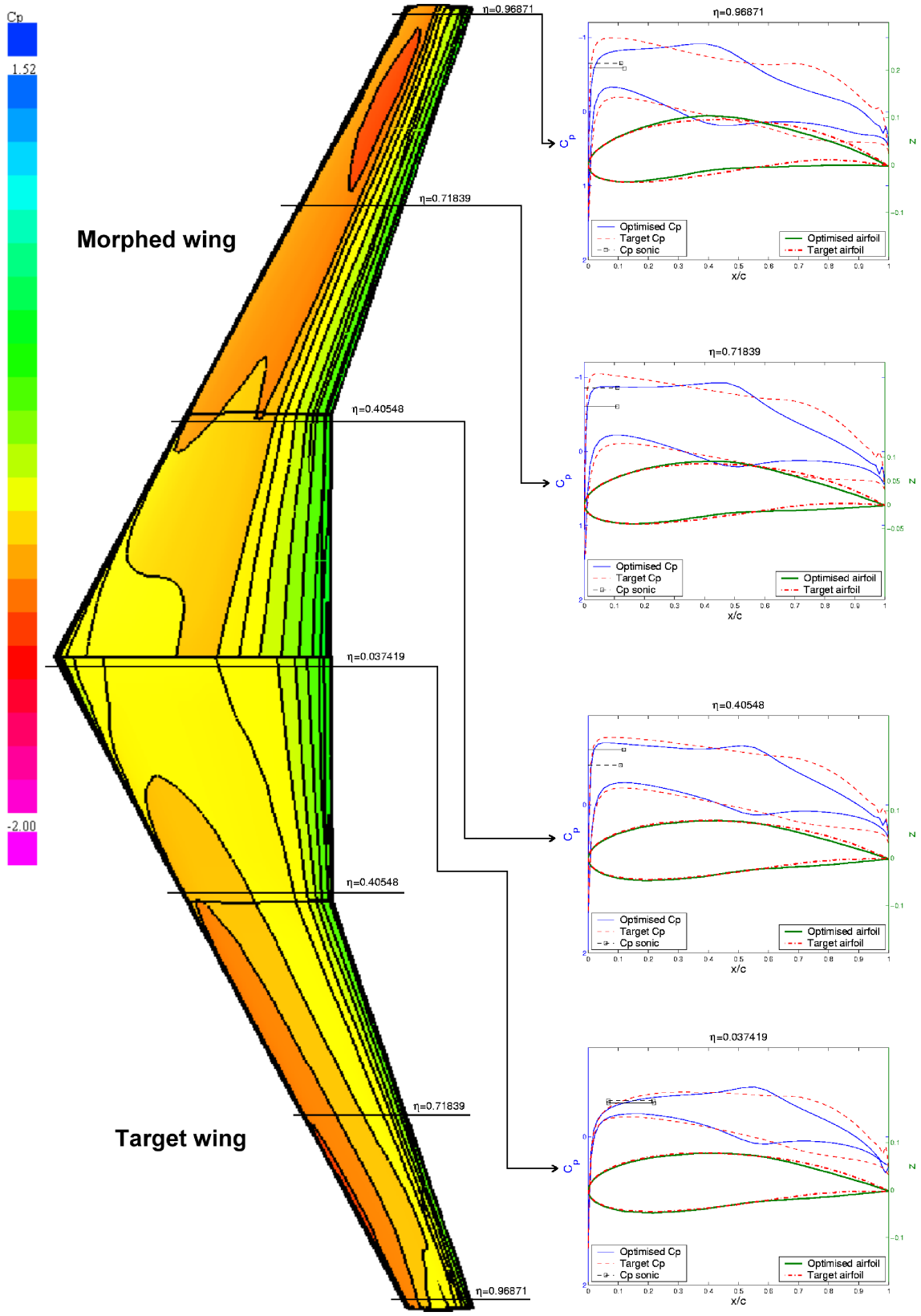

FIGURE 6.25: Pressure contours of a design validated point (full Krig), Pareto front $f_1 - f_{sec3}$

multi-objective optimisation by means of approximation models. The complexity of the problem requires a careful examination of the cost functions and the surrogate modeling involved. The global approximation of the spinal structure provides a means of aerodynamic shape control, enhanced by prescribed structural shapes. The morphing capabilities show good roll control when compared to a classical wing with small aileron deployment. The performance of the wing is strictly related to the accuracy of the approximation model that would need further updates for additional refinement.

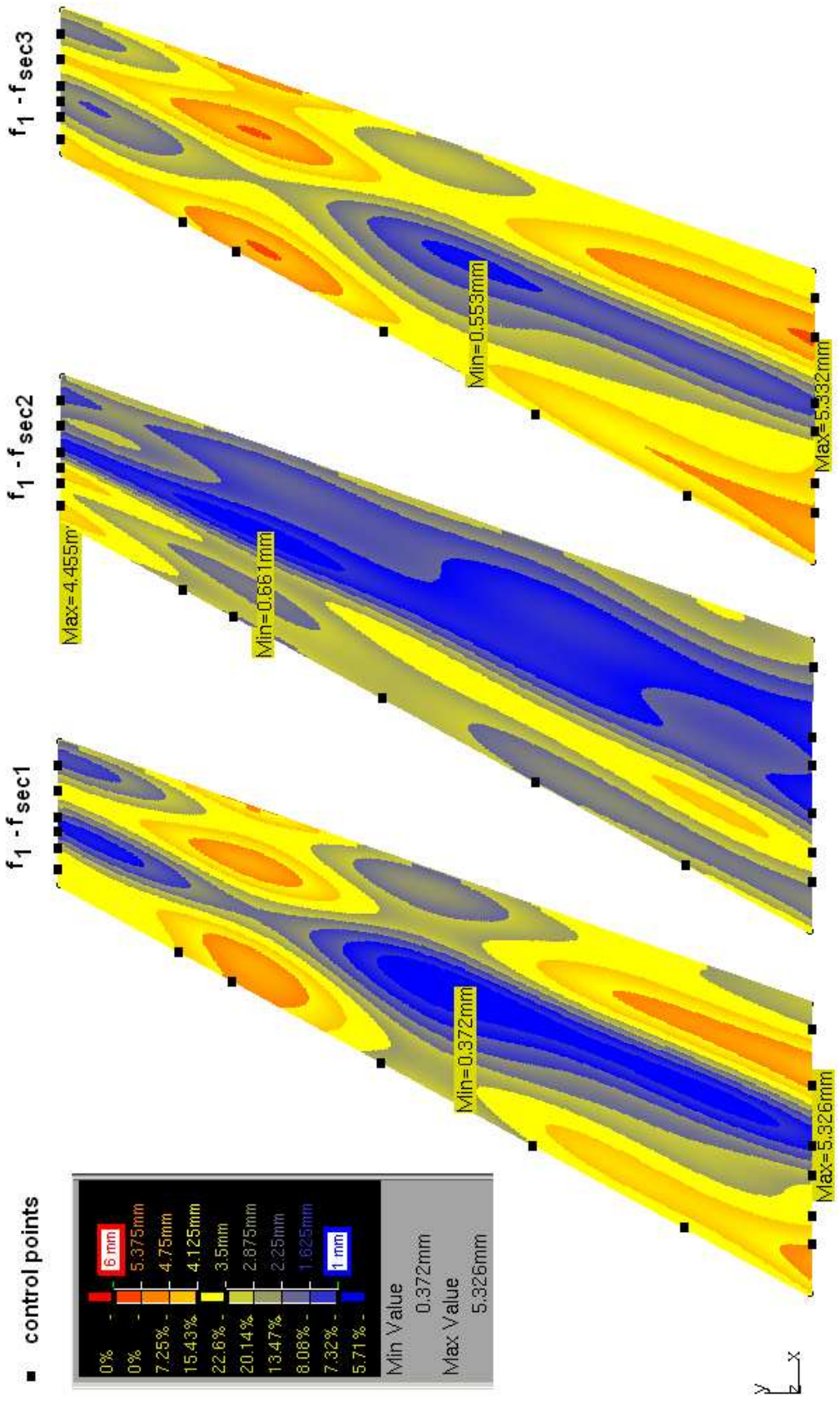

FIGURE 6.26: Camber contours for the design validated points (full Krig) from Pareto fronts $f_1 - f_{sec1}$, $f_1 - f_{sec2}$ and $f_1 - f_{sec3}$.

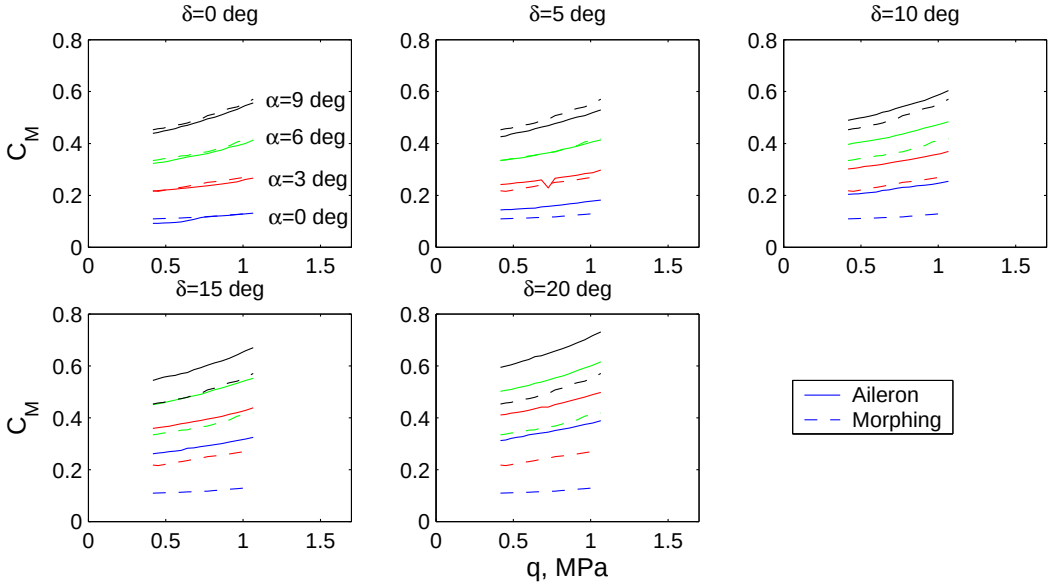

FIGURE 6.27: Roll enhancement of a design validated point (full Krig), Pareto front $f_1 - f_{sec1}$

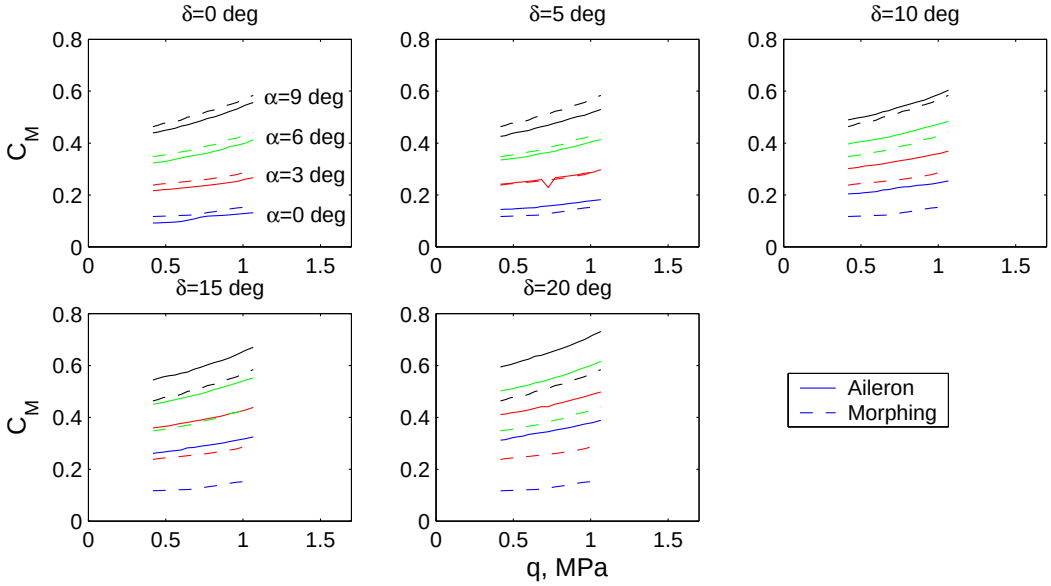

FIGURE 6.28: Roll enhancement of a design validated point (full Krig), Pareto front $f_1 - f_{sec2}$

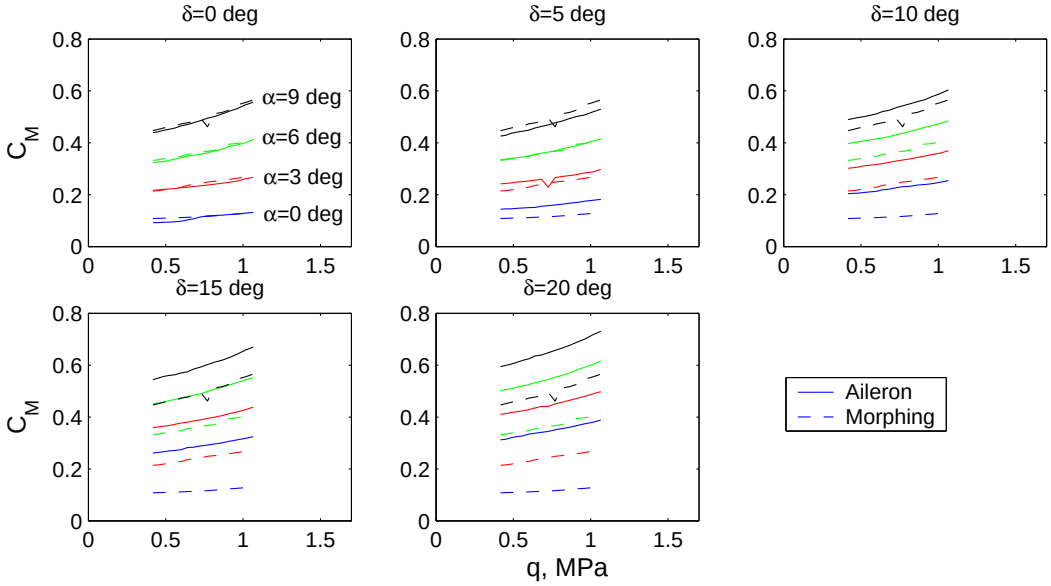

FIGURE 6.29: Roll enhancement of a design validated point (full Krig), Pareto front $f_1 - f_{sec3}$

Chapter 7

Conclusions

This chapter briefly reviews the milestones of the present research and summarises the thesis with a brief synopsis of the main conclusions and contributions of the research effort. It also outlines some directions for future research.

7.1 What has been accomplished

The main focus of this research was on the design of adaptive structures for achieving global multi-shape morphing aerodynamic configurations, by using deforming slender structures. This work pursued two threads towards global optimisation, i.e., providing means of aerodynamic enhancement, using efficient structural shape optimisation.

Modern wing morphing concepts require structural strategies as a means to actively alter the aerodynamic properties and adapt it to new flight conditions. When controlling the shape of a wing, compliant internal structures must be used, and a flexible outer skin is needed to give good aerodynamic performance. Given the space and weight constraints that apply inside aircraft wings, design requirements lead to the need for simple yet powerful ways of controlling the aerodynamic shape. Such devices must be extremely reliable and have low maintenance and operational power requirements.

The proposed two-pronged approach for global shape control followed here treats the airfoils and wings in a hierarchical fashion. The core of the concept resides on slender structures, that can exhibit large changes in shape under limited offset loading. The non-linear feature of the post-critical deformation state is exploited by means of incremental-iterative numerical algorithms, with the benefit of controlled stable structural solutions. The deflection state of the spinal structures links to the aerodynamic performance through a cladding that forms the airfoil. A two-stage heuristic structural design optimisation for the slender structures improves the aerodynamic properties of the associated airfoils. First, a single shape morphing airfoil has been investigated, in

conjunction with a number of parameterisation schemes which exemplifies the approach. The second part augments the approach by adopting an enhanced multi-shape morphing study, where a structural-related figure of merit successfully links improved structural capabilities to incremental changes in the airfoils in a hybrid optimisation. This demonstrates that large changes in shape can be achieved while keeping prescribed flow characteristics on an aeroelastically stable airfoil. The airfoil camber and two-dimensional global shape control is finalised with a study on a complete airfoil configuration, that provides the means to improve upon the correlation between the incremental deflection state of the spinal structure and the desired aerodynamic surface. A study on the constitutive parameters of claddings adds a practical aspect to the global shape control.

The multi-shape morphing airfoil work provides a step towards the goal of global shape control of 3D aircraft wings. Here, a three-dimensional study is applied to aerodynamic design for roll control. A hierarchical strategy is employed, interleaving parameterisation enhancement by means of a CAD tool, followed by structural optimisation into the aerodynamic design process. This MDO approach for constrained multi-objective search is enhanced using a global approximation methodology, since expensive and interdependent 'black-boxes' are used to tackle the expensive solutions. The main goal of the MDO was to achieve enhanced roll while minimising drag. This figure of merit is complemented by structural metrics and constraints so as to maintain product integrity by enabling the control surface to blend smoothly the grid-controlled sections and avoid spurious designs. The approximation models are combined with NSGA-II to enhance the Pareto front framework. The performance of the resulting designs is somewhat limited due to the complexity of the problem being studied, and leaves room for further refinement of the response surfaces.

To summarise, the main contributions of the thesis are:

- Single-shape morphing structural optimisation, with in-depth study of parameterisation techniques;
- Multi-shape morphing hybrid optimisation (i.e., purely structural inverse design, followed by an aerodynamical inverse design) to enhance the structural outcome, by linking it directly to the aerodynamic behavior of the airfoils;
- Cladding optimisation to improve upon the correlation between the analytical representation of the airfoil and the true aerodynamic surface;
- Aerolastically stable airfoil global shape control with prescribed aerodynamic performance;
- The definition of a 3D morphing wing design;

- Wing global shape control to provide roll control, making use of global approximation methods, by means of full and hybrid Krig based response surfaces, combined with NSGA-II to search the Pareto front framework.

The following publications are based on this research:

- N. M. Ursache, A. J. Keane, and N. W. Bressloff. The Design of Post-Buckled Spinal Structures for Aifoils Camber and Shape Control. *AIAA Journal*, 2006 - provisionally accepted for publication.

- N. M. Ursache, A. J. Keane, and N. W. Bressloff. On the Design of Morphing Airfoils using Spinal Structures. *47th AIAA/ASME/ASCE/AHS/ASC Structures, Structural Dynamics, and Materials Conference*, 2006, 1-4 May, Newport, Rhode Island, AIAA 2006-1796.

- N. M. Ursache, A. J. Keane, and N. W. Bressloff. The Design of Adaptive Wings using Spinal Structures. *AIAA Journal* (submitted for review).

- N. M. Ursache, A. J. Keane, and N. W. Bressloff. The design of post-buckled spinal structures for airfoil shape control using optimization methods. *Proceedings of the 5th ASMO UK/ISSMO Conference on Design Optimisation*, 2004, 12-13 July, Stratford-upon-Avon.

7.2 Future Research

The present work approached a novel global shape control strategy with a detailed study for the two-dimensional problems, and tackled the main issues for the three-dimensional case. This work is open to improvement to fully realise the features of morphing wings controlled by slender structures and also points towards a myriad of aircraft applications and other areas which would benefit from shape control strategies. Some directions for future research are presented below:

- Update and refine the response surfaces to better approximate the proposed goals to enhance the Pareto front frameworks. Some of the update strategies were already mentioned in section E.2 and these represent promising avenues of future work. The Pareto front frameworks can be improved if the design strategies coped better with regions of unfeasible or failed points. The current approach encountered failed design evaluations that can alter the quality of the surrogate. Strategies that impute the missing data to enhance the surrogate are offered in the literature (Forrester et al. (2006) offer a reliable time-effective approximation over traditional global searches).

- A full adaptability of the wing to a required maneuver would benefit from a displacement-controlled loading study on the morphing wing. This would involve the exploitation of a range of incremental non-linear structural solutions. A design paradigm that would alleviate the drawbacks mentioned in section 6.2.2 by a monolithic control of the states fields via user defined subroutines and iterative control of the finite element would be useful algorithms. Such a framework would be particularly suitable for the study of static and dynamic aeroelastic phenomena, inherently caused by actively changing shapes in flight (Inman et al. (2001), Tian (2003)).

- Embedded localised beam-like spinal structure could be placed in traditional wings to control locally the curvature of the aerodynamic surface via an elastic skin, and thus the boundary layer (Natarajan et al. (2004)) or the circulation towards the trailing edge (i.e., Coanda effect, Carpenter and Green (1997)).

Appendix A

Conventional Numerical Techniques

This Appendix contains details of the theoretical background of the numerical algorithms employed in this thesis.

A.1 Newton's Method

To illustrate the formalism of the so-called Newton's procedure, attention can be focused on the iterative solution of one nonlinear equation. In a nonlinear analysis the solution is calculated by solving multiple systems of equations (n.b. the linear case would require a single system). Consequently, incremental augmentation of the solution via state variables is preferred when working toward the final solution. Therefore, the numerical procedure employed builds the equilibrium path incrementally, based on point-solutions at the end of each increment. Hence, the final solution is augmented by each incremental response. Each new equilibrium configuration is the result of an iterative two-pronged convergence check, viz. the norms of residual and state variable, respectively.

If prediction of the incremental solution k starts from initial point $({}_k\mathbf{u}^0, \ {}_k\lambda^0)$, with $\mathbf{u}$ the state variable and λ the control parameter, then the residuals and the constraint at iteration i in a Taylor series about iterative solution point $(\mathbf{u}_i^0, \ \lambda_i^0)$ can be expressed as:

$$\begin{aligned} \mathbf{R}^{i+1} &= \mathbf{R}^i + \frac{\partial \mathbf{R}}{\partial \mathbf{u}}\mathbf{c}^{i+1} + \frac{\partial \mathbf{R}}{\partial \lambda}\zeta^{i+1} + \ldots = 0 \\ \boldsymbol{\tau}^{i+1} &= \boldsymbol{\tau}^i + \frac{\partial \boldsymbol{\tau}}{\partial \mathbf{u}}\mathbf{c}^{i+1} + \frac{\partial \boldsymbol{\tau}}{\partial \lambda}\zeta^{i+1} + \ldots = 0, \end{aligned} \tag{A.1}$$

where $\mathbf{c}^{i+1} = \mathbf{u}^{i+1} - \mathbf{u}^{i}$ and $\zeta^{i+1} = \lambda^{i+1} - \lambda^{i}$ defines the iterative increments between corresponding parameters of two discrete solutions.

The augmented stiffness matrix and the incremental load vector become:

$$\mathbf{K} = \frac{\partial \mathbf{R}}{\partial \mathbf{u}}, \quad \mathbf{q} = -\frac{\partial \mathbf{R}}{\partial \lambda} \tag{A.2}$$

therefore, if $\mathbf{K}$ is non-singular, the system of Equations A.1 becomes:

$$\left(\frac{\partial \boldsymbol{\tau}}{\lambda} + \frac{\partial \boldsymbol{\tau}}{\partial \mathbf{u}}\mathbf{K}^{-1}\mathbf{q}\right)\zeta = -\boldsymbol{\tau} + \frac{\partial \boldsymbol{\tau}}{\partial \mathbf{u}}\mathbf{K}^{-1}\mathbf{R}. \tag{A.3}$$

The two-pronged convergence check that follows the Newton iteration is:

- displacement check is based on last augmented correction as function of state variable $\mathbf{u}$ and is a fraction of initial solution (i.e., 1% in Abaqus):

$$\| \mathbf{K}^{-1}\mathbf{R} + \zeta\mathbf{K}^{-1}\mathbf{q} \| \leq \epsilon_{disp} \tag{A.4}$$

- residual check against residual tolerance (i.e., 0.5% in Abaqus):

$$\| \mathbf{R} \| \leq \epsilon_{resid} \tag{A.5}$$

Various forms of Newton's technique are found in the literature, depending upon the computation of the stiffness matrix in the current configuration (e.g., $\mathbf{K}|_k = \mathbf{K}|_{k=0}$ is kept constant throughout in a 'Modified Newton') or the inverse of stiffness matrix is rather augmented in a 'quasi-Newton'; these methods lie outside the scope of this thesis.

A.2 Arc-Length Method

The arc length method proves to be a more accurate and equilibrium path follower in some nonlinear static analyses where, if the Newton's method is used, the stiffness matrix may become singular, in which case the structure either collapses or "snaps" to another stable equilibrium phase, Riks (1979). This method is generally used to predict the unstable, geometrically nonlinear collapse of a structure.

The basic algorithm remains the Newton's method which converges along an equilibrium *arc*, with a generalised arc length Δs, which is the independent variable controlling the convergence to equilibrium.

The equation that governs the non-linear static structural problems, called the residual force equation, can be expressed in the form:

$$\mathbf{R}(\mathbf{u}, \lambda) = \mathbf{P}_{int}(\mathbf{u}) - \mathbf{P}_{ext} = 0 \tag{A.6}$$

with

$$\mathbf{P}_{ext} = \mathbf{P}_0 + \lambda(\mathbf{P}_{ref} - \mathbf{P}_0) \tag{A.7}$$

where $\mathbf{P}_{int}(\mathbf{u})$ are the internal forces, $\mathbf{u}$ is the state vector, λ is the load parameter, $\mathbf{P}_{ext}$ is the fixed external loading function, $\mathbf{P}_0$ is the 'dead load' which exists in case of a pre-tensioned structure and $\mathbf{P}_{ref}$ is the reference load vector.

The predictor in an arc-length algorithm is based on the first order path equilibrium, and can be equated as:

$$\mathbf{R}' = \frac{\partial \mathbf{R}}{\partial \lambda} = \mathbf{K}\mathbf{u}' - \mathbf{q} = 0. \tag{A.8}$$

If $\mathbf{K}$ is non-singular, then $\mathbf{u}' = \mathbf{K}^{-1}\mathbf{q} = \boldsymbol{\psi}$ defines the incremental velocity vector that is the main quantity in an continuation-based method. The velocity flow determines a hypersurface (n.b. for one degree of freedom, the sypersurface is reduced to the equilibrium path from Figure A.1) from initial solution $(\mathbf{u}, \lambda)$ to an incremental point $(\mathbf{u} + \Delta\mathbf{u}, \lambda + \Delta\lambda)$:

$$\boldsymbol{\psi}^T \Delta\mathbf{u} + \Delta\lambda = 0 \tag{A.9}$$

The solution is found by applying an increment control strategy through a constraint on the tangent $\boldsymbol{\tau}(\Delta\mathbf{u}, \Delta\lambda)$ such that a distance Δl along the tangent is specified:

$$\boldsymbol{\tau}(\Delta\mathbf{u}, \Delta\lambda) = \frac{1}{v_n}|\boldsymbol{\psi}_n^T \Delta\mathbf{u}_n + \Delta\lambda_n| - \Delta l = 0 \tag{A.10}$$

Assuming $\mathbf{K}$ is nonsingular, from first order predictor $\mathbf{R}' = 0$, then

$$\Delta\mathbf{u}_n = \mathbf{K}^{-1}\mathbf{q}_n \Delta\lambda_n = \boldsymbol{\psi}_\Delta \lambda_n \tag{A.11}$$

and selecting the increment control strategy, the incremental state point and the incremental load become

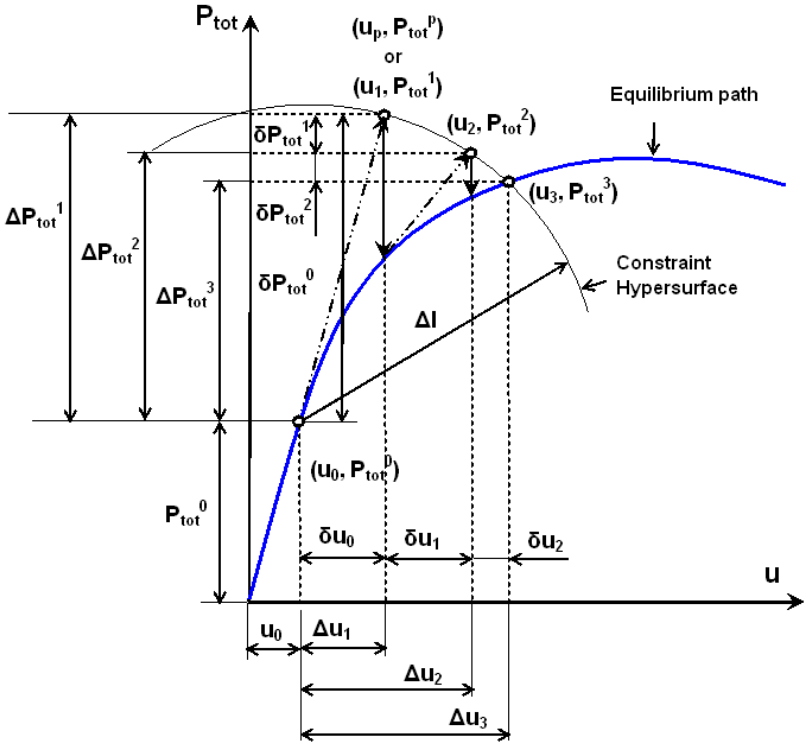

FIGURE A.1: Riks Algorithm.

$$\Delta \mathbf{u} = \pm \frac{\boldsymbol{\psi}_n \Delta l_n}{v_n}, \tag{A.12}$$

$$\Delta \lambda_n = \frac{\Delta l v_n}{\pm(\boldsymbol{\psi}_n^T \boldsymbol{\psi}_n + 1)}, \tag{A.13}$$

where $v_n = \sqrt{1 + \boldsymbol{\psi}^T \boldsymbol{\psi}}$ is the scaling factor.

The true path direction selection, in terms of orientation of the tangent, becomes crucial when passing critical points. There are two rules that can contribute feasible solutions:

- the sign is given by the current stiffness determinant, condition derived form the positiveness constraint of incremental predictor external work $\Delta P = \mathbf{q}^T \Delta \mathbf{u}_n > 0$

$$\mathbf{q}^T \boldsymbol{\psi} = \mathbf{q}^T \mathbf{K}^{-1} \mathbf{q}. \tag{A.14}$$

  This method behaves well at snap-back, but fails at bifurcation points and requires additional perturbation algorithms.

- angle constraint when the external work constraint is erroneously posed in problems with pitfalls in stiffness, therefore the tangent constraint is imposed:

$$\mathbf{t}_n^T \mathbf{t}_{n-1} > 0, \quad \text{where} \quad \mathbf{t}_n = \begin{bmatrix} \boldsymbol{\psi}_n \\ 1 \end{bmatrix} \tag{A.15}$$

  This method works well with the bifurcation point, but may fail in snap-back.

These two approaches are alternating during the analysis, depending upon the current path reference.

At this stage the corrector is based on the iterative Newton's method applied on Equations A.6 and A.10 to determine iterative displacement points $\delta\mathbf{u}_i$ and iterative load control $\delta\lambda_i$.

The three-pronged convergence check is akin to Newton's definition:

- a displacement check is based on last augmented correction as function of state variable $\mathbf{u}$ and is a fraction of initial solution:

$$\sqrt{(\delta\mathbf{u})^T(\delta\mathbf{u})} \leq, \epsilon_{disp} \tag{A.16}$$

- a residual check against residual tolerance:

$$\sqrt{(\mathbf{R})^T(\mathbf{R})} \leq \epsilon_{resid}, \tag{A.17}$$

- a energy check combines the other two tests:

$$\sqrt{(\delta\mathbf{u})^T(\mathbf{R})} \leq \epsilon_{disp}\epsilon_{resid}. \tag{A.18}$$

Although Newton's methods are not guaranteed to converge, some detection schemes are employed to stop advancing erroneous equilibrium paths:

$$\frac{\parallel \delta\mathbf{u}_n \parallel}{\parallel \mathbf{u}_n \parallel} \geq \zeta_{disp}, \tag{A.19}$$

$$\frac{\parallel \mathbf{R} \parallel}{\parallel \mathbf{R}_{pred} \parallel} \geq \zeta_{resid}. \tag{A.20}$$

Such factors forces the incremental method to cutback for poor initial guesses, when the hypersurface is highly multi-modal and there are pitfalls between two iterative points (i.e., when high a degree of nonlinearity occurs).

Appendix B

Aerodynamic Features of NURBS-based Morphing Airfoils

This Appendix contains the main aerodynamic results achieved with NURBS-based multi-shape morphing airfoils.

B.1 Global Search

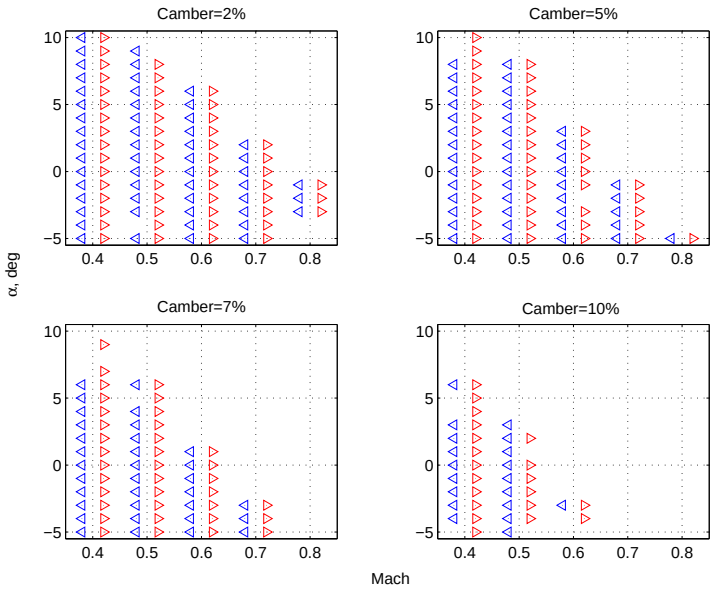

FIGURE B.1: Envelope of converged CFD runs on NURBS parameterised airfoil (global search), where '◁' represents successful runs for the computed airfoil and '▷' for the target.

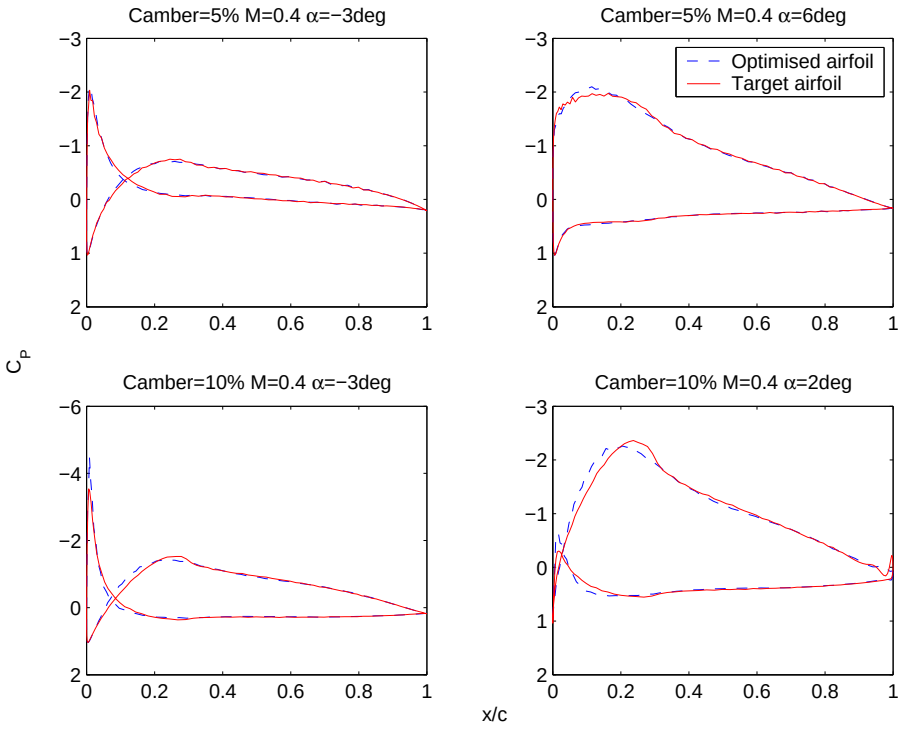

FIGURE B.2: Pressure distributions for morphed and target airfoils (global search), under mild flow conditions, NURBS.

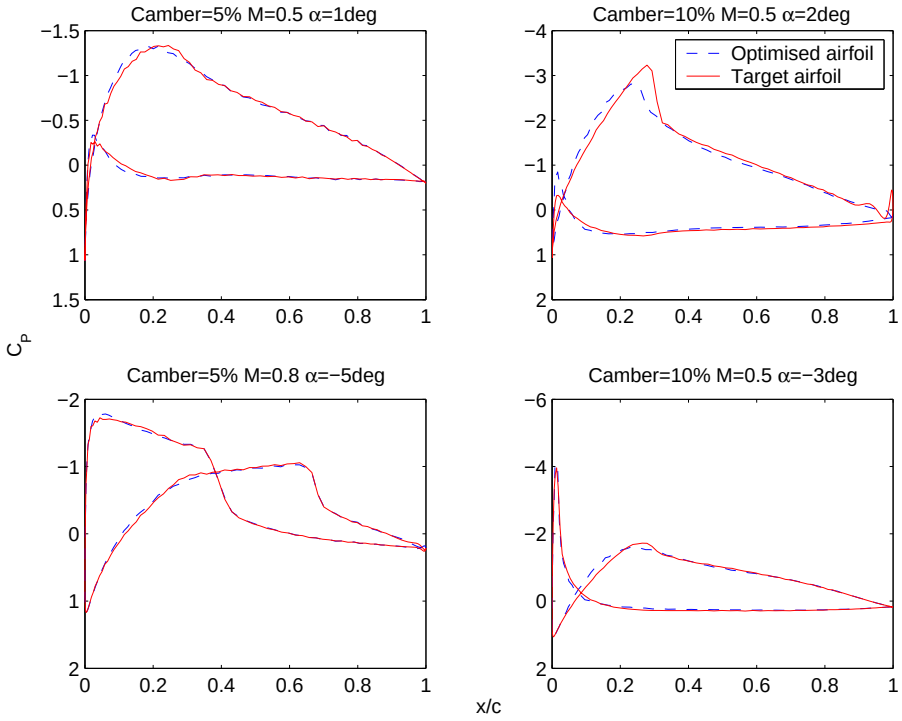

FIGURE B.3: Pressure distributions for morphed and target airfoils (global search), under severe flow conditions, NURBS.

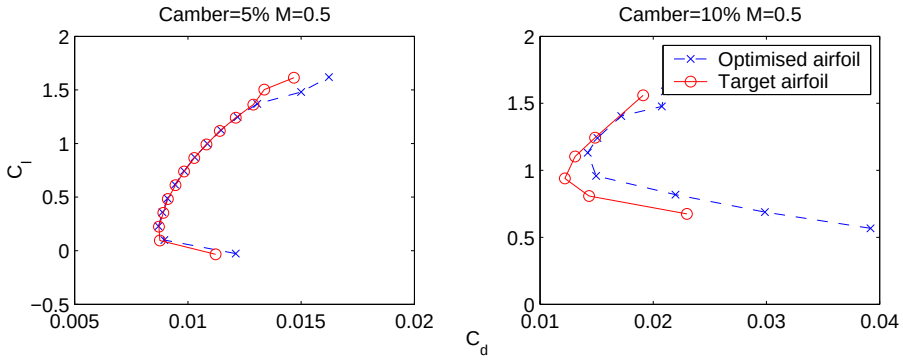

FIGURE B.4: Drag polars for 5% and 10% cambers (global search), NURBS.

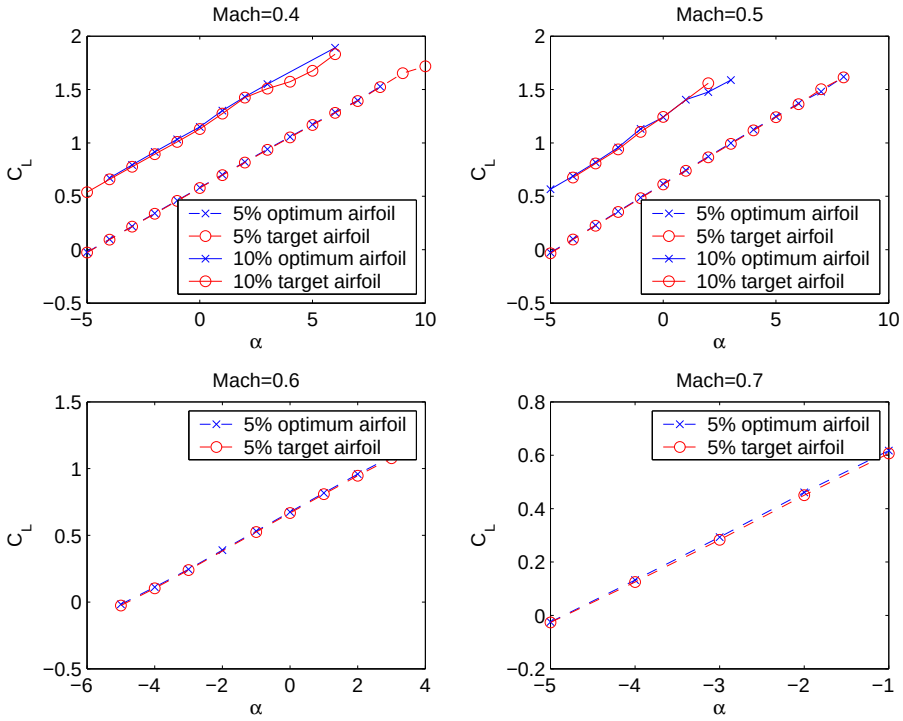

FIGURE B.5: Variation of lift coefficient vs. angle of attack with Mach number, for 5% and 10% cambers (global search), NURBS.

B.2 Gradient Search

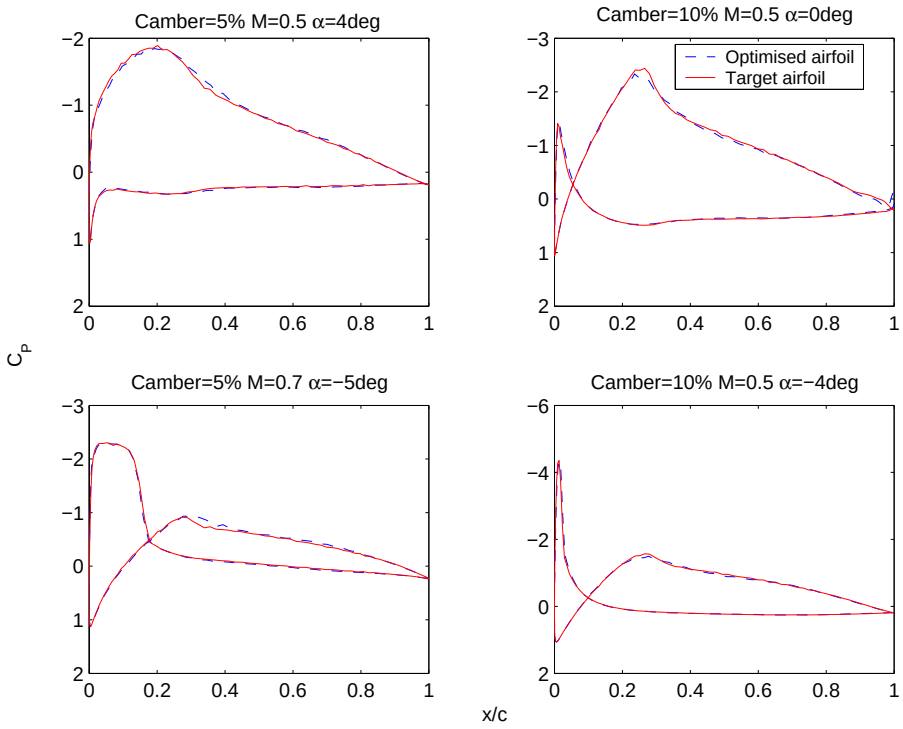

FIGURE B.6: Pressure distributions for morphed and target airfoils under severe flow conditions (gradient search), NURBS.

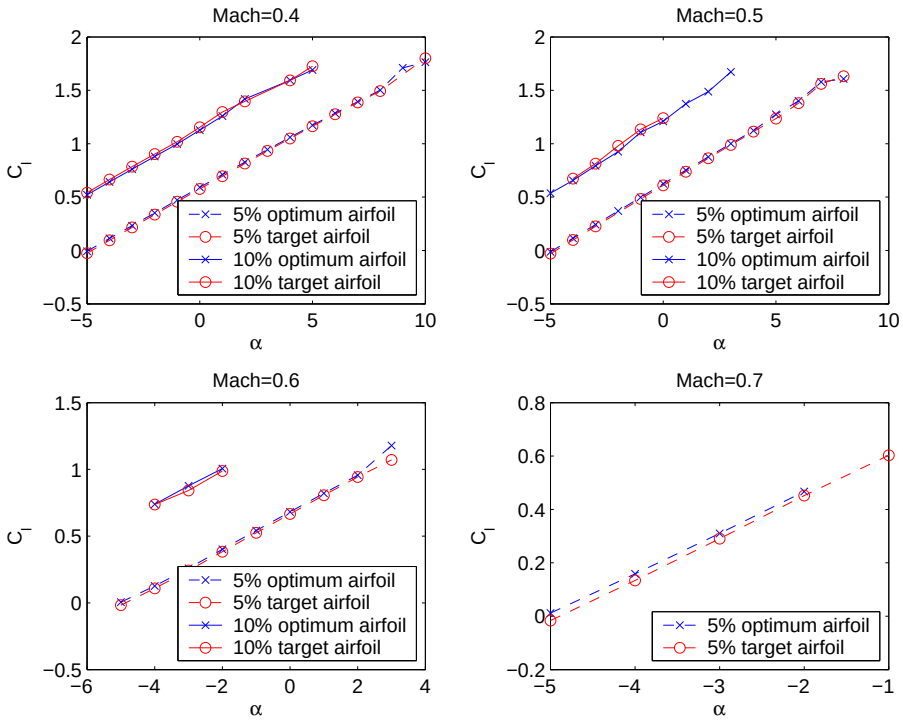

FIGURE B.7: Variation of lift with incidence across 5% and 10% cambers (gradient search), NURBS.

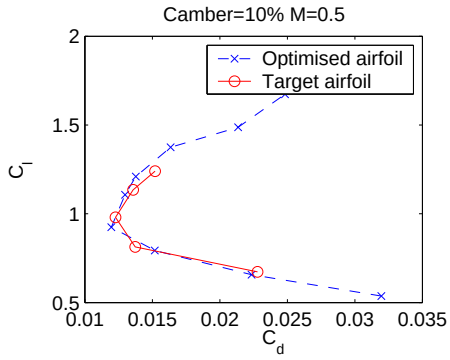

FIGURE B.8: Drag polar for 10% camber (gradient search), NURBS.

B.3 Aeroelastic Study

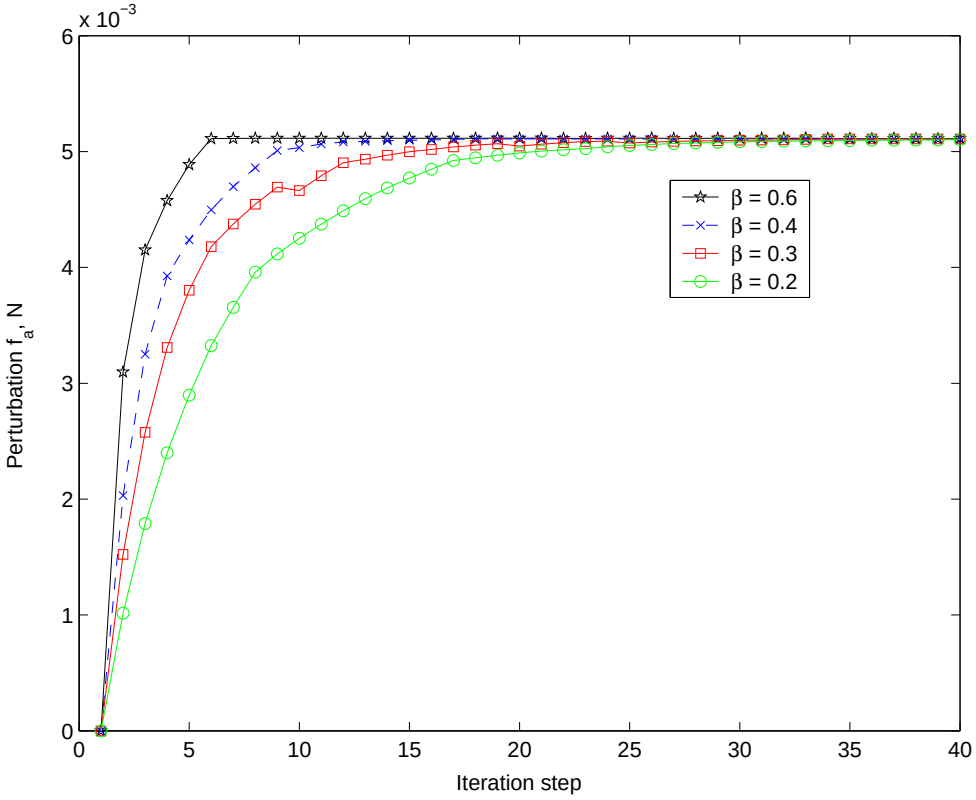

FIGURE B.9: Aeroelastic convergence studies, with relaxation factor $\beta = 0.2,\ 0.3,\ ,0.4,\ 0.6$, NURBS.

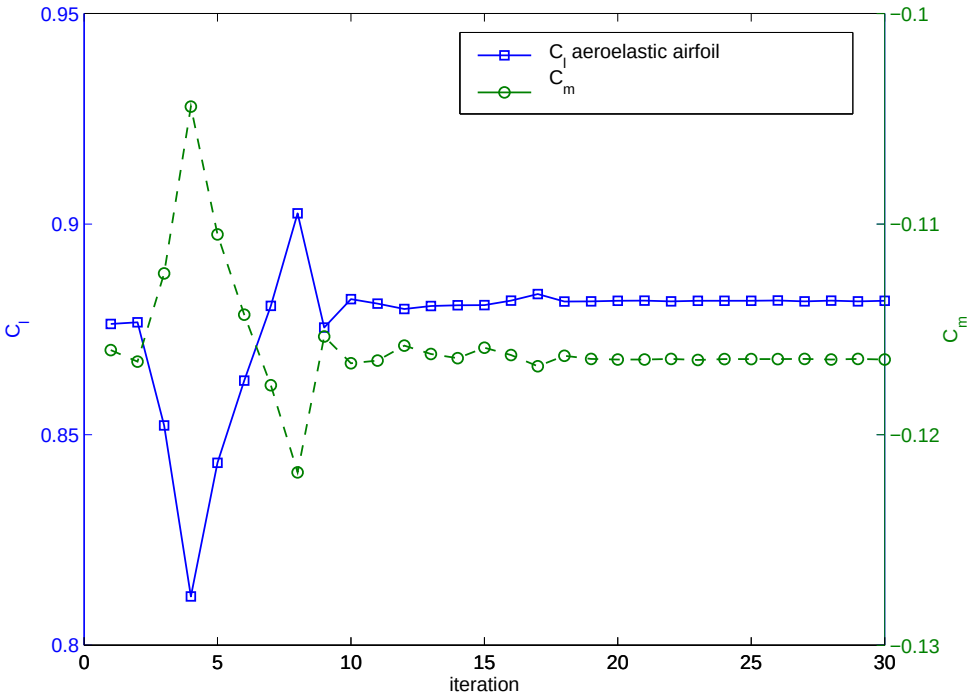

FIGURE B.10: Aeroelastic stability, $\beta = 0.4$, NURBS.

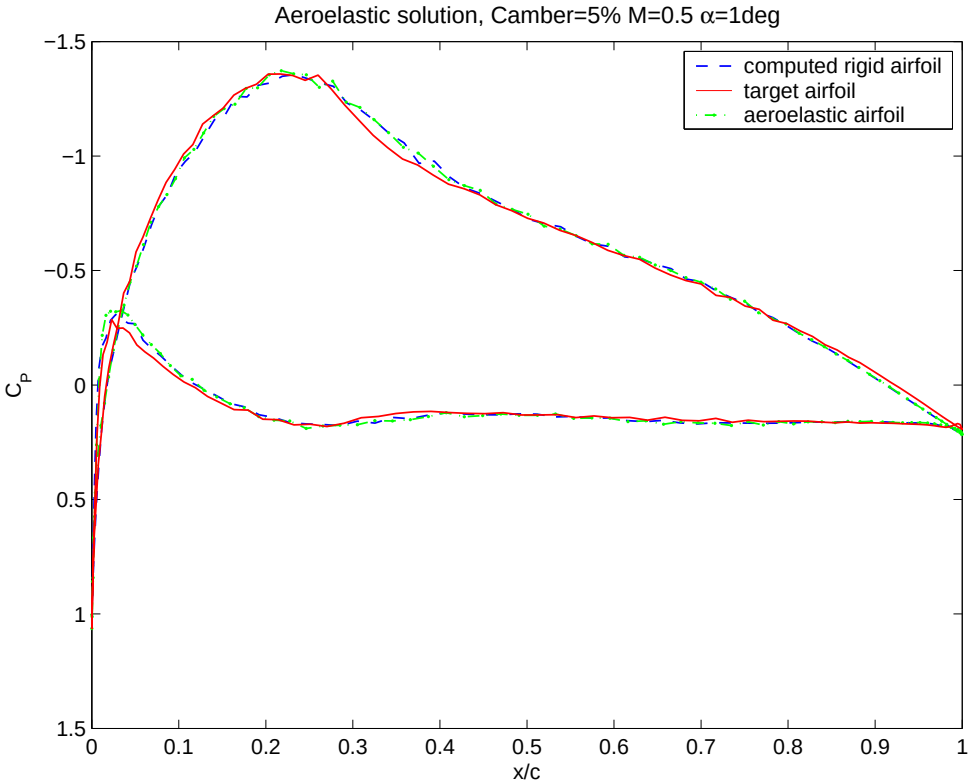

FIGURE B.11: Aeroelastic pressure distributions, $\beta = 0.4$, NURBS.

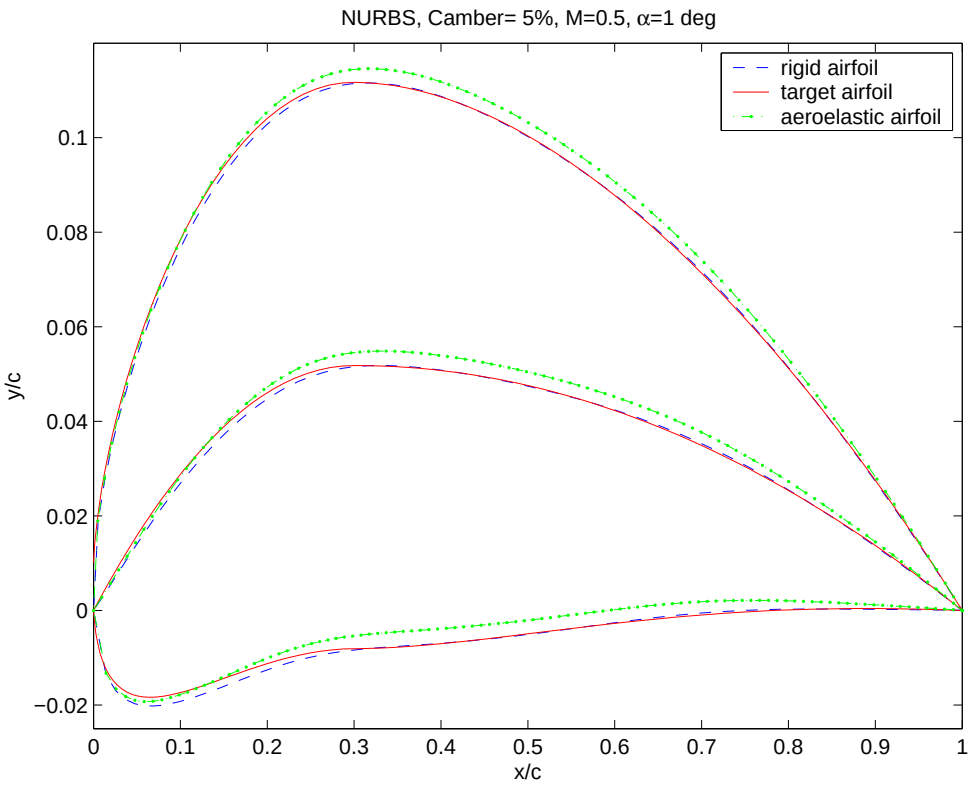

FIGURE B.12: Rigid and aeroelastic airfoils, $\beta = 0.4$, NURBS.

Appendix C

Statistical Components

This Appendix contains details of the numerical metrics employed to asses the quality of the approximations surfaces.

C.1 Linear Least Squares Regression

The least squares function can be stated as:

$$\mathbf{y} = \mathbf{X}\boldsymbol{\beta} + \boldsymbol{\epsilon} \tag{C.1}$$

and minimises the summed square of residuals of n data points:

$$L = \sum_{i=1}^{n} \epsilon_i^2 = \boldsymbol{\epsilon}^T \boldsymbol{\epsilon} \tag{C.2}$$

- $\mathbf{y} \in \mathbb{R}^{n \text{ x } 1}$ is the vector of responses
- $\boldsymbol{\beta} \in \mathbb{R}^{k \text{ x } 1}$ is the vector of regressor variables
- $\mathbf{X} \in \mathbb{R}^{n \text{ x } m}$ is the design matrix
- $\boldsymbol{\epsilon} \in \mathbb{R}^{n \text{ x } 1}$ is the vector of uncorrelated, normally distributed random noise, with $E(\epsilon_i) = 0$ and variance $Var(\epsilon_i) = \sigma^2$ (or $\epsilon \sim N(0, \sigma^2\mathbf{I})$), see Myers and Montgomery (1995))

Equation C.2 is minimised with respect to the coefficients $\boldsymbol{\beta}$ from equation C.2, leading to estimators $\hat{\boldsymbol{\beta}}$ by satisfying the condition:

$$\frac{\partial L}{\partial \boldsymbol{\beta}}\Big|_{\hat{\boldsymbol{\beta}}} = 0 \tag{C.3}$$

leading to normal equation and parameter estimates:

$$\hat{\boldsymbol{\beta}} = \left(\mathbf{X}^T\mathbf{X}\right)^{-1}\mathbf{X}^T\mathbf{y} \tag{C.4}$$

The fitted model can be expressed as:

$$\hat{\mathbf{y}} = \mathbf{X}\hat{\boldsymbol{\beta}} \tag{C.5}$$

and the residual vector becomes:

$$\mathbf{r} = \mathbf{y} - \hat{\mathbf{y}} \tag{C.6}$$

The root mean square error (RMSE), the unbiased estimate of σ is:

$$\hat{\sigma} = \sqrt{\frac{\mathbf{r}^T\mathbf{r}}{n-m}} \tag{C.7}$$

C.2 Weighted Least Squares Regression

The weighted least squares regression minimises the functional S or error estimate:

$$L = \sum_{i=1}^{n}(w_i r_i)^2 = (\mathbf{WR})^T\mathbf{WR} \tag{C.8}$$

leading to modified normal equation and parameter estimates:

$$\hat{\boldsymbol{\beta}} = \left(\mathbf{X}^T\mathbf{W}\mathbf{X}\right)^{-1}\mathbf{X}^T\mathbf{W}\mathbf{y} \tag{C.9}$$

as function of weights vector $\mathbf{W}$ defined by diagonal components

$$w_i = \left(\frac{1}{n}\sum_{i=1}^{n}(y_i - \bar{y})^2\right)^{-1}$$

A procedure to iteratively fit the data and minimise the effect of large noise points (i.e., extreme values) may be used over the simple weighted method, using as starting point the regular fit:

- compute *adjusted residuals* vector $\mathbf{r_{adj}}$ with respect to the *leverages* vector $\mathbf{h}$ (i.e., the components measure how far the corresponding point if from the centre of $\mathbf{X}$ data) in order to assign larger influence to observations with larger leverages (i.e., diagonal components of the hat matrix):

$$\mathbf{r_{adj}} = \frac{\mathbf{r}}{\sqrt{1-\mathbf{h}}} \tag{C.10}$$

- standardise adjusted residuals by the standard deviation of the error term v, as a function of the median absolute deviation (MAD),i.e., median(|r|)/0.6745 (see DuMouchel and O'Brien (1989)) and a tuning constant $B = 4.685$, from the fundamentals of Hubert (1981):

$$\mathbf{s_r} = \frac{\mathbf{r_{adj}}}{Bv} \tag{C.11}$$

- compute adjusted weights:

$$w_i = \begin{cases} (1-s_{r_i}^2)^2 & \text{if } |s_{ri}| < 1 \\ 0 & \text{otherwise} \end{cases} \tag{C.12}$$

- check the convergence condition:

$$\bigtriangledown\, \mathbf{s_r}\left(\hat{\boldsymbol{\beta}}\right) = 0 \tag{C.13}$$

  Using the residuals formulation C.11, the convergence criteria can be expressed as:

$$\mathbf{X}^T\mathbf{W}\left(\mathbf{s_r}\right)\mathbf{s_r} = 0 \quad \Longrightarrow \quad \mathbf{X}^T\mathbf{W}\mathbf{X}\hat{\boldsymbol{\beta}} = \mathbf{X}^T\mathbf{W}\left(\mathbf{s_r}\right)\mathbf{y} \tag{C.14}$$

  which can be iteratively formulated as:

$$\hat{\boldsymbol{\beta}}^{(i+1)} = \hat{\boldsymbol{\beta}}^{(i)} + \left[\mathbf{X}^T\mathbf{W}\left(\frac{\mathbf{y}-\mathbf{X}\hat{\boldsymbol{\beta}}^{(i)}}{Bv\sqrt{1-\mathbf{h}}}\right)\right]^{-1}\mathbf{X}^T\mathbf{W}\left(\frac{\mathbf{y}-\mathbf{X}\hat{\boldsymbol{\beta}}^{(i)}}{Bv\sqrt{1-\mathbf{h}}}\right)\left(\mathbf{y}-\mathbf{X}\hat{\boldsymbol{\beta}}^{(i)}\right) \tag{C.15}$$

Appendix D

Thin shell formulation

Let's consider a reference surface $\mathcal{S}$ with normal $\mathbf{n}$ (i.e., unit vector) and a material point in the undeformed state in terms of isoparametric coordinates $\mathbf{x}^0(\theta^1, \theta^2)$, and in the current position the point becomes $\mathbf{x}(\theta^1, \theta^2)$.

The linearised kinematics in terms of displacement field $\mathbf{u}$ can be expressed as:

$$\mathbf{x}(\theta^1, \theta^2) = \mathbf{x}^0(\theta^1, \theta^2) + \mathbf{u}(\theta^1, \theta^2) \tag{D.1}$$

Let us introduce the following kinematic variables (the fundamental forms of the shell surface) as functions of covariant basis vectors $\mathbf{x}_{,.}$:

$$\begin{aligned} 1^{st} \text{ fundamental form} : a_{\alpha\beta} &= \mathbf{x}_{,\alpha} \cdot \mathbf{x}_{,\beta} && \text{(D.2)} \\ 2^{nd} \text{ fundamental form} : \kappa_{\alpha\beta} &= \mathbf{x}_{,\alpha} \cdot \mathbf{n}_{,\beta} \\ &= -\frac{1}{2}\left(\frac{\partial \mathbf{n}}{\partial \theta^\alpha} \cdot \frac{\partial \mathbf{x}}{\partial \theta^\beta} + \frac{\partial \mathbf{n}}{\partial \theta^\beta} \cdot \frac{\partial \mathbf{x}}{\partial \theta^\alpha}\right) && \text{(D.3)} \end{aligned}$$

The membrane strain tensor in terms of first partial derivative of $\mathbf{u}$ expressed in local material directions, becomes:

$$\begin{aligned} \epsilon_{\alpha\beta} &= \frac{1}{2}\left(\mathbf{x}^0_{,\alpha} \cdot \mathbf{u}_\beta + \mathbf{x}^0_{,\beta} \cdot \mathbf{u}_\alpha\right) \\ &= \frac{1}{2}\left(\frac{\partial \mathbf{x}^0}{\partial \theta^\alpha}\frac{\partial \mathbf{u}}{\partial \theta^\beta} + \frac{\partial \mathbf{u}}{\partial \theta^\alpha}\frac{\partial \mathbf{x}^0}{\partial \theta^\beta}\right) && \text{(D.4)} \end{aligned}$$

and the symmetrical part of bending strain is:

$$\psi_{(\alpha,\beta)} = \frac{1}{2}\left(\mathbf{x}^0_{,\alpha}\cdot\Delta\mathbf{n}_\beta + \mathbf{x}^0_{,\beta}\cdot\Delta\mathbf{n}_\alpha + \mathbf{u}_{,\alpha}\cdot\mathbf{n}^0_{,\beta} + \mathbf{u}_{,\beta}\cdot\mathbf{n}^0_{,\alpha}\right) \tag{D.5}$$

The normal $\mathbf{n}$ is a unit vector, therefore only two independent variables are needed, the normal in current configuration is expressed with respect to the jacobian j:

$$\mathbf{n} = j^{-1}\left(\mathbf{x}_{,1}\times\mathbf{x}_{,2}\right) \tag{D.6}$$

and the linearised increment $\Delta\mathbf{n}$ can be derived as follows:

$$\Delta\mathbf{n} = \mathbf{n} - \mathbf{n}^0 \approx \left(j^0\right)^{-1}\left(\mathbf{u}_{,1}\times\mathbf{x}^0_{,2} + \mathbf{x}^0_{,1}\times\mathbf{u}_{,2}\right) \tag{D.7}$$

leading to partial derivatives of the increment:

$$\Delta\mathbf{n}_{,\alpha} = \left(j^0\right)^{-1}\left(\mathbf{u}_{,1\alpha}\times\mathbf{x}^0_{,2} + \mathbf{u}_{,1}\times\mathbf{x}_{,2\alpha} + \mathbf{x}^0_{,1\alpha}\times\mathbf{u}_{,2} + \mathbf{x}^0_{,1}\times\mathbf{u}_{,2\alpha}\right) \tag{D.8}$$

Since the element definition assumes only five degrees of freedom per node, a penalty function is used to constrain the in-plane rotation and the component strain to be penalised in the current configuration is:

$$\gamma_r = \mathbf{n}\cdot\frac{\mathbf{x}_{,\alpha}}{\sqrt{a_{\alpha\beta}}} \tag{D.9}$$

Since the integration points are the constitutive calculation points and control quantitatively the kinematic solution, the penalty function is applied on the area of reference surface $\Delta\mathcal{A}$ associated to its integration point. Such constraints are defined as an augmented stiffness as function of elastic moduli G_γ, thickness of shell t and a relaxation factor $q = 2.5\cdot10^{-5}$(Hughes et al. (1977)):

$$K_\gamma = \frac{G_\gamma t\Delta\mathcal{A}}{1+\frac{q\Delta\mathcal{A}}{t^2}} \tag{D.10}$$

A general form of the strain energy per unit area in terms of membrane strain and bending strains can be stated as:

$$W = \mathbf{A}\left(\epsilon_{\alpha\beta}\otimes\epsilon_{\alpha\beta}\right) + \mathbf{B}\left(\psi_{\alpha\beta}\otimes\psi_{\alpha\beta}\right) \tag{D.11}$$

where **A** and **B** are constant rank four contravariant tensors, formulated with respect to shape of undeformed surface and its properties.

And internal energy becomes dependent on transverse shear stiffness constrained at integration points r, and also, adjusted stiffness with the active 6^{th} degree of freedom on node n:

$$\Phi^{int} = \int_{\Omega} W \mathrm{d}\Omega = \int_{\mathcal{A}} \int_{h} \sigma_{\alpha\beta} \epsilon_{\alpha\beta} \mathrm{d}z \mathrm{d}A + \sum_{r} K_{\gamma} \gamma_r \delta\gamma_r + \sum_{n} K_n \gamma_n \delta\gamma_n \tag{D.12}$$

where $\sigma_{\alpha\beta}$ are Kirchhoff stresses at a point

Appendix E

Global Approximation

This Appendix contains details of the surrogate model employed in this thesis, after a brief insight into the approximation models used in the literature.

E.1 Overview of approximation methods

Optimisation in the engineering design field, especially in the area of aerospace structures, is iterative in nature and includes large scale analyses required by computational models. The cost of such models is increased by the number of mutually interacting disciplines employed and also by the number of conflicting goals. Such applications often call high-fidelity codes to assess the performance of the system under consideration, becoming prohibitively expensive, and limiting the exploration of the design space. Consequently, statistical approximation methods have been developed over the past 15 years and gained large popularity for their use in exploring multi-modal design spaces.

As these methods have grown in popularity, a variety of curve fitting techniques have been employed to approximate engineering functions, starting from low order polynomials (typically cubic or quadratic), notoriously known for their capability of erroneously predicting optima of multimodal functions, to more advanced methods, such as *Kriging* (Sacks et al. (1989), Cressie (1993), Jones (2001b)). A key point in using surrogates to approximate unknown functions is whether the model is to be interpolated or regressed. The difference depends on the relationship of the data set to the fitting curve, by assuming the presence or absence of errors in the model. This has direct consequences on the accuracy of the approximation of augmented data sets, with improvements for interpolating surfaces (but only if the true function is smooth and continuous), whereas regressed models do not guarantee a more accurate representation.

The popularity of RSMs also stems from their reduced methodology complexity to attain the global optimum of a function. With a minimum computational budget, a database

can be built outside the optimiser by sampling the design space and using analysis tools (such approaches are often suited for use in a parallel computation environment), and then algebraic expressions are used to approximate the desired deterministic function.

The most simplistic response surface approximation is represented by polynomials and can be generalised as:

$$\hat{y}(\mathbf{x}_{n+1}) = \sum_{i=1}^{p} a_i \mathbf{\Phi}(\mathbf{x}_{n+1}). \tag{E.1}$$

where $(\mathbf{x}_{n+1})$ is a prediction point, a_i are coefficients derived using a singular value decomposition (see Press et al. (1992)) by solving the true function equation $\mathbf{y}$:

$$\mathbf{y} = \mathbf{\Phi}(\mathbf{x})\mathbf{a}. \tag{E.2}$$

and p is the number of regressors, $l < n$, with n the total number of points used in surface modeling and for $l = n$ an interpolation results. The function Φ determines the complexity of the approximation, and the simplest form can be described as a mean representation of the data $\mathbf{\Phi}_1(\mathbf{x}) = 1$. If the function has a linear variation, then $\mathbf{\Phi}_{1+i}(\mathbf{x}) = x_i$ is added to the mean. Squared terms added to the mean, in addition to the linear ones can be described as $\mathbf{\Phi}_{1+k+i}(\mathbf{x}) = x_i^2$ and also quadratic cross terms can enhance the shape by $\mathbf{\Phi}_{1+k+i}(\mathbf{x}) = x_i x_j$ with $j = \{i+1, \ldots, k\}$. As the degree of the predictor is increased, the system requires more data points in order to be built and can lead to ill-conditioned matrices, emphasising the practicality of low order polynomials, but which can lead to gross approximations in the global model of highly modal response surfaces.

The Radial Basis Function (RBF) approach offers more flexibility in the approximation model, by choosing a different representation of the kernel $\mathbf{\Psi}$, centered around the n points[1]:

$$\hat{y}(\mathbf{x}_{n+1}) = \sum_{i=1}^{p} a_i \mathbf{\Phi}(\mathbf{x}_{n+1}) + \sum_{i=1}^{n} b_i \mathbf{\Psi}(r_i), \tag{E.3}$$

where the coefficients b_i are derived to fit the data, and the kernel $\mathbf{\Psi}$ is based on the Euclidian distance $r_i = \| \mathbf{x}_{n+1} - \mathbf{x}_i \|$ of the data set $\mathbf{x}_i$ in conjuction to the interest point $\mathbf{x}_{n+1}$. The kernel can take up various forms to enhance the RBF representation, such as:

[1]The first term based on polynomials compactly supports RBS kernels to have sparse Gram matrices, and can add a significant advantage for specific applications dealing with large data sets (Wendland (1995))

$$
\begin{aligned}
\mathbf{\Psi}(r_i) &= \| \mathbf{x}_{n+1} - \mathbf{x}_i \| && \text{linear spline} \\
&= \| \mathbf{x}_{n+1} - \mathbf{x}_i \|^3 && \text{cubic spline} \\
&= \| \mathbf{x}_{n+1} - \mathbf{x}_i \|^2 \log(\| \mathbf{x}_{n+1} - \mathbf{x}_i \|) && \text{thin-plate spline} \\
&= \exp\left(-\frac{\| \mathbf{x}_{n+1} - \mathbf{x}_i \|}{\sigma^2} \right) && \text{Gaussian} \\
&= \exp\left[-\sum_{j=1}^{k} \theta_j (\| \mathbf{x}_{n+1,j} - \mathbf{x}_{i,j} \|^{p_j}) \right]. && \text{Kriging}
\end{aligned} \tag{E.4}
$$

where the variance σ^2 (i.e., Gaussian parameter) is optimised to make the kernels more robust to large variations across the design space (see Sacks et al. (1989)); θ_j and p_j are the hyperparameters in the Kriging process, which are stochastic in nature, and provide good statistical information about the quality of the approximation, including the effectiveness of the design variables in modeling the surrogate (see Jones (2001a)). In a full definition, the hyperparameters are assigned to each variable or groups of variables if statistical inference of local design spaces is required and are also tuned upon an improvement criteria to locate a maxima that potentially represents an optimum surrogate (such searches may require update methodologies in order to improve the RSM; these aspects are discussed in the following sections).

E.2 Kriging

The term Kriging is more widely known in statistics as Gaussian stochastic process modeling (Cressie (1993)). It was first used by Matherton (1963) who published the mathematical formulation for kriging, a development of the statistical techniques applied in mining and petroleum industry by the engineer D. G. Krige.

Considering a design space $\mathbf{x}$ of n independent and identically distribute variables, $\mathbf{x} = [\mathbf{x}_1, \ldots, \mathbf{x}_n]$, the general form of the Krig function is based on a linear regression kernel, that gives the trend of the true function

$$
\mathrm{y}(\mathbf{x}) = \sum_{i=1}^{k} \beta_i h_i(\mathbf{x}) + Z(\mathbf{x}), \tag{E.5}
$$

where h_i and β_i are known basis functions and their associated coefficients, and $Z(\mathbf{x})$ is a Gaussian random function that creates a local deviation from the global model (bias) and has zero mean and covariance:

$$Z(x_1, x_2) = \sigma^2 \mathbf{R}(x_1, x_2). \tag{E.6}$$

In most previous engineering applications, the Krig function is approximated by a constant in addition to the errors, where the constant can have different statistical meanings, e.g., mean of data (Jones (2001b)), or a random variable from Bayesian statistics with known *a priori* distribution (Sacks et al. (1989)).

The Kriging and Gaussian basis functions from equations E.4 are centered around a sample point and dependent on the Euclidian distance from it. Intuitively, a sampled point near the parameter space strongly influences the surface and less if the point is farther away. This influence is intrinsically linked to the norm r_i that respectively increases and diminishes. Statistically, one can state that the vectors in the norm are correlated, so that the uncertainty in the model can readily be derived. Sacks et al. (1989) offered a choice for the directional spatial correlation parameter as a matrix form:

$$\mathbf{R}(\mathbf{x}_i, \mathbf{x}_j) = \exp\left[-\sum_{j=1}^{k} 10^{\theta_j} \left(\parallel \mathbf{x}_{n+1,j} - \mathbf{x}_{i,j} \parallel^{p_j}\right)\right] + 10^{\lambda}\delta_{ij}, \tag{E.7}$$

where λ is a third hyperparameter that controls the degree of regression of the data (set to zero, the data is interpolated); $\mathbf{R}(\mathbf{x}_i, \mathbf{x}_j)|_{i=j} = 1 + 10^{\lambda}$ (i.e., perfect correlation) and δ_{ij} is the Dirac delta function. The regularisation constant λ is considered in all the underlying models in this work due to the noise encountered during the MDO process, that can alter the smoothness and continuity of the response.

The correlation matrix $\mathbf{R} \in \mathbb{R}^{n\,\mathbf{x}\,n}$ for all the points becomes:

$$\mathbf{R} = \begin{pmatrix} 1 + 10^{\lambda} & \mathbf{R}(\mathbf{x}_1, \mathbf{x}_2) & \cdots & \mathbf{R}(\mathbf{x}_1, \mathbf{x}_n) \\ \mathbf{R}(\mathbf{x}_2, \mathbf{x}_1) & 1 + 10^{\lambda} & \cdots & \mathbf{R}(\mathbf{x}_2, \mathbf{x}_n) \\ \vdots & & \ddots & \vdots \\ \mathbf{R}(\mathbf{x}_1, \mathbf{x}_2) & \mathbf{R}(\mathbf{x}_n, \mathbf{x}_2) & \cdots & 1 + 10^{\lambda} \end{pmatrix}. \tag{E.8}$$

If the vector of responses is defined as $\mathbf{y} = [\mathbf{y}_1, \ldots, \mathbf{y}_n]^T$ with mean μ, then the Gaussian probability density function (i.e., normal PDF) associated to the response vector $\mathbf{y}$ is defined as:

$$\text{pdf}\left(\mathbf{y} \mid \sigma^2, \mu\right) = \frac{1}{\sigma\sqrt{2\pi}} \exp\left(-\frac{(y-\mu)^2}{2\sigma^2}\right), \tag{E.9}$$

where the stochastic parameters σ^2 is the variance and μ is the mean of the response vector $\mathbf{y}$. Therefore, the likelihood function for a set of independent predictors can be written as:

$$\begin{aligned} L\left(\mathbf{y} \mid \sigma^2, \mu\right) &= \prod_{i=1}^{n} \text{pdf}\left(y_i \mid \sigma^2, \mu\right) \\ &= \frac{1}{\left(\sigma^2\right)^{\frac{n}{2}} (2\pi)^{\frac{n}{2}} |\mathbf{R}|^{\frac{1}{2}}} \exp\left(-\frac{(\mathbf{y}-\mathbf{1}\mu)\mathbf{R}^{-1}(\mathbf{y}-\mathbf{1}\mu)}{2\sigma^2}\right). \end{aligned} \tag{E.10}$$

Mathematically, the likelihood function E.10 is easier to manipulate by taking its logarithm of it. This log-likelihood function has the form:

$$\ln L\left(\mathbf{y} \mid \sigma^2, \mu\right) = -\frac{n}{2}\log\left(\sigma^2\right) - \frac{1}{2}\log(|\mathrm{R}|) - \frac{(\mathbf{y}-\mathbf{1}\mu)\mathbf{R}^{-1}(\mathbf{y}-\mathbf{1}\mu)}{2\sigma^2} + \text{constant} \tag{E.11}$$

Thus, the parameter estimates (which maximise equation E.11) are derived from setting the partial derivative of the log function to zero:

$$\frac{\partial\left(\ln L\left(\mathbf{y} \mid \sigma^2, \mu\right)\right)}{\partial\sigma^2} = 0 \tag{E.12}$$

$$\text{and} \quad \frac{\partial\left(\ln L\left(\mathbf{y} \mid \sigma^2, \mu\right)\right)}{\partial\mu^2} = 0 \tag{E.13}$$

and the parameter estimates become:

$$\hat{\sigma}^2 = \frac{(\mathbf{y}-\mathbf{1}\hat{\mu})^T\mathbf{R}^{-1}(\mathbf{y}-\mathbf{1}\hat{\mu})}{n} \tag{E.14}$$

$$\hat{\mu} = \frac{\mathbf{1}^T\mathbf{R}^{-1}\mathbf{y}}{\mathbf{1}^T\mathbf{R}^{-1}\mathbf{1}} \tag{E.15}$$

Substituting values of estimators $\hat{\mu}$ from equation E.15 and $\hat{\sigma}^2$ from equation E.14 into equation E.11, the concentrated log-likelihood function can be expressed as:

$$\ln L_{max}\left(\mathbf{y} \mid \hat{\sigma}^2, \hat{\mu}\right) = -\frac{n}{2}\log\left(\hat{\sigma}^2\right) - \frac{1}{2}\log(|\mathrm{R}|) \tag{E.16}$$

The hyperparameter estimates $\hat{\theta_j}$, $\hat{p_j}$ and $\hat{\lambda}$ are tuned (i.e., optimised) to best represent the data $\mathbf{y}$ upon the maximum log-likelihood function. Since the underlying problem can be highly modal, a hybrid search is required, comprising usually of a global search

(e.g., GA), followed gradient-based search (e.g., DHC). Once the parameters are tuned, a prediction $\hat{\mathbf{y}}$ at new point $\mathbf{x}_{n+1}$ is possible. By augmenting the initial set of points $\mathbf{x}_n$ (see equation E.17), quantitative measures of the consistency of the estimate of the new point are provided using the set of hyperparameters that maximised the log-likelihood function

$$\check{\mathbf{y}} = (\mathbf{y}, \hat{y}_{n+1})^T . \tag{E.17}$$

The augmented correlation matrix becomes:

$$\check{\mathbf{R}} = \begin{pmatrix} \mathbf{R} & \vdots & \mathbf{r} \\ \dots & & \\ \mathbf{r}^T & & \mathbf{1} + 10^{\lambda} \end{pmatrix} \tag{E.18}$$

where component $\mathbf{r}$ is the vector of correlations of the initial data set and the new prediction point:

$$\mathbf{r} = (\mathbf{R}(\mathbf{x}_1, \mathbf{x}_2), \dots, \mathbf{R}(\mathbf{x}_1, \mathbf{x}_{n+1})^T \tag{E.19}$$

The augmented log likelihood which is to be maximised following the kernel of equation E.11 becomes:

$$\ln \check{L}_{max}\left(\mathbf{y} \mid \hat{\sigma}^2, \hat{\mu}\right) = -\frac{(\check{\mathbf{y}} - \mathbf{1}\hat{\mu})\check{\mathbf{R}}^{-1}(\check{\mathbf{y}} - \mathbf{1}\hat{\mu})}{2\hat{\sigma}^2} \tag{E.20}$$

The explicit augmented log-likelihood function (ignoring the constant terms) can be expressed by substituting equations E.17 and E.18 into E.20, as follows:

$$\ln \check{L}_{max}\left(\mathbf{y} \mid \hat{\sigma}^2, \hat{\mu}\right) = \frac{\begin{pmatrix} \mathbf{y} - \mathbf{1}\hat{\mu} \\ \hat{y}_{n+1} - \hat{\mu} \end{pmatrix}^T \begin{pmatrix} \mathbf{R} & \vdots & \mathbf{r} \\ \dots & & \\ \mathbf{r}^T & & \mathbf{1} + 10^{\lambda} \end{pmatrix}^{-1} \begin{pmatrix} \mathbf{y} - \mathbf{1}\hat{\mu} \\ \hat{y}_{n+1} - \hat{\mu} \end{pmatrix}}{2\hat{\sigma}^2} \tag{E.21}$$

Based on Goldberger (1964), the inverse of the augmented correlation matrix can be expressed using partitioned inverse formulae, such as:

$$\check{\mathbf{R}} = \begin{pmatrix} \mathbf{R}^{-1} + \mathbf{R}^{-1}\mathbf{r}\left(\mathbf{1} - \mathbf{r}^T\mathbf{R}^{-1}\mathbf{r}\right)^{-1}\mathbf{r}^T\mathbf{R}^{-1} & \mid & -\mathbf{R}^{-1}\mathbf{r}\left(\mathbf{1} - \mathbf{r}^T\mathbf{R}^{-1}\mathbf{r}\right)^{-1} \\ -\left(\mathbf{1} - \mathbf{r}^T\mathbf{R}^{-1}\mathbf{r}\right)^{-1}\mathbf{r}^T\mathbf{R}^{-1} & \mid & \left(\mathbf{1} - \mathbf{r}^T\mathbf{R}^{-1}\mathbf{r}\right)^{-1} \end{pmatrix} \tag{E.22}$$

leading to the final form of augmented log-likelihood function, i.e., quadratic in $\hat{y}_{n+1}$:

$$\ln \check{L}_{max}\left(\mathbf{y} \mid \hat{\sigma}^2, \hat{\mu}\right) \simeq \left[\frac{-1}{2\hat{\sigma}^2\left(\mathbf{1} - \mathbf{r}^T\mathbf{R}^{-1}\mathbf{r}\right)}\right]\left(\hat{y}_{n+1} - \hat{\mu}\right)^2 + \left[\frac{\mathbf{r}^T\mathbf{R}^{-1}\left(\mathbf{y} - \mathbf{1}\hat{\mu}\right)}{\hat{\sigma}^2\left(\mathbf{1} - \mathbf{r}^T\mathbf{R}^{-1}\mathbf{r}\right)}\right]\left(\hat{y}_{n+1} - \hat{\mu}\right) \tag{E.23}$$

leading to the Kriging predictor solution, that maximises the augmented likelihood:

$$\hat{y}(\mathrm{x}_{n+1}) = \hat{\mu} + \mathbf{r}^T\mathbf{R}^{-1}(\mathbf{y} - \mathbf{1}\hat{\mu}) \tag{E.24}$$

Intuitively, if the prediction point $\mathbf{x}_{n+1}$ coincides to any of the $\mathbf{x}_i$ point in the initial data set ($\forall\, \mathrm{i} \in \{1, \ldots, n\}$), then $\mathbf{r} = \mathbf{R}_i$, and hence

$$\mathbf{r}^T\mathbf{R}^{-1} = \left(\mathbf{R}^{-1}\mathbf{r}\right)^{-1} = \left(\mathbf{R}^{-1}\mathbf{R}_i\right)^{-1} = \mathbf{e}_i^T \tag{E.25}$$

leading to the final check of the predictor that is interpolated:

$$\hat{y}(\mathrm{x}_{n+1}) = \hat{\mu} + \mathbf{e}_i^T(\mathbf{y} - \mathbf{1}\hat{\mu}) = \hat{\mu} + (\mathbf{y}_i - \hat{\mu}) = \mathbf{y}_i \tag{E.26}$$

More robust and sophisticated strategies to enhance the surrogate capabilities by means of convergence speed and also accuracy, are provided in literature, such as *mean square error* and *expected improvement*. The former method, being an attribute of the fitness of the RSM, minimises the uncertainty evolved under the prediction of a given data set $(\mathbf{x}, \mathbf{y})$, under the correlation effect of the error of the prediction point (i.e., the correlation also shows confidence of the prediction). The uncertainty factor is represented by the third expression in equation E.27 (see Sacks et al. (1989) and Cressie (1993) for full derivation of this formula). Intuitively, if the prediction point coincides to any of the points in the initial data set, following the procedure from equations E.25 and E.26, one can determine the mean square is zero, since the true deterministic function is known *a priori* in the sampled point.

$$s\left(\mathbf{x}_{n+1}\right)^2 = \hat{\sigma}^2\left[1 - \mathbf{r}^T\mathbf{R}^{-1}\mathbf{r} + \frac{\left(\mathbf{1} - \mathbf{r}^T\mathbf{R}^{-1}\mathbf{1}\right)^2}{\mathbf{1}^T\mathbf{R}^{-1}\mathbf{1}}\right] \tag{E.27}$$

In a minimisation problem, the *expected improvement* calculates the expectation of finding an improvement I over the current best functional f_{min} (Schonlau (1997)), and the improvement can be stated as $I = f_{min} - \hat{\mathbf{y}} > 0$, where $\hat{y}$ is a random variable in Kriging. The expected improvement $E(I)$ can be shown to be:

$$E\left[I(\mathbf{x})\right] = \begin{cases} \left(f_{min} - \hat{y}(\mathbf{x})\right)\Phi\left(\dfrac{f_{min} - \hat{y}(\mathbf{x})}{s(\mathbf{x}}\right) + s(\mathbf{x})\phi\left(\dfrac{f_{min} - \hat{y}(\mathbf{x})}{s(\mathbf{x})}\right) & \text{if } s(\mathbf{x}) > 0 \\ 0 & \text{if } s(\mathbf{x}) = 0 \end{cases} \tag{E.28}$$

where functions Φ and ϕ are the cumulative distribution function and the probability distribution function, respectively. The expectation E is zero if the root mean square error is null, this means the point $\mathbf{x}$ selected has already been sampled with no further room for improvement. This characteristic enhances the use of such methodology when the initial data set is augmented using deterministic tools. Hybrids of this approach are also suggested in the literature, for instance, Sóbester et al. (2005) who used a weighted formulation of the expected improvement, $E(I) = w\left[u\ \mathrm{cdf}(u)\right] + (1-w)\mathrm{pdf}(u)$, with emphasis on the trade-offs between local exploitation (w=1) and global exploration (w=0) of the design space, by switching between the predictor improvement (the first term) and the error of the predictor (second term). These schemes are readily used with single and multi-objective search tools, featured or not by weighting functions, so as to evolve high quality Pareto sets. The multi-objective frameworks often have drawbacks related to the balance between exploration and exploitation on the RSMs when building surrogates for each of the objectives. These issues are addressed and alleviated by Keane (2006), where enhanced statistical estimates of joint pdfs' (computed for two objectives) are developed in an expected improvement updating criteria. The updating point is sought to improve the Pareto front, and not only one objective (but these advances are outside the scope of this thesis).

References

I. H. Abbott and A. E. Von Doenhoff. *Theory of wing sections*. Dover, New York, 1959.

M. Abdulrahim, H. Garcia, and R. Lind. Flight characteristic of shaping the membrane wing of a micro air vehicle. *Journal of Aircraft*, 42(1):131–137, January-February 2005.

Report AGARD-AR-211. Test cases for inviscid flow field methods, May 1985.

J. J. Alonso, P. LeGresley, E. van det Weide, J. R. Martins, and J. J. Reuther. pyMDO: A framework for high-fidelity multi-disciplinary optimization. *AIAA 2004-4480*, August 30-1 September 2004.

C. F. An and R. M. Barron. Transonic euler computation in streamfunction co-ordinates. *International Journal for Numerical Methods in Fluids*, 20(1):75–94, 2005.

J. D. Anderson. *Introduction to Flight*. McGraw-Hill Book Company, New York, 1978.

F. Austin, M. J. Rossi, W. Van Nostrand, G. Knowles, and A. Jameson. Static shape control for adaptive wings. *AIAA Journal*, 32(9):1895–1901, September 1994.

M. J. Balas. Optimal quasi-static shape control for large aerospace antennae. *Journal of Optimization Theory and Applications*, 46(2):153–170, 1985.

F. Bauer, P. Garabedian, and D. Korn. Supercritical wing sections. *Lecture Notes in Economics and Mathematical Systems*, 66, Springer-Verlag, New York 1972.

Z. P. Bažant and L. Cedolin. *Stability of structures*. Dover , Mineola, New York, 1991.

P. G. Bergan, G. Horrigmoe, B. Krakeland, and T. H. Søreide. Solution techniques for nonlinear finite element problems. *International Journal of Numerical Methods in Engineering*, 12:1677–1696, 1978.

L. J. Bjarke. Flow visualisation study of a 1/48-scale AFTI/F111 model to investigate horizontal tail flow disturbances. Technical Report NASA-TM-101698, Ames Flight Research Centre, Edwards, CA, 1990.

B. Bochenek. On postbuckling constraints in structural optimization against instability. *Proceedings of the First World Congress of Structural and Multidisciplinary Optimization*, Edit. N. Olhoff and G. N. Rozvani, Germany:717–724, 1995.

V. V. Bolotin. *Dynamic stability of elastic systems.* Chapter 3, Holden-Day, Oakland, CA, 1964.

V. Braibant and C. Fleury. Shape optimal design using B-spline design. *Computer Methods in Applied Mechanics and Engineering*, 44:247–267, August 1984.

R. D. Braun, I. M. Kroo, and P. J. Gage. Post-optimality analysis in aerospace vehicle design. Technical Report AIAA-93-3932, NASA, 1993.

F. A. Brogan and B. O. Almroth. Practical methods for elastic collapse analysis of shell structures. *AIAA Journal*, 9:2321–2325, 1971.

B. Budiansky, P. Seide, and R. A. Weiberger. The buckling of a column on equally spaced deflectional and rotational springs. Technical Report 1519, NACA, 1948.

D. Cadogan, T. Smith, F. Uhelsky, and M. MacKusic. Morphing inflatable wing development for compact package unmanned aerial vehicles. *AIAA 2004-1807 SDM Adaptive Structures*, 2004.

J. Cai and F. Liu. Static aero-elastic computation with a coupled CFD and CSD method. *AIAA 01-0717*, January 8-11 2001.

K. J. Calahan and G. E. Weeks. Optimum design of composite laminates using genetic algorithms. *Composite Engineering*, 2(3):149–160, 1992.

R. I. Campbell. An approach to constrained design with application to airfoils. Technical Report NASA-TP-3260, NASA, 1992.

R. L. Campbell. Efficient viscous design of realistic aircraft configurations. Technical Report AIAA-98-2539, NASA, 1998.

R. H. Carmichael and W. Pfenninger. Low drag boundary layer suction experiments in flight on the wing glove of an F94A airplane, Phase III: laminar suction airfoil tolerances. Technical Report BLC-101, Northrop Aircraft Inc., 1957.

R. H. Carmichael, R. C. Whites, and R. E. Wisma. Low drag boundary layer suction experiments in flight on the wing glove of an F94A airplane, Phase IV: suction through 81 slots between 8% chord and 95% chord. Technical Report BLC-102, Northrop Aircraft Inc., 1957.

P. W. Carpenter and P. N. Green. The aeroacoustics and aerodynamics of high-speed Coanda devices, Part 1: conventional arrangement of exit nozzle and surface. *Journal of Sound and Vibration*, 208(5):777–801, 1997.

E. Carrera. A study on arc-length type methods and their operation failures illustrated by a simple model. *Computers and Structures*, 50, 1994.

E. Chatlynne, N. Rumingny, M. Amitay, and A. Glezer. Virtual aero-shaping of a Clark-Y airfoil using synthetic jet actuators. *AIAA 2001-0723*, 2001.

Z. Chaundhry and C. A. Rogers. Bending and shape control of beams using SMA actuators. *Journal of Intelligent Material Systems and Structures*, 2, October 1991.

F. J. Chen and G. B. Beeler. Virtual shaping of a two-dimensional NACA 0015 airfoil using synthetic jet actuator. *AIAA 2002-3273*, 2002.

J. Cohen. A power primer. *Pshychological Bulletin*, 112:155–159, 1992.

F. S. Collier. An overview of recent subsonic laminar flow control flight experiments. *21st AIAA Aerospace Sciences Meeting*, AIAA 93-2987, January 10-13, Reno, US 1993.

N. A. C. Cressie. *Statistics for spatial data*. John Wiley & Son, Inc, 1993.

M. A. Crisfield. *Non-linear Finite Element Analysis of Solids and Structures*, volume 1. John Wiley & Sons Ltd, England, 1997.

M. A. Crisfield and J. Shi. *A review of solution procedures and path-following techniques in relation to the non-linear finite element analysis*. Non-Linear Computational Mechanics, Editors: P. Wriggers and W. Wagner, Springer-Verlag, 1991.

W. J. Crowther. Control of separation on a trailing edge flap using air jet vortex generators. *Journal of Aircraft*, 2005.

T. Dang, S. Damle, and X. Qiu. Euler-based inverse method for turbomachine blades, Part 2: three-dimensional flows. *AIAA Journal*, 38(11):2007–2013, 2000.

D. J. Dawe. Buckling and vibration of plate structures including shear deformation and related effects. Aspects of the Analysis of Plate Structures, Ed. by Dawe, D. J., Horsington, R. W., Kamtekar, A. G. and Little, G. H., New York, Oxford University Press, 1985.

K. Deb, S. Agrawal, A. Pratap, and T. Meyarivan. A fast elitist non-dominated sorting algorithm for multi-objective optimization: NSGA-II. *Lecture Notes in Computer Science*, 1917:848–849, 2000.

A. Demeulenaere. An Euler/Navier-Stokes inverse method for compressor and turbine blade design. *Inverse design and optimisation methods*, Lecture Series, Rhode-Saint-Genese Belgium, 21-25 April 1997.

C. D. Diebler and S. B. Cumming. The active aeroelastic wing aerodynamic model development and validation for a modified F/A-18A airplane. Technical Report NASA-TM-2005-213668, NASA Kennedy Space Center, Florida, 2005.

J. Dong, K. K. Choi, and N. H. Kim. Design optimization for structural-acoustics problems using FEA-BEA with adjoint variable method. *Journal of Mechanical Design*, 126(3):527–533, 2004.

G. S. Dulikravich and B. H. Dennis. Inverse design and optimization using CFD. *European Congress on Computational Methods in Applied Sciences and Engineering*, ECCOMAS 2000, September 2000.

W. H. DuMouchel and F. L. O'Brien. Integrating a robust option into a multiple regression computing enviroment. *Computer Science and Statistics: Proceedings of the 21^{s}t Symposium on the Interface*, 1989.

A. Eriksson, C. Pacoste, and A. Zdunek. Numerical analysis of complex instability behaviour using incremental-iterative strategies. *Computer Methods in Applied Mechanics and Engineering*, 179:265–305, 1999.

H. A. Eschenhauer, V. V. Kobelev, and A. Schumacher. Bubble method for topology and shape optimization of structures. *Structural Optimization*, 8:121–139, 1994.

G. Farin. *Curves and surfaces for Computer-Aided geometric Design: a practical guide.* Academic Press, 1992.

W. B. Fichter and M. W. Pinson. Load-shortening behavior of an initially curved eccentrically loaded column. Technical Report NASA-TM-101643, NASA, 1989.

J. J. Finnigan. A streamline coordinate system for distorted two-dimensional shear flows. *Journal of Fluid Mechanics Digital Archive*, 30:241–258, 1983.

C. M. Fonseca and P. J. Fleming. Genetic algorithms for multiobjective optimization: formulation, discution and generalization. *Proceedings of Fifth International Conference on Genetic Algorithms*, 849-858, 1993.

A. J. Forrester, Andras Sóbester, and A. J. Keane. Optimization with missing data. *Proceedings of the Royal Society*, 462:935–945, 2006.

P. K. Freakley and A. D. Payne. *Theory and Practice of Engineering with Rubber.* London: Applied Science Publishers, 1978.

M. I. Frecker. Recent advances in optimization of smart structures and actuators. *Journal of Intelligent Material Systems and Structures*, 14:207–216, April-May 2003.

S. E. Gano, J. E. Renaud, S. M. Batill, and A. Tovar. Shape optimization for conforming airfoils. *AIAA 2003-1579*, 2003.

P. R. Garabedian and D. G. Korn. Numerical design of numerical airfoils. *Proceedings of SYNSPADE*, Academic Press, New York:253–271, 1971.

F. H. Gern, D. J. Inman, and R. K. Kapania. Structural and aeroelastic modeling of general planform wings with morphing airfoils. *AIAA Journal*, 40(4):628–637, April 2002.

L. J. Gibson and M. F. Ashby. *Cellular Solid Structures and Properties.* Cambridge University Press, 2^{nd} edition, 1977.

J. L. Gilarranz, L. W. Traub, and O. K. Rediniotis. A new class of synthetic jet actuators - Part I: Design, fabrication, and bench top characterization. *Journal of Fluids Engineering*, 127:367–376, 2005a.

J. L. Gilarranz, L. W. Traub, and O. K. Rediniotis. A new class of synthetic jet actuators - Part II: Application to flow separation control. *Journal of Fluids Engineering*, 127: 377–387, 2005b.

M. B. Giles and M. Drela. Two-dimensional transonic aerodynamic design method. *AIAA Journal*, 25(9):1199–1206, 1987.

G. Gilyard. In-flight transport performance optimization: an experimental flight research program and an operational scenario. Technical Report NASA-TM-97-206229, Dryden Flight Research Centre, Edwards, CA, 1997.

G. Gilyard, J. Georgie, and J. S. Barnicki. Flight test of an adaptive configuration optimization system for transport aircraft. Technical Report NASA-TM-1999-206569, Dryden Flight Research Centre, Edwards, CA, 1999.

A. S. Goldberger. *Econometric theory*. John Wiley, New York, 1964.

G. P. Guruswamy. Coupled finite-difference/finite-element approach for wing-body aeroelasticity. *AIAA Paper 92-4680*, September 1992.

R. T. Haftka and B. Prasad. Optimum structural design with plate bending elements - a survey. *AIAA Journal*, 19:517–522, 1981.

W. E. Haisler, J. A. Stricklin, and J. E. Key. Displacement incrementation in nonlinear structural analysis by self-correcting method. *International Journal of Numerical methods in Engineering*, 11(1):3–10, 1977.

H. R. Henne. Wing design by numerical optimization. *Journal of Aircraft*, 15:407–412, 1978.

P. A. Henne. An inverse transonic wing design method. *Journal of Aircraft*, 18(2): 121–127, 1981.

J. H. Holland. *Adaptation in natural and artificial systems: an introductory analysis with applications to biology, control and artificial intelligence*. The MIT Press, 1992.

P. J. Hubert. *Robust Statistics*. Wiley-Interscience, New York, 1981.

T. J. R. Hughes, R. L. Taylor, and W. Kanoknukulchai. A simple and efficient finite element for plate bending. *International Journal for Numerical Methods in Engineering*, 11(10):1529–1543, 1977.

D. J. Inman, F. H. Gern aand H. H. Robertshaw, R. K. Kapania, G. Pettit, A. Natarajan, and E. Sulaeman. Comments on prospects of fully adaptive wings. 8^{th} *International Conference on Smart Structures and Materials*, Newport Beach, CA, March 5-8 2001.

A. Jameson and J. C. Vassberg. Computational fluid dynamics for aerodynamic design: Its current and future impact. *39th AIAA Aerospace Sciences Meeting & Exhibit*, AIAA 2001-0538, January 2001.

D. R. Jones. Global optimization based on response surfaces. *Journal of global optimization*, 21:345–383, 2001a.

D. R. Jones. A taxonomy of global optimization methods based on response surfaces. *Journal of Global Optimisation*, 21:345–383, 2001b.

T. V. Karman. *Mathematical methods in engineering*. McGraw-Hill, New York, 1940.

A. J. Keane. Statistical improvement criteria for use in multiobjective design optimization. *AIAA Journal*, 44(4), 2006.

A. J. Keane and P. B. Nair. *Computational methods for aerospace design: the pursiut of excellence*. John Wiley and Sons, Chicester, 2005.

J. J. Keller. Inverse euler equations. *Z. Angew. Math. Phys.*, 49:363–383, 1998.

J. J. Keller. Inverse equation. *Physics of Fluids*, 11(2):513–520, March 1999.

N. S. Khot, K. Appa, J. Ausman, and F. E. Eastep. Deformation of a flexible wing using an actuating system for a rolling maneuver wihtout ailerons. *AIAA 98-1802*, pages 876–884, 1998.

M. T. Kikuta. Mechanical properties of candidate materials for morphing wings. Master's thesis, Blacksburg, Virginia, 2003.

H. Kim. *Statistical Modeling of Simulation Errors and Their Reduction via Response Surface Techniques*. PhD thesis, Virginia Polytechnic Institute and State University, June 2001.

U. Kirsch. *Structural optimization: fundamentals and applications*. Springer-Verlag, Berlin, 1993.

W. T. Koiter. Some properties of completely symmetric multilinear forms with an application to Ho's theorem for multi-mode buckling. Laboratory report, Technological University of Delft, 1976.

J. N. Kudva. Overview of DARPA/AFRL/NASA smart wing program. *SPIE Proceedings*, 3674(26), March 1-4, Newport Beach, CA 1999.

J. N. Kudva. Overview of the DARPA smart wing project. *ournal of Intelligent Material Systems and Structures*, 15:261–267, 2004.

J. N. Kudva, K. Appa, C. B. Van Way, and A. J. Lockyer. Adaptive smart wing design for military aircraft: requirements, concepts, and payoffs. *Proceedings of SPIE*, Smart Structures and Materials: Industrial and Commercial Applications of Smart Structures Technologies, 2447:35–44, 1995.

F. Lalande, Z. Chaundhry, and C. A. Rogers. A simplified geometrically nonlinear approach to the analysis of the Moonie actuator. *IEEE Trans. on Ultrasonics, Ferroelectrics and Frequency Control*, 42(1):21–27, January 1995.

O. Leonard. Subsonic and transonic cascade design. *AGARD*, Special Course on Inverse Methods for Airfoil Design for Aeronautical and Turbomachinery Applications(SEE N91-18035 10-02), 1990.

R. Levy and A. Ganz. Analysis of optimized plates for buckling. *Computers and Structures*, 41:1379–1385, 1991.

Q. S. Li. Buckling analysis of non-uniform bars with rotational and translational springs. *Engineering Structures*, 25:1289–1299, 2003.

M. J. Lighthill. A mathematical method of cascade design. *Reports and Memoranda*, 2104, 1945a.

M. J. Lighthill. A new method for two-dimensinal aerodynamic design. *Reports and Memoranda*, 2112, 1945b.

R. Lind, M. Abdulrahim, K. Boothe, and P. Ifju. Morphing for flight control of micro air vehicles. *Proceedings of the European Micro Air Vehicle Conference*, Braunschweig, Germany, July 2004.

M. Love, T. De La Garza, E. Charlton, and D. Egle. Computational aeroelasticity in high performance aircraft flight loads. *ICAS Congress*, 2000.

M. H. Love, P. S. Zink, R. L. Stroud, D. R. Bye, and C. Chase. Impact of actuation concepts on morphing aircraft structures. *45^{th} AIAA/ASME/ASCE/AHS/ASC Structures, Structural Dynamics & Materials Conference, AIAA 2004-1724, Palm Springs, CA*, 19-22 April 2004.

A. E. Lovejoy and R. K. Kapania. Static and vibration analyses of general wing structures using equivalent-plate models. Technical Report CCMS-94-09 Center for Composite Materials and Structures, Polytechnic Inst. and State Univ., Blacksburg, Virginia, August 1994.

K. J. Lu and S. Kota. Synthesis of shape morphing compliant mechanisms using a load path representation method. *Smart Structures and Materials*, 5049:337–348, 2003.

E. Lund, H. Møller, and L. A. Jacobsen. Shape design optimization of stationary fluid-structure interaction problems with large displacements and turbulence. *Structural and Multidisciplinary Optimization*, 25:383–392, 2003.

G. Lyn and N. J. Mills. Design of foam crash mats for head impact protection. *Sports Engineering*, 4:153–163, 2001.

F. T. Lynch. Commercial transports aerodynamic design for cruise performance efficiency. *Transonic Perspective Symposium, Progress in Aeronautics and Astronautics*, 81:81–147, 1982.

D. Manickarajah, Y. M. Xie, and G. P. Steven. Evolutionary method for optimization of plate buckling resistance. *Finite Elements in Analysis and Design*, 29:205–235, 1998.

C. A. Martin, J. Bartley-Cho, and B. F. Carpenter. Design and fabrication of smart wing model and SMA control surfaces. *SPIE Proceedings*, 3674(27), March 1-4, Newport Beach, CA 1999.

J. D. Martin and T. W. Simpson. Use of Kriging models to approximate deterministic computer models. *AIAA Journal*, 43(4):853–863, April 2005.

G. Matherton. Principles of geostatistics. *Economic Geology*, 58:1246–1266, 1963.

G. B. McFadden. An artificial viscosity method for the design of supercritical airfoils. Technical Report COO-3077-158, New York University, 1979.

A. M. R. McGowan, A. E. Washburn, G. Horta, Lucas, G. Bryant, Robert, E. Cox, E. David, E. J. Siochi, P. L. Sharon, and N. M. Holloway. Recent results from NASA's morphing project. *Proceedings of SPIE*, Smart Structures and Materials 2002: Industrial and Commercial Applications of Smart Structures Technologies, 4698:97–111, 2002.

R. Mead. *The design of experiments*. Cambridge University Press, 1998.

G. Meauze. An inverse time marching method for the definition of cascade geometry. *Journal of Engineering Power, ASME*, 104:650–656, 1982.

N. Metropolis, A. W. Rosenbluth, A. H. Teller, and E. Teller. Equation of state calculations by fast computing machines. *Journal of Chemical Physics*, 21:1087–1092, 1953.

K. M. Miettinen. *Nonlinear multiobjective optimization*. Kluwer, Boston, 1999.

N. J. Mills and A. Gilchrist. Modelling the indentation of low density polymer foams. *Celullar Polymers*, 19:389–412, 2000.

N. J. Mills and G. Lyn. Design of foam padding for rugby posts. *Proceedings of TMS Conference on Materials and Science in Sports*, San Diego:105–117, 2001.

R. D. Mindlin. Influence of rotatory inertia and shear on flexural motions of isotropic,elastic plates. *Journal of Applied Mechanics*, 18:31–38, 1951.

D. Munday and J. Jacob. Active control of separation on a wing with conformal camber. *39^{th} AIAA Aerospace Sciences Meeting and Exhibit*, January 8-11, Reno 2001.

R. H. Myers and D. C. Montgomery. *Response Surface Methodology: Process and Product Optimization using Designed Experiments*. New York, John Wiley & Sons, Inc., 1995.

A. Natarajan, R. K. Kapania, and D. J. Inman. Aeroelastic optimization of adaptive bumps for yaw control. *Journal of Aircraft*, 41(1):175–185, January-February 2004.

D. A. Neal, M. G. Good, C. O. Johnston, H. H. Robertshaw, W. H. Mason, and D. J. Inman. Design and wind tunnel analysis of a fully adaptive aircraft configuration. *45^{th} AIAA/ASME/ASCE/AHS/ASC Structures, Structural Dynamics & Materials Conference, AIAA 2004-1727, Palm Springs, CA*, 19-22 April 2004.

G. Norris. Laminar flow control - smooth and supersonic. *Flight International*, 145 (4421):32–33, May 18-24 1994.

J. D. A. Ochoa. Large deflection stability of slender beam-columns with semirigid connections: Elastica approach. *Journal of Engineering Mechanics*, 130(3):274–282, March 2004.

J. T. Oden. Numerical formulation of nonlinear elasticity problems. *Journal of Structural Division*, ASCE, 93(ST3):235–256, June 1967.

R. W. Ogden. Large deformation isotropic elasticity: on the correlation of theory and experiment for compressible rubberlike solids. *Proceedings of the Royal Society of London, Series A*, 328(1575):567–583, June 1972.

R. W. Ogden. *Non-Linear Elastic Deformation*. Ellis Horwood, Chichester, UK, 1984.

R. W. Ogden, G. Saccomadi, and I. Sgura. Fitting hyperelastic models to experimental data. *Computational Mechanics*, 34:484–502, 2004.

N. Olhoff, L. A. Krog, and E. Lund. Optimization of multimodal eigenvalues. *Proceedings of the First World Congress of Structural and Multidisciplinary Optimization*, Edit. N. Olhoff and G. N. Rozvani, Germany:701–708, 1995.

M. D. Pandey and A. N. Sherbourne. Mechanics of shape optimization in plate buckling. *Journal of Engineering Mechanics, ASCE*, 118:1249–1266, 1992.

J. S. Pardo and J. A. Ochoa. Buckling reversals of axially restrained imperfect beam-columns. *Journal of Engineering Mechanics*, 125(4):401–409, April 1999.

Les Piegl and W. Tiller. *The NURBS book*. Springer Verlag, 2^{nd} edition, January 1997. ISBN 3540615458.

J. L. Pinkerton and R. W. Moses. A feasibility study to control airfoil shape unsing Thunder. Technical Report NASA TM-4767, Langley Research Centre, Hampton, VA, November 1997.

G. H. Powell and J. Simons. Improved iteration strategy for nonlinear structures. *International Journal of Numerical Methods in Engineering*, 17(1455-1467), 1981.

W. H. Press, B. P. Flannery, S. A. Teukolsky, and W. T. Vetterling. *Numerical Recipes in FORTRAN: The Art of Scientific Computing*. Cambridge, England: Cambridge University Press, 2^{nd} edition, 1992.

A. Rasheed. *Passive hypervelocity boundary layer control using an ultrasonically absorptive surface*. PhD thesis, California Institute of Technology, Pasadena, CA, 2001.

M. Redhe and L. Nilsson. Using space mapping and surrogate models to optimize vehicle crashworthiness design. *Proceedings of the 9^{th} AIAA/ISMO Symposium on Multidisciplinary Analysis and Optimization*, AIAA-2002-5536, September 4-6, Atlanta, Georgia 2002.

E. Reissner. The effect of transverse shear deformation on the bending of elastic plates. *Journal of Applied Mechanics*, 12:69–77, 1945.

E. Riks. The application of Newton's method to the problem of elastic stability. *Journal of Applied Mechanics*, Trans. ASME, 39:1060–1065, 1972.

E. Riks. An incremental approach to the solution of snapping and buckling problems. *International Journal of Solids and Structures*, 15:529–551, 1979.

M. R. Rivello. *Theory and mechanics of flight structures*. Chapter 14, McGraw-Hill, New York, 1969.

R. S. Rivlin. Large elastic deformations of isotropic materials. Fundamental concepts. *Philosophical Transactions of the Royal Society of London*, Series A 240:459–490, 1948.

D. W. Rossen and I. R. Grosse. A feature based shape optimization technique for the configuration and parametric design of flat plates. *Engineering with Computers*, 8(2): 81–91, March 1992.

P. J. Rousseuw and A. M. Leroy. *Robust Regression and Outlier Detection*. Wiley, New York, 1987.

G. I. N. Rozvany. *Structural design via optimality criteria*. Kluwer Academic Publishers, Dordrecht, 1989.

G. I. N. Rozvany, M. P. Bendsøe, and U. Kirsch. Layout optimization of structures. *Applied Mechanics Reviews*, 48:41–119, 1995.

J. Sacks, W. J. Welch, T. J. Michel, and H. P. Wynn. Design and analysis of computer experiments. *Statisical Science*, 4(4):409–435, 1989.

L. Saggere and S. Kota. Static shape control of smart structures using compliant mechanisms. *AIAA Journal*, 37(5):572–578, May 1999.

J. A. Samareh. of shape parameterization techniques for high-fidelity multidisciplinary shape optimization. *AIAA Journal*, 39(5):877–883, 2001.

B. Sanders, F. E. Eastep, and E. Forster. Aerodynamic and aeroelastic characteristics of wings with conformal control surfaces for morphing aircraft. *Journal of Aircraft*, 40(1):94–99, January-February 2003.

L. B. Scherer, C. A. Martin, K. Appa, J. N. Kudva, and M. N. West. Smart wing test results. *SPIE Proceedings*, 3044(2), 1997.

L. B. Scherer, C. A. Martin, M. West, J. P. Florance, C. D. Wieseman, A. W. Burner, and G. A. Fleming. DARPA/AFRL/NASA smart wing second wind tunnel test results. *SPIE Proceedings, Smart Structures and Materials*, 3674:249–259, 1999.

M. Schonlau. *Computer Experiments and Global Optimization*. PhD thesis, University of Waterloo, Waterloo, Canada, Ontario, 1997.

U. Schram and W. D. Pilkey. The application of rational B-splines for shape optimization. *Proceedings of the 1st World Congress of Structural and Multidisciplinary Optimization*, Ed. N. Olhoff and G. N Rozvany, 1995.

M. Schrodt, G. Benderoth, A. Kühhorn, and G. Silber. Hyperelastic description of polymer soft foams at finite deformations. *Technische Mechanik*, 25(3-4):162–173, 2005.

A. Seifert, S. Eliahu, D. Greenblatt, and I. Wygnanski. Use of piezoelectric actuators for airfoil separation control. *AIAA Journal*, 36(8):1535–1537, 1998.

T. W. Simpson, T. M. Mauery, J. J. Korte, and F. Mistree. Kriging models for global approximation in simulation-based multidisciplinary design optimization. *AIAA Journal*, 39(12):2233–2241, December 2001.

B. Smith, G. Rinaudot, K. Reed, and T. Wright. Initial graphics exhange specification (IGES), version 4.0. US Dept. of Commerce, National Bureau of Standards (NIST), NBRSIR 88-3813, June 1988.

M. J. Smith, D. H. Hodges, and C. E. S. Cesnik. An evaluation of computational algorithms to interface between CFD and CSD methodologies. Technical Report WL-TR-96-3055, USAF Wright Laboratories, November 1995.

A. Sóbester, S. J. Leary, and A. Keane. On the design of optimization strategies based on global response surface approximation methods. *Journal of Global Optimization*, 33(1):31, 59 2005.

I. M. Sobol. On the systematic search in a hypercube. *SIAM Journal of Numerical Analysis*, 16:790–793, 1979.

W. R. Spillers and R. Levy. Optimal design for plate buckling. *Journal of Structural Engineering, ASCE*, 116:850–858, 1990.

E. Stanewski. Adaptive wing and flow control technology. *Progress in Aerospace Sciences*, 37(7):583–667, October 2001.

J. D. Stanitz. Design of two-dimensional channels with prescribed velocity distributions along the channel walls. Technical Report 1115, NASA, 1953.

J. D. Stanitz. General design method for three-dimensional potential flow fields. Technical Report NASA-CR-3288, NASA, 1980.

E. Steen. Application of the perturbation method to plate buckling problems. Research Report in Mechanics 98-1, Mechanics Division, Department of Mathematics, University of Oslo, 1998.

M. Stein. The phenomenon of change in buckle pattern in elastic structures. Technical Report NASA-TR-R39, NASA, 1959.

J. A. Stricklin, W. E. Haisler, and W. A. Von Riesemann. Self-correcting initial value formulations in nonlinear structural mechanics. *AIAA Journal*, 9:2066–2067, 1971.

R. D. Thomson, A. E. Birkbeck, W. L. Tan, L. F. McCafferty, S. Grant, and J. Wilson. The modelling and performance of training show cushioning systems. *Sports Engineering*, 2:109–120, 1999.

B. Tian. *Computational aeroelastic analysis of aircraft wings including geometric nonlinearity*. PhD thesis, Aerospace Engineering and Engineering Mechanics, University of Concinnati, 2003.

P. S. Timoshenko and J. M. Gere. *Theory of Elastic Stability*. McGraw-Hill, 1961.

M. A. Torkamani, M. Sonmez, and J. Cao. Second-order elastic plane-frame using finite element method. *Journal of Structural Engineering*, 123(9):1225–1235, 1997.

E. H. Twizell and R. W. Odgen. Non-linear optimization of the material constants in Ogden's stress-deformation function for incompressible isotropic elastic materials. *Journal of the Australian Mathematical Society*, B 24:424–434, 1983.

G. N. Vanderplaats. *Numerical optimization techniques for engineering design, with applications*. McGraw-Hill, New York, 1984.

J. J. Varona. An inverse method for transonic wing design. *International Journal of Numerical Methods in Engineering*, 44:249–264, 1999.

M. A. Vaz and D. F. C. Silva. Post-buckling analysis of slender elastic rods subjected to terminal forces. *International Journal of Non-Linear Mechanics*, 38:483–492, 2003.

Farnborough DERA VGK. Method for two-dimensional aerofoil sections. ESDU 96028, ESDU 96029, 1997.

G. Volpe and R. E. Melnik. The design of transonic aerofoils by a well-posed inverse method. *International Journal for Numerical Methods in Engineering*, 22(2):341–361, June 1986.

T. Von-Karman. Festigkeitsprobleme in maschienbau. *Encyklopädie der matematischen Wissenschafen*, 4:349, Chapter 27, 1970.

D. Voracek, E. Pndleton, E. Reichbach, K. Griffin, and L. Welch. The active aeroelastic wing phase I flight research through january 2003. Technical Report NASA-TM-2003-210741, Dryden Flight Research Centre, 2003.

I. Voutchkov and A. J. Keane. Multiobjective optimization using surrogates. *Proceedings of the 7^{th} International Conference on Adaptive Computing in Design and Manufacture (ACDM)*, Bristol:167–175, 2006.

T. D Wager, M. C. Keller, S. C Lacey, and J. Jonides. Increased sensitivity in neuroimaging analyses using robust regression. *Neuro Image*, 26:99–113, 2005.

C. Y. Wang. Post-buckling of a clamped-simply supported elastica. *International Journal of Non-Linear Mechanics*, 32(6):1115–1122, 1997.

G. A. Wempner. Discrete approximations related to nonlinear theory of solids. *International Journal of Solids and Structures*, 7(11):1581–1591, 1971.

H. Wendland. Piecewise polynomial, positive definite and compactly supported radial basis functions of minimal degree. *Advances in Computational Mathematics*, 4:389–396, 1995.

Y. W. Wong and S. Pellegrino. Computation of wrinkle amplitudes in thin membranes. *43^{th} AIAA/ASME/ASCE/AHS/ASC Structures, Structural Dynamics and Materials Conference, US*, 22-25 Apr 2002.

D. Xu and G. K. Anamthasuresh. Freeform skeletal shape optimization of compliant mechanism. *Journal of Mechanical Design*, 125(2):253–261, 2003.

W. Ye, S. Mukherjee, and N. C. MacDonald. Optimal shape design of an electrostatic comb drive in microelectromechanical systems. *Journal of Microelectromechanical Systems*, 7(2):16–26, 1998.

H. S. Yoon, G. Washington, and W. H. Theunissen. Analysis and design of doubly curved piezoelectric strip-actuated aperture antennas. *IEEE Trans. on Antenna and Propagation*, 48(5):755–763, May 2000.

D. Yuret and M. de la Maza. Dynamic Hill Climbing: overcoming the limitations of optimization techniques. *Proceedings of the 2^{nd} Turkish Symposium on AI and ANNI*, 1993.

M. Zhou, Y. X. Gu, and G. N. Rozvany. Application of DCOC method to plates and shells. *Proceedings of the First World Congress of Structural and Multidisciplinary Optimization*, Edit. N. Olhoff and G. N. Rozvani, Germany:25–32, 1995.

E. Zitzler and L. Thiele. An evolutionary algorithm for multi-objective optimization: the Strength Pareto Approach. Computer Engineering and Communication Network Lab (TIK) 43, Swiss Federal Institute of Technology (ETH), Zurich, Switzerland, 1998.